Lipid Oil Nanodroplets for Hydrophobic Drug Delivery

Antonia Charalambous

Submitted in accordance with the requirements for the degree of
Doctor of Philosophy

The University of Leeds
School of Medicine

June 2018

The candidate confirms that the work submitted is her own, except where work which has formed part of jointly-authored publications has been included. The contribution of the candidate and the other authors to this work has been explicitly indicated below. The candidate confirms that appropriate credit has been given within the thesis where reference has been made to the work of others.

Chapter 4 contains data from a study describing the production of LONDs and their characterisation and *in vitro* evaluation.

V. Mico, **A. Charalambous**, S.A. Peyman, R.H. Abou-Saleh, A.F. Markham, P.L. Coletta and S.D. Evans. (2017). Evaluation of Lipid Stabilised Tripropionin Nanodroplets as a Delivery Route for Combretastatin A4. *International Journal of Pharmaceutics*, 526 (1-2), 547-555

Within the paper Figures 7 and 8 were produced by the author. The data in these figures is presented in a different format in Chapter 4.

Acknowledgements

I would firstly like to thank my supervisor Dr Louise Coletta for her invaluable help and support throughout this project, for giving me the opportunity to continue my MSc project into this PhD and enabling me to learn and develop my skills. Your enthusiasm is infectious and it was a pleasure working and learning from you. I would also like to thank my other supervisors, Professor Sir Alex Markham, Dr Ian Carr and Professor David Bonthron for their help and useful discussions.

Thank you to Professor Steve Evans for developing the LONDs and to Dr Sally Peyman and Dr Victoria Mico for producing them and providing all the characterisation information. Victoria, thank you for putting up with me and all my questions, for teaching me how to make LONDs and always being there when I needed support. I would also like to thank the Leeds Microbubble Consortium for useful discussions. Thank you to Dr James McLaughlan for developing the UARP and helping with ultrasound related work. Thank you to Professor Paul Loadman and Antonia Wierzbicki for their help in developing the LC-MS/MS method and to Jade Spencer and Amanda Race.

I would also like to thank everyone on Level 9, WTBB especially Ms Sarah Perry for teaching me different techniques and Professor Mark Hull for his constructive comments during lab meetings. Thank you to Dr Gemma Marston for assisting in the experimental work, in teaching me several techniques and for general support throughout this project. A special thank you to Dr Milene Volpato and Dr Nicola Ingram for helping me in various experiments and answering all my questions. Nikki much appreciation for reading parts of this thesis and for your feedback.

Thank you to my lab partner Dr Laura McVeigh for always being there, encouraging me and of course all your help in various experiments. Thank you to Imeshi Wijetunga for her support and for being up for a teacake and coffee break. I would also like to thank Anastasia Alataki my best friend, for always supporting me, for being there during the happy moments and the not so happy moments. If it wasn't for you and your "Νίτσα, μπορείς, πάμε δυναμικά" I don't think I would have come this far without giving up some days.

Lastly, I would like to thank my family and especially my grandparents, Androulla, Antonis, Winifred and Terry for being the best, always supporting me and believing in me. I will always be very grateful for your unconditional love. Thank you to Constantinos for always being by my side and supporting me through everything. Thank you to my brother Stefanos for making me laugh and just being you and of course for making me an auntie to my gorgeous niece Anastasia Katerina. Lastly, I would like to thank my parents Catherine and Pambos for always loving me and supporting me. Mum thank you for encouraging me to even go to university, for driving me there every day, holding my hand and telling me everything is going to be ok. Dad thank you for spoiling me and always believing in me. This thesis is dedicated to Catherine and Pambos Charalambous, mum and dad I love you.

Abstract

Delivery of anti-cancer drugs to tumours is a fundamental requirement for cancer treatment. However, failure of drugs to reach tumours at sufficient concentrations due to poor bioavailability, rapid metabolism and elimination compromises effective treatment. A substantial number of potent anti-cancer drugs, exhibit hydrophobic properties that hinder their clinical use. Therefore, there is an urgent need for the development of a hydrophobic drug delivery system (DDS) that aims to effectively deliver and controllably trigger the release of these agents. This may improve drug bioavailability, efficacy and reduce severe side effects.

Lipid-Oil-NanoDroplets (LONDs) are nanosized nanoemulsions and are proposed as a novel hydrophobic DDS for colorectal cancer (CRC) treatment. LONDs were produced using a two-step high pressure homogenisation process, producing LONDs with size ranges between 100-300 nm. The hydrophobic vascular disrupting agent Combretastatin A4 (CA4) was encapsulated and used as a proof-of-concept for LOND evaluation *in vitro* and *in vivo*. CA4 was dispersed in triacetin or tripropionin oil to form the LOND core, stabilised by a phospholipid-shell. Using a microfluidic production platform, CA4 LONDs were attached on-chip to gas-filled, phospholipid-shelled therapeutic microbubbles (thMBs). CA4 thMBs were targeted to vascular endothelial growth factor receptor 2 (VEGFR-2) and used as LOND delivery vehicles. An external ultrasound (US) destruction pulse applied at the tumour site was used to trigger targeted release and enhance delivery.

This project showed CA4 release and/or uptake from LONDs in both endothelial and human CRC cells by immunofluorescence and flow cytometry. Intratumoural delivery of CA4 LONDs was observed and quantified in CRC xenografts using liquid chromatography tandem mass spectrometry (LS-MS/MS). Administration of CA4 LONDs resulted in a modest tumour growth inhibition *in vivo,* while a reduction in tumour perfusion was observed with CA4 thMBs. Combination therapy of CA4 thMBs with a chemotherapeutic agent, irinotecan, further reduced tumour growth compared to irinotecan alone, potentially through reduction in tumour perfusion. These results suggest that LONDs may serve as a novel hydrophobic DDS, while thMBs could further enhance tumour specific delivery.

Table of Contents

List of Tables

List of Figures

Abbreviations

AAs	Anti-angiogenic agents
ADMET	Absorption, distribution, metabolism elimination and toxicity
APC	Adenomatous polyposis coli
Atto590-DOPE	Atto590 1,2-dioleoyl-sn-glycero-3-phosphoethanolamine
BSA	Bovine serum albumin
C_4F_{10}	Perfluorobutane
C_6F_{14}	Tetradecafluorohexane
CA4	Combretastatin A4
CA4G	Combretastatin A4 Glucuronide
CA4P	Combretastatin A4 Phosphate
CD31	Cluster of differentiation 31
Cdc2	Cyclin division cycle protein 2
CEHDA	Coaxial eletrohydrodynamic atomisation
CEPs	Circulating endothelial progenitor cells
CEUS	Contrast enhanced ultrasound
CIN	Chromosomal instability
CMSs	Consensus molecular subtypes
COX-2	Cyclooxygenase-2
CPT	Camptothecin
CPT-11	7-ethyl-10-[4-(1-piperidino)-1-piperidino] carbonyloxy camptothecin
CRC	Colorectal Cancer
CTFG	Connective tissue growth factor
DAB	3,3'-Diaminobenzidine
DAPI	6-diamidino-2-phenylindole
DCE-MRI	Dynamic contrast enhanced magnetic resonance imaging
DDS	Drug Delivery System

DLS	Dynamic Light Scattering
DMEM	Dulbecco's modified Eagle's medium
DMSO	Dimethyl Sulfoxide
DNA	Deoxyribonucleic acid
DOPE	1,2-Dioleoyl-sn-glycero-3-phosphoethanolamine
DOX	Doxorubicin
DPPC	1,2-dipalmitoyl-sn-glycero-3-phosphocholine
DPX	Dibutylphthalate polystyrene xylene
DSPC	1,2-distearoyl-sn-glycero-3-phosphocholine
DSPE	1,2-distearoyl-sn-glycero-3-phosphoethanolamine
DSPE-BPEG$_{2000}$	1,2-distearoyl-sn-glycero-3-phosphoethanolamine-N[biotinyl(polyethylene glycol-2000]
EDTA	Ethylenediamine tetraacetic acid
EE	Encapsulation efficacy
EMT	Epithelial to mesenchymal transition
EPR	Enhanced permeability and retention
ERK 1/2	Extracellular-regulated kinase 1 and 2
ESI	Electrospray ionisation
EtOH	Ethanol
FCS	Foetal calf serum
FDA	U.S Food and Drug Administration
FITC	Fluorescein-isothiocyanate
FOV	Field of view
GdDTPA	Gadolinium diethylenetriaminepentaacetate
GDP	Guanosine diphosphate
GTP	Guanosine triphosphate
H & E	Haematoxylin and Eosin
HFUS	High frequency Ultrasound
Hoechst 33342	bisBenzimide H 33342 trihydrochloride

HPLC	High-performance liquid chromatography
HRP	Horseradish peroxidase
HUVECs	Human Umbilical Vein Endothelial Cells
i.p.	Intraperitoneal
i.v.	Intravenous
ICAM-1	Intracellular adhesion molecule-1
IF	Immunofluorescence
IHC	Immunohistochemistry
KDR	Kinase insert domain
LC-MS/MS	Liquid chromatography tandem-mass spectrometry
LCT	Long chain triglyceride
LOD	Limit of detection
***Log*P**	Log_{10}*(Partition Coefficient)*
LONDs	Lipid Oil Nanodroplets
LOQ	Limit of Quantification
MALDI-MSI	Matrix-Assisted Laser Desorption/Ionisation Mass Spectrometry Imaging
MAPK	Mitogen activated protein kinase
MBs	Microbubbles
MeOH	Methanol
MI	Mechanical index
MMP-9	Matrix metalloproteinase 9
MPS	Mononuclear phagocytic system
MRI	Magnetic resonance imaging
MRM	Multiple reaction monitoring
MRS	Magnetic resonance spectroscopy
MSI	Mass Spectrometry Imaging
MT	Microtubules
MTD	Maximum tolerated dose

MVD	Microvessel density
MW	Molecular weight
NO	Nitric oxide
NP	Nanoparticle
O/W	Oil in water
OCT	Optical cutting temperature
PA	Peak area
PBS	Phosphate buffered saline
PD	Pharmacodynamics
PDI	Polydispersity index
PDX	Patient derived xenografts
PEG	Poly-(ethylene) glycol
PET	Positron emission tomography
PFA	Paraformaldehyde
PI	Propidium iodine
PI3K	Phosphatidylinositol 3-kinase
PK	Pharmacokinetics
PMMA	Poly(methyl methacrylate)
POPC	1-palmitoyl-2-oleoyl-sn-glycero-3-phosphocholine
Prep.	Preparation
PRF	Pulse repetition frequency
PTFE	Polytetrafluoroethylene
RBCs	Red blood cells
RGD	Cyclic arginine-glycine-aspartic acid
RPMI	Roswell Park Memorial Institute
s.c.	Subcutaneous
SCT	Short chain triglyceride
SEM	Scanning electron microscopy

SIR	Single ion recording
SMC	Smooth muscle cells
SN38	7-ethyl-10-hydroxycamptothecin
T	Trigger
TA	Triacetin
TBS	Tris buffered saline
TBST	Tris buffered saline with Tween-20
TEM	Transmission electron microscope
TGF-β	Transforming growth factor
ThMB	Therapeutic Microbubble
TI	Thermal index
TIMP-1	Tissue inhibitor of metalloproteinase-1
TNM	Tumour-node-metastasis
TPP	Tripropionin
Tx	Treatment
UARP	Ultrasound Array Research Platform
UDPGA	Uridine 5'-diphosphoglucuronic acid
UGTs	Uridine diphosphate (UDP)-glucuronosyltransferase
US	Ultrasound
UV-VIS	Ultraviolet-visible
VDAs	Vascular disruptive agents
VE	Vascular endothelial
VEGF	Vascular endothelial growth factor
VEGFR-2	Vascular endothelial growth factor receptor-2
5-FU	5-Fluorouracil

Chapter 1

Introduction

1.1 Colorectal Cancer

Colorectal cancer (CRC) is a major cause of cancer morbidity and mortality. It is the fourth most common cause of cancer related deaths worldwide and second most common in the UK, with over 1 million people diagnosed annually worldwide and over 40,0000 in the UK alone (Cancer Research UK, 2015). Although, a decline in the mortality and incidence rates of CRC has been reported since the early 1970s due to improved screening programmes for early detection, better and newly developed treatments, improved surgical techniques with an improved standard of pre and post-operative care and improvements in adjuvant therapy, more than 40% of patients diagnosed do not survive the disease (Cancer Research UK, 2015; Welch & Robertson, 2016).

1.1.1 CRC Carcinogenesis and molecular subtypes

Cancer is a disease whereby normal cells acquire the ability through a number of genetic alterations to divide, grow uncontrollably and avoid apoptosis (Hanahan & Weinberg, 2000, 2011). CRC carcinogenesis is a multistep process whereby a number of genetic alterations which may be inherited or occur sporadically over time from several years to decades (Welch & Robertson, 2016).

Vogelstein and Fearon (1988, 1990) first described CRC as a linear progression, following studies in colon tumours that arose in patients sporadically or occurred from hereditary Familial adenomatous polyposis, an autosomal dominant condition in which numerous benign adenomas develop in the colon of an affected person (Vogelstein *et al.*, 1988; Fearon & Vogelstein, 1990). Firstly, mutations in the Adenomatous polyposis coli (*APC*) tumour suppressor gene in the colon provide a growth advantage to the normal epithelium leading to the growth of a small benign adenoma, small adenomas are characterised by chromosomal instability (CIN) (Vogelstein *et al.*, 1988; Fearon & Vogelstein, 1990; Vogelstein *et al.*, 2013). CIN results from an imbalance in chromosome number, defects in chromosomal segregation, telomerase stability and DNA damage response (Pino & Chung, 2010). The *APC* gene along with other proteins such as Axin and glycogen synthase kinase 3 β (GSK3 β) form a complex that regulates the β-catenin-dependent Wnt signalling pathway, the activation of this pathway due to mutations in *APC* is regarded as one of the initiating events in CRC (Aoki & Taketo, 2007; Markowitz & Bertagnolli, 2009; Fearon, 2011). The Wnt signalling pathway is activated when β-catenin accumulates in the cytoplasm, followed by its translocation in the nucleus where it binds to DNA binding proteins (T cell factor-lymphocyte enhancer family, TCF), this binding

complex acts as a transcription activator of genes involved in cellular activation such as the c-Myc, proto-oncogene (Markowitz & Bertagnolli, 2009; Fearon, 2011).

Another major initiating step in the development of an adenoma is the activation of growth factor pathways such as prostaglandin signalling (Eberhart, Charles *et al.*, 1994; Sano *et al.*, 1995). Cyclooxygenase-2 (COX-2) is one of the enzymes mainly responsible for the production of prostaglandin E_2 (PGE_2), which promotes inflammation and cell proliferation (Eberhart, Charles *et al.*, 1994; Sano *et al.*, 1995). Over expression of COX-2 was reported in approximately 60% of CRC (Eberhart, Charles *et al.*, 1994; Sano *et al.*, 1995; Chan, Andrew, Ogino & Fuchs, 2007).

The acquisition of a second mutation in the *KRAS* gene results in further growth, leading to a large adenoma (Vogelstein *et al.*, 1988; Fearon & Vogelstein, 1990; Powell *et al.*, 1992; Jones *et al.*, 2008; Vogelstein *et al.*, 2013). Subsequent mutations in transforming growth factor (*TGF)-β,* SMAD family member 4 (*SMAD4)*, *p53* and other pathways such as phosphatidylinositol 3-kinase (PI3K), allow the tumour to evolve from a large adenoma to a carcinoma, carcinomas are malignant, they have the ability to invade and metastasise to other tissues (Jones *et al.*, 2008). It takes approximately 17 years for a large adenoma to become an advanced carcinoma, however it takes only about 2 years for the advance carcinoma to invade and metastasise to the liver (Jones *et al.*, 2008). Approximately 85% of sporadic or inherited CRC have mutations in the *APC* gene, *KRAS* and are characterised by high CIN, the remaining 15% are characterised by microsatellite instability and are caused by mutations or epigenetic changes in genes for DNA mismatch repair, mainly MutL homologue 1 (MLH1) and mutS homologue 2 (MSH2) (Vilar & Gruber, 2010; Fearon, 2011) (Figure 1.1).

Although, the model for CRC described above provided evidence for a step-wise accumulation of various genetic alterations leading from small adenomas to metastatic carcinomas, it did not fully provide an insight into the complexity and heterogeneity of CRC. Recently, in an effort to provide a more complete picture of CRC complexity and to provide a useful stratification tool for clinical translation and targeted therapies, the CRC Subtyping Consortium was formed (Guinney *et al.*, 2015). Members of the Consortium combined their genomic databases and generated four subgroups of CRC, these are termed the consensus molecular subtypes or CMSs (Guinney *et al.*, 2015; Dienstmann *et al.*, 2017).

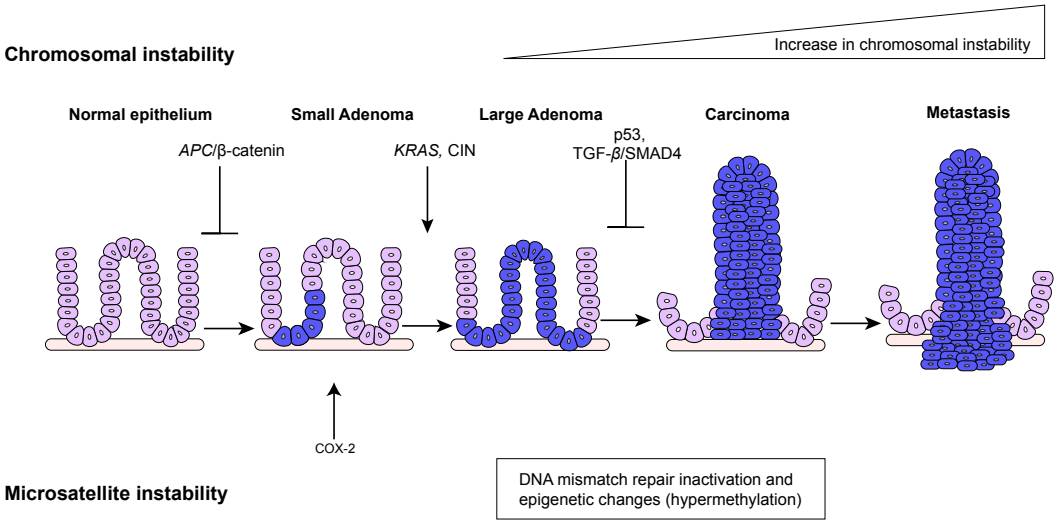

Figure 1.1 CRC Development from Adenoma to Metastatic Carcinoma.
According to Vogelstein and colleagues, the initial step in CRC tumorigenesis is the formation of a small benign adenoma which is associated with a mutation in the *APC* tumour suppressor gene. The *APC* gene is part of a destruction complex that degrades *β*-catenin, mutations in the *APC* lead to the activation of the Wnt signalling pathway and the over-accumulation of *β*-catenin in the nucleus which acts as a transcription factor for genes involved in cellular activation. A further mutation in *KRAS* results to further growth, from a small adenoma into a large adenoma. Mutations in p53, TGF-*β* and downstream target SMAD4 lead to the development of a malignant carcinoma. Carcinomas can acquire further changes that can promote metastasis and invasion into other tissues. CRC with microsatellite instability are characterised by inactivation of DNA mismatch repair system and epigenetic changes and do not develop in the same manner described for CIN, however mutations in *KRAS* and alterations in Wnt signalling are described (Walther *et al.*, 2009). Figure adapted from Walther *et al.,* 2009.

CMS1 represents 14% of early stage tumours and have a distinct developmental pattern, these are mostly tumours with microsatellite instability, characterised by hypermutation, hypermethylation, frequent *BRAF* mutations and immune infiltration, mainly T helper (T_H) 1 cells and cytotoxic T cells (Guinney *et al.*, 2015). Tumours in CMS2-4 develop via the proposed model by Vogelstein and colleagues by acquiring mutations in the *APC* gene (Fearon & Vogelstein, 1990; Dienstmann *et al.*, 2017). CMS2 represents 37% of tumours and is characterised by high CIN; tumours in this subtype are epithelial and have a significant upregulation of WNT and *MYC* downstream targets (Guinney *et al.*, 2015). Tumours in the CMS3 subtype represent 13% of tumours and have a number of altered metabolic gene signatures and *KRAS* mutations (Guinney *et al.*, 2015). 23% of tumours are CMS4 and these are characterised by an upregulation of genes involved in epithelial-to-mesenchymal transition (EMT) and activation of *TGF-β* signalling, vascular endothelial growth factor receptor (VEGFR) upregulation, complement pathway activation and stromal infiltration which suggests that this subtype is pro-metastatic (Guinney *et al.*, 2015). In terms of survival, CMS4 tumours have the worst survival rates and worst relapse free survival, while CMS1 tumours have a very poor survival only after relapse (Guinney *et al.*, 2015).

In light of this CMS classification system, research is now being focused on subtype-specific therapies (Linnekamp *et al.*, 2018). A panel of CRC cell lines, primary cultures and patient derived xenografts (PDX), were classified in the four CMSs, the aim being to ensure that CRC is modelled appropriately (Linnekamp *et al.*, 2018). The authors used a number of available gene expression datasets used to classify the selected CRC cell lines and positively identified all four CMCs in approximately 67% of CRC cell lines tested, primary cultures and PDX (Linnekamp *et al.*, 2018). Morphologically culture of CMS2/3 cell lines were distinct and grew in colonies, while CMS4 cell lines were more dispersed and elongated. Moreover drug sensitivity assays revealed that CMS1-3 were more sensitive to conventional chemotherapy such as 5-Fluorouracil (5-FU) than CMS4 cell lines (Linnekamp *et al.*, 2018). The data reported by Linnekamp *et al.*, (2018), will be particularly important for future design of CMS-specific therapies (Linnekamp *et al.*, 2018).

1.1.2 Current treatments for CRC

Staging of CRC is the most important prognostic factor for patients and also determines the appropriate treatment schedule (Wolpin & Mayer, 2009). The tumour-node-metastasis (TNM) described by the American Joint Committee of Cancer is the most commonly used staging system (Greene, Stewart & Norton, 2002). The TNM

system is based on tumour size, depth of penetration into the bowel wall, extent of lymph node involvement and presence of metastasis (Greene, Stewart & Norton, 2002). The depth of tumour penetration defines the T stage which increases from T1 to T4, as T increases the risk of lymph node involvement increases, this defines the N stage from N0 (no lymph node involved) to N1 and N2 (more than 3 lymph nodes involved), metastasis is defined by the M stage and can be M0 (no metastasis) or M1, apparent metastasis detected (Wolpin & Mayer, 2009). The results from the TNM staging are combined and the stage of CRC is determined from I to IV (Wolpin & Mayer, 2009). As the stage of CRC increases the five year survival rates dramatically decreases: stage I > 90%; stage II > 80%; stage III > 60%; stage IV < 10% (Cancer Research UK, 2015). The CMS classification for CRC has not yet been adopted in the clinical setting, however, clinical translation would potentially improve patient stratification for treatment towards precision medicine and reduce the number of patients that undergo unsuccessful treatments (Inamura, 2018).

Surgical resection is the first line of treatment for early stage CRC (Cancer Research UK, 2015). Following surgical resection, patients with stage II and above undergo chemotherapy (Cancer Research UK, 2015). As well as chemotherapy patients may also receive radiotherapy before or after surgery as an adjuvant therapy to prevent re-occurrence (Cancer Research UK, 2015). Patients with unresectable advanced CRC at stage IV also undergo chemotherapy with the main aim of converting unresectable CRC to resectable CRC, to prolong survival and to improve tumour-related symptoms (Cutsem, Nordlinger & Cervantes, 2010). Some of the most commonly used chemotherapeutic agents for CRC include 5-FU, Irinotecan, Leucovorin and Oxaliplatin (Cutsem, Nordlinger & Cervantes, 2010).

1.1.2.1 5-Fluorouracil

5-FU has been approved for use in CRC for almost 60 years, it is an antimetabolite drug which works by inhibiting thymidylate synthase (TS) and by incorporating its active metabolites into RNA and DNA (Longley, Harkin & Johnston, 2003). Overall 5-FU as a monotherapy agent in CRC has a low response rate, however, several adaptations have been made to increase the toxicity of 5-FU (Longley, Harkin & Johnston, 2003). The addition of folinic acid (leucovorin) greatly enhanced the anti-tumour activity of 5-FU (Longley, Harkin & Johnston, 2003). In clinical trials however, the overall survival of patients was not greatly improved by 5-FU and leucovorin, leading to further combination with Oxaliplatin (Gramont *et al.*, 2000). A clinical trial using the combination of leucovorin/5-FU and Oxaliplatin (FOLFOX) reported better

response rates than leucovorin/5-FU alone however, with neurosensory toxicity (Gramont *et al.*, 2000).

1.1.2.2 Irinotecan

7-ethyl-10-[4-(1-piperidino)-1-piperidino] carbonyloxy camptothecin (CPT-11), commonly referred to as irinotecan is the water soluble analog of camptothecin (CPT) which was first isolated from a plant *Camptotheca acuminate* native to the south of China (Kunimoto *et al.*, 1987). Irinotecan was found to have a broad spectrum anti-tumour activity and was less toxic than CPT (Kunimoto *et al.*, 1987). Irinotecan acts as a prodrug as it is converted by carboxylesterases to 7-ethyl-10-hydroxycamptothecin (SN38). SN38 is 100-1000 fold more potent than irinotecan (Mathijssen *et al.*, 2001). SN38 works by inhibiting topoisomerase I an enzyme that catalyses the breakage and rejoining of DNA strands during DNA replication, it leads to DNA fragmentation and apoptosis (Mathijssen *et al.*, 2001). Irinotecan has a very complex metabolic profile, following conversion by esterases to SN38, SN38 is further detoxified by undergoing glucuronic acid conjugation to form the glucuronide SN38G (Gupta *et al.*, 1994; Mathijssen *et al.*, 2001). SN38G is 100 fold less active than SN38 at inhibiting topoisomerase I (Mathijssen *et al.*, 2001). The gut microflora can convert SN38G back to SN38 and this was found to be responsible for the diarrhoea associated with irinotecan (Gupta *et al.*, 1994). Moreover, the combination of leucovorin/5-FU/irinotecan (FOLFIRI) is also used and has shown good response rates (Segal & Saltz, 2009).

Efforts have been made in the clinical setting to evaluate the association of molecular subtype and response to irinotecan-based therapies for metastatic CRC (Del Rio *et al.*, 2017). Using gene expression profiling of tumour samples (primary tumour site), Del Rio *et al.,* (2017) identified a subtype of CRC which represented 28% of patients and these patients in particular had a high response and a longer overall survival when treated with FOLFIRI (Del Rio *et al.*, 2017). This subtype was characterised by an upregulation in Wnt signalling and CIN, the molecular subtype specifically was C5 which was described by Marisa, *et al.,* (2013) as a classification prior to the CMSs, however was closely related to CMS4 (Del Rio *et al.*, 2017; Marisa *et al.*, 2013). Further clinical trials are required to evaluate the molecular subtypes and their correlation to patient response.

1.1.2.3 Chemotherapy and its side effects

Despite the overall success of chemotherapy, one of the major obstacles to effective cancer treatment is the number of side effects associated with systemic

chemotherapy which can be intolerable and have detrimental effects on the quality of life of patients. Clinical trials with FOLFOX and FOLFIRI reported a number of moderate adverse events such as diarrhoea, nausea, vomiting and severe side effects such as neutropenia, thrombocytopenia and neuropathy in patients with CRC (Goldberg *et al.*, 2006a, 2006b; Fuchs *et al.*, 2007).

Conventional chemotherapy although used successfully in many cases in others is limited by systemic toxicity. With the gain of knowledge throughout the years on the step-wise development of cancer and moving away from the one gene one drug approach, more sophisticated and targeted therapies in combination with chemotherapy are being developed to target multiple genes/processes in cancer development.

1.2 Vascular Targeting Therapies

One of the key events and hallmarks of cancer development is the growth of new blood vessels through the process of angiogenesis, the oxygen and nutrients supplied by the new vasculature being crucial to the survival of cancer cells (Hanahan & Weinberg, 2000). The concept of tumour angiogenesis was first described by Folkman who hypothesised that for a tumour to grow it required new blood vessels and introduced anti-angiogenesis as a therapeutic strategy specifically preventing the growth of tumour blood vessels (Folkman, 1971, 1990). During tumour development the “angiogenic switch” drives tumour angiogenesis *e.g.* by upregulation of angiogenesis activators such as vascular endothelial growth factor (VEGF) (Hanahan & Folkman, 1996).

Since the importance of angiogenesis in tumour development was observed vascular targeting therapies (VTTs) which include two distinct classes of agents: the anti-angiogenic agents (AAs) and the vasculature disrupting agents (VDAs) have been developed and used clinically (Chase, Chaplin & Monk, 2017). AAs prevent the development of new blood vessels (angiogenesis) which is necessary for tumour growth (Chase, Chaplin & Monk, 2017).

As VEGF has a crucial role in angiogenesis, a monoclonal antibody against VEGF was developed, bevacizumab (Avastin) to inhibit angiogenesis and tumour growth (Presta *et al.*, 1997; Hurwitz *et al.*, 2004). Initial work in CRC showed that bevacizumab in combination with leucovorin increased the survival of patients with metastatic CRC to 20.3 months when compared to the 15.6 months median survival time from patients treated with leucovorin (Hurwitz *et al.*, 2004). Bevacizumab as well

as inhibiting the growth of new blood vessels, may also normalise the tumour vasculature and decrease interstitial fluid pressure, resulting in more efficient delivery of chemotherapeutics (Willett *et al.*, 2004; Jain, 2005). Due to these improved survival rates in cancer patients bevacizumab was approved for use in patients with metastatic CRC in 2004 in the USA and 2005 in the EU and is usually used in combination with FOLFOX or irinotecan (FDA, 2004; European Medicines Agency, 2005; Cohen *et al.*, 2007).

In contrast to AAs, VDAs target the established tumour vasculature, which is characterised as chaotic and lacking a proper endothelial cell lining (Siemann, Chaplin & Horsman, 2017). Often the endothelial cells have irregular shapes, poor investiture of smooth muscle cells (SMCs) or pericytes, subsequently leading to high vascular permeability and high interstitial fluid pressure (Baluk, Hashizume & McDonald, 2005). Treatment of the tumour vasculature with VDAs due to these morphological abnormalities leads to a rapid and catastrophic shutdown of blood flow (Tozer, Kanthou & Baguley, 2005). It should be noted that some agents can have both anti-angiogenic and anti-vascular properties (Tozer, Kanthou & Baguley, 2005). Currently, a number of VDAs are in clinical development and clinical trials however none have been approved for treatment of cancer (Siemann, Chaplin & Horsman, 2017).

The first classical VDA described was colchicine which was isolated from the meadow saffron, *Colchicum autumnale* (Lu *et al.*, 2012). Colchicine was found to have a very low therapeutic index and a number of toxic side effects such as neutropenia, bone marrow damage and anaemia (Lu *et al.*, 2012). Colchicine, however was approved for oral use by the U.S Food and Drug Administration (FDA) in 2009 as a monotherapy for gout and Familial Mediterranean fever (Lu *et al.*, 2012).

1.2.1 Combretastatin A4

1.2.1.1 The origin of Combretastatins and the isolation of CA4

Combretastatins are natural products originally extracted from the African tree *Combretum caffrum* with VDA activity (Pettit *et al.*, 1988, 1989). Structurally related to colchicine, the combretastatins were found to be potent inhibitors of microtubule (MT) polymerisation by binding near the colchicine binding site on tubulin (Pettit *et al.*, 1988, 1989). Combretastatin A4 (CA4) was one of the most cytotoxic and competitive inhibitors for the colchicine binding site from the 17 isolated compounds (Lin *et al.*, 1988; Pettit *et al.*, 1988, 1989). CA4 consists of two phenyl rings A and B linked by a carbon-carbon double bond bridge (ethylene) (Figure 1.2 A). CA4 can

exists as two isoforms *cis* and *trans,* active *cis*-CA4 can be isomerised to the less active *trans*-CA4 (Lin *et al.*, 1988). The structure of CA4 in the two isoforms *cis* and *trans* is shown in Figure 1.2 A and B respectively. Isomerisation from *cis* to *trans* isomer can occur under the influence of heat and light (Tron *et al.*, 2006).

1.2.1.2 CA4 binding to tubulin

CA4 binds to tubulin with high avidity, however this binding is reversible (Lin *et al.*, 1989). The rate at which colchicine or CA4 dissociates from tubulin is referred to as the dissociation rate and for colchicine this is 405 min (Lin *et al.*, 1989). In contrast, CA4 rapidly binds and dissociates from tubulin, with a dissociation rate of 3.6 min at 37°C (Lin *et al.*, 1989).

MTs are composed of *α* and *β*-tubulin heterodimers, existing in a dynamic equilibrium between their polymerised from and *αβ*-tubulin heterodimers (Rozas, 2017). MTs undergo elongation by the addition of *αβ*-tubulin heterodimers, bound to Guanosine triphosphate (GTP) to the MT polymer (Figure 1.3). The MT cylinder is mainly composed of Guanosine diphosphate (GDP)-bound tubulin however this is protected from depolymerisation by a stabilisation cap (Figure 1.3). MT catastrophe occurs following loss of the stabilisation cap and by the release of *αβ*-tubulin heterodimers (Rozas, 2017). Tubulin heterodimers in MTs assume a “straight” structure, in contrast, to un-polymerised heterodimers which assumes a “curved” structure, the curved-to-straight transition occurs during polymerisation (Gaspari *et al.*, 2017; Brouhard & Rice, 2014). Recently, the crystal structure of *cis*-CA4 complexed with tubulin, specifically binding to *β*-tubulin has been resolved by Gaspari *et al.,* (2017). *Cis*-CA4 inhibits tubulin by not only binding to the colchicine binding site but also because it inhibits the tubulin transition from “curved” to “straight” tubulin, which is essential for microtubule formation (Gaspari *et al.*, 2017; Rozas, 2017). The difference in activity between the *trans* and *cis*-CA4 isomer was attributed to their interaction with tubulin as the interaction with the *cis* isomer is more stable (Gaspari *et al.*, 2017). Using metadynamic stimulation Gaspari *et al.*, (2017) studied the unbinding kinetics of colchicine and CA4, their results showed that *cis*-CA4 caused a small disturbance to the *β*-tubulin T7 loop structure during unbinding whereas colchicine required the complete displacement of the loop to be able to exit tubulin (Gaspari *et al.*, 2017).

As MTs are essential cellular structures required for maintaining cell shape, motility, intracellular trafficking, cell division and mitosis, they are an obvious target for cancer therapy (Jordan & Wilson, 2004). A number of clinically available compounds used

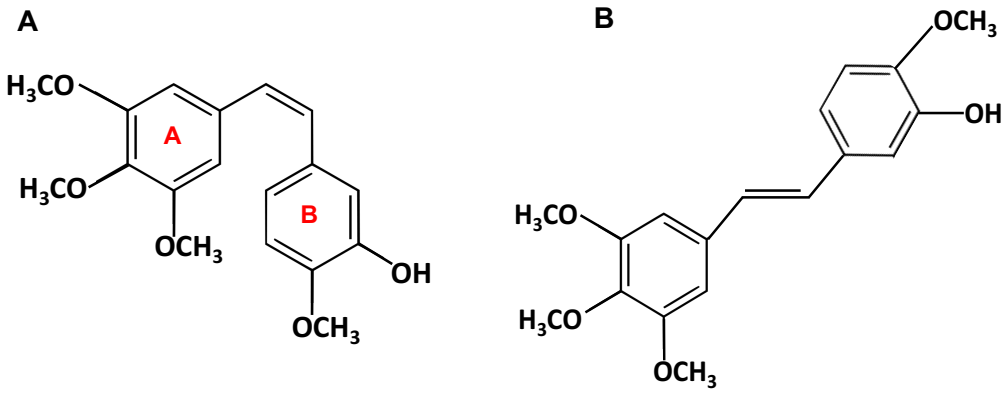

Combretastatin A4

***Cis*-isomer**

Combretastatin A4

***Trans*-isomer**

Figure 1.2 Chemical structures of Combretastatin A4 *cis* and *trans* isomers. The structure of Combretastatin A4 (CA4) consists of two phenyl rings A (containing a 3,4,5-trimethoxy group) and B that can be oriented either in *cis* (A) or *trans* (B) isomerisation. The two phenyl rings are linked by a carbon-carbon double bond (ethylene). *Cis*-CA4 is more active than *trans*-CA4 (Lin *et al.*, 1988).

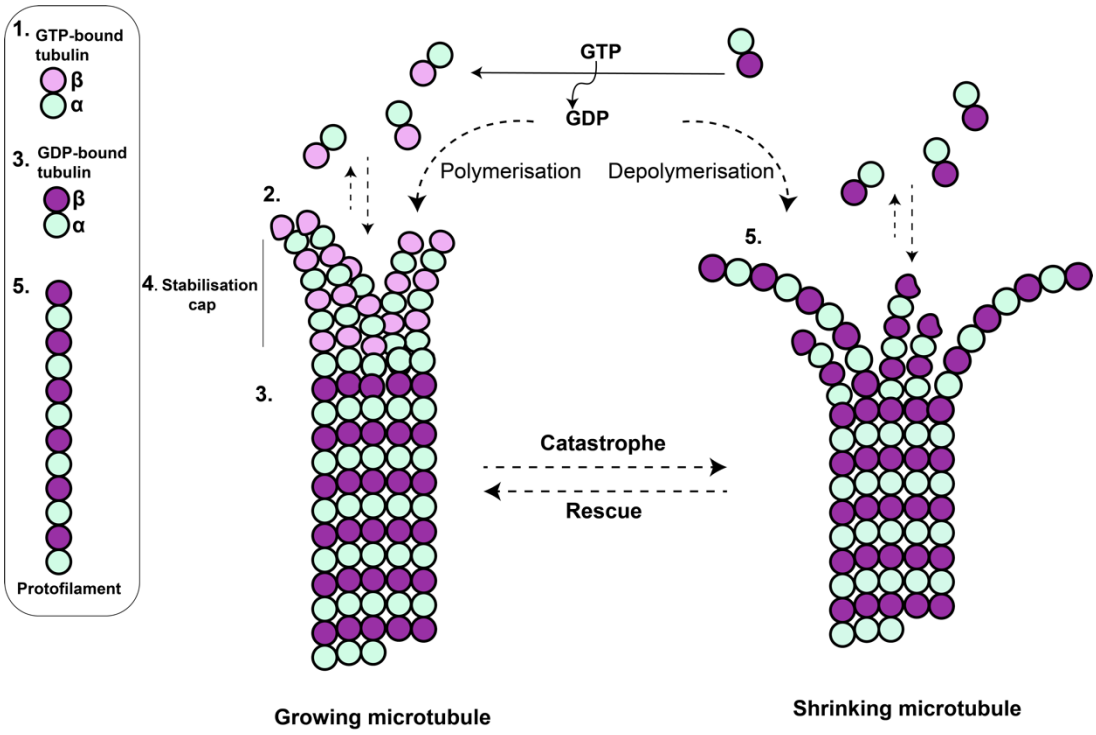

Figure 1.3 Schematic showing the polymerisation and depolymerisation of microtubules.

MTs are hollow cylinders composed of *αβ*-tubulin heterodimers. MT polymerisation and depolymerisation is directed by the hydrolysis and exchange of guanine nucleotide GTP to GDP on *β*-tubulin subunit. MT polymerisation is initiated by the addition of GTP-bound *αβ*-tubulin (1) onto the MT ends. The growing MT varies between slightly curved and straight filaments (2). During GTP hydrolysis and shortly after incorporation into the growing MT the phosphate is released (GTP to GDP), leaving the core of the MT consisting of GDP bound-tubulin (3). The MT core is protected by the stabilisation cap on the GTP-bound tubulin which stabilises and maintains the MT structure (4). Loss of the stabilisation cap leads to MT depolymerisation whereby the curved protofilaments peeling outwards at the shrinking MT ends (5). Catastrophe refers to the switch from growth to shrinkage, while rescue refers to the switch from shrinkage to growth (Akhmanova & Steinmetz, 2008; Brouhard & Rice, 2014). Figure adapted from Akhmanova & Steinmetz, 2008 and Brouhard & Rice, 2014.

for cancer therapy bind to MTs and either stabilise them such as paclitaxel or destabilise them such as vinblastine, vincristine, CA4 and colchicine, however CA4 and colchicine are not approved for cancer (Mukhtar, Adhami & Mukhtar, 2014). Vinblastine and Vincristine bind to the vinca domain while paclitaxel binds to the taxane site on *β*-tubulin (Mukhtar, Adhami & Mukhtar, 2014).

1.2.1.3 CA4 phosphate and CA4 derivatives

Although, CA4 was the most potent competitive inhibitor of colchicine for the tubulin binding site, it has a low water solubility with a *log*P[1] value of 3.57 (Pettit *et al.*, 1995; Royal Society of Chemistry, 2015). For further developmental studies using CA4, a water soluble phosphate salt of CA4 (CA4P) was synthesised with a *logP* of 1.98, by replacing the hydroxyl group on ring B with a phosphate group (Pettit *et al.*, 1995; Royal Society of Chemistry, 2015). CA4P acts as a prodrug and it is rapidly cleaved by phosphatases to CA4 (Pettit *et al.*, 1995). Following, the synthesis and development of CA4 and CA4P, a number of *in vitro*, preclinical and clinical evaluations were conducted. Most *in vitro* and preclinical work conducted *in vivo* has been performed using CA4P. However as CA4P acts as a prodrug data presented from herein applies to CA4.

Hundreds of CA4 derivatives have been developed in order to avoid the *cis*/*trans* isomerisation such as the *cis*-locked analogues to improve the pharmacokinetics (PK) of the compound (Tron *et al.*, 2006). Due to the simplicity of the structure of CA4 (Figure 1.2 A), a large number of modifications can be carried out on either one of the phenyl rings or the double bond (Jaroch *et al.*, 2016). However, the *cis*-conformation of the double bond and the 3,4,5-trimethoxy group on ring A are essential for the biological activity of CA4 (Siebert *et al.*, 2016). Duan *et al.,* (2016) produced a CA4 analogue by replacing the double bond bridge and the B-ring on the CA4 structure resulting in a compound that retained the ability to inhibit tubulin polymerisation and *in vivo* inhibited the growth of lung cancer xenografts (Duan *et al.*, 2016). Moreover, replacing the double bond bridge and also adding a second hydroxyl group greatly increased the solubility of the CA4 analogue while retaining tubulin inhibition and increasing the potency of the compound against CRC

[1] The partition coefficient (P) describes the tendency of an uncharged compound to dissolve in an lipid (oil, fat or organic solvent solution) and water. The *LogP* is a constant which is defined by $LogP=\log_{10}(P)$; P=[organic]/[aqueous], [] indicates the concentration of a solute in the organic and aqueous partition. A negative *log*P means that the compound is more hydrophilic as the compound has a higher affinity for the aqueous phase; *log*P=0, the compound is equally partitioned between the oil and aqueous phase; a positive *log*P, means that the compounds has a higher affinity for the lipid phase and is therefore more hydrophobic or lipophilic (Bhal, n.d.).

xenografts (Tripodi *et al.*, 2012; Valtorta *et al.*, 2014). The CA4 derivative, AVE8062 (Ombrabulin) was also developed by modifying the hydroxyl group on ring B (Jaroch *et al.*, 2016). Ombrabulin entered clinical trials, however it failed to demonstrate clinical benefit in patients with ovarian cancer and had a number of side effects reported such as neutropenia (Chase, Chaplin & Monk, 2017).

1.2.1.4 Cellular mechanism of action of CA4

Short (< 2 h) exposure of endothelial cells to CA4 and CA4P leads to complete cytoskeletal disorganisation of MTs (Grosios *et al.*, 1999; Galbraith *et al.*, 2001). Disruption of MTs leads to the activation of Rho-GTPase, Rho kinase and mitogen protein kinase signalling pathways, which are responsible for further morphological and cytoskeletal changes (Kanthou & Tozer, 2002). The activation of Rho and Rho kinase leads to increased phosphorylation of myosin light chain (MLC), leading to the formation of actin lined surface protrusions referred to as blebs and increase in endothelial cell monolayer permeability (Kanthou & Tozer, 2002; Tozer, Kanthou & Baguley, 2005). The stress-activated protein kinase 2 (SAPK2)/ p38 pathway is also involved in the blebbing morphology, while extracellular-regulated kinase 1 and 2 (ERK1/2), and MCL kinase protected against blebbing (Kanthou & Tozer, 2002). It was therefore believed that inhibiting ERK1/2 enhanced the cytotoxicity of CA4, whereas inhibition of p38 mitogen activated protein kinase (MAPK) compromised the cytotoxicity. Further reports however using hepatocellular carcinoma cells have shown that inhibition of p38 MAPK and not ERK1/2 synergistically enhanced rather than inhibited the activity of CA4 (Quan, Xu & Lou, 2008). The role of Rho and Rho kinase has also been observed *in vivo* (Williams *et al.*, 2014).

CA4 also promotes cell junction disassembly of unstable nascent tumour neovessels, lacking periendothelial support by SMC an indication of an anti-angiogenetic activity (Vincent *et al.*, 2005). The way in which CA4P targets nascent tumour neovessels is by causing rapid disengagement of Vascular Endothelial (VE)-cadherin/β-catenin complexes which are essential for endothelial cell adhesion and survival during neovessel development and remodelling (Vincent *et al.*, 2005). Indeed, the VE-cadherin rearrangement rather than the loss of VE-cadherin on the cell surface, is responsible for increased vascular permeability (Shepherd *et al.*, 2017). CA4P was found to inhibit endothelial cell migration and tube formation *in vitro* also demonstrating the anti-angiogenic and anti-metastatic activity of CA4P (Ahmed *et al.*, 2003). As the VE-cadherin/*β*-catenin complex lies upstream of the PI3K/Akt pathway, it was proposed that inactivation of this pathway was the mechanism leading to the inhibition of tube formation (Vincent *et al.*, 2005).

The PI3K/Akt pathway plays a major role in cancer proliferation, migration, invasion/metastasis and apoptosis therefore, CA4P inhibiting angiogenesis through Akt inactivation, could also interfere with the proliferation of endothelial cells and metastasis (Vincent *et al.*, 2005). Subsequent studies showed that CA4 decreased p-AKT expression in gastric, bladder and thyroid cancer cells and inhibited metastasis and proliferation (Lin *et al.*, 2007; Shen *et al.*, 2010; Liang *et al.*, 2016). In thyroid cancer cells CA4, also decreased the expression of EMT related proteins such as N-cadherin, Vimentin, Snail1, Twist and ZEB1 further demonstrating the anti-metastatic activity of CA4 (Liang *et al.*, 2016). N-cadherin is an intracellular adhesion protein involved in the interaction between endothelial cells with SMC and pericytes (Shepherd *et al.*, 2017). The loss/disruption of N-cadherin caused by CA4P treatment was also observed in endothelial cells (Shepherd *et al.*, 2017).

It has also been suggested that CA4P exerts its anti-angiogenic activity by upregulating, the multifunctional extracellular matrix protein connective tissue growth factor (CTFG) in endothelial cells which has anti-angiogenic properties, an effect that is dependent on MT disruption (Samarin *et al.*, 2009). CTFG forms a complex with VEGF and interferes with VEGF induced angiogenesis (Samarin *et al.*, 2009). There data show that CA4 acts to promote severe cytoskeleton changes following MT disruption which subsequently lead to the downregulation of major signalling systems involved in angiogenesis, cell proliferation and metastasis (Sherbet, 2017).

1.2.1.5 CA4 induced cell-death

Prolonged exposure of many hours to CA4 leads to cell-death through apoptosis which can be caspase independent or dependent, mitotic catastrophe and/or polyploidy (≥ 4N DNA) (Nabha *et al.*, 2002; Shen *et al.*, 2010; Greene, Meegan & Zisterer, 2015). Apoptosis can occur by two distinct pathways the extrinsic pathway is mediated outside the cell via death receptors leading to the activation of caspase 8 (Elmore, 2007). In contrast, the intrinsic pathway is initiated inside cells through stress-induced signals which result in the release of apoptotic proteins from the mitochondria such as cytochrome c (Elmore, 2007). Mitotic catastrophe is a mechanism that involves a delayed mitosis-linked cell death which occurs from premature or inappropriate entry of cells into mitosis as a result of physical or chemical stresses (Vakifahmetoglu, Olsson & Zhivotovsky, 2008). DNA polyploidy is a phenomenon where cells fail to arrest and undergo apoptosis following early mitotic release and enter into S phase with > 4 N DNA content (Greene *et al.*, 2012).

Initial studies in endothelial cells reported the initiation of apoptosis by CA4 through the activation of caspase 3 (Iyer *et al.*, 1998). However, it was apparent that death of endothelial cells was not exclusively through apoptosis as only 10% of cells were observed to undergo apoptosis (Ahmed *et al.*, 2003). CA4 was observed to also cause mitotic catastrophe by arresting leukaemia cells in G2/M phase of the cell cycle (Nabha *et al.*, 2000). Cells in mitotic catastrophe are characterised by fragmented nuclei and the formation of giant multinucleated cells which are considered the hallmarks of mitotic catastrophe (Nabha *et al.*, 2000).

Nabha *et al.,* (2002) studied the molecular mechanisms underlying mitotic catastrophe in leukaemia cells. They observed that a 24 h exposure to CA4P lead to the over-accumulation of a mitosis promoting factor, cyclin B in the nucleus indicating that cells were able to exit the G2 phase and enter M phase prior to arrest (Nabha *et al.*, 2002). Cell-death through mitotic catastrophe was independent to apoptosis as CA4P did not change the expression of apoptotic proteins, however, it did induce caspase 9 activation presumably in the small proportion of cells undergoing cell-death through apoptosis (Nabha *et al.*, 2002). Cyclin B and p34/ cyclin division cycle protein 2 (cdc2) levels increase through prophase and metaphase and as cells move into anaphase, cyclin B1 is degraded leading to $p34^{cdc2}$ inactivation (Kanthou *et al.*, 2004). However, treatment of endothelial cells with CA4P for 24 h leads to the over-accumulation of cyclin B as observed in leukaemia cells, leading to the continued activation of $p34^{cdc2}$ and arrest of cells in metaphase (Kanthou *et al.*, 2004). This cell-death in endothelial cells without exiting mitosis was also caspase-independent (Kanthou *et al.*, 2004).

In lung cancer cells CA4 treatment induced the hallmarks of mitotic catastrophe, cells accumulated in metaphase with multinucleated cells observed (Vitale *et al.*, 2007). Activation of caspases 3 and 9 in lung cancer cells was reported (Vitale *et al.*, 2007). Further reports in lung cancer cells showed that MT disruption lead to the accumulation of the pro-apoptotic marker Bim in the mitochondria leading to the activation of caspases (Cenciarelli *et al.*, 2008). Mendez *et al.,* (2011) studied the role of Bim in apoptosis induced in lung cancer cells after exposure to CA4. Their results showed that Bim is physically bound to MTs through interactions with the cytoskeletal motor protein dynein, as MTs depolymerise as a result of CA4 treatment this results in the release of Bim from the MT network leading to its translocation to the mitochondria (Mendez *et al.*, 2011). At the mitochondria Bim bound to B-cell lymphoma 2 (Bcl-2) which subsequently lead to the release of pro-apoptotic factor Bax, which in turn results in caspase activation (Mendez *et al.*, 2011).

In human cervical cancer cells, an association between BubR1 a member of the spindle assembly checkpoint which prevents the premature exit from mitosis and CA4P was observed (Greene *et al.*, 2011). CA4P induced the phosphorylation of BubR1 and induced G2/M arrest by preventing the progression from metaphase to anaphase (Greene *et al.*, 2011). Moreover, activation of caspase 3 lead to the cleavage of BubR1 and the exit of cells from mitosis leading to polyploidy and subsequent apoptosis (Greene *et al.*, 2011). Phosphorylation of BubR1 followed by caspase 3 cleavage, formation of multinucleated cells and apoptosis also followed CA4 in bladder cancer cells, specifically human bladder transitional carcinoma TSGH 8301 and BFTC 905 cells (Shen *et al.*, 2010). Collectively there data show that CA4 or CA4P induce cell-death through various mechanisms dependent on cell-type and the machinery available (Vitale *et al.*, 2007). Mitotic catastrophe although initially considered as a separate form of cell-death, is now accepted as a pre-stage process, proceeding cell-death through apoptosis or necrosis (Vakifahmetoglu, Olsson & Zhivotovsky, 2008).

1.2.1.6 Rapid effects of CA4 on tumour vasculature *in vivo*

Initial investigations into the anti-vascular activity of CA4P in a preclinical setting, showed that CA4P caused severe and rapid (within minutes) alterations to the blood flow or perfusion of tumours (Chaplin, Pettit & Hill, 1996; Dark *et al.*, 1997). A number of methods such as uptake of radioactive molecules, fluorescence microscopy of the perfusion marker Hoechst 33342, magnetic resonance imaging (MRI), magnetic resonance spectroscopy (MRS) and contrast enhanced ultrasound (CEUS) were used to study perfusion in multiple preclinical models (Chaplin, Pettit & Hill, 1996; Dark *et al.*, 1997; Maxwell *et al.*, 1998; Grosios *et al.*, 1999; Zhang *et al.*, 2018). The observations included an almost complete vascular shutdown by 1 h which was sustained for up to 24 h in some tumour models, however after 24 h, tumour blood flow started to recover (Chaplin, Pettit & Hill, 1996; Dark *et al.*, 1997; Maxwell *et al.*, 1998). Table 1.1 summarises preclinical studies of CA4P and CA4 on perfusion, including the different tumour types and methods used to measure perfusion.

Reduction in blood flow was found to be dose-dependent in a mouse breast cancer model at doses between 100-400 mg/kg, a significant reduction was observed at 175 mg/kg and this reached a plateau at 250 mg/kg (Murata, Overgaard & Horsman, 2001). Further investigations, into blood flow reductions caused by CA4P showed distinct differences in activity towards the tumour periphery and the central core regions of the tumour (Beauregard *et al.*, 1998).

Table 1.1 Anti-vascular activity of CA4P and CA4.

Tumour type (origin/species)	Dose	Hours post injection	Perfusion (tumour) (% reduction)[a]	Imaging Modality	Reference
CaNT (Breast-mouse)	50 mg/kg (i.p.)	24	⬇ (> 60%)	Radioactivity (Rubidium-82 chloride-^{86}RbCl)	(Chaplin, Pettit & Hill, 1996)
CaNT (Breast-mouse)	100 mg/kg (i.p.)	1, 6, 18	⬇ (96% by 6 h, with little recovery by 18 h)	Hoechst 33342[b]	(Dark *et al.*, 1997)
Sarcoma F (mouse)	100 mg/kg (i.p.)	3	⬇, ⬆ tumour periphery	Magnetic resonance imaging (MRI)	(Beauregard *et al.*, 1998)
C3H (Breast-mouse)	100 mg/kg (i.p.)	1, 24	⬇ (33% reduction), recovery at 24 h	^{31}P magnetic resonance (MR) spectroscopy (MRS)/ ^{1}H MR spectroscopy	(Maxwell *et al.*, 1998)
P22 sarcoma (rat)	100 mg/kg (i.p.)	1, 6	⬇ (~ 75% reduction at 1 h and 100% at 6 h)	Autoradiography	(Tozer *et al.*, 1999)
MAC15 and MAC 15A (mouse-colon)	100 mg/kg (i.p.), *150 mg/kg (i.p.)	4	⬇	Hoechst 33342[b]	(Grosios *et al.*, 1999)
Liver metastases	100 mg/kg (i.p.)	1	⬇ (15% reduction), recovery by 6-24 h	Laser Doppler flowmetry	(Malcontenti-Wilson *et al.*, 2001)
P22 sarcoma (rat)	30mg/kg or 100 mg/kg (i.p.)	1	⬇ (> 95% reduction), recovery of 30 mg/kg group	Intravital Microscopy	(Tozer *et al.*, 2001)
Sarcoma F (mouse), LoVo, HT29 (human-colon)	100 mg/kg (i.p.)	3	⬇ (LoVo cells and Sarcoma F) (HT29 resistant)	MRI/MRS	(Beauregard *et al.*, 2001)
C3H (Breast-mouse)	250 mg/kg (i.p.)	1	⬇ (~ 70% reduction), recovery by 24 h	Radioactivity (Rubidium-82 chloride-^{86}RbCl)	(Murata, Overgaard & Horsman, 2001)
CaNT (Breast-mouse)	25 mg/kg (twice in one day with 3 h gap) (i.p.)	24	⬇ (~ 80% reduction)	Hoechst 33342[b]	(Hill *et al.*, 2002)
HT29, LS174T (colon-human)	100 mg/kg (i.p.)	3	⬇ (40% reduction), only in LS174T	MRI/MRS	(Beauregard *et al.*, 2002)
CaNT (breast-mouse)	100 mg/kg (i.p.)	24	⬇ (~ 80% reduction)	Hoechst 33342[b]	(Chaplin & Hill, 2002)
SW1222 (human-colon)	200 mg/kg (i.p.)	1, 24	⬇ (~ 87% reduction), recovery by 24 h at the tumour periphery	Hoechst 33342[b]	(El-Emir *et al.*, 2005)
13762NF (Breast-rat)	30 mg/kg (i.p.)	2, 24	⬇ (at 2 h 65% reduction in periphery and 70% in the centre of tumour), perfusion recovery only at tumour periphery at 24 h	Dynamic contrast enhanced (DCE)-MRI	(Zhao *et al.*, 2005a)
NSF14, (bladder-rat)	100 mg/kg (i.p.)	0.5	⬇ (20% reduction), some recovery at 24 h	Carbogen-based functional MRI (fMRI)	(Thomas *et al.*, 2006)
KHT sarcoma (mouse)	100 mg/kg (i.p.)	4, 48	⬇ (4 h 80% reduction), recovery by 48 h (whole tumour)	Hoechst 33342[b]	(Salmon & Siemann, 2007)
K1735 (melanoma-mouse)	100 mg/kg (i.p.)	2, 48	⬇, recovery by 48 h at the tumour periphery	Contrast-enhanced (microbubbles) power Doppler imaging	(Seiler *et al.*, 2007)
9L (brain-rat)	120 mg/kg (i.p.)	2, 24	⬇, recovery observed by 24 h	Dynamic bioluminescence imaging (BLI) and Hoechst 33342	(Liu, Mason & Gimi, 2015)
CT26 (colon-mouse)	100 mg/kg (i.p.)	2,12, 48	⬇, recovery observed by 48 h	Contrast Enhanced Ultrasound (CEUS)	(Zhang *et al.*, 2018)

*CA4 (hydrophobic). ⬇ indicates reduction in perfusion; ⬆ indicates increase in perfusion; [a] were possible the % reduction in vascular perfusion was recorded. i.p. Intraperitoneal. [b] Hoechst 33342 perfusion marker was used to stain the perfused vasculature *in situ* and visualised under fluorescence microscopy.

In a murine sarcoma model, blood flow was reduced significantly after 3 h in the central regions of the tumour but in sharp contrast, this increased in the periphery measured by MRI (uptake of gadolinium diethylenetriaminepentaacetate, GdDTPA) (Beauregard *et al.*, 1998).

Blood flow in the tumour as a whole initially decreased within 4 h, but significantly increased by 48 h, with a higher rate of recovery at the tumour periphery (Salmon & Siemann, 2007). Blood flow in a colon xenograft model decreased 1 h post-treatment, and by 24 h, perfusion was still reduced in the central parts of the tumour but had recovered at the tumour periphery (El-Emir *et al.*, 2005). As a result of 70-87% reduction of blood flow, oxygen levels in tumours are also altered leading to hypoxia in both the central and some parts of the tumour periphery (El-Emir *et al.*, 2005; Zhao *et al.*, 2005a). The oxygen levels seemed to recover by 24 h in the tumour periphery, the oxygen levels were measured by fluorescence staining of the hypoxic marker pimonidazole and distribution of hexafluorobenzene (El-Emir *et al.*, 2005; Zhao *et al.*, 2005a).

1.2.1.7 Mechanisms of CA4 induced blood flow shutdown

Rapid and direct vasoconstriction of the tumour-supplying arterioles has been reported for CA4P, subsequently leading to blood flow shutdown (Tozer *et al.*, 2001; Tozer, Kanthou & Baguley, 2005). Small decreases in tumour blood vessel diameters can occur via a number of ways, firstly the increase in tumour vascular permeability to plasma proteins, could lead to leakage of water from the plasma into the interstitial space (oedema), causing an increase in interstitial fluid pressure, thus leading to vascular collapse (Tozer *et al.*, 2001). Secondly, changes in diameter could be a result of the rounding up of tumour endothelial cells *in vivo*, which has been observed *in vitro* following low and/or short exposures to CA4P (Grosios *et al.*, 1999; Galbraith *et al.*, 2001; Tozer *et al.*, 2001). Blood viscosity is also increased from the arterial to the venous end in the microcirculation as a result of water loss (Tozer, Kanthou & Baguley, 2005). Slowing of the blood flow causes red blood cells (RBCs) to stack further increasing blood viscosity and slowing down of blood flow (Tozer *et al.*, 2001; Tozer, Kanthou & Baguley, 2005) (Figure 1.4). A positive feedback loop is formed between blood flow reduction which leads to stacking of RBCs and further blood flow reduction (Tozer *et al.*, 2001). Neutrophil infiltration following CA4P treatment into the tumour also contributes towards vascular damage due to the increase in myeloperoxidase (MPO) activity which subsequently leads to the generation of free radicals (Parkins *et al.*, 2000).

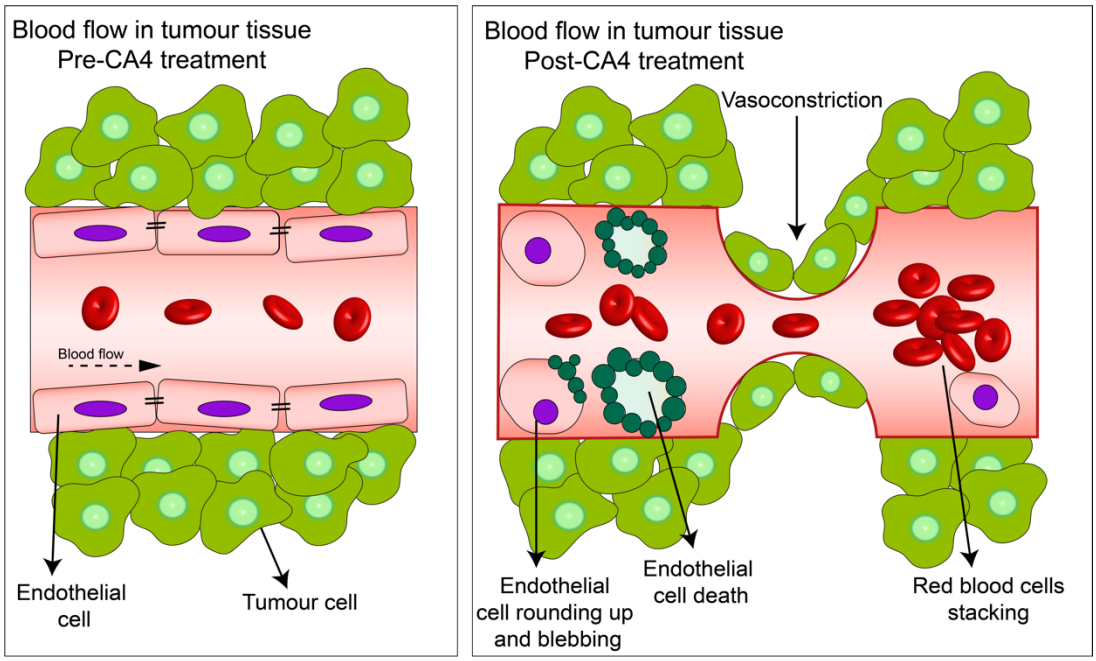

Figure 1.4 Cellular events leading to tumour blood flow reduction and/or shutdown *in vivo*.

Treatment of endothelial cells with CA4P causes endothelial cell changes due to the inhibition of tubulin polymerisation which leads to loss and/or disruption of cell-cell junctions such as VE-cadherin (Tozer, Kanthou & Baguley, 2005; Jaroch *et al.*, 2016). This is characterised by the cells rounding up and adopting a blebbing like morphology, leading to increased vascular resistance (Tozer, Kanthou & Baguley, 2005). An increase in vascular permeability to plasma proteins leads to water leaking into the interstitial space causing oedema. This leads to high interstitial fluid pressure and subsequent vascular shutdown (Tozer *et al.*, 2001; Tozer, Kanthou & Baguley, 2005). Blood viscosity is also increased due to water loss from the arterial to the venous end of the microcirculation and by red blood cells stacking due to reduced blood flow (Tozer *et al.*, 2001; Tozer, Kanthou & Baguley, 2005). A positive feedback look is formed as blood flow slows down, RBCs stack together which then leads to high blood viscosity (Tozer *et al.*, 2001; Tozer, Kanthou & Baguley, 2005). The figure was adapted from Tozer, Kanthou and Beguley 2005 and Jaroch *et al.*, 2016.

1.2.1.8 Susceptibility of tumour vasculature to CA4

Tumour perfusion is much more affected by CA4P than perfusion in normal tissues with no changes observed in heart and kidneys (Tozer *et al.*, 1999; Murata, Overgaard & Horsman, 2001). The basis for the selectivity of CA4P towards tumour vasculature has been attributed to the: (i) heterogeneity in tumour blood flow; (ii) differences between tumour and normal endothelial cells in terms of proliferation rate, post-translational modifications of tubulin, interactions between tubulin and the actin cytoskeleton; (iii) microenvironmental differences (*e.g.* oxygenation); (iv) normal tissue vasculature is more mature therefore can sustain more endothelial injury without leading to vascular shutdown, whereas the newly formed immature endothelial vessels of tumours cannot (Tozer *et al.*, 2001). Tumours with higher vessel permeability are also more susceptible to CA4P treatment (Beauregard *et al.*, 2001).

1.2.1.9 Therapeutic effects of CA4 in preclinical models

Histological examinations of subcutaneous (s.c.) and orthotopically transplanted human and mouse tumours showed that both CA4 and CA4P result in extensive haemorrhagic necrosis, with only a small rim of viable tumour cells at the tumour periphery (Dark *et al.*, 1997; Grosios *et al.*, 1999; Tozer *et al.*, 1999). Haemorrhagic necrosis is apparent within the first few hours of treatment eventually leading to secondary central necrosis with a “viable rim” at the tumour periphery within 24 h of treatment (Dark *et al.*, 1997; Grosios *et al.*, 1999; Malcontenti-Wilson *et al.*, 2001). This haemorrhage occurring within the first few hours of treatment is due to the loss in perfusion and increase in vascular permeability caused by mechanisms mentioned above which leads to leakage of blood. The viable rim is composed of well perfused vessels which have rapidly recovered after CA4 treatment. Tumours can re-vascularise from the viable rim by acquiring a nutritive supply from the surrounding normal tissue (Chaplin & Hill, 2002).

The effects of a single treatment with CA4 or CA4P on the growth of tumours is either none or very limited with modest growth delays only observed at doses higher than 100 mg/kg. This is mainly attributed to the viable rim remaining post-treatment (Dorr *et al.*, 1996; Grosios *et al.*, 1999; Chaplin & Hill, 2002). In an effort to improve the anti-tumour activity of CA4, multiple dosing regimens have been used (Boehle *et al.*, 2001; Malcontenti-Wilson *et al.*, 2001). Daily dosing of 50 mg/kg CA4P for 21 consecutive days caused a significant growth delay in non-small cell lung carcinomas (Boehle *et al.*, 2001). Comparing dosing regimens in a lymphoma model, it was

observed that dividing a dose of 800 mg/kg CA4P into 4 x 200 mg/kg resulted in better anti-tumour activity (Nabha *et al.*, 2001). Repeated doses on the same day in a murine breast tumour model also increased the effectiveness of CA4P. However, this also resulted in some toxicity (Hill *et al.*, 2002).

The increased effectiveness when repeated doses of CA4P were administered may be due to "self-trapping" of CA4 within the tumour tissue, leading to a longer exposure time to the drug and therefore preventing rapid recovery and eventually leading to tumour cell death (Hill *et al.*, 2002). Table 1.2 summarises the anti-tumour activity of CA4P and CA4 used as a monotherapy and the importance of scheduling, repeated dosing, tumour type and vascular characteristics.

1.2.1.10 Pharmacokinetics of CA4P

For successful translation of drugs such as CA4P to the clinic it is important to understand the PK of these drugs in terms of absorption, distribution, metabolism and elimination (ADME), the toxicity (T) of a drug is also considered in ADMET (Hodgson, 2001). Absorption generally concerns orally delivered drugs (Hodgson, 2001). Often the inefficient or incorrect ADME is what leads to undesirable side effects and early exclusion of a drug progressing into the clinic (Hodgson, 2001). In general drug metabolism involves a number of reactions categorised into phase I and phase II (Jaroch *et al.*, 2018). Phase I includes reduction, hydrolysis and oxidation in contrast, phase II mainly involves lipophilic compounds and occurs via the conjugation with endogenous compounds such as glucuronic acid or sulphate (Jaroch *et al.*, 2018). Glucuronidation is a key metabolic process specifically designed to eliminate endogenous compounds from the body and it is the main metabolic pathway involved in CA4 clearance (Aprile, Del Grosso & Grosa, 2010).

The metabolism of CA4P has been investigated in humans, dogs and mice while the distribution and excretion has been studied in rats (Dowlati *et al.*, 2002; Rustin *et al.*, 2003; Kirwan *et al.*, 2004; Wang *et al.*, 2009; Xu *et al.*, 2012). Early studies in CBA mice showed that CA4P had a very short plasma half-life approximately 15 min, which may explain the lack of anti-tumour activity observed (Tozer *et al.*, 1999). CA4 also bound to plasma proteins, which further reduced its activity as demonstrated *in vitro* (Tozer *et al.*, 1999). The mean plasma terminal half-life[2] of CA4P and CA4 in humans was found to be 0.47 h and 4.2 h respectively (Dowlati *et al.*, 2002).

---

[2] Terminal half-life in plasma is defined as the time required to divide the plasma concentration of a drug by two (Toutain & Bousquet-Mélou, 2004).

Table 1.2 Anti-tumour activity of CA4P and/or CA4 monotherapy in preclinical models.

Cancer type	Dose	Response	Toxicity	Reference
Breast	500 mg/kg (i.p.)	No growth delay	-	(Chaplin & Hill, 2002)
Colon	*50-200 mg/kg or 100 mg/kg (i.p.)	Modest growth delay at ≧ 100 mg/kg	200 mg/kg toxic	(Grosios *et al.*, 1999)
Leukemia	100-200 mg/kg or 100 mg/kg daily for 9 days (i.p.)	No growth delay	Dose-limiting toxicity	(Dorr *et al.*, 1996)
Non-small cell lung cancer	50 mg/kg daily for 21 days (i.p.)	Significant growth delay	-	(Boehle *et al.*, 2001)
Liver metastases	1-25 mg/kg for 14 days (s.c. infusion)	Significant growth delay at 15 mg/kg	Toxicity at ≧ 25 mg/kg	(Malcontenti-Wilson *et al.*, 2001)
Lymphoma	1 x 800 mg/kg , 2 x 400 mg/kg, 4 x 200 mg/kg or 8 x 100 mg/kg (i.v.)	Significant growth delay ≧ 200 mg/kg	-	(Nabha *et al.*, 2001)
Breast	x1 500 mg/kg, 10 x 50 mg/kg or 25 mg/kg twice per day for 10 days (i.p.)	Significant growth delay in 25 mg/kg x 2 daily for 10 days	Body weight loss	(Hill *et al.*, 2002)
Rhabdomyosarcoma	25 mg/kg x 1 or x 2 or 10 mg/kg daily for 5 days (i.p.)	Significant growth delay	-	(Ahmed *et al.*, 2003)

*CA4 (Hydrophobic); i.p: intraperitoneal injection; i.v.: intravenous injection; s.c.: subcutaneous –: No data reported.

A further human study showed that CA4P was rapidly dephosphorylated (within seconds) to the active form CA4, CA4 was further metabolised at a slower rate (minutes) to the glucuronide, CA4G (Rustin *et al.*, 2003).

The alpha half-life[3] of CA4 was reported to be 0.2-0.3 h, while the beta half-life[4] was approximately 2 h in humans (Rustin *et al.*, 2003). In mice the half-life of CA4 reported in plasma was 0.35 h (Kirwan *et al.*, 2004). In beagle dogs the plasma half-life of CA4 was reported to be 2.27-2.75 h depending on the initial dose administered (Wang *et al.*, 2009). The plasma terminal half-life of CA4 in rats was 0.39 to 1 h (Xu *et al.*, 2012). Kirwan *et al.,* (2004) also studied the PK of CA4P and CA4 in MAC29 colon tumours following an i.p. injection of CA4P at 150 mg/kg and reported a tumour half-life of 0.72 h and 9.62 h for CA4P and CA4 respectively (Kirwan *et al.*, 2004).

Distribution studies 15-90 min after intravenous (i.v.*)* administration of CA4P in rats, showed that CA4 was found mainly in the heart, intestine, lung, liver and spleen while to a lesser extent in the kidneys, stomach and brain (Xu *et al.*, 2012). Excretion of CA4 in humans is through the urine as CA4G (Rustin *et al.*, 2003). CA4 in rats was also mainly excreted as CA4G in the urine, however CA4 was also recovered in the faeces, urine and bile (Rustin *et al.*, 2003; Xu *et al.*, 2012). Toxicity associated with CA4P is discussed in the clinical trials section (1.2.1.12).

Phase I and II drug metabolism of CA4 was studied *in vitro* using human and rat liver microsomes and *in vivo* in rats. This resulted in the identification of a number of metabolites including glucuronide and sulphate metabolites (Aprile *et al.*, 2007; Aprile, Del Grosso & Grosa, 2009). Uridine diphosphate (UDP)-glucuronosyltransferases (UGTs) are major phase II metabolising enzymes in humans that catalyse the conjugation with UDP-glucuronic acid (Aprile, Del Grosso & Grosa, 2010) (Figure 1.5). Glucuronidation mainly occurs in the liver where UGT1A is present, however it can occur in other extrahepatic tissues (Aprile, Del Grosso & Grosa, 2010). UGT1A9 was the main isoform observed to be involved in catalysing the glucuronidation of CA4, UGT1A6 was also recognised to play a major role in the process (Aprile, Del Grosso & Grosa, 2010).

---

[3] Alpha half-life: is defined as the rate of decline of a drug in plasma concentration as a result of drug redistribution from central to peripheral compartments (Teboul & Chouinard, 1990).

[4] Beta half-life: is defined as the rate of decline of a drug as a result of drug elimination due to the process of drug metabolism (Teboul & Chouinard, 1990).

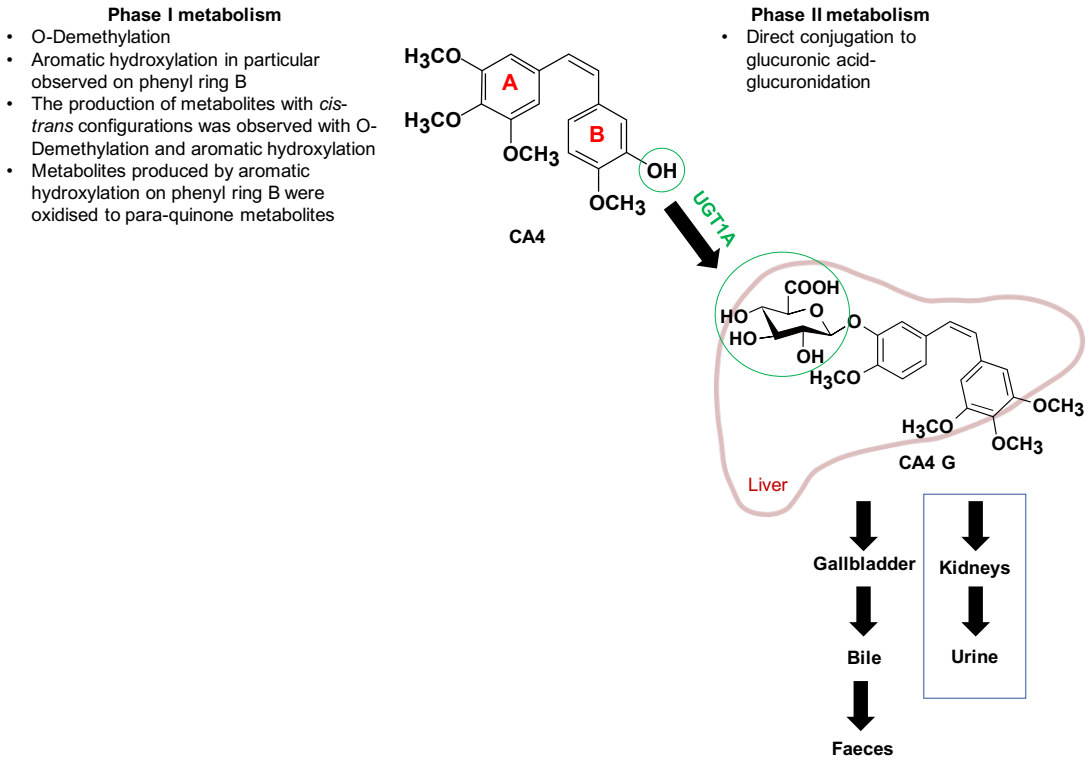

Figure 1.5 Metabolism of CA4.

The metabolism of CA4 has been studied *in vitro* using rat and human liver microsomes and in rats *in vivo* (Aprile *et al.*, 2007; Aprile, Del Grosso & Grosa, 2009). O-demethylation and aromatic hydroxylation were the two pathways during phase I metabolism and resulted in metabolites with *cis* and *trans* configurations (Aprile *et al.*, 2007). The metabolites produced by aromatic hydroxylation on phenyl ring B were further oxidised to para-quinone metabolites (Aprile *et al.*, 2007). Phase II metabolism involved direct conjugation to glucuronic acid and or sulphate (Aprile, Del Grosso & Grosa, 2009). *In vivo* experiments in rats revealed that CA4 is excreted in faeces, urine and bile approximately 30% of the injected drug, as most of it excreted in the urine as CA4G (Xu *et al.*, 2012). In humans CA4 is exclusively excreted as CA4G through the urine (Rustin *et al.*, 2003).

1.2.1.11 Combination treatments with CA4

Resistance of the viable rim which leads to tumour regrowth and the short plasma half-life limits the effectiveness and anti-tumour activity of CA4. Due to the resistance of the viable rim, CA4 is a good candidate drug for combination treatments. Tumour cells in the viable rim are well oxygenated and rapidly proliferating and are therefore, good targets for conventional treatments (Chaplin & Hill, 2002).

Nitric oxide (NO) protects against neutrophil infiltration and vascular damage induced by CA4, indeed tumours with higher NO synthase activity tend to be more resistant to CA4P induced vascular damage (Parkins *et al.*, 2000). Using NO inhibitors simultaneously or after CA4P treatment significantly potentiates its anti-vascular activity (Tozer *et al.*, 1999; Parkins *et al.*, 2000). Using anti-angiogenic agents such as anti-VE-cadherin agents in combination with anti-vascular CA4P also potentiated the anti-tumour activity (Vincent *et al.*, 2005).

There needs to be careful considerations of the timing of CA4 administration with conventional chemotherapy or radiotherapy, as for example the reduction in oxygen levels caused by CA4 will hinder radiotherapy (Siemann, 2011). However, there have been conflicting reports when CA4 or CA4P were administered with chemotherapy. Gemcitabine uptake in liver tumours for example was significantly decreased when CA4 was administered a few hours before gemcitabine (Fruytier *et al.*, 2016). However CA4P in combination with irinotecan enhanced the anti-tumour activity of irinotecan and this was found to be independent of administration sequence (Wildiers *et al.*, 2004). Administration of 5-FU 20 min prior to CA4P in a mouse colon cancer model also significantly enhanced anti-tumour activity (Grosios *et al.*, 2000).

1.2.1.12 Clinical trials with CA4P

CA4P entered clinical trials in 1998 (Galbraith *et al.*, 2003). It has been used both as a monotherapy and in combination with chemotherapy and radiotherapy. Much like the preclinical work, measurements of tumour perfusion in Phase I clinical trials using DCE-MRI and positron emission tomography (PET), showed that doses of ≥ 52 mg/m^2 significantly reduced tumour perfusion within the first few hours post CA4P treatment (Anderson *et al.*, 2003; Galbraith *et al.*, 2003). No changes in perfusion in normal tissues were observed (Galbraith *et al.*, 2003).

Clinical trials are assessed for response using the response evaluation criteria in solid tumours (RECIST) guidelines, complete response refers to the disappearance of all target lesions; partial response, means at least a 30% decrease in the diameter of

the lesion; progressive disease is at least a 20% increase in the diameter of the lesion and stable disease is no change, either decrease or increase in the lesion (Eisenhauer *et al.*, 2009) (Table 1.3).

Dose limiting toxicities including hypertension, neuropathy and vomiting were observed at doses > 68 mg/m^2 (Anderson *et al.*, 2003; Rustin *et al.*, 2003). The maximum tolerated dose (MTD) in humans was determined to be ≤ 60 mg/m^2 (Dowlati *et al.*, 2002). The MTD dose in humans is equivalent to a drug dose of 1.6 mg/kg. In mice this is equivalent to 0.13 mg/kg, the commonly used dose of CA4P in mice is 100 mg/kg which is equivalent to 8 mg/kg in humans (or approximately 300 mg/m^2) calculated using the guidelines provided by the FDA, indicating that this is five times higher than the MTD in humans (U.S. Department of Health and Human Services Food and Drug Administration, 2005).

The main concern associated with CA4P treatment is cardiovascular toxicities, 2/25 patients with advanced tumours had acute coronary events, in a Phase I study assessing the cardiovascular safety of CA4P (Cooney *et al.*, 2004). Cardiovascular toxicities have also been recorded in a Phase II trial, with 1/26 patients stopping treatment (Mooney *et al.*, 2009). A further toxicity as well as vomiting and nausea that was frequently reported in Phase I and II trials was tumour pain (Dowlati *et al.*, 2002; Rustin *et al.*, 2003; Mooney *et al.*, 2009). Although one patient with advanced thyroid cancer had complete response to CA4P monotherapy (Dowlati *et al.*, 2002), most clinical trials focused on combination regimes.

The combination of CA4P and carboplatin simultaneously, resulted in CA4 altering the PK of carboplatin resulting in severe thrombocytopenia and lead to early termination of the study (Bilenker *et al.*, 2005). Phase I trials have also been conducted in combination with radiotherapy and bevacizumab (Nathan *et al.*, 2012; Meyer *et al.*, 2009). Both studies reported reduction in tumour perfusion, however had no complete or partial responses, patients either showed stable disease or progressive disease. However, side effects including neutropenia, myelosuppression, tumour pain and nausea were also reported (Meyer *et al.*, 2009; Nathan *et al.*, 2012). In particular, the combination of bevacizumab with CA4P seemed to potentiate the effects of CA4P (Nathan *et al.*, 2012).

Table 1.3 Clinical trials with published data looking at efficacy, safety and tolerability of CA4P as monotherapy or in combination.

Cancer type	Phase	N	Co-treatment	Dose	Imaging Modality	Response	Adverse effects	Reference
Solid tumours	I	18	none	5-114 mg/m^2	DCE-MRI	X[a]	-	(Galbraith *et al.*, 2003)
Solid tumours	I	34	none	5-114 mg/m^2	DCE-MRI	X[b], no CR or PR	Tumour pain, hypertension, Vomiting	(Rustin *et al.*, 2003)
Solid tumours	I	34	none	5-114 mg/m^2	PET	X[c]	Hypertension, neuropathy	(Anderson *et al.*, 2003)
Advanced tumours	II	25	none	18-90 mg/m^2	DCE-MRI	4% CR, 8% SD	Tumour pain, hypertension, vomiting	(Dowlati *et al.*, 2002)
Advanced anaplastic thyroid carcinoma	II	26	none	45 mg/m^2	-	no CR or PR, 27% SD	Tumour pain, nausea, vomiting, cardiovascular	(Mooney *et al.*, 2009)
Solid tumours	I	16/16	Carboplatin	27-36 mg/m^2	-	37.5% SD, no CR	Neutropenia, nausea, vomiting, thrombocytopenia	(Bilenker *et al.*, 2005)
Gastrointestinal carcinoma	I	11/12	Radiotherapy with ^{131}I-A5B7 Anti-CEA	45 mg/m^2	DCE-MRI	25% SD, 58.3% PD, no CR or PR	Neutropenia, nausea, tumour pain, fever, hypertension, myelosuppression	(Meyer *et al.*, 2009)
Advanced tumours	I	13/15	Bevacizumab (Avastin)	15-63 mg/m^2	DCE-MRI	60% SD, 27% PD	Hypertension, 1/15 patients severe liver hemorrhage (previous history), pain	(Nathan *et al.*, 2012)
Non-small cell lung cancer (NSCLC)	II	17/63	Carboplatin, Paclitaxel, Bevacizumab	60 mg/m^2	-	66.7% PR, 33.3% SD	Neutropenia, nausea, diarrhoea	(Garon *et al.*, 2016)

N: Number of patients in the trial/ number of patients that have completed the trial. DCE-MRI: Dynamic contrast enhanced magnetic resonance imaging; PET: positron emission tomography; The aims of the trials were to X[a]: demonstrate the use of DCE-MRI at measuring the anti-vascular activity of CA4P; X[b]: test the Safety and Pharmacokinetics; X[c]: to demonstrate the use of PET at measuring the anti-vascular activity of CA4P; CR: complete response; PR: partial response; PD: Progressive disease;

Although CA4P in preclinical models has shown some promising results as a monotherapy and in combination, in humans the rapid plasma half-life, metabolism and various adverse side effects has hindered its progression into clinical use. It would therefore be of interest to develop and evaluate a smart drug delivery system (DDS) for CA4 or CA4P that may overcome some of these problems.

1.3 Nanoparticles as Drug Delivery Systems

About 40% of currently approved and almost 90% of compounds in the discovery pipeline are poorly water soluble (Kalepu & Nekkanti, 2015). A number of these compounds also suffer from low permeability, rapid metabolism and elimination from the body and are characterised by poor safety and tolerability profiles (Kalepu & Nekkanti, 2015). Due to this, modified formulations of existing drugs such as CA4P are being developed. Formulation and delivery of hydrophobic drugs is particularly challenging and encapsulation in nanoparticles (NPs) may offer an alternative route to enable their formulation in aqueous solutions.

NPs, as DDS have been designed to alter the PK of drugs in patients and enable the delivery of smaller doses to targeted tissues in an effort to improve the therapeutic index and reduce overall systemic toxicity (Wilhelm *et al.*, 2016). This remains the key aim of an ideal NP for drug delivery. NP properties such as size, structure, surface properties including targeting ligands are amongst the most important factors extensively studied.

A plethora of NP formulations are being studied including liposomes, polymer-based NPs, gold NPs, micelles, silica NPs, quantum dots, dendrimers, magnetic NPs, hydrogels and nanoemulsions. All these different NP formulations could be potentially engineered to encapsulate hydrophilic drugs or hydrophobic drugs. Liposomes are the most studied NPs and the first to be approved for clinical use. Doxil® a liposome with doxorubicin (DOX) was approved in 1995 and in 2015 Onivyde® a liposomal formulation of irinotecan was approved (Tran *et al.*, 2017).

1.3.1 Size, Shape and Surface properties

NP DDS aimed at cancer therapy can be modified in terms of size, shape and surface properties to treat specific tumours. NP size and size distribution are amongst the most important characteristics of NPs, it determines their *in vivo* biodistribution, toxicity and targeting ability. It also influences drug loading capacity, release and stability (Sing & Lillard Jr, 2009). A number of modalities are used to measure NP

size and size distribution including dynamic light scattering (DLS), transmission electron microscopy (TEM) and scanning electron microscopy (SEM) (Valencia *et al.*, 2011; Poojari, Srivastava & Panda, 2015). In terms of size distribution the polydispersity index (PDI) is usually quoted (Gaumet *et al.*, 2008). Using a scale of 0 to 1, a PDI lower than 0.1 is generally associated with a monodispersed particle population while higher PDI values are associated with a broader size distribution (Gaumet *et al.*, 2008).

Upon i.v. injection, NPs undergo opsonisation and are rapidly taken up by the mononuclear phagocytic system (MPS). The MPS includes a number of phagocytic cells in the liver, spleen and lymph nodes (Blanco, Shen & Ferrari, 2015). NPs can escape from the circulation via openings called fenestrations in the endothelial barrier (Gaumet *et al.*, 2008). NPs of approximately 150 to 300 nm are usually found in the liver and spleen, particles of 30 to 150 nm are found in the bone marrow, heart, kidney and stomach after i.v. injection (Banerjee *et al.*, 2002; Gaumet *et al.*, 2008). In regards to spherical particles, i.v. administration of NP with a size ≤ 5.5 nm results in rapid accumulation and clearance from the kidneys (Choi *et al.*, 2007). NP size also plays a major role in tumours with poor vascularity (Cabral *et al.*, 2011). NPs of 30-100 nm all accumulated within a tumour model with hyper-permeability whereas only NPs <50 nm were able to accumulate in hypo-vascular and hypo-permeable tumour (Cabral *et al.*, 2011). This difference in uptake according to vascularity, demonstrates the effect of tumour-type heterogeneity in determining NP efficacy.

Particle size also influences release kinetics, NPs less than 150 nm have a high surface area to volume, resulting in most of the drug incorporated at or near the surface of the NP resulting in rapid release (Redhead, Davis & Illum, 2001). Larger particles enable a high degree of drug incorporation per NP and give a slower release (Redhead, Davis & Illum, 2001; Sing & Lillard Jr, 2009).

NP shape directly influences their intracellular uptake, rod-shaped NPs tend to have a higher delivery efficiency compared with spherical, plate or other shaped particles (Wilhelm *et al.*, 2016). For example direct comparison of nanorods and nanospheres with the same hydrodynamic diameter[5] measured by DLS, showed that nanorods diffused into tumours faster and deeper compared to nanospheres (Chauhan *et al.*,

[5] The hydrodynamic diameter measured by DLS is defined as the size of a hypothetical hard sphere that diffuses in the same manner as the particle being measured in the sample (Malvern Instruments, 2011).

2011). Moreover, NPs with neutral charge exhibit the highest delivery efficacy compared to positive or negatively charged particles (Wilhelm *et al.*, 2016).

Surface modifications can prevent rapid uptake by the MPS. Several surface modifications have been adopted to "camouflage" NPs from the MPS (Blanco, Shen & Ferrari, 2015). NPs can be functionalised with poly(ethylene glycol) (PEG) termed PEGylation, PEG is incorporated onto the surface of NPs, forming a hydrated shell that protects the NP from rapid clearance by the MPS (Milton Harris & Chess, 2003). PEGylation also increases NP half-life in the circulation and improves stability (Milton Harris & Chess, 2003). For example PEGylated liposomes had an 8 fold increase in plasma half-life compared to un-PEGylated liposomes (Harris, Martin & Modi, 2001).

Another method to prolong the circulation time of NPs is to modify NPs to include "self-markers" that prevent normal cells from activating the MPS (Shi *et al.*, 2016). The top-down approach involves coating NPs with membrane lipids and associated proteins of erythrocytes therefore, mimicking RBCs and avoiding elimination by the MPS (Che-Ming *et al.*, 2011). These erythrocyte-membrane NPs (in that case polymeric NPs) also had longer circulating half-lives when compared to PEG-coated NPs (Che-Ming *et al.*, 2011). The bottom-up approach involves the chemical conjugation of "self" markers that specifically bind and signal to phagocytes to inhibit clearance (Rodriguez *et al.*, 2013). One such self-marker is the "don't eat me" marker CD47 "self" peptide and like the erythrocyte membrane prolonged NP circulation compared to PEG (Rodriguez *et al.*, 2013).

1.3.2 Nanoemulsions

Nanoemulsions are oil in water (O/W) or water in oil (W/O) dispersions of two immiscible liquids (Mason *et al.*, 2006). Their size is usually less than 500 nm (Singh *et al.*, 2017). Among other applications, nanoemulsions have been used in the pharmaceutical industry to solubilise insoluble drugs, these hydrophobic drugs are dispersed directly into the oil phase (Zhang *et al.*, 2014). Nanoemulsions as DDS, can improve the bioavailability of drugs, protect them from early metabolism and enable controlled release (Zhang *et al.*, 2014).

The oil phase can be soybean oil, coconut oil, sesame oil, peanut oil, olive oil, long chain triglycerides (LCT) such as peanut oil and short chain triglycerides (SCT) such as triacetin (TA) and tripropionin (TPP) (Singh *et al.*, 2017). Choosing the appropriate oil is important as this will impact on drug loading, size, chemical properties and

stability (Ganta *et al.*, 2014). Coalescence and Ostwald ripening[6] effect nanoemulsion stability (Ganta *et al.*, 2014). Oswald ripening is a phenomenon whereby larger droplets in a nanoemulsion grow at the expense of the smaller droplets (Wooster, Golding & Sanguansri, 2008). SCT produce smaller droplets that are resistant to physical destabilisation by coalescence however the high water solubility of STC oils can result in Oswald ripening (Ganta *et al.*, 2014). Larger droplets produced by LCT are more stable to Oswald ripening (Wooster, Golding & Sanguansri, 2008).

An emulsifier is used to stabilise the oil water interface of an emulsion and impacts on nanoemulsion stability (Ganta *et al.*, 2014). The emulsifier should rapidly absorb at the oil water interface and reduce interfacial tension and prevent nanodroplet coalescence (Ganta *et al.*, 2014; Singh *et al.*, 2017). These can be an amphiphilic molecule such as a surfactant, phospholipids, polysaccharides or polymers (Ganta *et al.*, 2014). PEG can also be attached to nanoemulsions to increase their blood circulation half-life (Jarzyna *et al.*, 2009)

Nanoemulsions can be produced by high energy emulsification or low energy emulsification (Qian & McClements, 2011). High energy emulsification uses mechanical devices such as high pressure valve homogenizers, microfluidic devices and sonication techniques, capable of producing disruptive forces that breakup the oil and water, subsequently leading to oil droplet formation (Qian & McClements, 2011). Low energy emulsification involves spontaneous emulsification of oil droplets through temperature or environmental alterations in an oil-water-emulsifier system (Qian & McClements, 2011). The previously methods described for NP sizing are also applied to nanoemulsions. To ensure the safety of these nanoemulsions for clinical use, they undergo sterilisation (Ganta *et al.*, 2014). Due to the nature of nanoemulsions they cannot withstand high pressure and high temperatures, therefore, the most commonly used method for sterilisation is by filtering through a 0.22 μm filter (Ganta *et al.*, 2014). Nanoemulsions are routinely checked for microbial contamination through plating for microbial growth or incubating in tissue culture growth medium (Ganta *et al.*, 2014). In addition to nanoemulsions being excellent carriers for hydrophobic drugs, they have a good long-term stability and shelf-life up

[6] Ostwald ripening: is the process by which oil molecules from small droplets move to larger droplets *i.e.* larger particles grow at the expense of smaller particles. The speed of the process is dependent on the solubility of the oil in the aqueous phase (Capek, 2004).

to approximately 3 months (Jarzyna *et al.*, 2009). This long-term stability is determined by measuring changes in size as an indication of particle alteration.

Nanoemulsions have also been produced with multifunctional capabilities; imaging for diagnosing disease and visualising *in vivo* biodistribution and for delivery of therapeutic payload, the so called “theranostic” agents (Gianella *et al.*, 2011). Gianella *et al*., (2011) produced a theranostic nanoemulsion, the particle had a soybean oil core encapsulating iron oxide nanocrystals for MRI imaging and a therapeutic agent. The lipid-shell included a PEG arm to ensure long blood circulation and enabled the attachment of a tumour specific targeting ligand and fluorescent dye for further fluorescence imaging.

1.3.2.1 Lipid Oil NanoDroplets

Lipid-based nanoemulsions have been produced for the hydrophobic delivery of CA4 (Mico *et al.*, 2017). Lipid Oil NanoDroplets (LONDs) were a concept developed by Professor Stephen Evans at the School of Physics and Astronomy at the University of Leeds and were produced by Dr Sally Peyman and Dr Victoria Mico at the School of Physics and Astronomy at the University of Leeds. Figure 1.6 is a schematic illustration of LONDs. Although, CA4 was used in this project as a proof-of-concept, LONDs are novel generic formulations that can be used to encapsulate other hydrophobic compounds or anti-cancer drugs.

1.3.3 Passive and active targeting of NPs

1.3.3.1 Passive targeting and the enhanced permeability and retention effect of NPs

Tumour angiogenesis produces new blood vessels that are irregular and have fenestrations that range between 200-2000 nm depending on the tumour type and its microenvironment (Bertrand *et al.*, 2014). These fenestrations enable the enhanced permeation of NPs, while the poor lymphatic system in tumours allows retention of NPs as they cannot efficiently be cleared (Bertrand *et al.*, 2014).

This preferential accumulation or passive targeting is referred to as the enhanced permeability and retention (EPR) effect and it was first described by Matsumura and Maeda (1986), which described the accumulation and retention of macromolecules in solid tumours through the leaky vasculature and poor lymphatic drainage (Matsumura & Maeda, 1986). The EPR effect is mainly associated with fenestrations in the tumour vasculature that allow extravasation of NPs with NP size, shape and

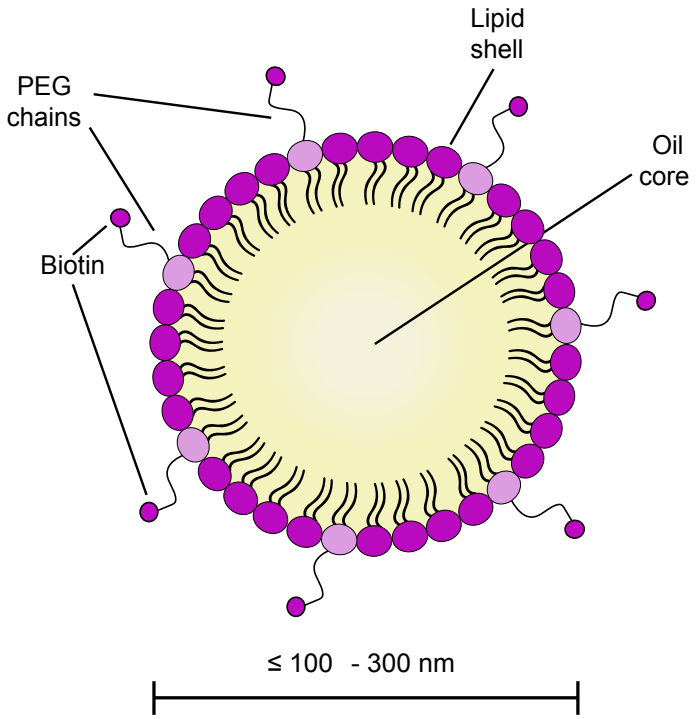

Figure 1.6 Schematic of a Lipid Oil NanoDroplet.

LONDs consist of an oil core within which the hydrophobic drug Combretastatin A4 is dispersed. LONDs are stabilised by a lipid shell. Biotinylated and pegylated lipids are also incorporated to increase stability and to enable further ligand attachment. LONDs can be ≤ 100-300 nm in diameter.

surface properties influencing their ability to do so. However, tumour type also influences uptake, with only smaller NPs able to penetrate hypo-permeable and hypo-vascular tumours (Cabral *et al.*, 2011).

Vascular permeability and ultimately the size of the tumour endothelial fenestrations in solid tumours is enhanced by the presence of permeability factors, such bradykinin, prostaglandins, NO and VEGF (Maeda, 2001; Maeda *et al.*, 2003). The success of the EPR effect allowing NP uptake was also shown to be affected by the degree of collagen fibers in the basement membrane (Yokoi *et al.*, 2014). A study by Yokoi *et al.,* (2014) investigated the accumulation of PEG-liposomal DOX in a range of tumours and found that the relative ratio of Matrix metalloproteinase (MMP)-9 and its endogenous inhibitor, tissue inhibitor of metalloproteinase (TIMP)-1 correlated with the level of NP accumulation (Yokoi *et al.*, 2014). High MMP-9 levels were associated with increased vascular permeability (Yokoi *et al.*, 2014).

Although passive targeting via EPR enhances the retention of NPs in tumour tissues, it does not necessarily mean that NPs encapsulating nucleic acids for example will reach their pharmacological target (Bertrand *et al.*, 2014). For these NPs specific targeting is a more appropriate approach.

1.3.3.2 Active targeting of NPs

Active targeting or ligand-mediated targeting, involves the attachment of specific ligands on the surface of NPs, this increases retention and subsequent uptake by the targeted disease cells (Bertrand *et al.*, 2014). Ligand recognition by its target substrate is the main mechanism underlying active targeting (Bertrand *et al.*, 2014). Ligands include antibodies, proteins, peptides and nuclei acids, while target molecules can be proteins or lipids that are either tumour-specific or tissue-specific (Yu *et al.*, 2010; Bertrand *et al.*, 2014). Tumour specific ligands may include receptors that are upregulated in tumour vasculature (Yu *et al.*, 2010). However, it is challenging identifying tumour specific ligands that are only present in tumour cells and not normal cells and therefore specificity is an important criterion for active targeting systems (Bertrand *et al.*, 2014).

Ligand conjugation on the NP is achieved through chemical conjugation or physical interaction (Yu *et al.*, 2010). Conjugation can be done before (for small molecules, peptides and aptamers) and after (for small molecules, peptides, aptamers, antibodies and proteins) NP formation (Bertrand *et al.*, 2014). Self-assembly NPs including a targeting ligand, cyclic arginine-glycine-aspartic acid (RGD) peptide

attached on their surface were produced through a chemical interaction with PEG on the surface and poly(-lactide-co-glycolide) (PLGA) as the core (Valencia *et al.*, 2011). The RGD peptide, binds to $\alpha v\beta 3$ integrin which is upregulated on the tumour vasculature and it is one of the most frequently used tumour targeting ligands (Desgrosellier & Cheresh, 2010).

Another covalent interaction includes the conjugation of a maleimide group on the NP surface to a thiol group on a ligand (Bertrand *et al.*, 2014). Moreover, PEG incorporated into the surface of NPs can be used as a linker between the NP and the targeting ligands (Yu *et al.*, 2010). For example PEG incorporated into the NP (liposome) bilayer via a lipid anchor 1,2-distearoyl-sn-glycero-3-phosphoethanolamine (DSPE) including maleimide was used to attach a thiolated monoclonal antibody to human epidermal growth factor receptor 2 (HER2) (Eloy *et al.*, 2017).

Non-covalent interactions include the most commonly used avidin-biotin interaction, NPs coated with avidin can bind to biotinylated ligands (Bertrand *et al.*, 2014). A molecular superstructure can be constructed whereby a biotin is covalently attached to the PEG chain on the surface of a NP, this can then bind to one avidin molecule (Gref *et al.*, 2003). The remaining biotin binding sites on avidin available can allow the further attachment of a different biotinylated ligand (Gref *et al.*, 2003). The targeted ligand can then bind to its target molecule (Gref *et al.*, 2003). LONDs mentioned previously through their biotinylated PEG chains have the potential to be targeted through the building of such a targeted molecular superstructure. It should be noted that this conjugation method has a limitation, the presence of avidin which is an exogenous protein on the surface of NPs can result in an immunological reaction and therefore clinical application of this system is limited (Friedman, Claypool & Liu, 2013). However, avidin can be replaced by NeutrAvidin a non-glycosylated analogue of avidin which prevents the nonspecific binding to cell surface proteins (Jain & Cheng, 2017).

1.3.4 Cellular uptake mechanisms of NPs

Following extravasation into the tumour microenvironment either by EPR or specific active targeting, NPs must undergo cellular internalisation to allow for payload release and subsequent therapeutic effect. The NP properties mentioned; size, shape and charge, will also influence the rate and cellular mechanism of uptake. The cellular mechanism of uptake will also depend on cell type and the machinery available. In general NPs are taken up by the process of endocytosis. During this,

the NP is engulfed in a membrane invagination and then pinched off to form an endosome (Sahay, Alakhova & Kabanov, 2010). The endosome, sometimes referred to as a phagosome, eventually fuses with a lysosome leading to the acidic degradation of the particle (Sahay, Alakhova & Kabanov, 2010). This endocytosis entry mechanism can be: 1: Clathrin dependent; 2: Caveolin-dependent; 3: Clathrin/Caveolin independent – diffusion; 4: Direct translocation. During clathrin dependent endocytosis a clathrin coated pit is formed and pinched off the membrane (Sahay, Alakhova & Kabanov, 2010; Selby *et al.*, 2017). The caveolin dependent pathway leads to the fusion with a "caveosome" which has a natural pH and in some cases can bypass lysosomes (Sahay, Alakhova & Kabanov, 2010). Alternatively NPs can completely bypass these intracellular trafficking pathways and enter through membrane diffusion or direct translocation across the membrane (Selby *et al.*, 2017).

Due to lysosome degradation in particular for NPs carrying nucleic acids for example, a number of studies have focused on strategies for NP escape from the endosomes. Adding natural lipids such as 1,2-Dioleoyl-sn-glycero-3-phosphoethanolamine (DOPE) to cationic liposomes enables stabilisation and promotes the rapid fusion with the endosomal lipid bilayer (Du *et al.*, 2014). Moreover, membrane destabilising peptides have also been used to promote endosomal escape (Martens *et al.*, 2014). The negatively charged endosomal membrane can interact with the positively charged NPs that are entrapped within the endosome and induce a flipping and further destabilisation ("flip-flop") mechanism (Martens *et al.*, 2014). Another strategy for endosomal escape is the proton sponge effect, here NPs absorb protons in response to acidification inside the endosome and leading to swelling, increased pressure and disruption of the endosome (Iversen, Skotland & Sandvig, 2011).

Surface charge also plays a role in NP uptake, so much so that researchers have created surface charge switchable NPs for enhanced cellular uptake (Yuan *et al.*, 2012). Switchable NPs are able to change their surface charge as a response to external stimuli such as the pH in endosomes or in the tumour extracellular space (Yuan *et al.*, 2012). For example Yuan *et al*., (2012) demonstrated that a DOX loaded NP having a negative charge was able to change to a positive charge NP in the acidic tumour environment (Yuan *et al.*, 2012). This resulted in an improved tumour cell internalisation and increased *in vivo* responses (Yuan *et al.*, 2012).

NPs are excellent drug-loading carriers enabling the loading of both hydrophilic and hydrophobic agents. However, they need to be specifically engineered to avoid non-specific binding and *in vivo* accumulation. Some NP designs, like LONDs lack

properties that enable externally triggered manipulation. In these cases conjugation to acoustically active Microbubbles (MBs) to create a multi-structure DDS would be of interest.

1.4 Microbubbles

1.4.1 Microbubble structure and production

MBs are small microspheres with diameters ranging from 1-10 *μ*m (Sirsi & Borden, 2009). MBs are intravascular traces and have been used routinely as contrast agents for diagnostic Ultrasound (US) (Sirsi & Borden, 2009). The first generation of MBs used for contrast imaging were air filled (*e.g*. Albunex®), however the high water solubility of these limited there *in vivo* life-time to a few seconds (Sirsi & Borden, 2009). This led to the production of MBs with insoluble gas (perfluorocarbon) cores which greatly increased their *in vivo* lifetime from seconds to minutes (Sirsi & Borden, 2009). The shell surrounding the gas core is usually a protein, phospholipid, surfactant or biocompatible polymer (Hernot & Klibanov, 2008). The shell improves MB stability against gas loss, dissolution and coalescence (Hernot & Klibanov, 2008).

MB size is particularly important in terms of their ability to pass through the circulation and their US responsive properties (Hettiarachchi *et al.*, 2007). Although, MBs exist which are approximately 10 *μ*m they need to ideally be less than 7 *μ*m to pass safely through the lungs without causing obstruction therefore, the optimum MB size range is between 2 to 5 *μ*m in diameter (Hettiarachchi *et al.*, 2007). Traditionally MBs were produced via mechanical agitation or sonication, these methods resulted in MBs with very high variation in size, poly-dispersed populations of MBs (Martin & Dayton, 2013).

MB production via sonication involves dispersing liquid or gas in a suspension with a suitable coating using high intensity US (Stride & Edirisinghe, 2008). The size of the resulting MB depends on the US frequency, power and pulse regime (Stride & Edirisinghe, 2008). Due to the variability in MB size from methods such as sonication a number of techniques have been applied to improve MB size such as Coaxial eletrohydrodynamic atomisation (CEHDA) and microfluidic systems (Stride & Edirisinghe, 2008). CEHDA although results in the formation of near monodispersed MBs their size ranges between 5-12 *μ*m in diameter, over the optimum size for *in vivo* application (Farook *et al.*, 2007; Stride & Edirisinghe, 2008).

In contrast, microfluidic systems have been utilised for the production of MBs with smaller size ranges (Garstecki *et al.*, 2004; Talu *et al.*, 2006; Hettiarachchi *et al.*, 2007; Peyman *et al.*, 2012). Microfluidics utilise a flow-focusing geometry whereby a liquid/lipid is forced under pressure to focus a stream of gas through a narrow opening referred to as orifice (Garstecki *et al.*, 2004; Hettiarachchi *et al.*, 2007). A microjet is created due to the focusing effect of the liquid which "pinches" off at the orifice due to the sudden change in pressure into MBs (Hettiarachchi *et al.*, 2007). MBs <5 *μ*m have been produced using this flow-focusing geometry (Hettiarachchi *et al.*, 2007). However, the size of the MBs depends on the gas and liquid flow rates and the diameter of the orifice (Talu *et al.*, 2006). Moreover CEHDA and microfluidic devices enable the production of MBs in a single-step and can also be used for the production of MBs with multiple layers (Stride & Edirisinghe, 2008).

1.4.2 Drug loading in MBs

Due to their thin shell and gaseous interiors MBs have a very low drug-loading capacity (Wang & Kohane, 2017). A number of ways have been described for the attachment of payload to the MB shell, drugs can be dissolved in an oil layer inside the MB shell; Directly incorporated within the shell; Conjugated through electrostatic interactions onto the outside of the shell (Lentacker, De Smedt & Sanders, 2009). Another way and the one utilised in this project is by attachment of NPs onto the outside shell of the MBs via avidin-biotin linkages (Lentacker, De Smedt & Sanders, 2009) (Figure 1.7).

Binding of DNA onto the surface of albumin-shelled MBs with a perfluorocarbon core through electrostatic interactions protected the DNA against nucleases and thus rapid degradation (Lentacker *et al.*, 2006). Unger *et al.,* (1998) were among the first to incorporate an extra drug-encapsulating oil layer inside the phospholipid shell as observed in Figure 1.7 (Unger *et al.*, 1998). Specifically paclitaxel was dissolved in soybean oil and used to form phospholipid shelled MBs with a perfluorobutane (C_4F_{10}) core, these were tested *in vivo* and significantly reduced the toxicity of paclitaxel (Unger *et al.*, 1998).

Paclitaxel has also been dissolved in TA oil and used to produce a MB containing an oil layer inside the phospholipid shell, these MBs are also referred to as acoustically active lipospheres (AAL) (Tartis *et al.*, 2006). Zhao *et al.,* (2005b) were one of the first to report the incorporation of hydrophilic therapeutic compound, Hirudin a thrombin inhibitor within the phospholipid membrane (Zhao *et al.*, 2005b) (Figure 1.7).

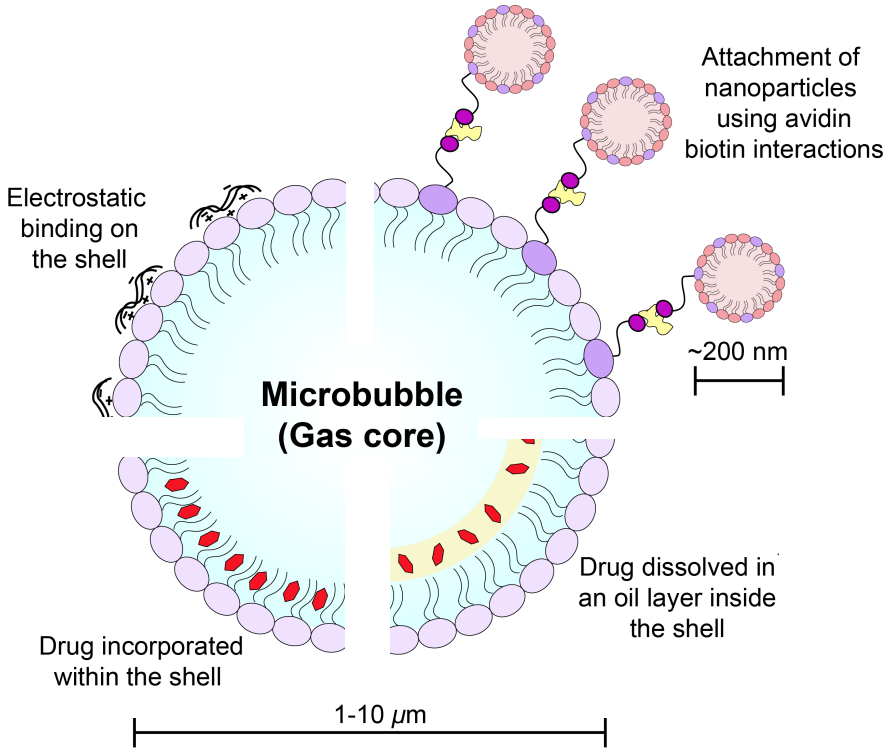

Figure 1.7 Schematic of drug loading strategies to microbubbles.

Drugs can be electrostatically attached to the shell of microbubbles; Nanoparticles encapsulating drugs can be attached onto the shell of microbubbles via avidin-biotin linkages; Drugs can be dissolved in an oil layer inside the microbubble phospholipid shell; Drugs can be incorporated within the shell of the microbubble. Image adapted from Lentacker, De Smedt & Sanders, 2009.

Liposomes with a phospholipid shell incorporating a biotinylated PEG chain (DSPE-$BPEG_{2000}$) were linked via NeutrAvidin to phospholipid-shelled MBs with DSPE-$BPEG_{2000}$) (Kheirolomoom *et al.*, 2007). Liposome incorporation increased the drug-loading capacity of the MB-liposome DDS, approximately 10^5 liposomes were linked to each MB (Kheirolomoom *et al.*, 2007). The authors also compared avidin and NeutrAvidin binding and found that there was a 3-fold increase in binding with NeutrAvidin (Kheirolomoom *et al.*, 2007). The same principles of attachment to MBs via avidin-biotin have been applied to DOX containing liposomes (Lentacker *et al.*, 2010). A common feature of all these payload-carrying MBs is that they retain their US responsiveness, this is particularly important as the release of the payload can be triggered by US (this will be further discussed below, external triggering section 1.5).

Another alternative approach is echogenic liposomes. These are liposomes that can encapsulate both drugs and gases (Huang, McPherson & MacDonald, 2008). The gas in echogenic liposomes can either reside between the two monolayers of the liposome bilayer or can exist as a separate air bubble covered by a single phospholipid monolayer within the aqueous compartment of the liposome (Huang, McPherson & MacDonald, 2008). Huang *et al.,* (2008) produced an echogenic liposome containing both gas and a hydrophilic drug-like molecule calcein using a pressure-freezing method, freezing of the liposomes under high pressure promoted the encapsulation of gas (Huang, McPherson & MacDonald, 2008).

1.4.3 MBs passive and active targeting

Unlike NPs, micron-sized MBs cannot passively accumulate in tumours via the EPR effect. However, it has been shown that MBs can be passively targeted up to a certain point owing to their specific shell characteristics (Paefgen, Doleschel & Kiessling, 2015). For example albumin and lipid-shelled MBs preferentially accumulate in injured tissues with ischemia/reperfusion and inflammation (Lindner *et al.*, 2000a). This preferential accumulation is due to the binding of MBs to activated leukocytes (monocytes and neutrophils) that are bound to the venular endothelium in response to injury (Lindner *et al.*, 2000a, 2000b). The binding of albumin MBs is due to interactions with integrins while the binding of lipid-MBs is due to interactions with the complement system (Lindner *et al.*, 2000a).

Active targeting refers to modifications on the surface of MBs to permit the attachment of targeting ligands to allow for subsequent binding to specific receptors (Kiessling *et al.*, 2012). Targeting ligands can either be attached before (incubated

with the phospholipids prior to MB formation) or after (via non-covalent interactions with avidin-biotin) MB production (Kiessling *et al.*, 2012). Several factors such as VEGFR2 are overexpressed on the tumour endothelium due to angiogenesis and are good targeting ligands (Willmann *et al.*, 2008). Using streptavidin-biotin interactions an anti-VEGFR2 antibody was successfully attached onto the surface of lipid-shelled MBs (Willmann *et al.*, 2008).

An alternative approach was used when VEGFR2 binding peptides were pre-conjugated onto phospholipids that were used to form MBs (Pysz *et al.*, 2010). A clinical trial used this VEGFR2 or kinase insert domain (KDR) in humans targeted MB as a contrast agent for the molecular imaging and monitoring of KDR-expressing tumours (Willmann *et al.*, 2017). Their results showed that the KDR-targeted MBs (or BR55) were well tolerated, and the US imaging signals matched the immunohistochemistry (IHC) results for KDR expression (Willmann *et al.*, 2017). The shells of the AAL (section 1.4.2) were prepared with an RGD peptide, the targeting increased *in vitro* binding of the AAL compared to non-targeted MBs (Tartis *et al.*, 2006). MBs have also been prepared with antibodies specific for intracellular adhesion molecule-1 (ICAM-1) covalently attached on their shells (Villanueva *et al.*, 1998). *In vitro* data showed a significant increase in binding to activated endothelial cells overexpressing ICAM-1, when MBs were targeted to ICAM-1 compared to control cells not overexpressing ICAM-1 (Villanueva *et al.*, 1998).

1.5 External Triggering and controlled release for Drug Delivery – Ultrasound

1.5.1 Definition of Ultrasound parameters

US is defined as a longitudinal pressure wave at frequencies above the audible limit of human hearing (>20 kHz) (Wang & Kohane, 2017). US has been used as an imaging modality in medicine however, it has gained much interest in drug delivery (Wang & Kohane, 2017). US can be regulated by changing different parameters such as frequency (expressed in MHz), intensity (expressed as W/cm^2) or acoustic pressure amplitude (or peak negative pressure expressed as kPa) and duty cycles; frequency regulates the depth of penetration which is inversely proportional to the frequency, in contrast, intensity regulates the amount of energy delivered to a desired site (US exposure) and duty cycle refers to the exposure time and succession of pulses (Boissenot *et al.*, 2016). US can be described as low frequency (0.02-3 MHz) or high frequency (>3 MHz) (Boissenot *et al.*, 2016). Lower US frequencies are

generally used for drug delivery as it ensures deeper tissue penetration, while higher US frequencies are used for diagnostic purposes as it ensures higher tissue resolution (Chowdhury, Lee & Willmann, 2017). For drug delivery *in vivo* the frequency can range between 0.3 to 2.2 MHz, the intensity from 0.06 to 3 W/cm^2 and the duty cycles from 0.25 to 50% (Lammertink *et al.*, 2015). Thermal index (TI) gives the rise in temperature in degrees for example a TI=1 will increase temperature by 1.0°C, the FDA limit for TI is a body temperature rise of 6°C (Duck, 2007). Mechanical index (MI) is alternative parameter used to define US intensity, mainly used for medical US scanners it is expressed as the ratio of the peak negative pressure in MPa to the square root of the frequency in MHz (Lammertink *et al.*, 2015). Mechanical indices are usually used between 0.1 and 1.9, however, due to the potential of US causing increase heat and therefore tissue damage, the FDA has set an upper limit for MI at 1.9 (Chowdhury, Lee & Willmann, 2017). Both TI and MI are used as safety indices for medical imaging (Duck, 2007). US alone can enhance drug delivery however it can also be used to the trigger the release of drug payloads from MBs (Wang & Kohane, 2017).

1.5.2 Sonoporation via stable and inertial cavitation

MBs that are exposed to an US pressure wave start to cavitate, cavitation is defined as the alternate shrinking and growing of MBs in response to the US pressure wave (Lentacker, De Smedt & Sanders, 2009). Stable cavitation or non-inertial cavitation mostly occurs at lower US intensities (peak negative pressure of < 100 kPa and MI < 0.1) whereas inertial cavitation occurs at higher US intensities (peak negative pressure 100 to ≥ 500 kPa, MI from 0.1 to ≥ 0.5) (Lentacker, De Smedt & Sanders, 2009; Boissenot *et al.*, 2016). Both stable and inertial cavitation can contribute towards MB mediated drug delivery (Chowdhury, Lee & Willmann, 2017).

During stable cavitation MBs demonstrate linear low amplitude oscillations, these stable oscillations result in liquid flow around MBs referred to as microstreams (Lentacker, De Smedt & Sanders, 2009). When MBs are close to cell membranes the microstreaming causes shear stress on the membrane that may result in the transient opening of the cell membrane (Lentacker, De Smedt & Sanders, 2009). This transient opening of the cell membrane caused by US exposure is known as sonoporation (Lentacker *et al.*, 2014). *In vitro* work using high-speed imaging has shown that oscillating MBs need to be in direct contact to the cell membrane to cause this transient pore formation (van Wamel *et al.*, 2006). This pore formation allowed for the transient uptake of small molecules like propidium iodine (PI) (van Wamel *et al.*, 2006). Moreover, stable cavitation caused by targeted to cluster of differentiation-31

(CD31) for example MBs also cause membrane pore formation (sonoporation) more effectively than non-targeted MBs (Kooiman *et al.*, 2011). Targeting is particularly important especially *in vivo* as it will ensure the close contact of the MBs with the endothelial cells (Kooiman *et al.*, 2011).

Improved drug uptake via small pore formation is not the only mechanism associated with improved drug delivery via stable cavitation, endocytosis has also been described (Meijering *et al.*, 2009). An investigation into the mechanisms of uptake of fluorescently labelled dextrans following exposure to MBs and US revealed that the uptake of smaller molecules (≤70 kDa) was via the transient pores while uptake of larger molecules (≥155 kDa) was via endocytosis (Meijering *et al.*, 2009).

In contrast, during inertial cavitation the oscillation amplitude of the MBs can increase rapidly eventually causing MB collapse (Lentacker *et al.*, 2014). This collapse results in the breakdown of the MB into smaller MBs (Lentacker *et al.*, 2014). As the MB collapses shock waves are generated in the fluid close to the MB, if a cell is close to the collapsing MB a jet of liquid is formed towards the cell surface (Lentacker, De Smedt & Sanders, 2009; Lentacker *et al.*, 2014). Moreover, these shock waves and resulting microjets cause very high forces that can also form membrane pores and may also permeabilise blood vessels (Lentacker *et al.*, 2014). Pore formations were reported on the cell membranes of cells that were exposed to both US and MBs (Yang *et al.*, 2008). The sizes of the pores strongly correlated with acoustic pressure, as pressure increased the size of the pores increased, with pore sizes ranging from a few nm (1 nm) up to a few *μ*m (4 *μ*m) (Yang *et al.*, 2008). It should be noted that pores in the *μ*m range are not transient and the cells are unable to repair this therefore non reparable sonoporation or sonolysis takes place eventually causes cell death (Yang *et al.*, 2008).

Sonoporation through stable cavitation requires direct contact of the MB with the cell membrane in contrast, to inertial cavitation where MBs can cause pore formations to cells that are in a certain distance (Zhou *et al.*, 2012; Lentacker *et al.*, 2014). This distance also the location of the MB at the start of the US was determined as the ratio of the distance (D) between the bubble and the cell and the diameter (d) of the MB, D/d which was found to be 0.75 (Zhou *et al.*, 2012). The size of the pores also depends on the US pressure and duration as these can range from 0.1 *μ*m to 0.8 *μ*m (Zhou *et al.*, 2012). US can therefore, be used to trigger the release of payload from MBs and depending on the US parameters such as frequency, pressure, MI and

pulse duration can either cause payload uptake via stable or inertial cavitation. More importantly drug delivery via MBs is restricted to the ultrasound treated region.

De Cock *et al.,* (2016) studied how NP-loaded MBs were able to deliver the NPs intracellularly. They predicted that loading rather than co-delivery improved intracellular delivery (De Cock *et al.*, 2016). Using real-time imaging they showed that MBs deposited NPs directly onto the cell membrane a process that the group termed as “sonoprinting” (De Cock *et al.*, 2016).

1.6 Therapeutic Microbubbles

Peyman *et al.,* (2012) have previously used a microfluidic platform for the on-chip production of liposome-loaded MBs in a single step approach (Peyman *et al.*, 2012). This microfluidic platform was used to generate therapeutic microbubbles (thMBs), these are MBs consisting of non-covalently via NeutrAvidin-biotin interactions attached liposomes encapsulating irinotecan or SN38 and targeted to VEGFR2 (P.L.Coletta, personal communication). Using the same single step approach chip design and different chip design in a two-step approach, LONDs encapsulating CA4 in an oil core were attached to MBs to produce thMBs for targeted triggered drug delivery. Figure 1.8 is a schematic representation of a thMB with LONDs.

It is hypothesised that thMBs are able to travel through the circulation undisrupted and bypass normal tissues. Traveling through the circulation thMBs can bind specifically to VEGFR2 which is upregulated on the surface of the tumour endothelium. Following binding, a low frequency US destruction pulse directly applied at the tumour would lead to high amplitude MB oscillations that would cause MB collapse and subsequent release of the LONDs or fragments of LONDs and CA4 near the tumour region, enhancing intratumoural and intracellular uptake of CA4. The collapsing MB would cause the production of high forces that would promote the transient pore formation (sonoporation) at tumour endothelium further enhancing LOND and CA4 intratumoural uptake. This proposed mechanism of delivery is summarised in Figure 1.9. This delivery platform specifically used in this project for CA4, can alter the PK by potentially preventing rapid metabolism, clearance and off-site tissue distribution to enable restricted and controlled delivery only to US-exposed areas reducing any potential off-site toxicities.

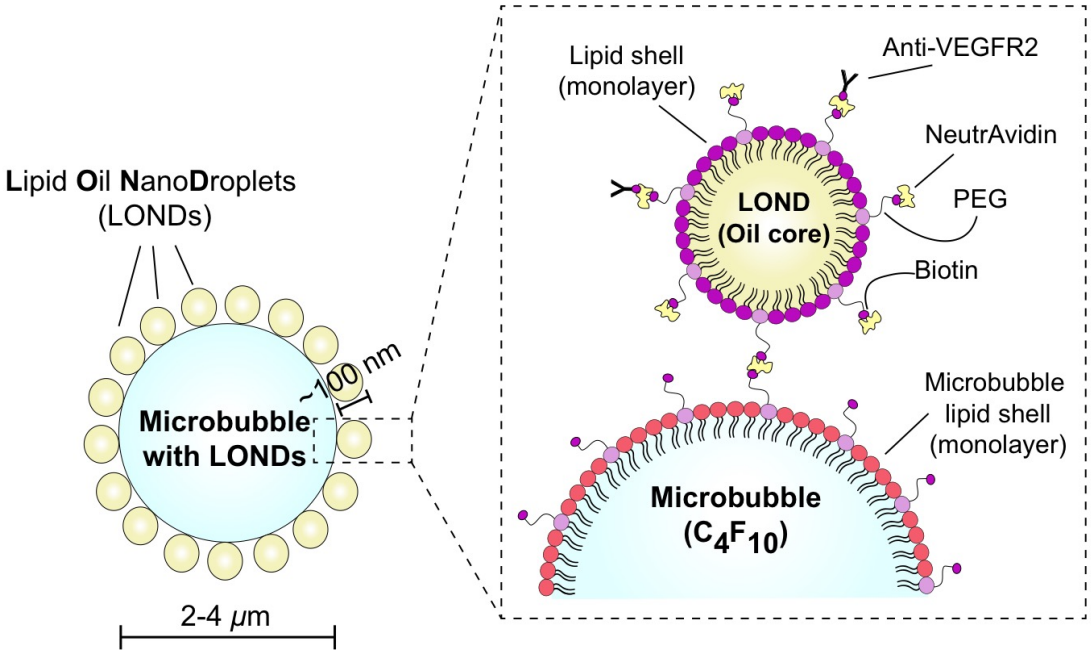

Figure 1.8 Therapeutic Microbubble with Combretastatin Lipid Oil Nanodroplets.

Therapeutic Microbubbles (thMBs) are defined as targeted microbubbles (MBs) loaded with CA4 encapsulating Lipid Oil NanoDroplets (LONDs) via NeutrAvidin-Biotin non-covalent interactions. Briefly, Combretastatin A4 (CA4) is dispersed in oil and used to prepare the LONDs. The lipid monolayer shells of LONDs are then functionalised with NeutrAvidin and used for LOND-MB production. Prior to MB formation, C_6F_{14} is included into the lipids that form the MB lipid-monolayer to increase MB stability and lifetime (Abou-Saleh *et al.*, 2016). The gas core of the MB is C_4F_{10} (perfluorobutane). Both LONDs and MBs have covalently attached biotinylated poly-(ethylene) (PEG) chains on their shells. This biotinylated PEG chain provides a linkage between the LONDs and the MB as a NeutrAvidin linker is added. Following production of a LOND-MB construct a biotinylated anti-VEGFR antibody can bind to the remaining NeutrAvidin binding site on the LONDs and the MBs, providing specific targeting to the tumour vasculature. The size of thMBs is usually between 2-4 μm in diameter, measured by light microscopy. Approximately 1-2 x 10^3 LONDs can be loaded onto a single MB depending on the LOND and MB diameters.

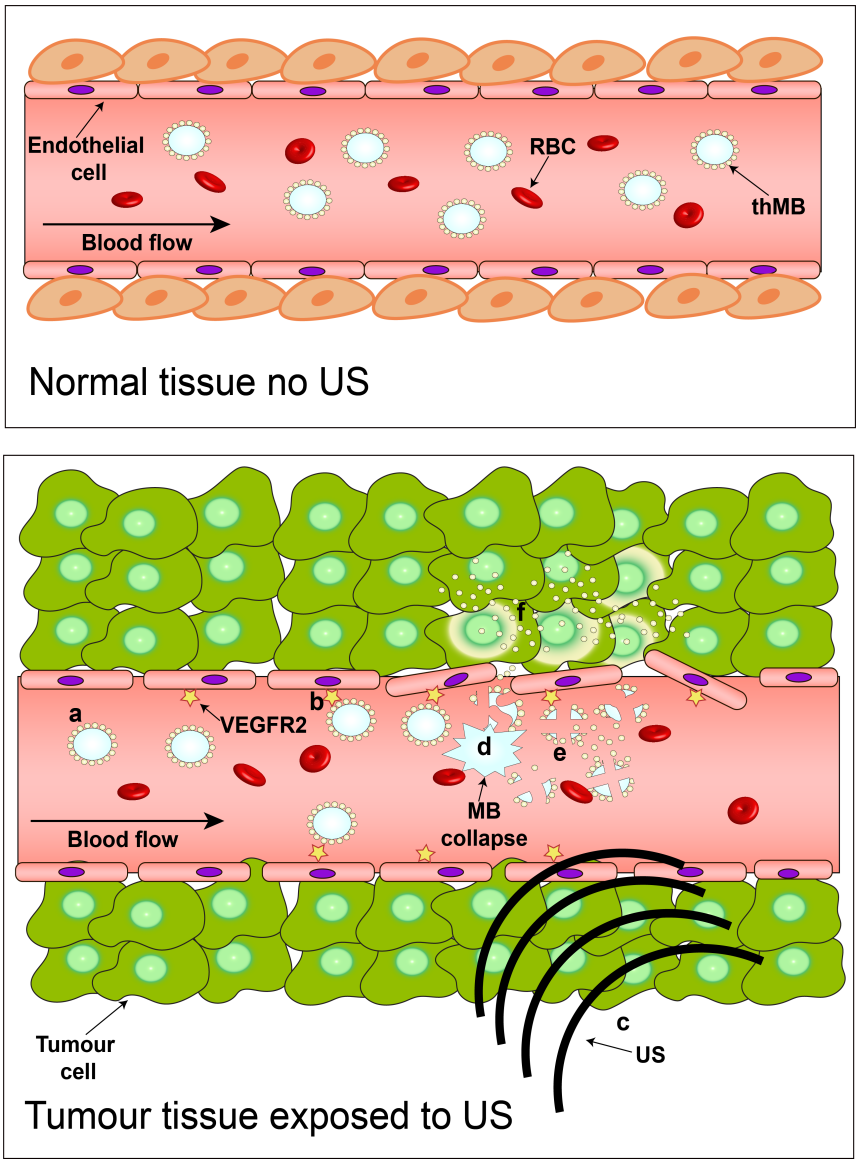

Figure 1.9 Proposed mechanism for therapeutic delivery of drugs via LONDs and US triggered MBs.

Intravenously injected thMBs can travel through the vasculature of normal tissue without releasing their payload (top panel) due to the lack of an US destruction pulse, trigger. Bottom panel (a) Upon arrival in the tumour vasculature thMBs can bind to their target VEGFR2 which is overexpressed on the tumour endothelium (b). Following binding an US destruction pulse, trigger (c) is applied directly at the tumour region causing high amplitude MB oscillation eventually leading to MB collapse (d) and release of LONDs and/or fragments of LONDs, CA4 and MBs (e). This collapse can lead to extreme forces that can enhance LOND and/or CA4 release, followed by intratumoural uptake via the transient opening of pores in the endothelial tumour membrane (sonoporation). Intratumoural LONDs or free CA4 can then be taken up intracellularly, intact LONDs release CA4 (f).

1.7 Project Aims

The aim of this work was to test the efficacy of LONDs encapsulating CA4 alone or attached to MBs (thMBs) as a hydrophobic DDS in a CRC model.

Specific aims of the project were:

- To develop qualitative and quantitative assays to assess the drug delivery capability of LONDs *in vitro* by investigating the MT defects caused by delivery of the CA4 payload
- To establish a liquid chromatography tandem mass spectrometry (LC-MS/MS) protocol for the specific measuring of CA4 in LONDs and in tissue samples
- To demonstrate intratumoural delivery and potential off-site delivery of CA4 by LONDs and/or CA4 thMBs *in vivo* by measuring CA4 concentrations in tissue samples
- To develop qualitative and quantitative immunostaining techniques to assess *in vivo* pharmacodynamic (PD) responses of CA4 LONDs and/or CA4 thMBs
- To assess the use of an *in vivo* fluorescent technique (Hoechst 33342 marker for perfusion) to measure the effects of CA4 delivered via LONDs or CA4 thMBs
- To evaluate the anti-tumour activity and potential off-site toxicities of LONDs used as a monotherapy
- To evaluate the anti-tumour activity of CA4 thMBs used in combination with a conventional anti-tumour drug, irinotecan

Chapter 2
Materials and Methods

2.1 Cell lines

2.1.1 Cell line maintenance and stock production

Human Colorectal Adenocarcinoma cells SW480 were chosen as the *in vivo* model. SW480 cells are derived from a primary adenocarcinoma of the colon, these are part of the CMS4 subtype ("mesenchymal") (section 1.1.1 for details on CMSs of CRC), which are characterised by an upregulation of genes involved in EMT (Guinney *et al.*, 2015; Berg *et al.*, 2017). CMS4 tumours are classified as undifferentiated and are of particular interest for treatment as the have the worst prognosis (Berg *et al.*, 2017). SW480, SVR murine pancreatic islet endothelial cells and EA.hy926 human endothelial cells were all obtained from ECACC (European collection of authenticated cell cultures - ecacc.org.uk). EA.hy926 endothelial cells are hybrid cells of HUVECs with A549/8 human lung carcinoma cells used as an *in vitro* model of angiogenesis and provide an alternative to HUVECs primary cells (Aranda & Owen, 2009).

SW480 were grown in Roswell Park Memorial Institute (RPMI-1640) with 10% (v/v) foetal calf serum (FCS, Sigma-Aldrich, UK). SVR and EA.hy926 cells were grown in high glucose (4.5 g/L), GlutaMAX^{TM} Dulbecco's modified Eagle's medium (DMEM), supplemented with 5% and 10% (v/v) FCS respectively. All cell lines were maintained at 37°C in 5% CO_2. SW480 cells were authenticated by single tandem repeat (STR) profiling and all cell lines screened negative for mycoplasma. Cells were harvested via trypsinisation at 80% confluence. Stocks of all cell lines were prepared in freezing media containing FCS and 10% (v/v) dimethyl sulfoxide, DMSO (Sigma-Aldrich, UK) and stored in vaporised liquid nitrogen below -180°C.

2.2 LOND production and characterisation

2.2.1 Lipid preparation and CA4 solubilisation

The following lipids were purchased from Avanti® Polar Lipids, Inc. (Alabaster, Alabama, USA). 1-palmitoyl-2-oleoyl-sn-glycero-3-phosphocholine (POPC); 1,2-distearoyl-sn-glycero-3-phosphoethanolamine-N[biotinyl(polyethyleneglycol-2000] (DSPE-BPEG$_{2000}$); 1,2-distearoyl-sn-glycero-3-phosphocholine (DSPC). Fluorescently tagged lipids Atto590 1,2-dioleoyl-sn-glycero-3-phosphoethanolamine (Atto590-DOPE) were purchased from Atto-TEC (Siegen, Germany). All lipids were dissolved in 1:1 (v/v) chloroform/methanol.

CA4, TA and TPP oils were all purchased from Sigma (Sigma-Aldrich, UK). An initial stock concentration of CA4 25 mg/mL or 50 mg/mL was obtained by dissolving CA4 and vortexing vigorously in TA or TPP.

2.2.2 LOND production by high pressure emulsification and purification

LONDs were produced by a two-step high pressure homogenisation of an o/w solution containing lipids by Dr Victoria Mico and Dr Sally Peyman (School of Physics and Astronomy, University of Leeds) as previously described (Mico *et al.*, 2017). The lipid shell of TA LONDs was composed of 95:5 mol% POPC and DSPE-BPEG$_{2000}$ while the lipid shell of TPP LONDs was composed of 75:20:5 mol% DSPC, Cholesterol and DSPE-BPEG$_{2000}$. When required for fluorescence tracking 0.1 mol% Atto590-DOPE was added into the lipid mixture. After mixing the lipids, the chloroform/methanol solvents were evaporated under nitrogen for at least 30 min, these formed a lipid film around the walls of the vial. The lipid film was re-suspended in 0.7 mL of TA or TPP with or without CA4 (section 2.2.1) by vortexing and sonicating for approximately 10 min. Following this, phosphate buffered saline (PBS) was added to the lipid/oil/drug mixture to a final volume of 4 mL (Figure 2.1 A). The first homogenisation step was a blending step using the rotor-stator system, Polytron PT1300 D (Kinematic AG, Switzerland), at 12500 rpm for 10 min at 40°C and atmospheric pressure (Figure 2.1 B). The first homogenisation step roughly mixed the oil/lipid/PBS mixture. Following this, 6 mL of PBS was added to the mixture to a final volume of 10 mL. The second homogenisation step was performed with a high pressure homogeniser, Emulsiflex C5 (Avestin Europe GmbH, Germany) for 20 min. The pressure was maintained at 175 MPa (Figure 2.1 C).

LOND preparations were cleaned to remove any excess lipid and unencapsulated drug. Purification was done either through cross-filtration or dialysis performed by Dr Victoria Micro (School of Physics and Astronomy, University of Leeds). Briefly, during cross-filtration, the LOND sample passes tangentially along the surface of the filter. Particles smaller than the filter can permeate across the membrane whereas larger particles are retained and continue circulating. The LONDs were flowed at 40 mL/min for 2 h. Dialysis was performed using 8 kDa dialysis tubes (Mini Dialysis Kit, GE healthcare) which were filled with 2 mL of LONDs. The dialysis tube was then placed inside a beaker containing 1 L of PBS. The sample was then placed at 4°C and stirred overnight. After dialysis the sample was stored at 4°C.

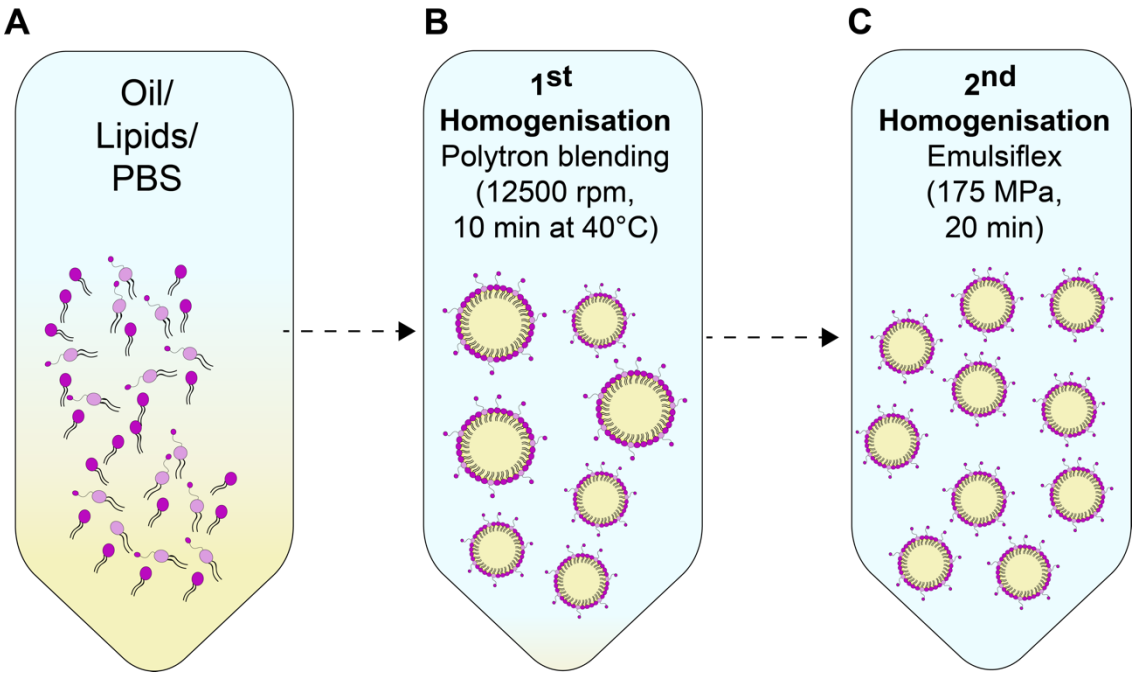

Figure 2.1 LOND production by a two-step high pressure homogenisation. (A) Lipids are re-suspended in 0.7 mL of oil (TA or TPP), PBS is added to the mixture up to a final volume of 4 mL. (B) The mixture is then introduced into the Polytron for initial blending at 12500 rpm for 10 min at 40°C for the first homogenisation step. This roughly mixes the lipids/oil/PBS and produces LONDs with a high variation in size. (C) The Emulsiflex C5 is used for the second fine homogenisation step at 175 MPa for 20 min. This second step reduces the size of the LONDs and improves the homogeneity.

2.2.3 Sizing and quantification of LONDs by DLS, qNano and NanoSight

The LOND size was measured by three different techniques: DLS using a ZetaSizer Nano (Malvern Instruments, UK), qNano (Izon Science, UK) and NanoSight (Malvern Instruments, UK) by Dr Victoria Mico, School of Physics and Astronomy, University of Leeds. DLS measures the hydrodynamic diameter and size distribution of particles that are dispersed in a liquid, by analysing the light scattering intensities of particles in Brownian motion. The hydrodynamic diameter was then calculated using the Stokes-Einstein equation (Murdock *et al.*, 2008; Varenne *et al.*, 2016). The q-Nano analyses particles using the Tunable Resistive Pulse Sensing principle by measuring the increase in electrical resistance as particles pass through a pore giving a precise measurement of concentration (Varenne *et al.*, 2016). Single particle tracking is performed using a NanoSight which utilises both light scattering and Brownian motion of particles to analyse size and particle concentration (Varenne *et al.*, 2016). Briefly, LONDs were diluted 1:100 in PBS and placed in a plastic disposable cuvette and analysed using a DLS system. The average size from three measurements was recorded. LONDs were diluted 1:100 and $1:10^6$ for measurements using q-Nano and NanoSight respectively.

2.2.4 Quantification of CA4 in LONDs by Ultraviolet-visible spectroscopy

Ultraviolet-visible (UV-VIS) spectroscopy (Perkin Elmer, USA) is frequently used to measure the amount of light absorbed by a substance, the absorbance being proportional to the concentration. UV-VIS spectroscopy measurements of CA4 concentration in LOND solutions were performed by Dr Victoria Mico (School of Physics and Astronomy, University of Leeds). Briefly, standards from 0-25 μg/mL were prepared for CA4 in the relevant oil (TA or TPP). The absorption of each concentration was measured at 300 nm, using quartz cuvettes with a 1 cm path length. A linear standard curve was produced and the equation of the line was used to calculate the concentration of CA4 in the LOND sample tested. The concentration of CA4 in LONDs was also confirmed by LC-MS/MS (section 2.6). The percentage encapsulation efficacy (% EE) for CA4 in LONDs was determined by dividing the CA4 concentration provided by the UV-VIS or LC-MS/MS by the input concentration of CA4 before LOND production in the oil/lipid PBS mixture x 100.

2.3 *In vitro* evaluation of CA4 TA or CA4 TPP LONDs

2.3.1 Cell cultivation in 6-well plates

SVR cells were cultured on glass coverslips (sterilised in 70% (v/v) ethanol) in 6-well plates at 5 x 10^5 cells/well. These were allowed to grow for 24 h at 37°C with 5% CO_2 prior to treatments. Cells were treated with 10 μM CA4 TA LONDs, equivalent volume of TA alone, equivalent volume of TA LONDs and 10 μM free CA4 in DMSO, for 2 h at 37°C or 0.5 μM CA4 TA LONDs and 0.5 μM free CA4 in DMSO for 24 h at 37°C. 2 mL of the appropriate treatment prepared in media (DMEM) were added to each well. Untreated cells were used as controls.

2.3.2 Cell cultivation in μ-Slides VI $^{0.4}$

Cells (SVR, SW480 or EA.hy926) were cultured in μ-Slides VI $^{0.4}$ (Ibidi, Germany). Briefly, 30 μL of cell suspension containing 3 x 10^5 cells/mL was plated in each of the six channels in the μ-Slides VI $^{0.4}$. The slides were then incubated for 1 h, at 37°C to allow cell adhesion. After 1 h, 60 μL of cell free medium was added. The cells were incubated for 24 h, at 37°C with 5% CO_2 prior to treatments. Following this, the media was removed and the cells were treated with: CA4 TA LONDs or free CA4 in DMSO at 100, 60, 40, 20 and 10 nM for 2 h at 37°C (SVR); CA4 TPP LONDs, free CA4 in TPP or DMSO all at 10 μM, or TPP alone at an equivalent volume for 2 h at 37°C (SVR, EA.Hy926 and SW480); CA4 TPP LONDs at 10 μM or 0.1 μM (or 100 nM) and free CA4 TPP at 10 μM for 30 min at 37°C (SVR); CA4 TPP LONDs at 100, 60, 40, 20, 10, 4, 8 and 2 nM or free CA4 in TPP at 8 and 2 nM for 2 h at 37°C (SVR); CA4 TPP LONDs or free CA4 in TPP both at 55 nM and 100 nM for 2 h or 24 h at 37°C. 30 μL of appropriate treatment reagent was prepared in fresh media and added to the cells for the specified treatment time. For 24 h treatments, 100 μL of reagent was added to each channel to avoid drying.

2.3.3 β-tubulin immunofluorescence and post-acquisition image analysis

β-tubulin was visualised following a three-step indirect immunofluorescence (IF) method. Cells were washed x 3 with PBS and fixed with 4% (w/v) paraformaldehyde (PFA) in PBS for 10 min at room temperature. Cells cultured in μ-Slides VI $^{0.4}$ were permeabilised with 0.1% Triton X-100 (v/v) in dH_2O for 5 min at room temperature. Cells were then incubated with antibody diluent (Thermo Fisher Scientific, UK) to block non-specific binding for 5 min at room temperature. 1:500 primary antibody, mouse monoclonal anti-β-tubulin (T4026 – Sigma-Aldrich, UK) in antibody diluent

was applied for 2 h, at room temperature. The primary antibody was then followed by sequential incubations of 1:200 biotinylated rabbit anti-mouse (E0354, DAKO) then 1:250 fluorescein-isothiocyanate (FITC)-labelled avidin D (Vector Laboratories) both prepared in antibody diluent for 1 h at room temperature. Coverslips from 6-well plates were mounted onto glass slides with Prolong Gold with DAPI (P36935, Thermo Fisher Scientific, UK). Cells were mounted directly with Prolong Gold with DAPI in *μ*-Slides VI $^{0.4}$. Fluorescent images were acquired using a Zeiss Axio Imager Z1 microscope (Carl Zeiss Microscopy, USA) with AxioVision software.

2.3.3.1 Semi-quantitative analysis of MTs

Immunofluorescent images were used for scoring. Five different fields of view (FOV) from each treatment and/or control group were taken. The length of ten MTs was measured from five randomly selected cells in each of the five FOV (total of 250 MTs lengths measured), using *Image J*. Where not possible less MT lengths were measured. The data was plotted using GraphPad Prism 7 (GraphPad Software Inc., La Jolla, California, USA).

2.3.4 Cell cycle analysis by flow cytometry

SW480 and SVR cells were cultured in 12-well plates at 2.5 x 10^4 cells/mL (2 mL per well), for 48 h at 37°C. Cells were then treated with 55 or 100 nM CA4 in DMSO and CA4 TPP LONDs at equivalent concentrations for 24 h at 37°C. Vehicle controls were used, DMSO at < 0.01%, and TPP LONDs at equivalent LONDs/mL number approximately 4 x 10^{10}/mL. After treatment all cells were collected as well as the media including any non-adherent cells. Cells were pelleted and washed with PBS. Cells pellets were obtained by centrifugation at 400 x *g* for 5 min. The supernatant was discarded and cells were fixed by drop-wise addition of 500 *μ*L of ice-cold 70% (v/v) ethanol in dH_2O. Samples were stored at -20°C until required. Fixed cells were transferred into round bottom polypropylene tubes (Thermo Fisher Scientific, UK), and pelleted by centrifugation at 200 x *g* for 3 min at 4°C. Cell pellets were extensively washed with 500 *μ*L buffer containing 0.1% (w/v) bovine serum albumin (BSA) (Sigma-Aldrich, UK), 0.1% (v/v) Tween-20 (Sigma-Aldrich, UK) in PBS. Following washing, cell pellets were obtained by centrifugation at 200 x *g* for 3 min at 4°C. 500 *μ*L of staining solution (200 *μ*g/mL Rnase A (Sigma-Aldrich, UK), 20 *μ*g/mL PI (Sigma-Aldrich, UK) in the same buffer as above) was used to re-suspend the cell pellets. These were incubated in the dark for 20 min and at least 10,000 cells were analysed using an Attune 2 Laser 6 Colour flow cytometer (Thermo Fisher Scientific). Data analysis was carried out using Modfit LT Win 32 software version 3 (Verity

Software). The set-up of the method was performed with the help of Dr Adam Davison (School of Medicine, University of Leeds).

2.4 ThMB production

ThMBs (Figure 1.8) were produced on-chip using a single step and a two-step process in a microspray regime. The single step method was used for the attachment of NeutrAvidin functionalised CA4 TA LONDs to MBs and the two-step method for the attachment of NeutrAvidin functionalised CA4 TPP LONDs. Both microchips used for the microfluidic production were fabricated by Epigem Ltd (Redcar, UK) in poly(methyl methacrylate) (PMMA) and SU-8. The number (N) of LONDs that can theoretically fit around a single MB is related to the surface area of the MB and the cross-section of a LOND and can be calculated by $N = 4\frac{radius\ of\ MB^2}{radius\ of\ LOND^2}$.

2.4.1 Lipid preparation

84 μL of 1,2-dipalmitoyl-sn-glycero-3-phosphocholine (DPPC) (20 mg/mL 1:1 chloroform/methanol) (Avanti Lipids (Alabaster, Al, USA) was mixed with 14 μL of DSPE-BPEG$_{2000}$ (25 mg/mL 1:1 chloroform/methanol) to a final concentration of 2 mg/mL for the single step and 1 mg/mL (42 μL of DPPC and 7 μL of DSPE-BPEG$_{2000}$) for the two-step on-chip production method. The lipids were evaporated under nitrogen for 1 h. A film of lipids was formed around the walls of the glass vial, these were stored at -20°C prior to use.

2.4.1.1 Single step on chip-production method

The lipids produced at 2 mg/mL were re-suspended in 1 mL of bubble buffer (4 mg/mL NaCl (VWR International, UK) and 1% (v/v) glycerol (Sigma-Aldrich, UK) in dH_2O), then vortexed for 1 min and placed in an unheated ultrasonic bath (VWR™ Ultrasonic Cleaner) for 1 h to facilitate re-suspension with additional vortexing every 15 min. Following this, the lipid solution was allowed to cool for 5 min at 4°C. 100 μL of CA4 TA LONDs were surface functionalised by incubating with 3 μM of NeutrAvidin (Thermo Fisher Scientific, UK) for 15 min. The lipid solution was then mixed with the functionalised CA4 TA LONDs and incubated for a further 15 min. 10 μL/mL of tetradecafluorohexane (C_6F_{14}) (Sigma-Aldrich, UK) was then added to the lipid/CA4 TA LOND solution to increase MB lifetime as described previously (Peyman *et al.*, 2012; Abou-Saleh *et al.*, 2016). Lipid/CA4 TA LOND solution was transferred to a 1 mL glass syringe (SGE gas tight luer lock, Supelco, Sigma-Aldrich, UK). An in-line filter (Santorius, Minisart SPR 4 mm x 45 μm slip, FIL6648) was then attached onto

the syringe to filter out any agglomerated lipids. The microchip had an inlet channel for gas (perfluorobutane, C_4F_{10}) and a liquid inlet. Both these inlets were evenly split on the chip to allow 4 simultaneous MB generation areas all feeding into one outlet. The multiplex microchip was mounted in a custom-built holder on a moveable stage of an inverted microscope (Eclipse Ti-U, Nikon, Japan). A manifold containing polytetrafluoroethylene (PTFE) tubes (Supelco Analytical USA) for the liquid and gas was tightly placed on the microchip using a lever clamping arm. Fluid from the lipids/CA4 TA LOND solution was delivered via the syringe at a rate of 60 μL/min and the gas flow was set on a digital gas flow controller (Alicat Scientific, USA) to 20 psi.

2.4.1.2 Two-step on-chip production method

The microchip design for the two-step production method incorporated a flow-focusing region for MB production using a microspray regime and a serpentine channel to allow time for slow mixing of MBs with NeutrAvidin functionalised CA4 TPP LONDs. The serpentine channel allowed extra time (approximately 1.14 s) for the NeutrAvidin functionalised CA4 TPP LONDs to bind onto the surface of the MB by increasing their contact time before collection (Figure 2.2 A). The microchip was mounted in a custom built holder with a manifold placed on top with PTFE tubes and sealed tightly. The fluid from the NeutrAvidin functionalised LONDs and lipids was delivered to the microchip via two syringe pumps (World Precision Instruments, USA) and the gas was controlled by a digital gas flow controller (Alicat Scientific, USA). The lipid syringe pump and gas controller were controlled via a PC while the NeutrAvidin functionalised CA4 TPP LONDs syringe pump was controlled manually. A schematic of the experimental set up is shown in Figure 2.2 B.

The lipid film (1 mg/mL) (section 2.4.1) was re-suspended in 1 mL of PBS, vortexed and placed in an unheated ultrasonic bath for 2 h with occasional vortexing every 15 min. CA4 TPP LONDs were diluted to a final concentration of 1 x 10^{11}/mL and LONDs incubated with 3 μM of NeutrAvidin with occasional gentle shaking for approximately 15 min, prior to MB production. 10 μL/mL of C_6F_{14} was added to the lipid solution to increase MB lifetime. The lipid solution was then allowed to cool for 5 min at 4°C. Following this, it was transferred to a 1 mL glass syringe and an in-line filter was then attached onto the syringe to remove any agglomerated lipids. The lipid solution was introduced into the microchip through the lipid inlet. The lipid flow rate was 20 μL/min and the C_4F_{10} gas was flowed through the central inlet at 15 psi. The NeutrAvidin functionalised CA4 TPP LONDs were introduced further downstream after MB production at a concentration of 10^{11} LONDs/mL at 20 μL/min flow rate.

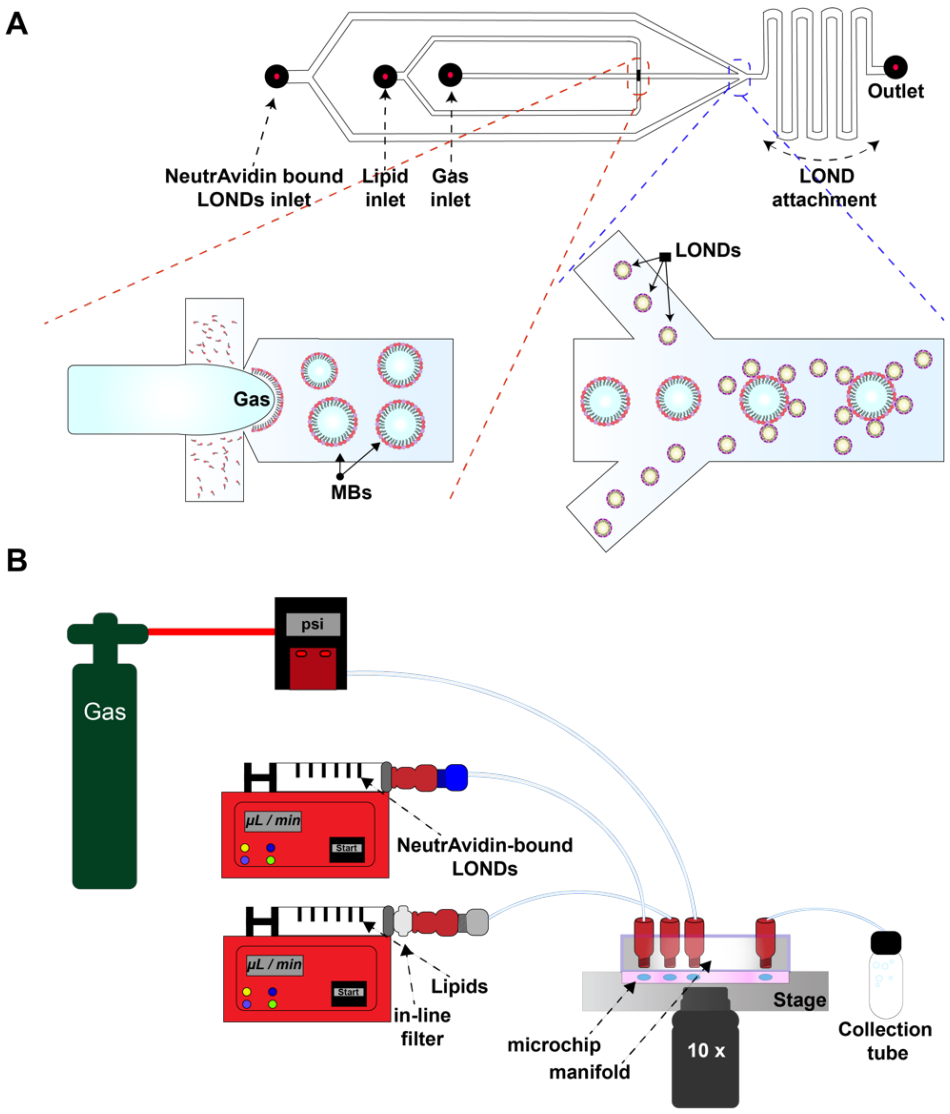

Figure 2.2 Two-step on-chip production of MB-LOND constructs.

(A) Schematic of the microchip design. Liquid was pumped through opposite inlets (lipid inlet) while the gas (C_4F_{10}) was flown through the centre (gas inlet). Post MB production through a flow-focusing microspray regime, NeutrAvidin functionalised CA4 TPP LONDs were introduced. (B) Schematic of the experimental set up for two-step on chip production of thMBs. The microchip was mounted in a custom-built holder on a moveable stage of an inverted microscope. The PMMA manifold was custom-built and contained PTFE tubes. The PTFE tubes were connected onto the inlets for introducing the gas, lipid and LONDs solutions and onto an outlet for sample collection. The manifold was placed onto the microchip and sealed tightly using a lever clamping arm. Two syringe drives were used to control the syringe containing the lipid solution used for MB production and one to control the syringe containing the NeutrAvidin functionalised CA4 TPP LONDs. An in line filter was placed onto the syringe with the lipid solution to filter out any lipid agglomerates.

2.4.2 LOND MB characterisation and VEGFR2 antibody targeting

The size and concentration of thMB constructs were measured by taking bright field images using a Nikon Eclipse microscope (Eclipse Ti-U, Nikon, Japan) built into the production platform. Briefly polyethylene spacers were placed on a glass microscope slide, a coverslip was placed on the spacers creating a chamber. The thMB sample was gently mixed and 10 μL was taken from the middle of the sample. This was diluted 1:10 in PBS or bubble buffer (section 2.4.1.1). 30 μL from this diluted sample was pipetted into the counting chamber. This was placed onto the stage and a set of 10 images were taken, using a 40 x objective with 1.5 x internal lens. The images were analysed using a macro written by Dr Sally Peyman (School of Physics and Astronomy, University of Leeds) specifically for MB sizing and counting in *Image J*.

The thMB count was used to determine the amount of biotinylated VEGFR2 antibody (13-5821, eBiosciences, UK) to be added to the sample. 0.1 μg of VEGFR2 antibody was added per 10^7 MBs. This was incubated for a further 20 min with gentle mixing. The optimal amount of VEGFR2 antibody used for specific binding *in vitro* and *in vivo* was determined empirically by Dr Nicola Ingram (School of Medicine, University of Leeds) by testing different concentrations of VEGFR2 antibody on the surface of MBs and assessing binding to VEGFR2 expressing SVR cells.

2.4.3 *In vitro* evaluation of CA4 thMBs

SVR cells were cultured in μ-Slides VI $^{0.4}$ (section 2.3.2), 24 h prior to treatment. CA4 thMBs were produced and characterised as described. Following production and characterisation of thMBs with CA4 TPP LONDs, these MBs were incubated with VEGFR2 expressing SVR cells. The μ-Slides VI $^{0.4}$ were inverted to allow binding of the CA4 thMBs to the SVR cells for 4 min. The lid on the μ-Slides VI $^{0.4}$ was removed and replaced by polypropylene luer adapters (10822, Luer Plug, Ibidi, Germany). After 4 minutes binding time, an US trigger (+T) was applied (section 2.5.5). The cells then remained in contact with thMBs-CA4 TPP LONDs for 2 h at 37°C before fixation.

2.5 Mouse models

Local approval was obtained and all experiments were undertaken in accordance with the UK Animals (Scientific Procedures) Act 1986. BALB/c and CD-1® nude mice were bred in-house under licence from Charles River Laboratories (Wilmington, MA, USA) and maintained in specific-pathogen free conditions in individual ventilated

cages (IVCs) with access to water and food *ad libitum*. During longitudinal studies mouse weights were monitored to ensure health status was maintained.

2.5.1 Materials

CA4P (Fosbretabulin disodium) and irinotecan (irinotecan hydrochloride) were purchased from Sigma (Sigma-Aldrich, UK). Peanut oil was purchased from a local supermarket. CA4 was dissolved in DMSO and then diluted in peanut oil, in this case the DMSO content was 10% (v/v) and the final concentration of CA4 was either 25 mg/mL or 0.72 mg/mL. CA4P was dissolved in PBS at 15 mg/mL and in saline with 0.9% NaCl (BD Biosciences, UK) at 0.00045 mg/mL. Irinotecan was dissolved in DMSO then diluted in PBS. The DMSO content was 1.5% (v/v) and the final concentration of irinotecan was 3 mg/mL.

2.5.2 SW480 human CRC xenografts

SW480 cells were cultured as described in section 2.1.1. The cells were trypsinised, washed with PBS, pelleted and re-suspended at 5 x 10^7 cells/mL in PBS. 100 μL (5 x 10^6) of cells were injected subcutaneously in the right hind flank of 5 – 6 week old BALB/c male mice or CD-1® nude male mice to form xenografts.

2.5.3 Tumour volume measurements by 3D High Frequency Ultrasound (HFUS)

Tumour xenografts were imaged using a VisualSonics Vevo 770 high-frequency ultrasound system (Fujifilm VisualSonics Inc, Ontario, Canada) equipped with a 40 MHz (RM-704) and 25 MHz (RM-710B) transducers as previously described (Abdelrahman *et al.*, 2012; Ingram *et al.*, 2013). Briefly, mice were anaesthetised using 5% (v/v) isoflurane in medical air at a flow rate of 2 L/min. Mice were then placed onto a heated pad (37°C), anaesthesia was maintained at 3%, heart rate and respiration were monitored throughout the procedure. Using the 3D B-mode, a 3D scan of the tumour was performed using the minimum step size possible for the length of the tumour. At the end of the procedure mice were allowed to recover in recovery chamber (37°C) and then placed back in their cages. Tumour volumes were calculated using an offline VisualSonics Vevo 770 version 3 software by delineating the tumour in the 3D mode single pane cube view (Figure 2.3 A) and subsequently reconstructing a 3D image of the tumour (Figure 2.3 B).

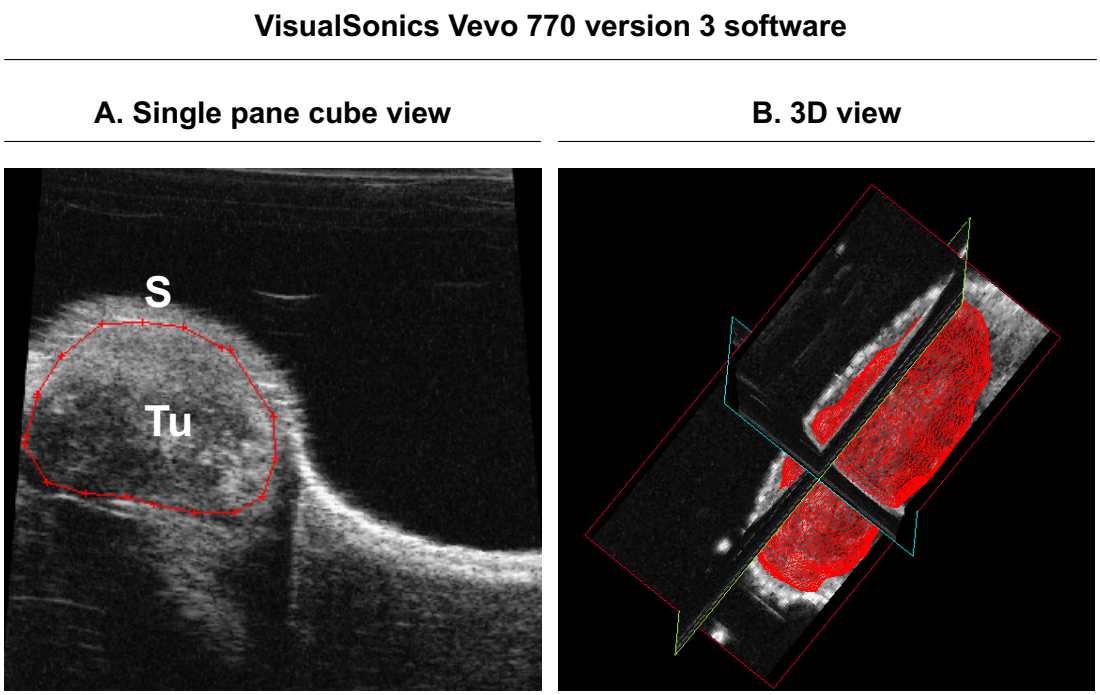

Figure 2.3 Tumour volume measurements by High frequency Ultrasound. Tumour volumes were measured by HFUS using a VisualSonics Vevo 770. The data was then analysed using VisualSonics Vevo 770 version 3 software. (A) Using the single pane cube view the tumour (Tu) outline was delineated at each point where the shape/outline changed. S: Skin. (B) 3D reconstruction of the tumour.

2.5.4 Tumour volume measurement with mechanical callipers

Tumours volumes were also measured with mechanical callipers twice per week once the tumour became palpable (approximately days 7-10). Tumour volume was calculated as follows:

$$\textit{Tumour volume} = (Length\ x\ width)^{\frac{3}{2}} \times \frac{\pi}{6}$$

2.5.5 US parameters

An US trigger (+T) was delivered to tumours using a specifically designed Ultrasound Array Research Platform (UARP) constructed by Dr James McLaughlan, School of Electrical and Electronic Engineering, University of Leeds. An unfocused ultrasound transducer with a centre frequency of 2.2 MHz (V323, Olympus NDT, UK) was placed on the *μ*-Slides channels or directly to xenografts, US contact gel was used as a coupling agent (15 mm distance between the transducer and the slide or xenograft). A 10 *μ*s tone burst was generated with a peak negative pressure of 260 kPa and 1 kHz pulse repetition frequency (PRF). The duration of the US was 5 s. 1% duty cycle and 29.4 mW/cm^2 intensity. The TI in soft tissue was 0.09 and the MI was 0.21.

2.5.6 Hoechst Perfusion Staining

bisBenzimide H 33342 trihydrochloride (Hoechst 33342) (Sigma-Aldrich, UK) was dissolved in sterile dH_2O at 4.5 mg/mL and administered at 15 mg/kg i.v. (100 *μ*L injection volume). One minute post-injection, mice were sacrificed by cervical dislocation and tumour, liver and heart tissues were harvested. The tissues were placed in peel-a-way embedding moulds containing optimal cutting temperature (OCT) compound (VWR International, UK), followed by slow freezing over dry ice. These were subsequently wrapped in foil, placed in liquid nitrogen and stored at –80°C until required.

2.5.7 Blood sample collections

Murine blood samples were obtained immediately after death by cardiac puncture in ethylenediamine tetraacetic acid (EDTA) containing tubes (BD Biosciences, UK). Plasma was separated by centrifugation at 1,000 x g for 10 min at 4°C. After centrifugation, plasma was transferred into a 1.5 mL Eppendorf tube and stored at -80°C.

2.5.8 Tissue processing and immunohistochemistry

Following harvesting at the end of each *in vivo* protocol tissues were cut in half and either fixed in 4% (w/v) PFA overnight at room temperature for IHC or snap-frozen in liquid nitrogen and stored at -80°C for LC-MS/MS analysis. Following PFA fixation, tissues were washed in PBS and dehydrated in 70% (v/v) ethanol. PFA fixed tissues were subsequently processed using a tissue processor and embedded in paraffin by the Leeds Institute of Cancer and Pathology (LICAP) service at the University of Leeds. Tissue paraffin blocks were placed at 4°C overnight prior to sectioning. Following this, blocks were placed on wet ice for 1-2 h. 4-5 μm central serial sections were cut using a Leica Biocute 2030 microtome (Leica Biosystems) and mounted on glass slides poly-L-lysine coated. Tissue sections were dewaxed and rehydrated with 100% (v/v) xylene, 100% (v/v) ethanol and water successively 4 x 3 min each.

2.5.8.1 Haematoxylin and Eosin

One section from each tissue sample was counterstained with haematoxylin and eosin (H & E). These were placed in haematoxylin for 2 min, followed by running water for 2 min and Scott's tap water (20 g sodium bicarbonate and 3.5 g magnesium sulphate in 1 L of distilled H_2O) for 2 min. Subsequently, sections were placed in eosin for 2 min followed by water for 1 min. Slides were then dehydrated in 100% (v/v) ethanol and xylene, 4 x 3 min each. The slides were then coverslipped using dibutylphthalate polystyrene xylene (DPX) mounting media (Sigma-Aldrich, UK) and left to dry overnight at room temperature.

2.5.8.2 Immunohistochemistry

IHC was performed for detection of CD31-positive blood vessels. Following, dewaxing and rehydration as described above, antigen retrieval was performed by heating the slides in 10 mM citrate buffer, pH 6.0 in a microwave (900 W) for 10 min. The slides were allowed to cool for 20 min at room temperature and then rinsed in water. Endogenous peroxidase activity was blocked by incubating with 0.3% (v/v) hydrogen peroxide (VWR International, UK), in MeOH for 10 min. The sections were rinsed in water and transferred to Tris Buffered Saline (TBS; 1 M Tris HCL, 6% NaCl, pH 7.4). Endogenous biotin and avidin were blocked using an Avidin/biotin blocking kit (Vectorlabs, Burlingame, USA). Slides were incubated with a drop of avidin for 15 min followed by 15 min in biotin block with a TBS wash in between. Non-specific antigen binding was blocked using antibody diluent (Thermo Fisher Scientific, UK) for 5 min. Sections were incubated with monoclonal rat anti-mouse CD31 antibody (DIA 310, clone SZ31, Dianova, GmbH, Germany) 1:20 (v/v) in antibody diluent for 1

h at room temperature. After washing, for 2 x 5 min in TBS + 0.1% (v/v) Tween-20 (TBST) and 1 x 5 min in TBS, the sections were incubated with a biotinylated rabbit anti-rat secondary antibody (E0468, DAKO, UK) at 1:200 (v/v) in antibody diluent for 30 min. Following washes in TBST and TBS as above, avidin/biotin/horseradish peroxidase complex (ABC/HRP) (Vectastain Elite ABC HRP Kit, Vectorlabs, Burlingame, USA) was prepared according to the manufacturer's instructions and applied for 30 min. The sections were washed in TBST and TBST and blood vessels were visualised by staining with 3,3'-Diaminobenzidine (DAB) + Substrate buffer (Imidazole-HCl buffer, pH 7.5 with hydrogen peroxide and anti-microbial agent) (DAKO, UK) for 10 min at room temperature. The sections were subsequently counterstained with haematoxylin, dehydrated and mounted using DPX as described above (section 2.5.8.1).

2.5.9 Immunohistochemistry analysis

Immunostained images of tissue sections were acquired using a Nikon Eclipse E1000 microscope (Nikon Instruments Inc.). The quantitation of CD31 positive blood vessels is given as microvessel density (MVD) and was measured by initially identifying areas with the highest CD31 positive microvessel density ("hot spots") within the entire tumour section. Then, individual CD31 positive vessels were counted from images of a sufficient area using *Image J* (0.79 mm^2 per field using x10 objective) as previously described (Zhang *et al.*, 2007). Four or five randomly selected "hot spots" were counted for each tumour. Some slides were digitally scanned at x 20 magnification using an Aperio digital slide scanner (AT2, Leica Biosystems) with Image Scope software (Leica Biosystems). Image Scope software was then used to manually annotate the area with haemorrhage (mm^2) per tissue section. Percentage haemorrhage was then determined by dividing the area of haemorrhage (mm^2) by the total area of the tumour section (mm^2) x 100. The same principles were applied to determine the percentage area of tumour with necrosis. The number of mitoses were also counted per mm^2.

2.5.10 Fluorescence immunohistochemistry

10 μm cryosections were cut from frozen tissue sections (section 2.5.6) at two different central levels using a Leica CM3050 S cryostat (Leica Microsystems, Ltd, UK), wrapped in foil and stored at – 80°C. After thawing, cryosections were fixed in 100% (v/v) ice-cold acetone for 10 min and then washed 3 x 5 min in PBS. After blocking in antibody diluent for 5 min, sections were incubated with a rat anti-mouse antibody against CD31 (Clone MEC 13.3 (550274) BD Biosciences, UK) at 1:100

(v/v) in antibody diluent for 1 h at room temperature. Following washing 3 x 5 min in PBS, the sections were incubated with a goat anti-rat IgG secondary antibody Alexa Fluor 568 (A-11077, Thermo Fisher Scientific, UK) at 1:300 (v/v) in antibody diluent for 30 min at room temperature. Sections were washed 3 x 5 min in PBS, mounted with ProLong™ Gold anti-fade mountant (Thermo Fisher Scientific, UK) and left over night at room temperature. Fluorescent images were acquired using a Zeiss Axio imager Z1 microscope as described in section 2.3.3.

2.5.10.1 Semi-quantitative analysis of perfusion

To quantitate perfusion tumour sections stained with Hoechst 33342 and CD31 from sections 2.5.6 and 2.5.10 were used. Different FOV in order to capture the whole tumour section were taken from the tumour core. A Hoechst 33342 intensity score was assigned to each FOV from a scale of 0 to 3, with 0 showing no staining or very weak staining of Hoechst 33342 and 3 showing highest Hoechst 33342 staining intensity. A score of 2 was moderate staining intensity and 1 was weak staining. For each data set a different set of representative fluorescent images were used as a guide for the scoring and are shown in the relevant chapters. A median score for each mouse was calculated from the different FOV and used for statistical analyses. In the case where two independent assessors quantified the FOV a median score for each mouse was calculated and the median score from the two assessors was used for statistical analyses.

2.6 Liquid chromatography tandem mass spectrometry

2.6.1 Standards preparation and calibration curves for CA4

The analytical reference standards of CA4 and colchicine used as internal standard (IS) were purchased from Sigma (Sigma-Aldrich, UK). DMSO and high-performance liquid chromatography (HPLC) grade methanol were purchased from Fisher Chemical (Thermo Fisher Scientific, UK). Filtered dH_2O was obtained from a Duo ultrapure and dH_2O water system (Triple red, UK). CA4 and colchicine stock solution were prepared in DMSO to a concentration of 10 mg/mL for CA4 and 5 *µ*g/mL for colchicine. All stock solutions were kept at -20°C. The IS working solution was prepared at 0.5 *µ*g/mL by diluting the stock solution in MeOH. A five-point calibration curve diluted 1:2 was prepared in MeOH 0-1 or 0-10 µ*g/*mL. Each calibration curve included a blank sample (no IS) and a zero blank sample (with IS).

2.6.2 Quantification of CA4 in analytical samples

For the quantification of CA4 loading in LONDs and thMBs-LOND preparation, LC-MS/MS was used. A five point calibration curve of CA4 was prepared in MeOH as described in 2.6.1. CA4 TA LONDs, CA4 TPP LONDs and thMBs were diluted accordingly within the range of the calibration curve in MeOH, vortexed and centrifuged at 10, 000 x g for 4 min at 4°C to remove lipids and oil. The supernatant was collected and transferred into a polypropylene fused insert vial with 9 mm screw thread (Chromatography Direct, Ltd, UK).

Tissues were weighed and placed in reinforced polypropylene tubes (2 mL reinforced tubes with Screw Caps & Silicone O-Rings, OMIN International Inc) containing 2.8 mm zirconium oxide beads (OMIN International Inc.). These were then transferred into a Bead Ruptor 24 Bead Homogenizer (OMIN International Inc.) for homogenisation in MeOH (1:4) (w/v) (instrument settings: speed: 5.6 m/s, number of cycles 2 x 45 sec, pause in between cycles 30 sec). Following homogenisation, the tubes were vortexed and centrifuged for 5 min at 10,000 x *g* at 4°C. The clear supernatant was then transferred to an Eppendorf tube and evaporated to dryness using a rotary evaporator (EZ2 plus rotary evaporator, Genevac Ltd, Suffolk, UK). The dried samples were reconstituted in MeOH with a volume depending on the initial sample volume. These were vortexed and transferred into a polypropylene fused insert vial with 9 mm screw thread (Chromatography direct, Ltd, UK).

Plasma was thawed at room temperature and mixed with MeOH (1:4). These were subsequently vortexed and centrifuged for 5 min at 10, 000 x g at 4°C. The clear supernatant was then transferred to an Eppendorf tube and dried using a rotary evaporator as described above. Following, these were reconstituted in MeOH and transferred in tubes as described above. All samples we analysed using the analytic method described below (section 2.6.4).

2.6.3 *In vitro* glucuronidation assay

CA4 glucuronidation was determined in mouse liver homogenates. CA4 (1 mg/mL) was incubated in a liver homogenate at 37°C, the reaction was activated by the addition of 10 μL uridine 5'-diphosphoglucuronic acid (UDPGA) for 1 h (final volume 120 μL). 20 μL from the reaction mixture was removed and added 1:4 in MeOH. Analytes were separated from the liver homogenate by centrifugation at 10, 000 x g at 4°C for 5 min. These were analysed by LC-MS/MS described below (section 2.6.4).

2.6.4 Instrument and analytic conditions

LC-MS/MS was conducted using a Waters Quattro Ultima triple quadruple mass spectrometer (Waters Corporation, Milford, MA, USA) with an electrospray ionisation (ESI) interface and in positive ionisation mode. Separation was obtained using an ACQUITY^{TM} UPLC BEH C18 column (1.7 μm, 2.1 x 100 mm) (Waters Corporation, Milford, MA, USA) that was maintained at 40°C. The autosampler was maintained at 8°C. The following instrument parameters were in place: ion source temperature 120°C; desolvation temperature 300°C; Capillary voltage 3 kV; Cone energy 20 V; Gas flow desolvation 650 L/h; Cone 71 L/h. The samples were eluted using a stepwise gradient in mobile phase A (90:10:0.1% (v/v) MeOH:dH_2O:formic acid) and mobile phase B (90:10:0.1% (v/v) dH_2O: MeOH:formic acid). The flow rate was 0.25 mL/min and 10 μL was injected for each analysis. The initial gradient of 70% A: 30% B was gradually increased over 18 min to 80% B and 20% A, then held for 2 min then returned to the initial gradient over 1 minute and held for 4 min, with a total run time of 25 min. A photodiode array detector which was connected with the LC-MS/MS system was used to detect samples between 190-400 nm. The mass spectra were initially scanned from m/z 50 to m/z 500. The analysis was performed in a multiple reaction monitoring (MRM) mode following optimisation to obtain the product ions with the highest signals. The full MRM settings are shown in Table 2.1. MassLynx software (Waters Corporation, Milford, MA, USA) was used to calculate the peak area (PA) under the curve and this was compared to a calibration curve to determine the concentration of CA4 in the samples.

2.6.5 LC-MS/MS method validation

The percentage extraction efficiencies were obtained by spiking tissue (tumour, liver, kidney, spleen, colon) and plasma with 1 μg/ml CA4 (A). The resulting peak areas were compared to those of 100% methanol spiked in the same way (B). The ratio of (A/B x 100) is defined as the % extraction efficiency. The limit of detection (LOD) and limit of quantification (LOQ) were determined by injecting decreasing concentrations of CA4 standard. Carry over between samples was assessed by injecting a blank sample following a 1 μg/ml CA4 standard and examination for any confounding mass peaks detected. A 5 mg/mL CA4 standard was subjected to three freeze thaw cycles at -80°C and rapidly thawing at 37°C. This was performed to ensure the stability of CA4 under these conditions. Evaporation of CA4 calibration curves compared to no evaporation was also assessed.

Table 2.1 LC-MS/MS MRM settings for colchicine, CA4 and CA4G.

Compound	Precursor/product ion (m/z)	Dwell (sec)	Cone voltage	Collision energy (volts)
Colchicine	400.6 > 295	0.20	15	30
Colchicine	400.6 > 310.1	0.20	15	30
Colchicine	400.6 > 267.22	0.20	15	30
Combretastatin A4	317.5 > 286.2	0.20	15	15
Combretastatin A4	317.5 > 271	0.20	15	15
Combretastatin A4-G	493 > 302.21	0.20	15	25
Combretastatin A4-G	493 > 317.31	0.20	15	25

2.6.6 LC-MS/MS for detection of Irinotecan, SN38 and SN38G

Concentrations of irinotecan, SN38 and SN38G in tissues was analysed using a method developed by Dr Laura McVeigh (School of Medicine, University of Leeds) and Ms Antonia Wierzbicki (Institute of Cancer Therapeutics, University of Leeds) with supervision by Prof. Paul Loadman (Institute of Cancer Therapeutics, University of Bradford). Irinotecan, SN38 (Sigma-Aldrich, UK) and SN38G (Santa Cruz Biotechnology, Inc.) stock solutions were prepared in DMSO to a concentration of 10 mg/mL, 1 mg/mL and 0.5 mg/mL respectively. All stock solutions were kept at -20°C. Seven point calibration curves for irinotecan, SN38 and SN38G diluted 1:2 were prepared in MeOH at 0-0.1 μg/mL, or 0-100 ng/mL or, 0-1 μg/mL respectively.

Tumours and tissues were weighed, homogenised, vortexed and centrifuged for the acquisition of a clear supernatant as described in section 2.6.2. The clear supernatant was diluted 1:20 in MeOH and transferred to polypropylene fused insert vials (Chromatography direct, Ltd, UK) and analysed by LC-MS/MS. LC-MS/MS was conducted using a Waters Quattro Ultima triple quadruple mass spectrometer (Waters Corporation, Milford, MA, USA) with an ESI interface and in positive ionisation mode using the same column (maintained at 40°C), mobile phases A and B, flow rate and injection volume as described in section 2.6.4. The following instrument parameters were in place: ion source temperature 120°C; desolvation temperature 250°C; Capillary voltage 3.5 kV; cone energy 12 V; Gas flow desolvation 650 L/h, Cone 60 L/h (information provided by Dr Laura McVeigh, School of Medicine, University of Leeds). Briefly, the samples were eluted using a stepwise gradient

method, the initial gradient of 80% A: 20% B was gradually increased over 15 min to 80% B and 20% A, then increased over 1 min to 100% B and held for 4 min then returned to the initial gradient over 1 minute and held for a further 14 min, with a total run time of 35 min (information provided by Dr Laura McVeigh, School of Medicine, University of Leeds). The MRM settings for irinotecan, SN38 and SN38G are shown in Table 2.2. MassLynx software (Waters) was used to calculate PA under the curve and this was compared to the calibration curves to determine the concentration of irinotecan, SN38 and SN38G in the samples.

2.7 Statistical analysis

All statistical analyses were performed using GraphPad Prism version 7 software (GraphPad Software Inc., La Jolla, California, USA). The statistical test used for each experiment are described in the text and figure legends.

Table 2.2 LC-MS/MS MRM settings for irinotecan, SN38 and SN38G.

Compound	Precursor/product ion (m/z)	Dwell (sec)	Cone voltage	Collision energy (volts)
Irinotecan	587.3 > 124.0	0.15	25	45
Irinotecan	587.3 > 167.0	0.15	25	45
SN38	393.2 > 264.2	0.15	35	30
SN38	393.2 > 293.0	0.15	35	30
SN38	393.2 > 349.1	0.15	35	30
SN38G	569.8 > 393.8	0.20	35	30
SN38G	569.8 > 349.9	0.20	35	30

Information used to compile this table was provided by Dr Laura McVeigh (School of Medicine, University of Leeds).

Chapter 3

Triacetin LONDs: Characterisation and *in vitro* and *in vivo* evaluation

3.1 Introduction

The pharmaceutical industry produces a substantial number of compounds which have a poor solubility in aqueous solutions (Kalepu & Nekkanti, 2015). Earlier, the main aim within the pharmaceutical industry was to produce compounds with high potency and selectivity towards their target, although, many compounds produced showed excellent *in vitro* activity when dissolved in solvents such as DMSO, this was not the case when tested in pre-clinical studies (Hodgson, 2001). Typical problems associated with poorly soluble compounds are low bioavailability, low permeability, rapid metabolism and elimination from the body and poor safety and tolerability (Muller, Jacobs & Kayser, 2001; Kalepu & Nekkanti, 2015).

A number of methods can be used such as pH modifications and the formation of salt forms of poorly soluble compounds in order to increase solubility. However, due to their high potency some compounds produced a number of toxic side effects upon systemic administration. Another way of improving solubility is by using co-solvents, however, these can also result in severe toxicity for example Cremophor®EL used to solubilise paclitaxel, is associated with nephrotoxicity, hypotension and anaphylactic reactions (Ganta *et al.*, 2014).

LONDs are proposed as a new hydrophobic DDS to overcome solubility and toxicity issues with such compounds. The first work with LONDs in this project used the VDA CA4 for a proof-of-concept study. Following production, a number of LOND preparations (prep.) were produced and characterised to assess reproducibility of the production method and the LOND structure in terms of drug encapsulation and size. Reproducibility is an important aspect of any proposed NP formulations aimed at large-scale synthesis for drug delivery (Tran *et al.*, 2017).

The aims of this study were therefore to establish qualitative and quantitative assays to assess drug release and/or uptake and/or cellular uptake of LONDs *in vitro*. Following this, the aim was to produce and test a multi-structure MB construct or thMB for drug delivery using CA4 TA LONDs *in vivo*.

3.2 CA4 TA LONDs: Physical and chemical characterisation

Prior to LOND production with CA4, initial solubility studies were performed by adding 25 mg of CA4 into 1 mL of each candidate oil which included squalane, olive oil and TA and then visually inspecting for presence of drug precipitation (or crystal formation) (information provided by Dr Sally Peyman and Dr Victoria Mico, School of

Physics and Astronomy, University of Leeds). Precipitation was an indication of poor solubility. CA4 had dispersed into TA and was insoluble in olive oil and squalane.

TA is a SCT, it has been recognised by the FDA as safe, nontoxic and it is commonly used as a carrier for food flavouring and cosmetic products (Fiume, 2003). TA has a *logP* value of 0.1 and it is soluble in water at 70 g/L (Fiume, 2003; Park *et al.*, 2015). TA has been previously used as the oil phase in nanoemulsions (Park *et al.*, 2014; Sobhani *et al.*, 2015). The chemical structure, physical and chemical properties of TA are shown in Figure 3.1.

TA LONDs with and without CA4 were produced, characterised and provided by Dr Sally Peyman and Dr Victoria Mico (School of Physics and Astronomy, University of Leeds). A total of six different prep. of TA LONDs were produced to evaluate reproducibility, *in vitro and in vivo* activity in terms of CA4 release and/or uptake for those preparations with encapsulating CA4. Briefly, 95:5mol% POPC and DSPE-$BPEG_{2000}$ were used to form the lipid monolayer shell of the CA4 TA LONDs, following solubilisation of CA4 in TA (stock concentration of CA4 1750 *μ*g), CA4 TA LONDs were produced by high pressure homogenisation (section 2.2 for details).

TA LONDs with and without CA4 had a mean size of 260 ± 124 nm (n=6 prep.) measured by DLS with a mean concentration of $2.4 \times 10^9 \pm 1.6 \times 10^9$ TA LONDs/mL (n=6 prep.) measured by qNano. Purification of TA LONDs was performed by cross-filtration or dialysis for the removal of excess lipid and/or unencapsulated CA4. The concentration of CA4 in the TA LOND solution was then measured by UV-VIS spectroscopy and the %EE for CA4 in TA LONDs was 55 ± 33% (n=5 prep.). The physical and chemical properties of TA LONDs with/out CA4 used in this study are shown in Table 3.1.

LONDs containing TA alone were produced as a drug-free control (prep. number 3 in Table 3.1). Prep. numbers 1, 3 and 4 were evaluated *in vitro*. To increase the final concentration of CA4 in the TA LOND prep. for *in vivo* use, an initial stock concentration of CA4 of 3500 *μ*g/mL was used (prep. number 6 in Table 3.1). This increase in initial CA4 stock concentration resulted in a 96.7% EE, however the mean size of the LONDs in prep. number 6 increased to 394 nm while the concentration decreased to 0.8×10^9 LONDs/mL.

A

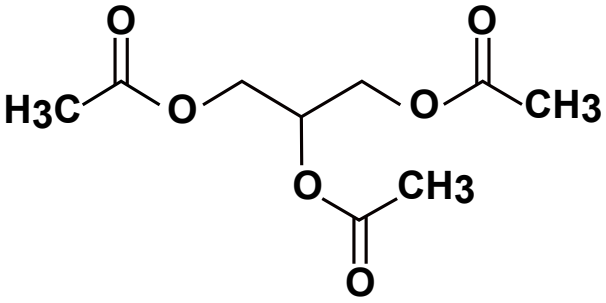

B

Chemical and physical properties of Triacetin	
Physical characterisation	Oily liquid
Molecular formula	$C_9H_{14}O_6$
LogP	0.1
Solubility in water	70 g/L

Figure 3.1 Chemical and physical properties of triacetin.

(A) Chemical structure of Triacetin. Adapted from MP Biomedicals (MP Biomedicals, 2018). (B) Chemical and physical properties of triacetin.

Table 3.1 TA LOND Characterisation: Physical and chemical properties.

Prep. number	Lipids	Solvent	CA4 Stock used (μg/ml)	Concentration of LONDs (x10^9/ml)	Mean size (nm) (DLS)	CA4 (μg/mL) (UV-Vis)	%EE	Purification technique	Evaluation (*in vitro/ in vivo*)
1	95*mol*% POPC and 5*mol*% DSPE-BPEG$_{2000}$	Triacetin	1750	N/D	N/D	825	47	Cross-filtration	*In vitro*
2			1750	N/D	N/D	1200	69	Cross-filtration	-
3			N/A	N/D	N/D	N/A	N/A	N/D	*In vitro*
4			1750	4	151	108	6	Cross-filtration	*In vitro*
5			1750	2.5	234	949	54	Dialysis	-
6			3500	0.8	394	3348	97	Dialysis	*In vivo*
Mean				2.4 x10^9	260	1286	55		
SD				1.6 x10^9	124	1222	33		

Six different preparations of TA LONDs were produced to assess reproducibility and *in vitro* and *in vivo* activity. 95mol% POPC and 5mol% DSPE-BPEG$_{2000}$ were used to produce the TA LONDs lipid monolayer shell. CA4 was dispersed in TA the oil core. CA4 stock concentration in *μ*g/mL refers to the concentration of CA4 in the oil/lipid/PBS mixture before LOND production. The concentration of LONDs/mL was measured by qNano while their size was measured by DLS in nm. CA4 concentration in the TA LONDs solution was measured by UV-VIS spectroscopy. %EE was calculated by dividing the CA4 measured by UV-VIS spectroscopy by the stock of CA4 prior to LOND production x 100. Cross-filtration and dialysis were used for purification (removal or excess lipid and/or CA4). Prep. numbers 1 and 4 were evaluated *in vitro*, 2, 3 and 5 were produced for LOND production reproducibility studies. Double the concentration of CA4 was used in prep. 6 to increase the total concentration of CA4 in the LONDs these were evaluated *in vivo*. N/D: No data; N/A: Not applicable; - not evaluate *in vitro* or *in vivo*. All data used to compile this table were provided by Dr Sally Peyman and Dr Victoria Mico (School of Physics and Astronomy, University of Leeds).

3.3 CA4 TA LONDs disrupt the MT cytoskeleton in endothelial cells

CA4 is known to cause MT disruption by inhibiting tubulin polymerisation within 30 min of exposure of human umbilical vein endothelial cells (HUVECs) to CA4P (Galbraith *et al.*, 2001; Kanthou & Tozer, 2002). Due to its effects on MT polymerisation *in vitro,* evaluation of CA4 TA LONDs was initiated by assessing the ability of CA4 TA LONDs to cause MT disruption in endothelial cells. VEGFR2 expressing angiosarcoma SVR murine endothelial cells (Willmann *et al.*, 2008) were used for *in vitro* evaluation. Although, the MT disruption occurs very rapidly after CA4P exposure, here, as CA4 TA LONDs are a novel hydrophobic DDS a 2 h treatment was used to account for any potential slow release and/or uptake of CA4 TA LONDs in SVR cells.

IF staining of *β*-tubulin in untreated SVR cells, showed filamentous MTs spreading throughout the cytoplasm presumably originating from the centrosomes (Figure 3.2 A). In contrast, 10 *μ*M CA4 TA LONDs showed disruption of MT within 2 h as tubulin inhibition by CA4 TA LONDs caused the MTs to depolymerise and tubulin to disperse throughout the cytoplasm which is subsequently uniformly stained (Figure 3.2 B). The same uniformed stained pattern has been reported for HUVECs treated with 10 *μ*M of CA4P (Galbraith *et al.*, 2001). The same effects were seen in SVR cells treated with 10 *μ*M CA4 dissolved in DMSO (Figure 3.2 C). TA LONDs and TA alone were used as controls to eliminate any potential MT cytoskeletal changes caused by the LOND structure itself and or the TA oil. No disruption of the MTs was observed when treating with TA LONDs or TA alone as the MTs appeared similar to untreated MTs (Figure 3.2 D and E).

MT disruption with CA4 TA LONDs was quantitated by measuring MT lengths where possible using *Image J* (Figure 3.3). A total of 50 cellular MT were measured in the untreated, TA LONDs and TA alone groups. As the effects of CA4 TA LONDs and CA4 in DMSO resulted in MT disruption (apparent from the uniformly stained cytoplasm with dispersed tubulin from depolymerised MTs) no MTs were measured in these groups, therefore, 0 *μ*m was used to produce the graph and for statistical analysis. As no MT were present in the groups treated with 10 *μ*M CA4 TA LONDs and 10 *μ*M CA4 in DMSO this resulted in a statistically significant difference when compared to untreated SVR cells and SVR cells treated with TA LONDs and TA alone ($p<0.0001$, Mann-Whitney U test, two-tailed). No significant differences were observed between untreated control SVR cells and TA LONDs or TA alone.

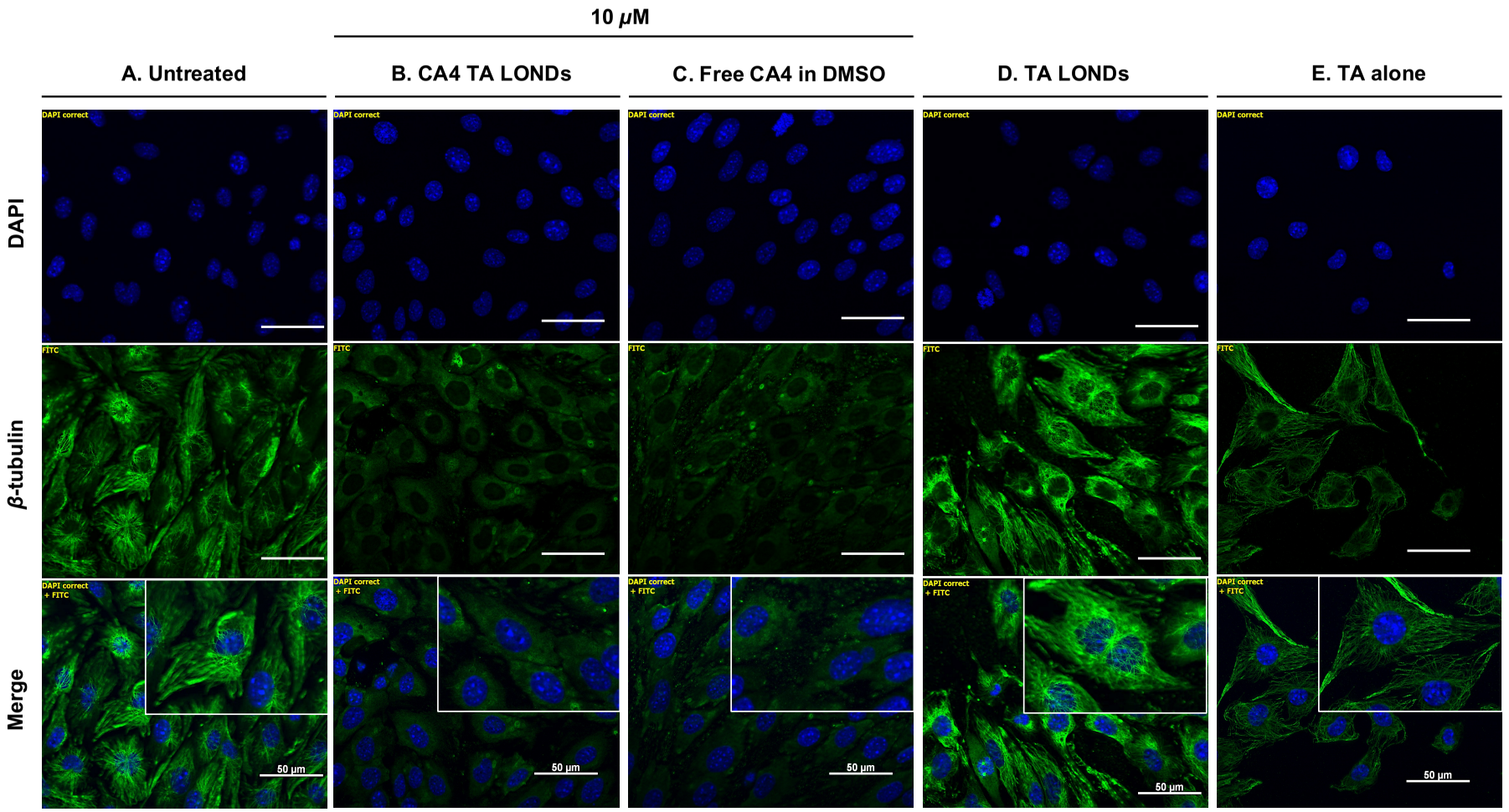
10 μM
A. Untreated
B. CA4 TA LONDs
C. Free CA4 in DMSO
D. TA LONDs
E. TA alone
DAPI
β-tubulin
Merge
DAPI correct
FITC
DAPI correct + FITC
50 μm

Figure 3.2 CA4 TA LONDs cause MT disruption.

To assess the efficacy of CA4 TA LONDs at causing MT disruption from the CA4 payload, SVR murine endothelial cells were cultured in 6 well-plates and treated with 10 μM of CA4 TA LONDs, 10 μM CA4 in DMSO was used as a positive control and untreated SVR cells were used as a free-drug control. TA LONDs and TA alone were also used as controls for the LOND structure and the TA oil. Following, a 2 h treatment at 37°C, cells were fixed, immunostained for β-tubulin using a mouse monoclonal anti-β-tubulin antibody and visualised using a biotinylated rabbit anti-mouse and FITC-labelled avidin. The slides were mounted with prolong Gold containing DAPI. (A) Untreated cells with filamentous MT structures. (B) 10 μM of CA4 TA LONDs resulted in tubulin inhibition by the CA4 payload. The tubulin from the depolymerised MTs had dispersed within the cytoplasm resulting in a uniform staining. (C) Free CA4 in DMSO at 10 μM also resulted in MT depolymerisation and the dispersion of tubulin into a uniform fluorescence inside the cytoplasm. (D) TA LONDs, did not show any disruption to the MTs. (E) TA alone did not result in MT disruption. Inset images show magnified cells in each panel. Scale bars indicate 50 μm. Prep. number 1 was used.

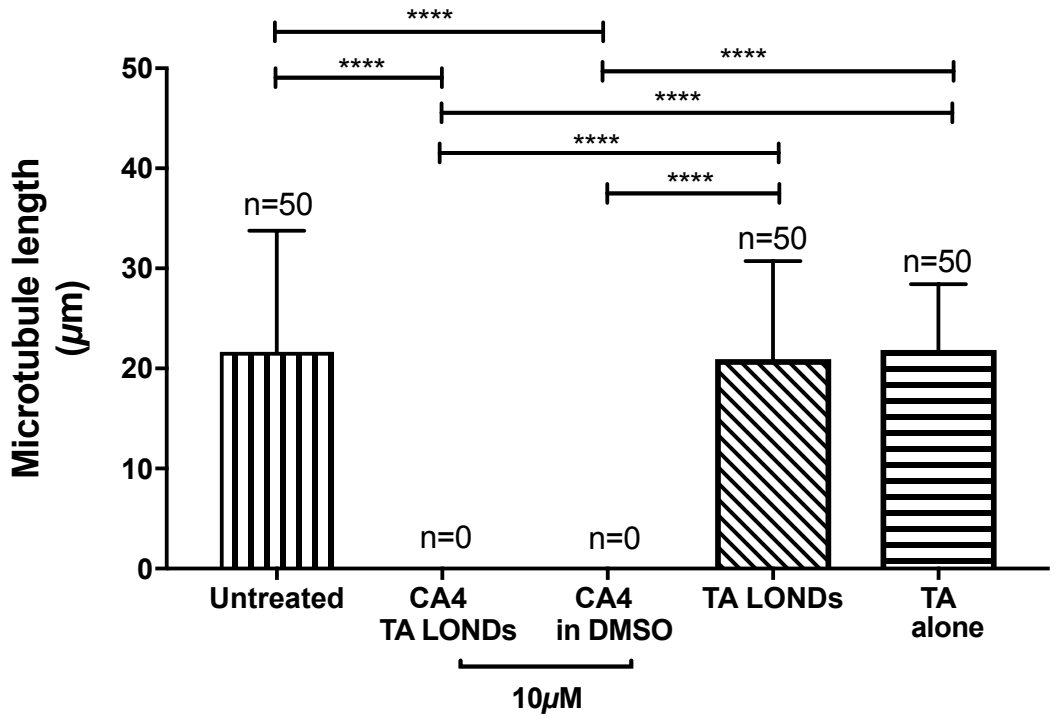

Figure 3.3 Quantitative analysis of MT lengths following treatment with CA4 TA LONDs.

Fluorescent images were used to quantitate MT disruption caused by treatment with CA4 TA LONDs. A total of 50 MT from five cells were measured using *Image J* from untreated SVR cells and treated with TA LONDs and TA alone. The treatment with CA4 TA LONDs and CA4 in DMSO resulted in MT disruption and the presence of depolymerised MTs in the cytoplasm. Therefore, no MTs were measured in these groups and 0 μm was used to plot the graph. Data represents the median value from the measured MTs (n=1 biological replicate) and the error bars represent the interquartile range. ****, $p<0.0001$ calculated by Mann-Whitney U test (two-tailed).

3.4 CA4 TA LONDs cause a concentration dependent MT disruption

To determine if CA4 TA LONDs had a concentration dependent effect on MT disruption, SVR cells were treated with escalating concentrations of CA4 TA LONDs. These experiments also investigated whether delivering CA4 in TA LONDs changed (enhanced or diminished) the ability of the CA4 payload to cause MT disruption. The effect of free CA4 in DMSO on MT disruption in HUVECs has been shown to be concentration dependent, with MT disruption observed at a concentration of 12.5 nM at a 30 min exposure time (Kim, Peshkin & Mitchison, 2012).

IF staining of *β*-tubulin after a 2 h exposure time showed untreated SVR cells with MT filaments. Treatment with 10 nM CA4 TA LONDs did not cause any apparent MT disruption as the MTs appeared similar to untreated cells (Figure 3.4 A and B). In contrast, a 20 nM concentration of CA4 TA LONDs showed the initiation of MT disruption (Figure 3.4 C). The image inset in Figure 3.4 C shows a magnified cell with shortening of the MT filaments at the distal ends at the cell periphery (white arrow). At 40 and 60 nM concentration of CA4 TA LONDs, MTs had lost their radial filamentous structure and were tangled around the nuclei presumably near centrosomes and indicative of MT disruption (shown in the magnified inset images in Figure 3.4 D and E). At 100 nM concentration the CA4 TA LONDs had caused complete MT depolymerisation and as a result tubulin had dispersed throughout the cytoplasm which was subsequently uniformly stained (Figure 3.4 F, magnified inset image).

MT disruption caused by CA4 TA LONDs at different concentrations was confirmed by measuring MT lengths using *Image J* (Figure 3.5 A and B). A total of 250 MTs were measured in control untreated SVR cells and those treated with 10, 20 and 40 nM of CA4 TA LONDs. A total of 232 MTs were measured in the 60 nM CA4 TA LONDs group. As a result of complete MT depolymerisation in SVR cells treated with 100 nM CA4 TA LONDs (Figure 3.4 F), no MT filaments were measurable and 0 *μ*m was used for graphical and statistical analyses. MT lengths in SVR cells treated with 20, 40, 60 and 100 nM of CA4 TA LONDs were significantly reduced or completely abrogated in the 100 nM group than those of untreated SVR cells ($p<0.0001$, Mann-Whitney U test, two-tailed) (Figure 3.5 A). Significant longer MT lengths were observed in the 10 nM CA4 TA LOND group compared to the untreated SVR cells ($p=0.03$ Mann-Whitney U test, two-tailed).

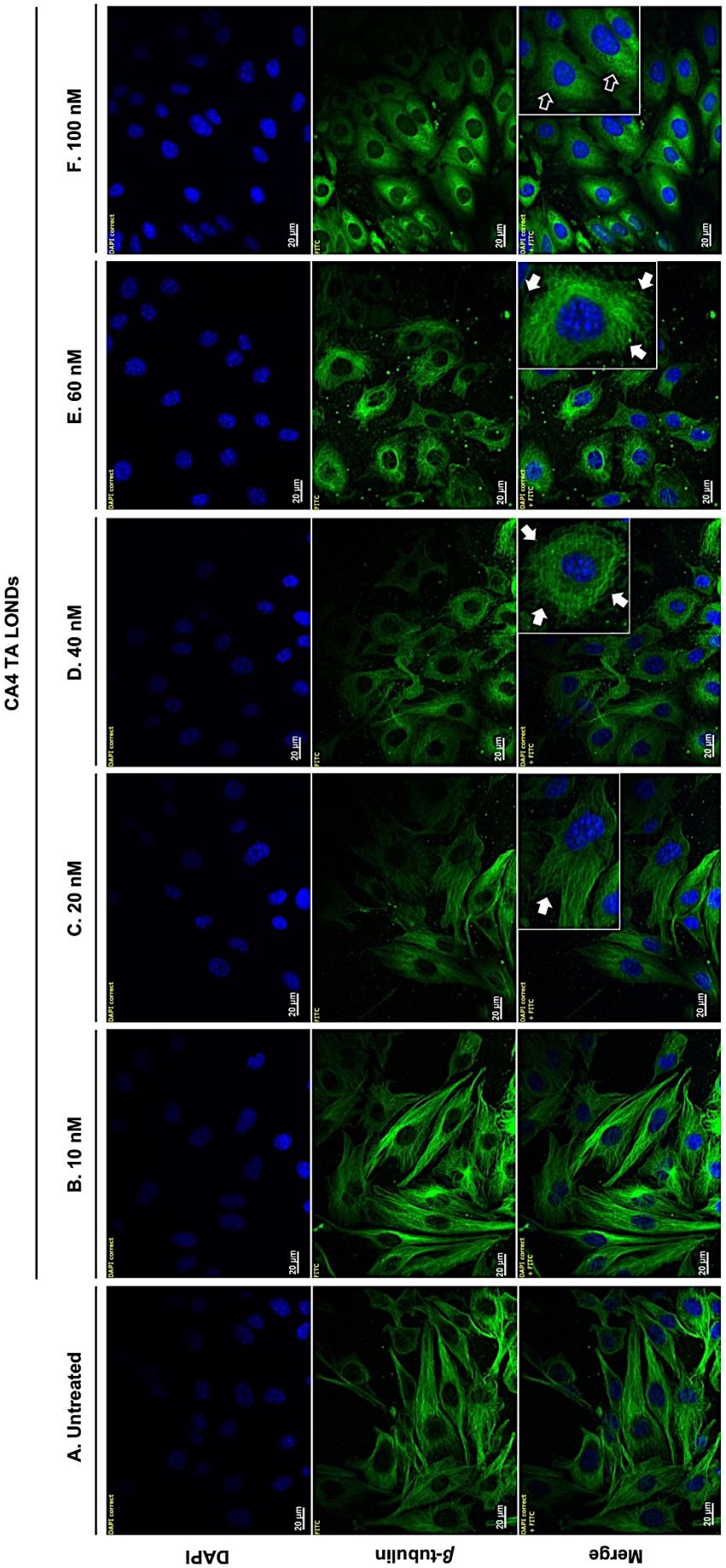
CA4 TA LONDs
A. Untreated
B. 10 nM
C. 20 nM
D. 40 nM
E. 60 nM
F. 100 nM
DAPI
β-tubulin
Merge

Figure 3.4 CA4 TA LONDs cause dose-dependent MT disruption in SVR endothelial cells.

SVR cells cultured in μ-slides VI $^{0.4}$ (ibidi) were treated with escalating concentrations of CA4 TA LONDs (10-100 nM) for 2 h at 37°C. The cells were subsequently fixed, immunostained for *β*-tubulin using a mouse monoclonal anti-*β*-tubulin antibody and visualised using a biotinylated rabbit anti-mouse and FITC-labelled avidin. The slides were mounted with prolong Gold containing DAPI. (A) Untreated cells showing MT filaments. (B) 10 nM CA4 TA LONDs, did not show any MT disruption as image is similar to untreated cells. (C) 20 nM CA4 TA LONDs treatment showed the start of MT disruption with evidence of shortening at the distal ends of MTs at the cell periphery as a result of MT depolymerisation; the inset image is a magnification of a cell showing this pattern (white arrow). (D) 40 nM CA4 TA LONDs treatment showed tangled MTs, white arrows in the small inset image shows a magnification of this. (E) 60 nM CA4 TA LONDs treatment also showed tangled MTs; small inset image of a magnified cell is shown with white arrows showing the tangled pattern. (F) 100 nM CA4 TA LONDs treatment resulted in a uniform fluorescence as a consequence of MT depolymerisation causing tubulin to disperse in the cytoplasm. The white open arrows in the small inset image shows cells with this pattern. Scale bars indicate 20 *μ*m. Prep. number 1 was used.

As no effect on morphology was apparent in SVR cells treated with 10 nM CA4 TA LONDs, it was concluded that these cells were similar to untreated cells. Therefore, the difference in MT length was due to a difference in cell population, for example the median values of MT lengths in untreated SVR cells observed in Figure 3.3 and Figure 3.5 A were 22 μm and 17 μm respectively whereas the median value of MT length in SVR cells treated with 10 nM CA4 TA LONDs was 19 μm (Figure 3.5 A) demonstrating that the median length of untreated SVR cells is within this range.

Significant differences were also observed between all the different CA4 TA LONDs concentrations tested and are shown in Figure 3.5 A and tabulated in Figure 3.5 B. This indicated that as the concentration of CA4 TA LONDs increased so did the ability of the CA4 payload to cause tubulin inhibition, starting from the loss of the long filamentous structure at 20 nM to tangled MTs at 40 and 60 nM eventually leading to complete depolymerisation at 100 nM. Using Spearman's correlation a significant negative correlation was observed between MT length and CA4 TA LOND concentration ($r=-1$, $p=0.02$) (Figure 3.5 C).

MT disruption was also studied in SVR cells treated with escalating concentrations of free CA4 in DMSO. IF staining of β-tubulin after a 2 h exposure time showed MTs of untreated SVR cells with long filamentous MTs (Figure 3.6 A). A 10 nM concentration of CA4 in DMSO caused MTs to lose their radial filamentous structure and tangle around the nuclei (Figure 3.6 B). The inset image in Figure 3.6 B shows a magnified cell with this pattern (white arrows). MTs in SVR cells treated with 20, 40, 60 and 100 nM of CA4 in DMSO had lost their filamentous structure and a uniform fluorescence was observed as a result of depolymerised MTs with tubulin dispersed in the cytoplasm (Figure 3.6 C-F, inset images of magnified cells, white open arrows). This effect was confirmed by measuring MT lengths where possible (Figure 3.7 A and B). A total of 250 MT lengths were measured in the untreated group and 100 MT lengths from the 10 nM free CA4 in DMSO group. MT lengths were significantly reduced or abrogated in SVR cells treated with 10, 20, 40, 60 and 100 nM CA4 in DMSO compared to untreated SVR cells ($p<0.0001$, Mann-Whitney U test, two-tailed). Due to the absence of any measurable MTs in SVR cells treated with 20, 40, 60 and 100 nM CA4 in DMSO, statistically significant differences were observed when compared with measurable MT lengths from SVR cells treated with 10 nM CA4 in DMSO ($p<0.0001$, Mann-Whitney U test, two-tailed) (Figure 3.7 B). Using Spearman's correlation a negative but statistically insignificant correlation was observed between MT length of SVR cells and CA4 in DMSO concentration (Figure 3.7 C).

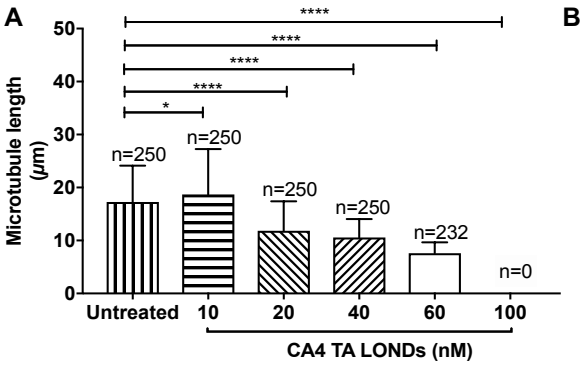

B

Statistical results: Mann-Whitney U test (two-tailed)

Groups	Significant	P value
10 nM CA4 TA LONDs vs.		
20 nM CA4 TA LONDs	yes	p<0.0001
40 nM CA4 TA LONDs	yes	p<0.0001
60 nM CA4 TA LONDs	yes	p<0.0001
100 nM CA4 TA LONDs	yes	p<0.0001
20 nM CA4 TA LONDs vs.		
40 nM CA4 TA LONDs	yes	p=0.002
60 nM CA4 TA LONDs	yes	p<0.0001
100 nM CA4 TA LONDs	yes	p<0.0001
40 nM CA4 TA LONDs vs.		
60 nM CA4 TA LONDs	yes	p<0.0001
100 nM CA4 TA LONDs	yes	p<0.0001
60 nM CA4 TA LONDs vs.		
100 nM CA4 TA LONDs	yes	p<0.0001

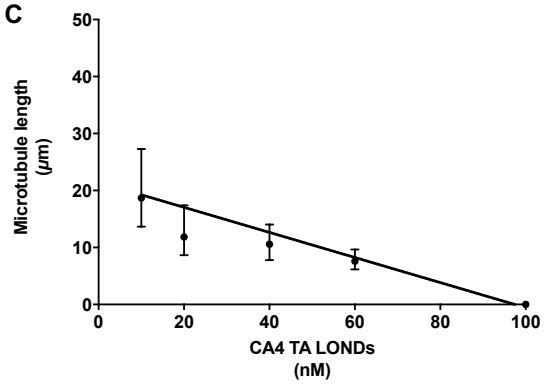

Figure 3.5 CA4 TA LONDs cause a dose-dependent change in MT lengths.

(A) Fluorescent images were used to quantitate MT disruption caused by treatment with escalating concentrations of CA4 TA LONDs for 2 h at 37°C. The lengths of 250 MTs were measured (10 MTs/cell in 5 cells per FOV, 5 FOV in total per condition) using *Image J* from untreated SVR cells and SVR cells treated with 10, 20 and 40 nM of CA4 TA LONDs and a total of 232 MTs from SVR cells treated with 60 nM CA4 TA LONDs. Treatment with 100 nM of CA4 TA LONDs resulted in depolymerisation of MTs with tubulin dispersed within the cytoplasm uniformly immunostained. Therefore, in this group no MTs were measured and 0 μm was used to plot the graph. Data represents the median value from the measured MTs (n=1 biological replicate) and the error bars represent the interquartile range. ****, p<0.0001, * p=0.03 calculated by Mann-Whitney U test (two-tailed). (B) Tabulated format of statistical results from A. (C) The relationship between MT length and CA4 TA LOND concentration using Spearman's correlation showed a significant negative correlation between the two variables (r=-1, *, p=0.02, two-tailed). Data shows the median value and error bars interquartile range.

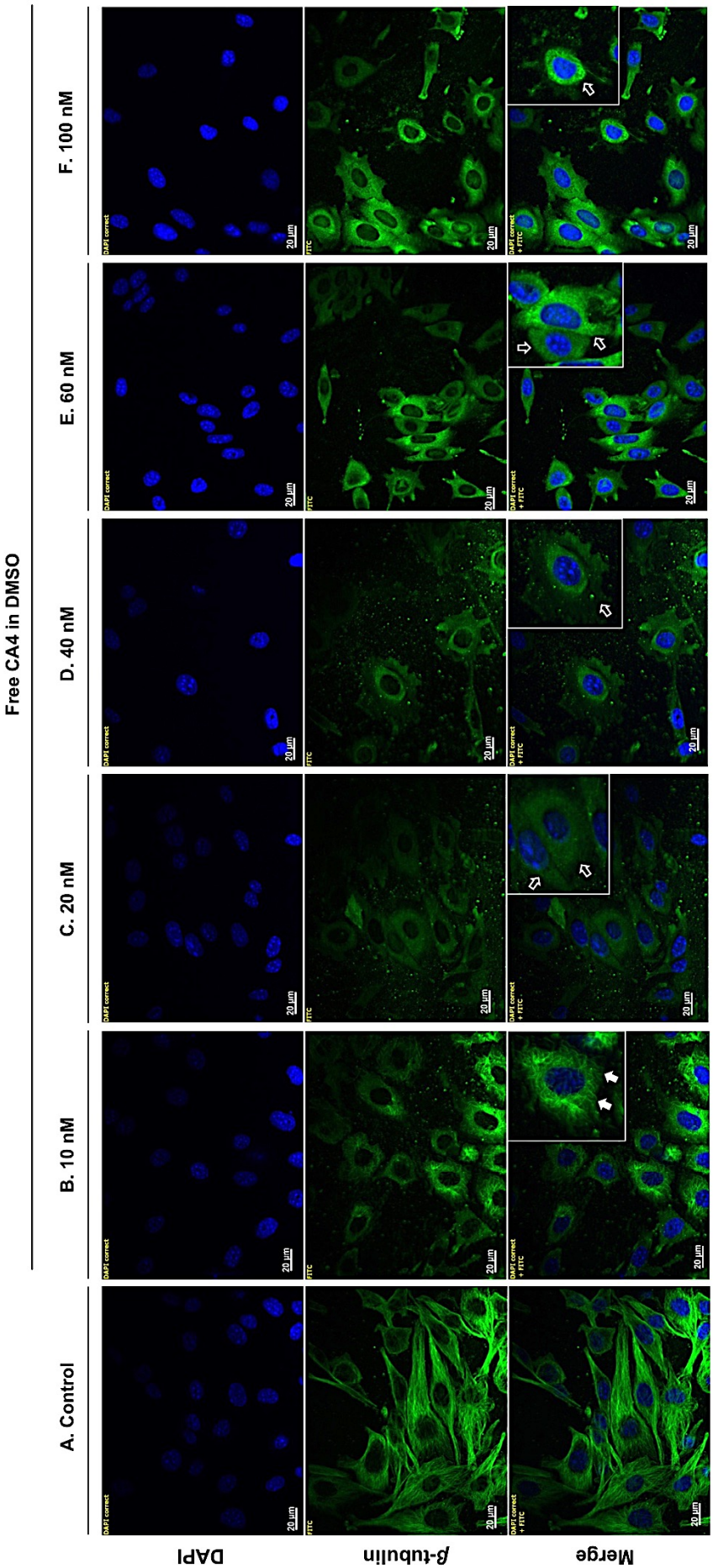
Free CA4 in DMSO
A. Control
B. 10 nM
C. 20 nM
D. 40 nM
E. 60 nM
F. 100 nM
DAPI
β-tubulin
Merge

Figure 3.6 Dose-response of free CA4 in SVR endothelial cells.

SVR cells cultured in µ-slides VI $^{0.4}$ (ibidi) were treated with escalating concentrations of free CA4 in DMSO (10-100 nM) for 2 h at 37°C. The cells were subsequently fixed, immunostained with *β*-tubulin using a mouse monoclonal anti-*β*-tubulin antibody and visualised using a biotinylated rabbit anti-mouse and FITC-labelled avidin. The slides were mounted with prolong Gold containing DAPI. (A) Untreated cells with MT filaments. (B) 10 nM free CA4 in DMSO showed tangled MTs (white arrows in inset magnified image of a cell). (C-F) 20, 40, 60 and 100 nM free CA4 in DMSO resulted in a uniform fluorescence throughout the cytoplasm from tubulin that had dispersed as a result of MT depolymerisation (white open arrows in inset magnified images of cells). Scale bars indicate 20 *µ*m.

A

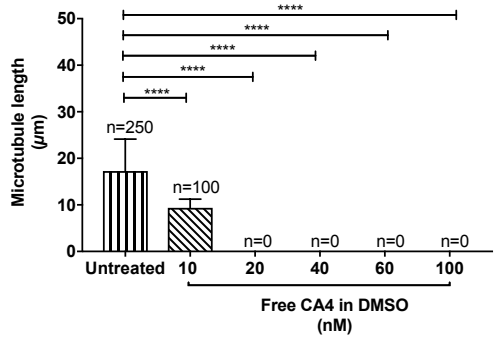

B

Statistical results: Mann-Whitney U test (two-tailed)		
Groups 10 nM CA4 in DMSO vs.	Significant	P value
20 nM CA4 in DMSO	yes	p<0.0001
40 nM CA4 in DMSO	yes	p<0.0001
60 nM CA4 in DMSO	yes	p<0.0001
100 nM CA4 in DMSO	yes	p<0.0001

C

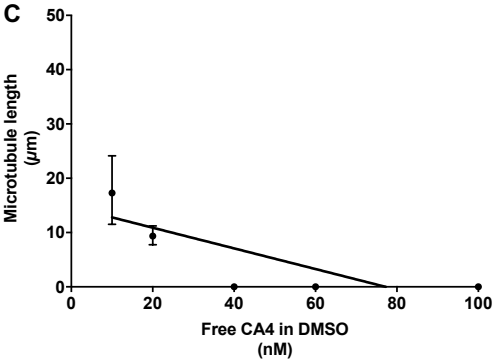

Figure 3.7 Quantitative analysis of MT lengths following treatment with free CA4 in DMSO.

Fluorescent images were used to quantitate MT disruption caused by treatment with escalating concentrations of CA4 in DMSO (10-100 nM) for 2 h 37°C. The lengths from 250 MTs (10 MTs/cell in 5 cells per FOV, 5 FOV in total per condition) were measured in the untreated control group while the lengths from 100 MTs in the 10 nM treatment group were measured using *Image J*. Treatment with 20, 40, 60 and 100 nM of free CA4 in DMSO resulted in depolymerised MTs with tubulin dispersed within the cytoplasm uniformly immunostained. Therefore, in this group no MTs were measured and 0 *μ*m was used to plot the graph. Data represents the median value from the measured MTs (n=1 biological replicate) and the error bars represent the interquartile range. ****, p<0.0001 calculated by Mann-Whitney U test (two-tailed). (B) Tabulated format of statistical results from A. (C) The relationship between MT length and CA4 in DMSO concentration using Spearman's correlation showed a negative but statistically insignificant correlation between the two variables (r=-0.9, p=0.1, two-tailed). Data shows the median value and error bars interquartile range.

3.5 CA4 TA LONDs cause endothelial cell morphological changes characteristic of mitotic catastrophe

Short term exposure (2 h) of SVR cells to CA4 TA LONDs at concentrations higher than 100 nM resulted in tubulin dispersed in the cytoplasm adopting a uniform fluorescence immunostained pattern as a result of complete MT depolymerisation. The experiments focused on the continuous exposure (24 h) of SVR cells to CA4 TA LONDs, as the delivery of CA4 TA LONDs or thMBs *in vivo* would potentially lead to a prolonged exposure of the tumour cells to LONDs due to the EPR effect. A concentration of 0.5 μM was used in order to equate to the dose that would be theoretically delivered *in vivo* using thMBs with CA4 TA LONDs (prep. number 4, Table 3.1).

IF staining of β-tubulin after a 24 h exposure time showed untreated SVR cells with MT filaments (Figure 3.8 A). Figure 3.8 B and C show SVR cells treated with 0.5 μM CA4 TA LONDs and 0.5 μM CA4 in DMSO respectively, some cells were enlarged (white arrows) and others were multinucleated with fragmented nuclei and micronuclei (white open arrows). These observations were consistent with previous reports with CA4P and HUVECs (Kanthou *et al.*, 2004).

3.6 Delivery of CA4 TA LONDs by ThMBs

To increase the drug delivery capabilities and enable controlled and triggered US release of CA4 TA LONDs, on-chip single step production of thMBs with CA4 TA LONDs was performed (section 2.4 for details). ThMBs (see Figure 1.8) are defined as a targeted (*e.g.* to VEGFR2) MB with attached LONDs via NeutrAvidin-biotin interactions, in this case CA4 TA LONDs. Work conducted by Dr James McLaughlan and Dr Victoria Mico (School of Electronic and Electrical Engineering and School of Physics and Astronomy, University of Leeds), showed that thMBs with CA4 TA LONDs retained the US properties of MBs and therefore, could be used as theranostic agents for both delivery of hydrophobic drugs such as CA4 and imaging (Mico, 2017).

Mice bearing SW480 human CRC xenografts were sorted according to tumour volume into two groups, one group received an i.v. injection through the tail vein of 4 x 10^8 thMBs with CA4 TA LONDs at 4.9 mg/kg and the other group received an intraperitoneal (i.p.) injection of free CA4 in TA at the same dose due to the oily nature of the TA solution (Figure 3.9 A and B) on day 23 of tumour growth.

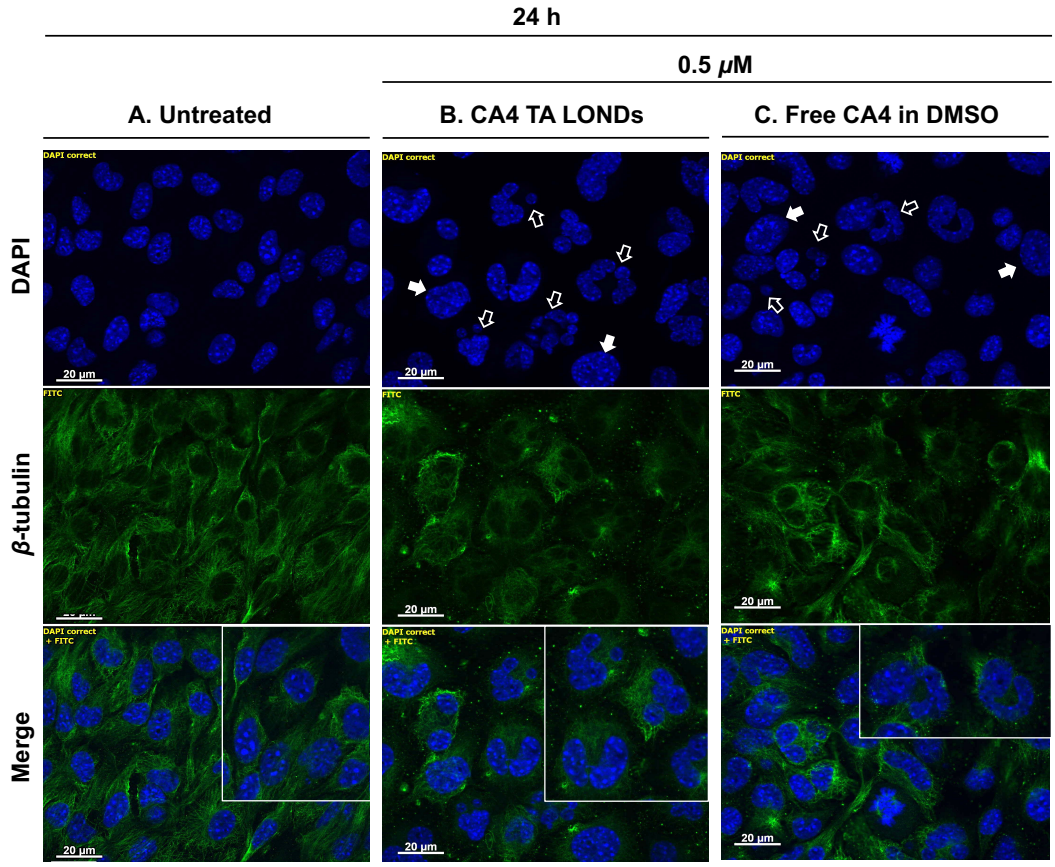

Figure 3.8 Continuous exposure of SVR cells to CA4 TA LONDs cause endothelial cell morphology changes characteristic of mitotic catastrophe. SVR cells cultured in 6-well plates were treated with 0.5 *μ*M CA4 TA LONDs or 0.5 *μ*M free CA4 in DMSO for 24 h at 37°C, untreated cells were used as control. Following 24 h treatment, cells were fixed, immunostained with *β*-tubulin using a mouse monoclonal anti-*β*-tubulin antibody and visualised using a biotinylated rabbit anti-mouse and FITC-labelled avidin. The slides were mounted with prolong Gold containing DAPI. (A) MTs and nuclei of untreated control cells at 24 h. (B) 24 h post-treatment with 0.5 *μ*M of CA4 TA LONDs resulted in MT disruption evident by depolymerised MTs with tubulin dispersed and uniformly fluorescent in the cytoplasm while some remaining MTs were tangled around the nuclei. Additionally the nuclei were enlarged (white arrows) and had fragmented into multiple and micro- nuclei per cell (open white arrows). (C) 24 h post-treatment with 0.5 *μ*M of CA4 free in DMSO resulted in MT disruption. The nuclei were also enlarged (white arrows) and cells were present with multi- and micro- nuclei (open white arrows). Inset images show magnified cells in each panel. Scale bars indicate 20 *μ*m. Prep. number 4 was used for B.

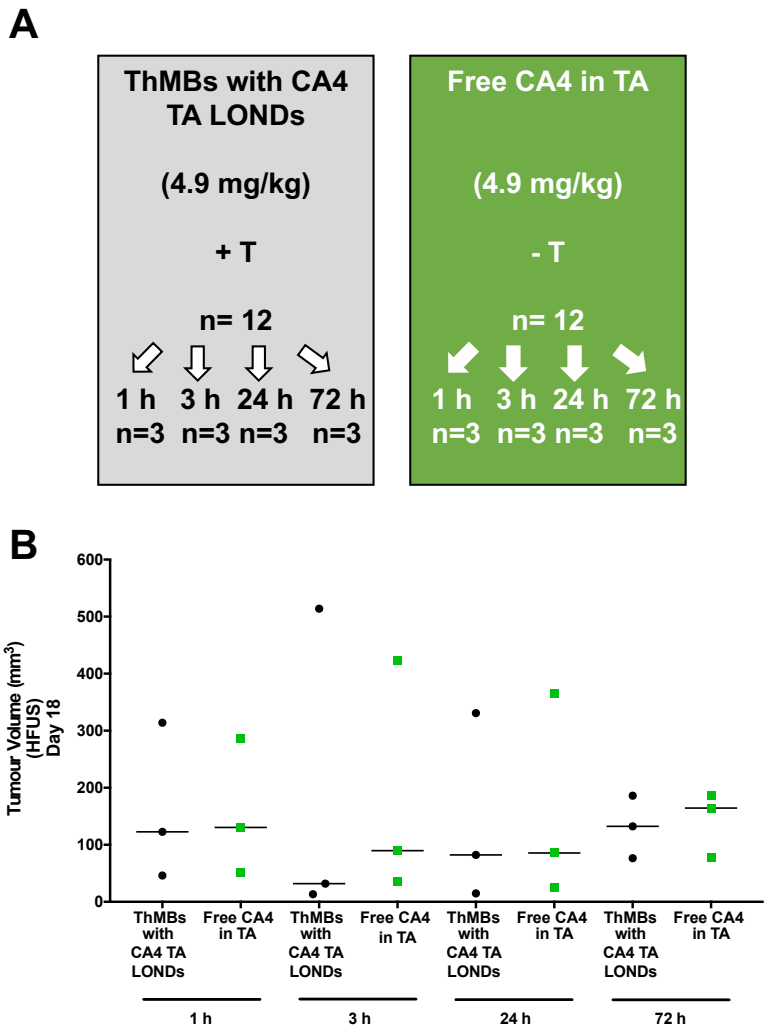

Figure 3.9 US triggered delivery of thMBs with CA4 TA LONDs and free CA4 in TA.

(A) SW480 tumour xenografts were established in BALB/c nude male mice by s.c. injection of 5 x 10^6 cells on day 0. On day 18 of tumour growth, mice were sorted according to tumour volume into two experimental cohorts: thMBs with CA4 TA LONDs plus an US trigger (+ T) and a free CA4 in TA without an US trigger (- T) group . Both groups had n=12 mice, these were further subdivided into n=3 per time point post-injection 1, 3, 24 and 72 h. Mice in the thMBs with CA4 TA LONDs plus + T group received an i.v. injection through the tail vein of 4 x 10^8 thMBs with CA4 TA LONDs at a 4.9 mg/kg CA4 dose. Mice in the free CA4 in TA group received an i.p. injection of 4.9 mg/kg CA4 pre-dissolved in TA. The injections were carried out on day 23 of tumour growth. (B) Tumour volumes measured by HFUS on day 18 used for randomisation. Straight lines (–) represent the median value. No statistically significant differences were observed by Mann-Whitney U test, two-tailed.

The injections were performed with the help of Dr Gemma Marston (School of Medicine, University of Leeds). A low frequency, high amplitude US pulse was applied at the tumour site using the specifically designed UARP (methods section 2.5.5) four minutes post-injection, to burst the thMBs. The time prior to the US trigger (+ T) allows for binding and retention of the thMBs to their target (VEGFR2) and was previously optimised by Dr Nicola Ingram (School of Medicine, University of Leeds). Previous contrast agents targeted to VEGFR2 used for molecular imaging of tumour vasculature in a breast cancer xenograft also showed optimal binding and retention of the contrast agents after a four minute waiting time (Lyshchik *et al.*, 2007). The concentration, diameter and CA4 loading of the thMBs measured by LC-MS/MS was 2 x 10^9 MBs/mL, 2.5 ± 1.2 μm and 488 μg/mL respectively (Appendix A, Figure A.1) (method development described below). The administration was well tolerated with no obvious toxic reaction observed.

3.6.1 ThMBs with CA4 TA LONDs potentially cause haemorrhage in SW480 human CRC xenografts

Previous *in vivo* data reported for CA4 and CA4P indicated that intratumoural delivery resulted in extensive haemorrhagic necrosis in the central regions of the tumour with only a small viable rim at the periphery (Dark *et al.*, 1997; Grosios *et al.*, 1999). These observations occurred within the first few hours of treatment and therefore haemorrhage in tumour sections from CA4 treated animals was used as an indicator of CA4 intratumoural delivery.

Following 1, 3, 24 and 72 h post-injection with thMBs-CA4 TA LONDs + T or free CA4 in TA – T, evidence of haemorrhage was observed, usually associated with stromal areas of the tumour sections (Figure 3.10 A-H). However, haemorrhage was not associated with necrosis (Figure 3.10 A-H). Tumour vasculature was subsequently assessed on adjacent sections by immunostaining of CD31, to assess any potential damage caused by CA4 and correlation with areas were haemorrhage was observed (Figure 3.11). The results showed no differences in the number of tumour blood vessels at each of the time points assessed 1, 3, 24 and 72 h post-injection with thMBs-CA4 TA LONDs and free CA4 in TA (Figure 3.11 A-H). To assess any potential differences between the two groups at the various time points, MVD (number of CD31+ vessels per 0.79 mm^2 of tumour) was determined (Figure 3.12). No statistically significant differences were observed between the groups by a Mann-Whitney U test (two-tailed).

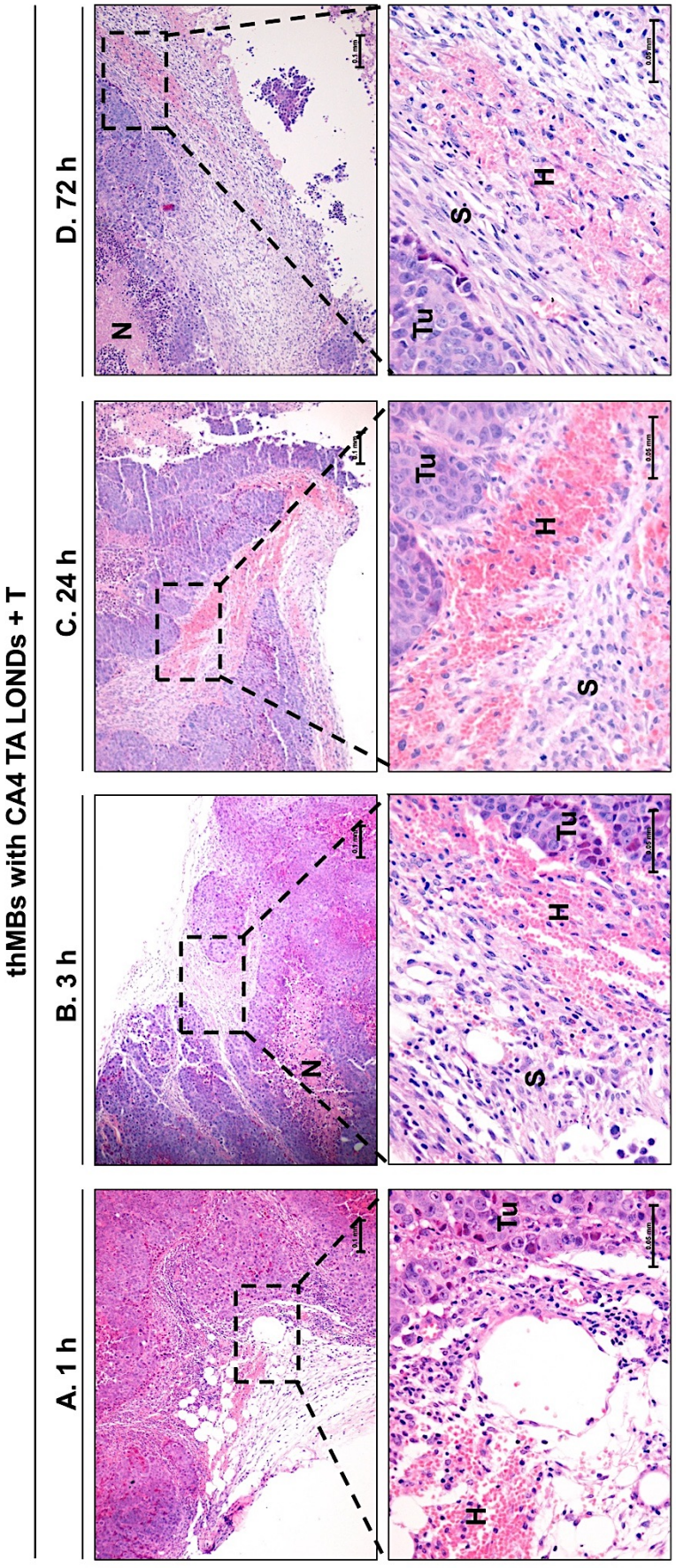
thMBs with CA4 TA LONDs + T
A. 1 h
B. 3 h
C. 24 h
D. 72 h
N
Tu
H
S

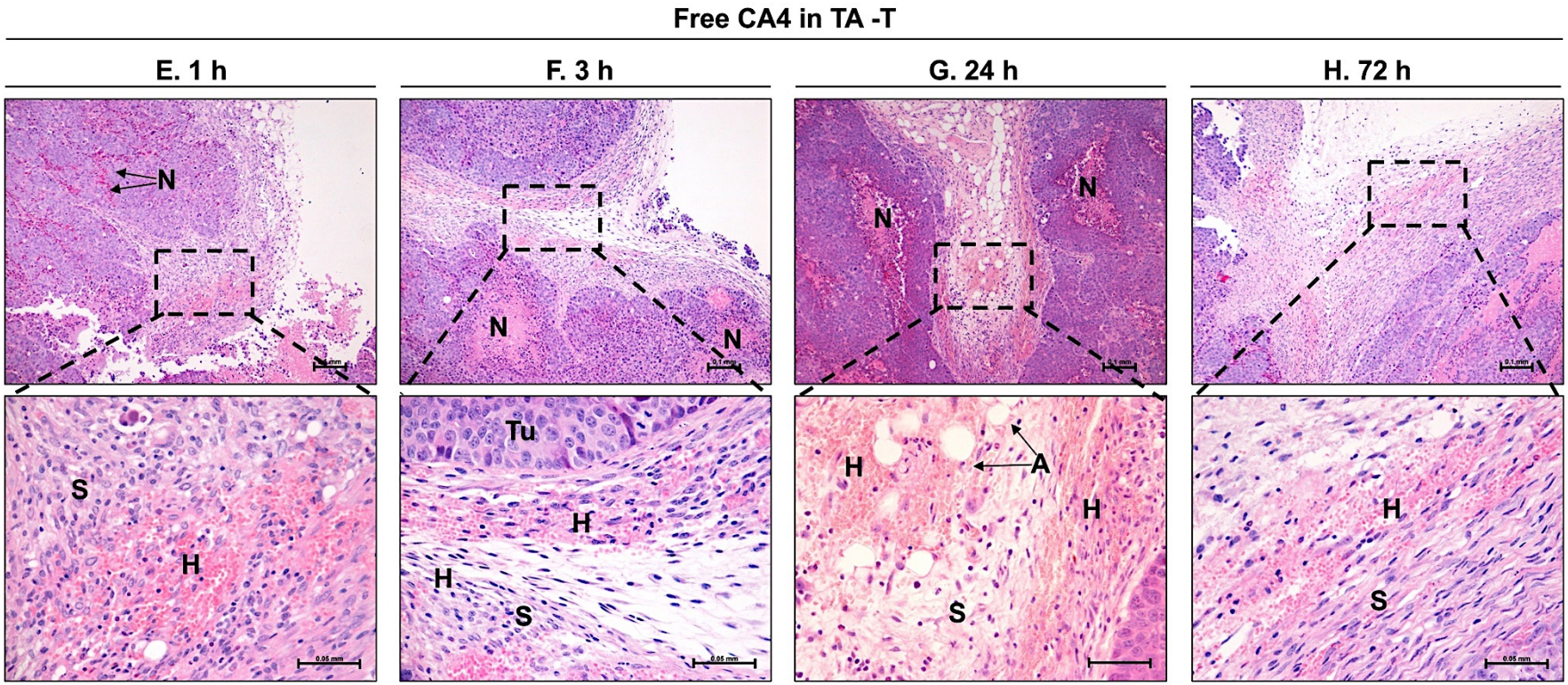

Figure 3.10 ThMBs with CA4 TA LONDs or free CA4 in TA potentially cause haemorrhage in SW480 xenografts.

Histological images of tumours stained with H & E. (A-D) 1, 3, 24 and 72 h post-injection with thMBs-CA4 TA LONDs. The tumours had evidence of haemorrhage (H) in the stromal (S) areas. Haemorrhage was used as an indicator of vascular damage caused by CA4, however this was surrounded by viable tumour cells (Tu). (E-H) 1, 3, 24 and 72 h post-injection with free CA4 in TA. The tumours appeared to have the same patterns as observed with thMBs-CA4 TA LONDs. Areas of haemorrhage (H) in the stroma (S), with only small areas of necrosis (N). The tumours (Tu) were mainly viable cells. Squares indicate the area of the bottom images in both groups. Scale bars top images in A-H indicate 0.1 mm (100 μm), bottom images of A-H indicate 0.05 mm (50 μm).

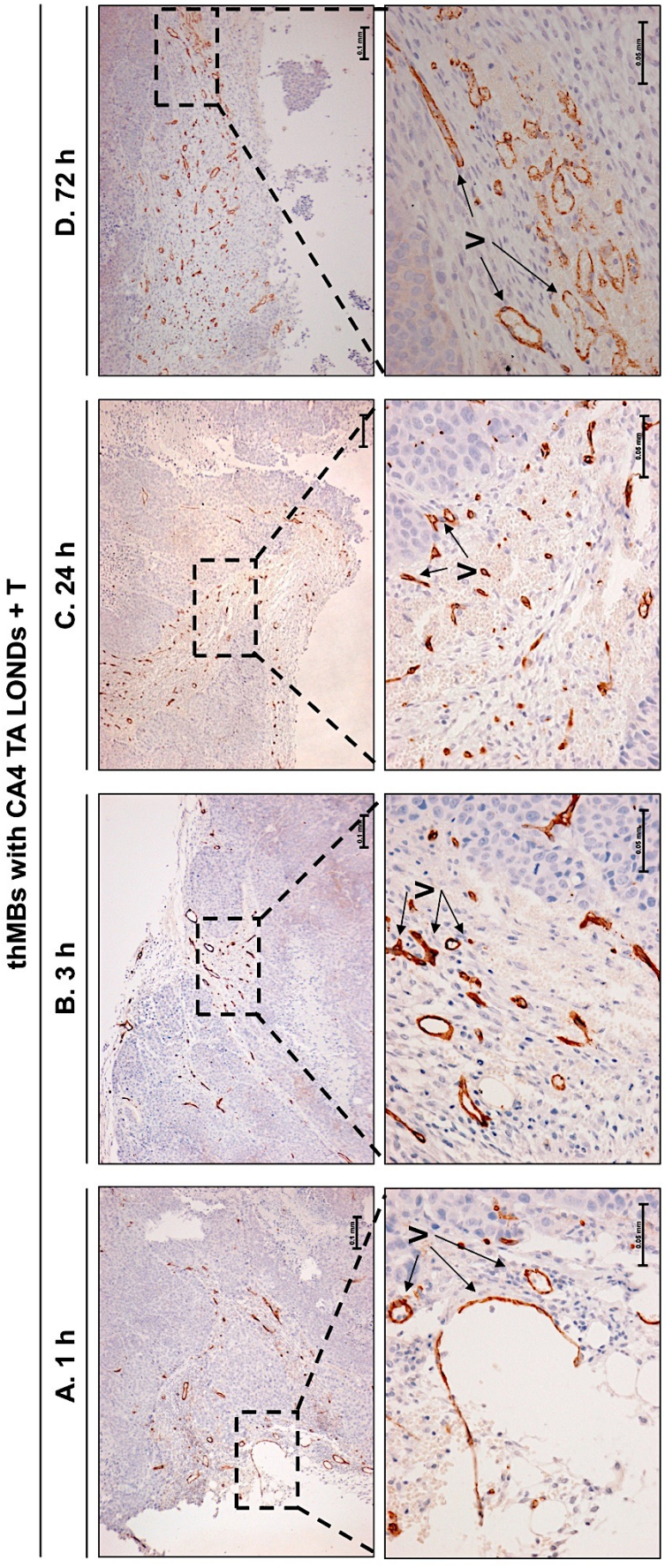
thMBs with CA4 TA LONDs + T
A. 1 h
B. 3 h
C. 24 h
D. 72 h
V
0.1 mm
0.05 mm
0.04 mm
0.05 mm

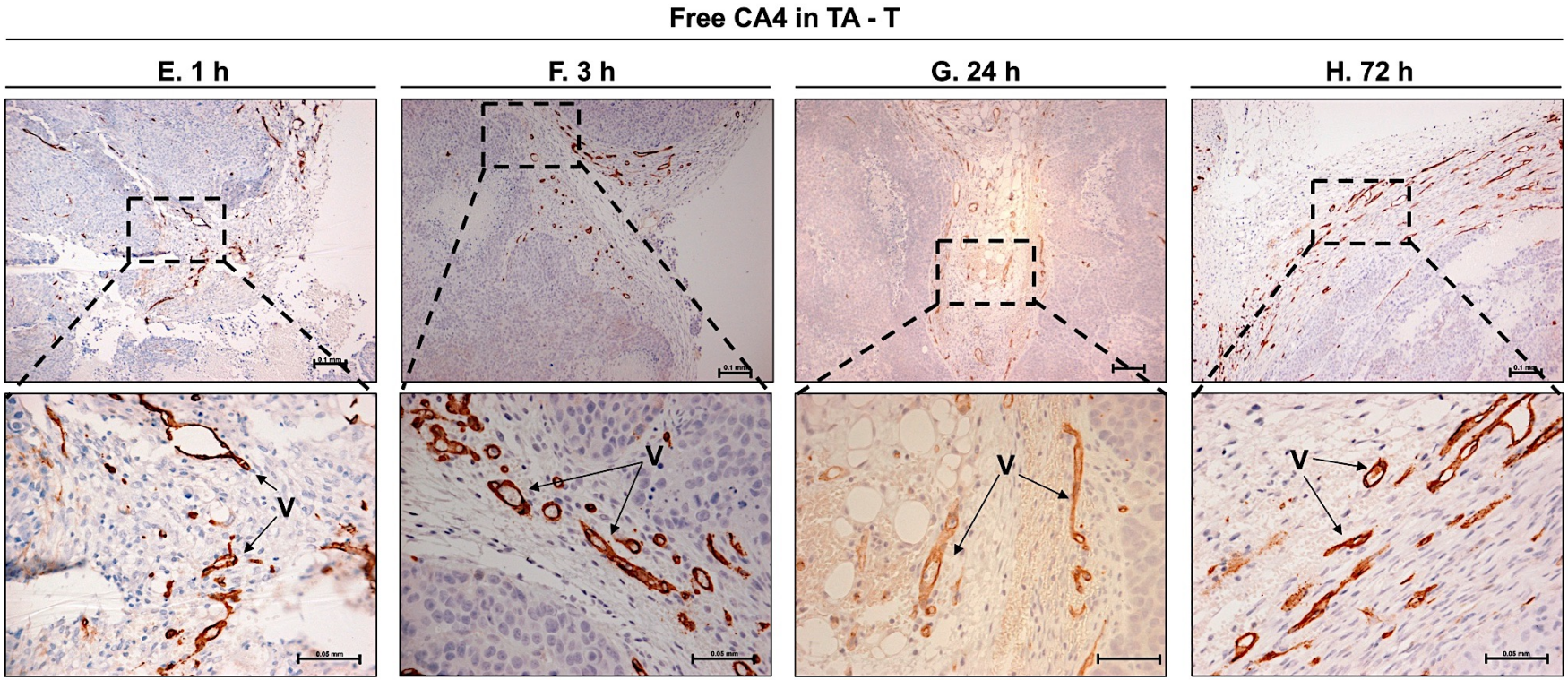

Figure 3.11 Tumour vasculature 1, 3, 24 and 72 h post-injection with US triggered thMBs-CA4 TA LONDs or free CA4 in TA. Immunohistochemical images of tumours stained with a rat anti-mouse CD31 antibody and CD31 + vessels were visualised with DAB. (A-D) 1, 3, 24 and 72 h post-injection with thMBs and CA4 TA LONDs respectively. The tumours had no evidence of microvessel damage. (E-H) 1, 3, 24 and 72 h post-injection with Free CA4 in TA respectively. Tumours had no evidence of damage to the vessels. Squares indicate the area of the bottom images in both groups. Scale bars top images in A-H indicate 0.1 mm (100 μm), bottom images of A-H indicate 0.05 mm (50 μm).

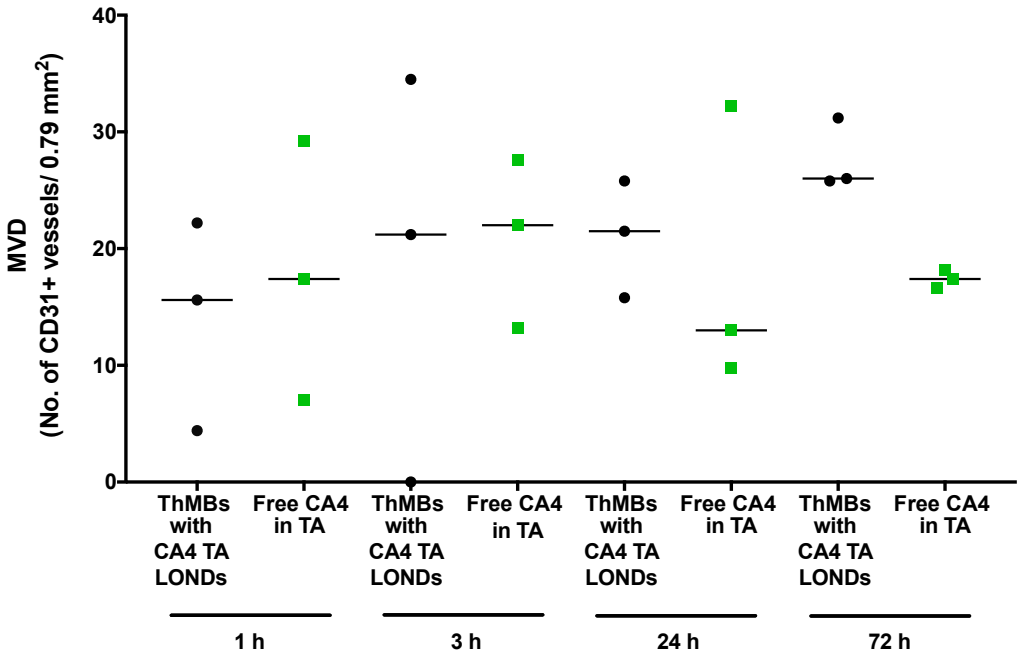

Figure 3.12 MVD post-injection with thMBs-CA4 TA LONDs or free CA4 in TA. CD31 immunostained tumour images (n=3 hot spots) were used to determine the MVD 1, 3, 24 and 72 h post-injection with either ThMBs with CA4 TA LONDs or Free CA4 in TA. Straight lines (–) represent the median value. No statistically significant differences were observed by Mann-Whitney U test (two-tailed).

3.6.2 Development of a LC-MS/MS method for quantification of CA4 and its main metabolite CA4G in tissues

LC-MS/MS represents the preferred analytical instrumental method for quantitative analysis of drugs due to its specificity and sensitivity (Rafiei, Michel & Haddadi, 2015). Specific LC-MS/MS methods have been developed for the quantification of drugs such as Docetaxel in NPs (Rafiei, Michel & Haddadi, 2015). The same LC-MS/MS methods can also be used to analyse tissue samples for PK and biodistribution studies, as performed for Docetaxel loaded NPs (Rafiei & Haddadi, 2017).

The aim of the first *in vivo* experiment with thMBs and CA4 TA LONDs was to obtain evidence of intratumoural delivery of CA4. In parallel, PK and *in vivo* biodistribution of CA4 LONDs was also investigated. To do this, a specific LC-MS/MS method was developed at the Institute of Cancer Therapeutics (ICT), University of Bradford with the help of Ms Antonia Wierzbicki and supervised by Prof. Paul Loadman. The same method could also be used for the measurement of CA4 in LONDs.

3.6.2.1 Method optimisation

Standards of CA4 (Figure 1.2 A), IS colchicine (Figure 3.14 A) and CA4G (Figure 3.15 A) were scanned and parent single ion recording (SIR) channels were established (Figure 3.13 A, Figure 3.14 B and Figure 3.15 B for CA4, colchicine and CA4G respectively). The precursor ions of CA4 *m/z* 317.5 (Figure 3.13 B), colchicine *m/z* 400.51 (Figure 3.14 C) and CA4G m/z 493.40 (Figure 3.15 C) passed through the first quadrupole into the collision cell and the collision energy was optimised to obtain the product ions with the highest signal. After fragmentation, the product ions for the three compounds were monitored in the third quadrupole at *m/z* 270.21, 286.12 and 317.23 for CA4 (Figure 3.13 C), *m/z* 310.05, 294.98, 267.22 for colchicine (Figure 3.14 D) and *m/z* 302.20 and 317.31 for CA4G (Figure 3.15 D). Full MRM settings including collision energy details are shown in Table 2.1.

CA4 was also monitored using the photodiode array capability to monitor *cis*-and *trans* conversion (Figure 3.13 D). The active *cis*-CA4 form was monitored at 290 nm (Figure 3.13 E) and the inactive *trans*-CA4 form at 330 nm (Figure 3.13 F). CA4, colchicine and CA4G had retention times of 11.07, 6.55 and 8.55 respectively, the total run time was 16 min.

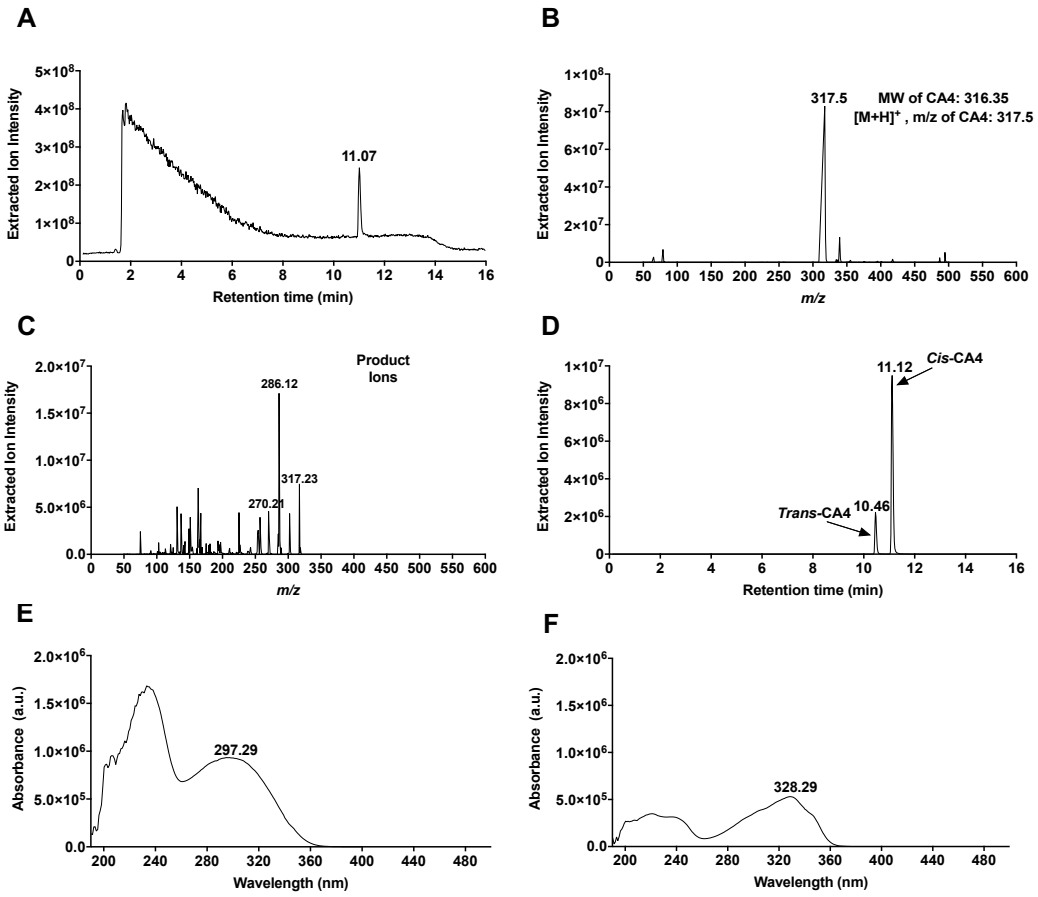

Figure 3.13 LC-MS/MS method development for CA4 detection.

(A) SIR scan for CA4 with retention time at 11.0 min. Total run time was 16 min. (B) Precursor ion for CA4 m/z 317.5 (molecular weight (MW) 316.35). (C) Product ions of CA4 m/z 286.12, 317.23, 270.21 after fragmentation. (D) Chromatogram with *trans*-CA4 (retention time 10.46 min) and *cis*-CA4 (retention time 11.12 min). (E) Photodiode array absorbance spectra monitoring for *cis*-CA4 at 290 nm. (F) Photodiode array absorbance monitoring for *trans*-CA4 at 320 nm. a.u.: arbitrary units.

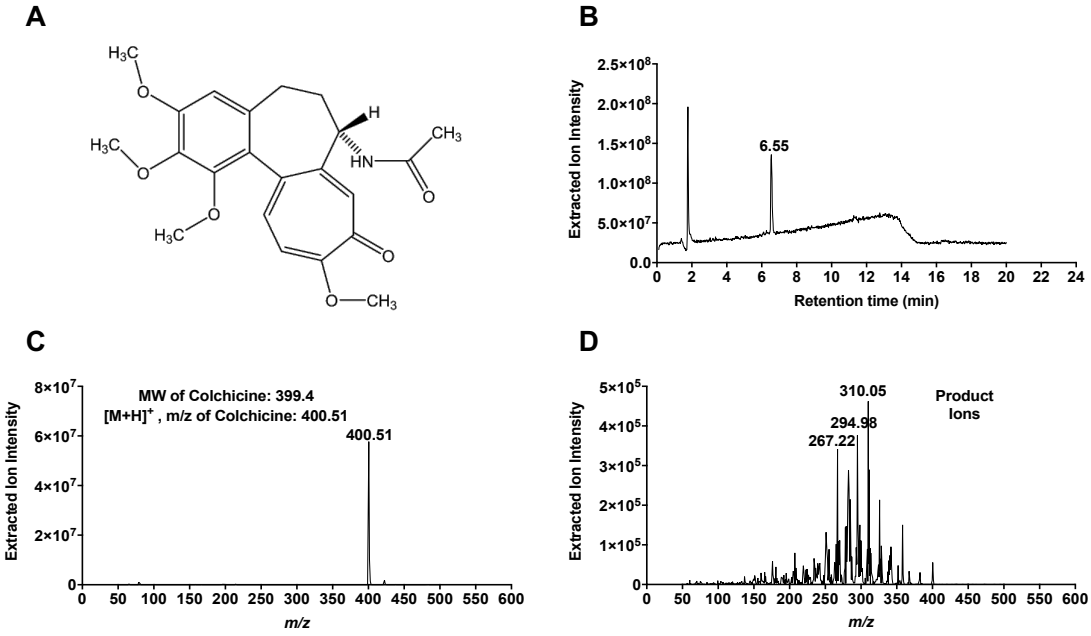

Figure 3.14 LC-MS/MS method development for colchicine detection.

(A) Chemical structure of colchicine. (B) SIR scan for colchicine with retention time 6.55 min. Total run time was 16 min. (C) Precursor ion for colchicine m/z 400.51 (molecular weight (MW) 399.4). (D) Product ions for colchicine m/z 267.22, 294.98 and 310.05 after fragmentation.

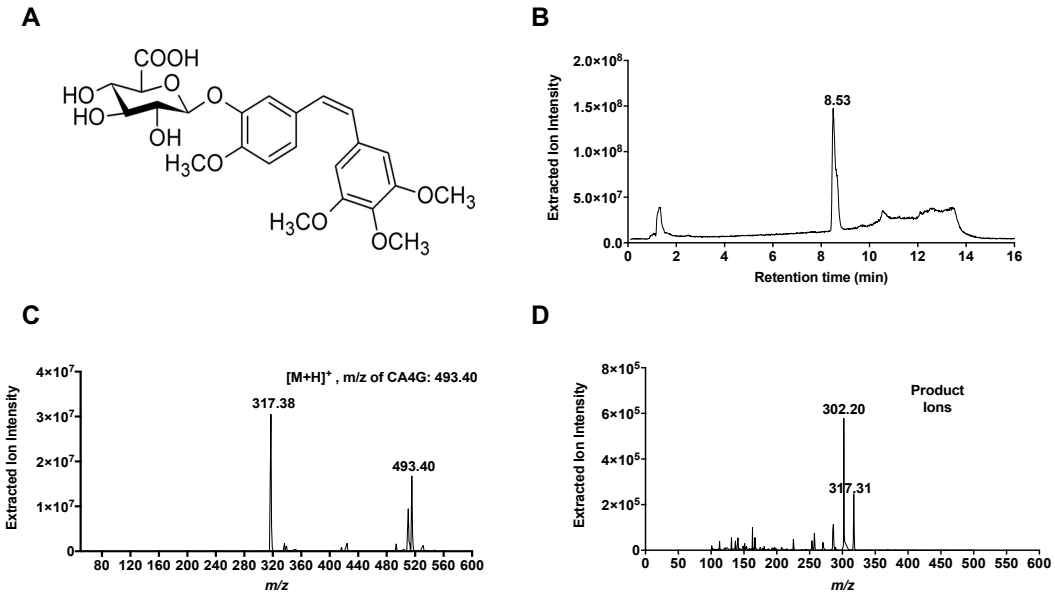

Figure 3.15 LC-MS/MS development for CA4G detection.

(A) Chemical structure of CA4G. (B) SIR scan for CA4G with retention time 8.53 min. (C) Precursor ion for CA4G m/z 493.40. (D) Product ions for CA4G m/z 302.20 and 317.31 after fragmentation.

3.6.2.2 Method validation

3.6.2.3 Calibration curve, limit of detection and carry over

A calibration curve of CA4 was prepared with the concentration range of 1-0.06 *μ*g/mL (Figure 3.16 A). The method described showed a linear response with a coefficient of determination (r^2) value of 0.9996 (Figure 3.16 A). It should be noted that due to the increase in run time (25 min) the retention time of CA4 was 14.8 min. The LOD and LOQ were determined to be 10 ng/mL (Figure 3.16 B). Carry-over was not observed following injection of 1 *μ*g/mL for CA4.

3.6.2.4 Reproducibility, stability and extraction efficiencies

Part of the method of extraction of CA4 from samples was drying (evaporating) at 37°C, therefore the reproducibility of the calibration curves for CA4 were assessed in MeOH before and after drying by comparing the slope of the curves. The results in Figure 3.17 A and B showed no significant difference in the slope. The freeze-thaw stability of CA4 was investigated following three freeze-thaw cycles. CA4 at 1 *μ*g/mL was stable following three freeze-thaw cycles (0.98 *μ*g/mL measured concentration) (Figure 3.17 C). The % extraction efficiency for CA4 was calculated from tumour, liver, spleen, kidney, colon and plasma spiked with 1 *μ*g/mL of CA4 compared with those spiked in methanol in the same way (Figure 3.17 D). The % extraction efficiency was expressed as the ratio of the PA of CA4 spiked into the relevant tissue by the PA of CA4 spiked in MeOH. All % extraction efficiencies for CA4 in the different tissues were within the FDA acceptable range of +/- 15% (U.S. Department of Health and Human Services Food and Drug Administration, 2013) (Figure 3.17 D).

3.6.3 *In vivo* biodistribution of CA4

The validated LC-MS/MS method above was used to quantitate the amount of CA4 in tumours and tissues from mice administered with 4.9 mg/kg CA4 either in an i.v. injection of thMBs-CA4 TA LONDs or as free drug in TA (i.p.). Initial testing of plasma, tumour and liver tissues 1 and 3 h post-injection showed no detectable levels of CA4 or CA4G. An example chromatogram of a liver tissue treated with free CA4 in TA 1 h post-injection is shown in Figure 3.18. Spiked IS was present at the expected retention time of 8.05 min for the 25 min run (Figure 3.18 A) but not CA4 (Figure 3.18 B) or CA4G. The presence of IS in the liver tissue excluded any instrument or method issues and suggested that CA4 and CA4G were below the LOD.

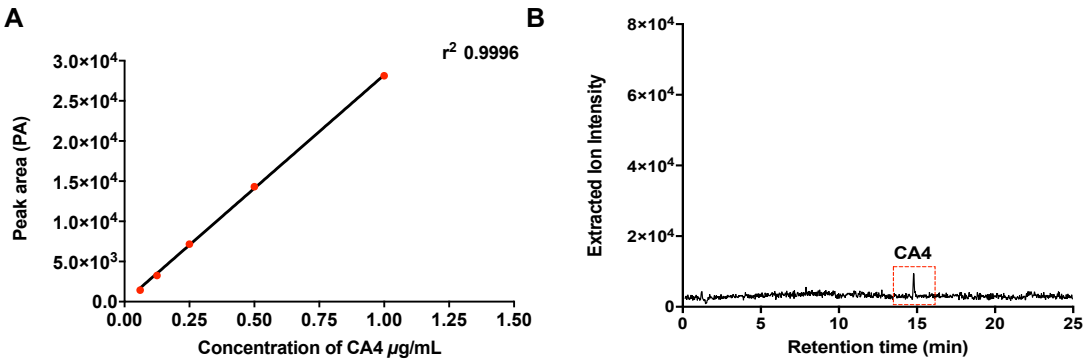

Figure 3.16 CA4 calibration curve and limit of detection.

(A) CA4 calibration curve. (B) LOD and LOQ at 10 ng/mL (Retention time of CA4 14.8 min due to longer run time of 25 min).

A

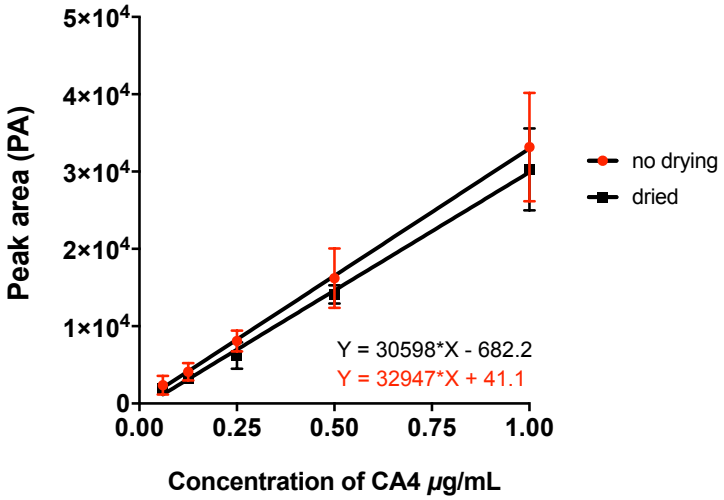

B

Linear regression equation (y=ax + b) (Best-fit value ± SE)			
	Slope (a)	Y-intercept (b)	Correlation (r^2)
MeOH (n=3)	32947 ± 409.9	41.1 ± 211.6	0.9995
MeOH – dried at 37ºC and re-suspendend in MeOH (n=3)	30598 ± 938.3	-682.2 ± 484.3	0.9972

C

Freeze/thaw Stability		
	CA4 Peak area (PA)	**Measured concentration µg/mL**
Standard	41185	1
F/T	40246	0.98
Mean	40715.5	0.99
SD	664	0.01

D

Extraction efficiency			
Sample	**CA4 (PA)[a]**	**MeOH[b]**	**Extraction (%)**
Tumour	30043	30368	98.9
Liver	32438	30294	107.1
Spleen	29029	28805	100.8
Kidney	30928	28818	107.3
Colon	31800	30091	105.7
Plasma	29772	29376	101.3

Figure 3.17 Reproducibility, stability and extraction efficiencies for CA4 detection.

(A-B) Reproducibility of CA4 calibration curves in MeOH before and after drying at 37°C by LC-MS/MS. The slopes of n=3 calibration curves was calculated using linear regression equation. No statistically significant differences between the slopes was observed (p=0.062), a single pooled slope was determined 31772. The intercepts were significantly different (p=0.008) which indicated that the lines were not identical but parallel. (C) Stability of CA4 1μg/mL standard following three freeze thaw (F/T) cycles. (D) Tissue homogenates (tumour, liver, spleen, kidney, colon and plasma) were spiked with 1 μg/mL of CA4 and compared with 100% methanol spiked in the same way. % extraction was calculated (a/b*100).

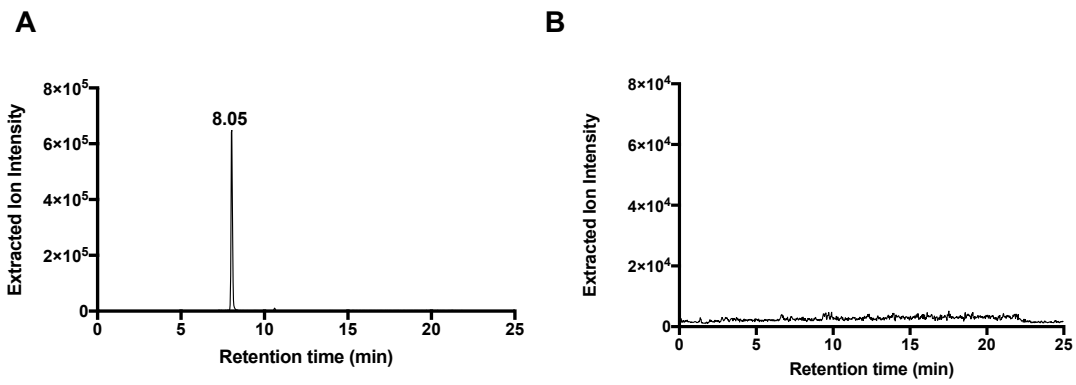

Figure 3.18 Chromatogram of liver tissue post-treatment with free CA4 in TA. (A) Example liver sample chromatogram following 1 h post-injection with free CA4 in TA. IS colchicine detection window showed a peak for colchicine at 8.05 min. (B) No detectable peak for CA4 at the CA4 detection window. Expected retention time was at 14.8 min.

3.7 Discussion

3.7.1 Development of LONDs for CA4 delivery

In the present work LONDs were evaluated as a novel hydrophobic DDS. Production of TA LONDs by high pressure homogenisation resulted in particles with sizes of approximately 150 to 400 nm and concentrations of 10^9 particles/mL. As with any novel DDS a crucial aspect to determine is the amount of drug encapsulated. This needs to be determined via an accurate, sensitive and reproducible analytical method (Rafiei, Michel & Haddadi, 2015). Some studies measure the amount of drug encapsulated by UV-VIS spectroscopy (Dhankar *et al.*, 2011; Poojari, Srivastava & Panda, 2015), others utilise HPLC methods (Danhier *et al.*, 2009; Torne *et al.*, 2010; Eloy *et al.*, 2017). The concentration of total CA4 in the TA LOND samples in this project was initially measured by UV-VIS spectroscopy following purification as this was used to remove excess lipids and any unencapsulated drug.

The observed variability between the different preparations of LONDs in terms of %EE of CA4 was potentially caused by the water solubility of triacetin (70 g/L), resulting in the possible escape of the oil plus CA4 into the aqueous phase before or during dialysis and cross-filtration. Prep. number 6 (Table 3.1) in particular had a very high %EE compared to previous preparations. As double the concentration of CA4 was used, this potentially lead to the formation of unencapsulated drug agglomerates. These agglomerates would have been unable to pass through the dialysis membrane and therefore, remained in the TA LOND solution resulting in the high %EE (Personal communications with Dr Victoria Mico, School of Physics and Astronomy, University of Leeds). A white precipitate was observed in the sample after a few hours that was initially thought as the lipids but further investigations showed that this contained approximately 80% of the total CA4 which suggested poor encapsulation and/or retention (Personal communications with Dr Victoria Mico, School of Physics and Astronomy, University of Leeds).

CA4 has been incorporated in a number of DDS such as nanocells, liposomes, nanocapsules, dedrimers and micelles (Sengupta *et al.*, 2005; Nallamothu *et al.*, 2006a; Wang & Ho, 2010; Zhang *et al.*, 2010, 2011; Dai *et al.*, 2012; Yang *et al.*, 2012; Su *et al.*, 2014). CA4 in most of these DDS was incorporated into the lipid shell with %EE reported between 70-80% (Zhang *et al.*, 2010; Dai *et al.*, 2012; Su *et al.*, 2014). The mean size of CA4 TA LONDs was 260 nm with specifically prep. 6 being 394 nm, these were bigger than previously reported CA4 NPs which had size ranges between 20-200 nm measured by DLS (Zhang *et al.*, 2010; Yang *et al.*, 2012; Su *et*

al., 2014). The size differences between CA4 TA LONDs and other CA4 nanovehicles are due to the use of different surfactants, core material and production methods. NP size greatly influences their uptake, biodistribution and clearance and an ideal NP size for cancer therapy is reported to be between 70 to 200 nm (Gaumet *et al.*, 2008). Although, CA4 TA LONDs could enter the tumour endothelium as the fenestrations present in tumour vasculature can be up to 2000 nm, the large diameter of these LONDs could potentially lead to them being trapped in organs such as the spleen and lungs (Gaumet *et al.*, 2008).

3.7.2 *In vitro* evaluation of CA4 delivery by TA LONDs

The next stage following TA LOND production and characterisation was *in vitro* evaluation of CA4 delivery to cells by TA LONDs. It should be noted that the precise mechanisms of uptake and/or potential release of LONDs into cells were not studied at this stage. Therefore, disruption of MTs by the CA4 payload was used as an indicator for drug release and/or uptake.

In vitro work using CA4P has shown that MT disruption occurs within the first 30 min of exposure of HUVECs to CA4P (Kanthou & Tozer, 2002). A 2 h incubation period was used to allow for any potential delayed responses by the TA LONDs, which resulted in MT disruption characteristic of depolymerised MTs uniformly staining the cytoplasm (Figure 3.2). Encapsulating CA4 in TA LONDs did not appear to enhance the MT disruption caused by CA4 when compared to a free drug control (CA4 in DMSO) at the same concentration. Poojari *et al.,* (2005) have reported that encapsulating CA4P in PEGylated polymeric NPs enhanced the MT disruption caused by CA4P when compared to free CA4P (Poojari, Srivastava & Panda, 2015). Unlike in this study, they treated human liver cells continuously for 24 h with 15.2 nM of CA4P polymeric NPs.

Initial work showed that CA4 TA LONDs caused the same effects as free CA4, however, further investigations using different concentrations of CA4 TA LONDs revealed some differences. Free CA4 in DMSO caused depolymerised MTs to uniformly immunostain the cytoplasm at concentrations ≥ 20 nM consistent with previous reports (Kim, Peshkin & Mitchison, 2012) while CA4 TA LONDs caused this at concentrations ≥ 100 nM. These differences indicated the potential that CA4 was not being released by the TA LONDs sufficiently and this was only evident at lower concentrations.

The ability of CA4 TA LONDs to cause the characteristics of mitotic catastrophe following a continuous exposure for 24 h was studied. The results confirmed that CA4 TA LONDs like free CA4 in DMSO lead to cells with multiple nuclei, micronuclei and enlarged nuclei as previously reported for CA4P (Nabha *et al.*, 2002; Kanthou *et al.*, 2004). The *in vitro* data demonstrated that encapsulating CA4 in TA LONDs altered the ability of CA4 to cause MT disruption at lower concentrations potentially due to poor release when compared to free drug, while following a continuous exposure CA4 TA LONDs caused the characteristics of mitotic catastrophe.

3.7.3 On-chip single step production of thMBs with CA4-TA LONDs and their *in vivo* evaluation

CA4 TA LONDs were attached to thMBs to increase drug delivery and to enable the controlled and targeted release of CA4 only to areas exposed to US such as the tumour region. The US MI was 0.2, which is considered safe (Chowdhury, Lee & Willmann, 2017). The targeting ligand that was chosen and incorporated in the construct was VEGFR2 which is overexpressed during the process of angiogenesis. A VEGFR2 contrast agent (BR55) has been used successfully for the molecular imaging of tumour angiogenesis (Pochon *et al.*, 2010). SW480 human CRC cells were used to produce xenografts, previous reports have shown that SW480 xenografts and human clinical samples express 60% VEGFR2 positive blood vessels (Patten *et al.*, 2010).

SW480 tumour bearing mice were therefore administered with thMBs-CA4 TA LONDs and free CA4 in TA to investigate differences in *in vivo* biodistribution at early and late time points. The dose used was based on the maximum number of CA4 TA LONDs that could fit around a MB and was also dependent on the initial encapsulation of CA4 in the LONDs. Previous *in vivo* work with CA4 and CA4P have used doses 20 to 40 times higher (Grosios *et al.*, 1999).

As a secondary aim to *in vivo* biodistribution, tumour histology was used to investigate any potential enhancement of effect by the CA4 payload when delivered by thMBs in contrast, to free drug. Histological assessment of treated tumours showed evidence of haemorrhage which was not associated with necrosis and no differences were observed between the groups. 24 h post CA4P administration of 20 times the dose used in this study, resulted in severe central necrosis with only a small viable rim of tumour cells (Dark *et al.*, 1997; Griggs *et al.*, 2001). Similar data reported that following i.p. administration of CA4 (dissolved in 10% DMSO/oil combination at 150 mg/kg), haemorrhagic necrosis was apparent at 2 h post-treatment with

extensive necrosis by 24 h (Grosios *et al.*, 1999). Central haemorrhagic necrosis with only a viable rim of tumour cells, 24 h post-treatment with CA4P were also reported for SW1222 tumour xenografts (El-Emir *et al.*, 2005). These effects were due to the almost complete reduction in vascular perfusion associated with severe haemorrhage induced by CA4P 1 h post-injection (Chaplin, Pettit & Hill, 1996; Dark *et al.*, 1997; Tozer, Kanthou & Baguley, 2005). As a consequence of this, the central regions of tumours were deprived of oxygen and nutrients resulting in cell death while cells in the tumour periphery acquire a nutritive supply from nearby normal blood vessels (Chaplin & Hill, 2002).

Haemorrhage and the anti-vasculature effects of CA4P are often associated with a reduction in blood vessel number. In this study, no reduction in the number of tumour associated blood vessels was observed at any time point between the two groups tested. Previous work with CA4P, using approximately 20 and 160 times higher the dose showed a significant reduction in the number of blood vessels, 24 and 48 h post-treatment (Nabha *et al.*, 2001). However, they did report that after 48 h an increase in blood vessels number consistent with tumour recovery reports following treatment with CA4P was observed (Nabha *et al.*, 2001). Potentially the dose used in this study was too low to cause any reduction in MVD.

CA4P following i.v. administration was distributed throughout the body (heart, intestine, lungs, liver and spleen) as studied in rats (Xu *et al.*, 2012). Excretion of CA4 is mainly through urine as CA4G (Rustin *et al.*, 2003). The primary aim of this study was to investigate whether delivering thMBs with CA4 TA LONDs improved the biodistribution of CA4 and increased intratumoural delivery compared to free CA4 in TA. Variations in the PK of the two delivered agents was expected due to the different administration routes i.v. vs i.p.. I.v. allows for 100% of the drug to be in the bloodstream while drugs administered i.p. could potentially undergo hepatic metabolism before reaching the bloodstream (Turner *et al.*, 2011).

In order to undertake the PK study, an LC-MS/MS method was developed specifically for the detection of CA4 and its main metabolite CA4G. A gradient method in positive ionisation mode with a total run time of 16 min was initially developed and this was further optimised to achieve better separation to a total run time of 25 min. The LOD and LOQ was 10 ng/mL compared to a previously reported LOD for CA4 using LC-MS/MS which was 5 ng/mL (Wang *et al.*, 2009). This difference may be explained by different instruments used, mobile phases or method (ionisation mode, run time).

The developed and validated method was applied to the study where, surprisingly no CA4 or CA4G was detected in plasma, tumour or liver tissues tested at the very early time points. This could be explained by rapid clearance < 1 h which would be plausible for free CA4 as studies in mice have shown a very rapid half-life in plasma approximately 15 to 35 min (Tozer *et al.*, 1999; Kirwan *et al.*, 2004). Due to the low dose administered (4.9 mg/kg), another plausible explanation is that any CA4 or CA4G present was below the LOD. This further suggested that CA4 was potentially free and not encapsulated in TA LONDs, leading to its rapid metabolism and elimination.

3.7.4 Study limitations

The semi-quantitative analysis of MT lengths had some limitations, this technique measured MTs in five cells per FOV (five in total) following one biological replicate as the effect of CA4 TA LONDs and free CA4 on the MTs was predicted and expected. The process of measuring individual MTs using *Image J* was time consuming, in the future other more efficient and less time consuming methods for measuring the effects of CA4 in LONDs or free on MTs would be preferred. Methods utilising high-content imaging systems such as the Operetta fluorescent microscope could be used to measure changes in cellular morphology following MT depolymerisation (Martin *et al.*, 2014).

The lack of a free-drug control hindered the study as it was difficult to draw any conclusions seen in the histology of tumours. The two treatment groups had no histological differences and the lack of a control resulted in the lack of evidence to show that the effects caused were due to the treatment. However, the primary aim of the present study was to investigate differences in drug biodistribution and histology was a secondary aim.

The method for assessing MVD using “hot spots” had some limitations as the areas within the tumour stroma were in most cases the ones with the greatest expression of CD31 positive vessels and therefore scored. To improve the quantification, a specific macro in *Image J* in the future could be designed to assess MVD in the whole tumour section or to delineate and exclude areas of the stroma in order to assess MVD only in tumour cells.

3.7.5 Conclusions

Although TA LONDs encapsulating CA4 were successfully prepared, the *in vitro* data showed that potentially CA4 was not fully released or taken up into the SVR cells, in

contrast the *in vivo* data pointed towards CA4 particularly in prep. number 6 leaking from the LONDs or even potentially being free in the LOND solution due to the formation of drug agglomerates. *In vitro* assays utilising dialysis have been used to quickly study drug leakage from liposomes and micelles (Nallamothu *et al.*, 2006a; Wang *et al.*, 2010). Briefly, this is performed by placing a dialysis cassette with an aliquot of liposome or NPs of interest and further placing this in a beaker containing release medium (reverse osmosis water or PBS) and rotating the cassette (Nallamothu *et al.*, 2006a). At different time points sample is taken from the release medium and replaced to maintain equal volume, the sample is then analysed by HPLC or any analytical method used to quantify drug (Nallamothu *et al.*, 2006a).

Dr Victoria Mico (School of Physics and Astronomy, University of Leeds), later studied leakage of CA4 from LONDs in particular prep. number 5 (Table 3.1) using the dialysis method, her results showed that almost 100% of CA4 had leaked out from the LONDs (Mico, 2017). Further analysis by Dr Victoria Mico (School of Physics and Astronomy, University of Leeds) into the single step production method for thMBs with CA4 TA LONDs showed that due to the high forces required for MB production this resulted in destabilisation of the LOND structure (Mico, 2017). In light of these limitations both the LOND structure and the production of thMBs with LONDs were refined.

Chapter 4

Tripropionin LONDs: Characterisation and *in vitro* evaluation

4.1 Introduction

The production of TA LONDs demonstrated that the novel LOND structure was capable of delivering a drug, in this case CA4, *in vitro*. However, stability and solubility issues regarding the structure and the TA oil used potentially caused the rapid disassembly of the particle and subsequent release of CA4 into the solution. Therefore, CA4 did not benefit by encapsulation in TA LONDs. The aim next was to firstly refine the LOND structure by substituting the TA oil core to a less water soluble oil, TPP and to increase the stability and rigidity of the shell. CA4 TPP LONDs were produced and following this the aim was to evaluate CA4 release and/or uptake from TPP LONDs *in vitro*.

4.2 CA4 TPP LONDs: Physical and chemical characterisation

TPP LONDs with and without CA4 were kindly produced and characterised by Dr Victoria Mico (School of Physics and Astronomy, University of Leeds). CA4 was soluble in TPP, which is structurally similar to TA however is less water soluble 0.003 g/L at 37°C and has a *logP* value of 1.7 (Figure 4.1) (National Center for Biotechnology Information, 2005). TPP is used as a food flavouring agent (National Center for Biotechnology Information, 2005). The LONDs produced with TPP were stabilised with DSPC, cholesterol, DSPE-BPEG$_{2000}$ in a 75:20:5 molar ratio % and 0.1 mol% Attto590-DOPE was added for fluorescence imaging when required. This monolayer shell composition has been used previously to stabilise nanoemulsions (Hak *et al.*, 2012, 2015). POPC used previously in TA LONDs was substituted to DSPC. DSPC has a higher transition temperature 55°C than POPC which is -2°C (Avanti Polar Lipids Inc., 2016). The transition temperature is the temperature at which phospholipids transit from a gel to a liquid phase (Li *et al.*, 2014). The higher transition temperature of DSPC, means that at room temperature it is in a gel phase and as a result diffuses slower into the LOND shell subsequently this increases the rigidity of the shell and therefore reduces the leakage of TPP (Li *et al.*, 2014; Mico, 2017). In addition cholesterol in the shell reduces the permeability of LONDs and improves their stability as it induces a dense packing of the phospholipids by reducing the area per phospholipid (Bozzuto & Molinari, 2015). Cholesterol induces local ordering of the phospholipid acyl tails, these then are more extended causing the membrane to condense laterally and thicken to fit the extended tails (Olsen *et al.*, 2013).

A

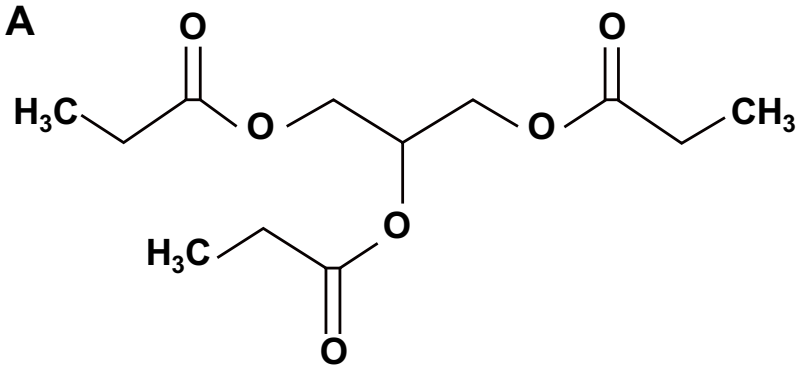

B

Chemical and physical properties of Tripropionin	
Physical characterisation	Oily liquid
Molecular formula	$C_{12}H_{20}O_6$
LogP	1.7
Solubility in water (37°C)	0.003 g/L

Figure 4.1 Chemical and physical properties of tripropionin.

(A) Chemical structure of TPP. (B) Chemical and physical properties of TPP. Details taken from National Center for Biotechnology Information, 2005.

A total of four prep. of TPP LONDs were produced using high pressure homogenisation, three encapsulating CA4 (prep. numbers 7, 8 and 10) and one without CA4 (prep. number 9). These were characterised in terms of size, number/mL and %EE for CA4 (Table 4.1). Using the previously developed LC-MS/MS method (section 3.6.2) the concentration of CA4 in the LOND solution was measured in prep. numbers 7, 8 and 10 and compared to UV-VIS spectroscopy. The PDI was lower than 0.2 (Mico, 2017). The mean size of LONDs was 96 ± 10 nm by DLS and 89 ± 11 by NanoSight with a mean concentration of $1.5 \times 10^{14} \pm 4.25 \times 10^{13}$ per mL measured by NanoSight. Purification by filtering through a 0.22 *μ*m filter was difficult with TPP LONDs due to the increased rigidity of the shell (Dr Victoria Mico, School of Physics and Astronomy, University of Leeds, personal communication) however, cross-filtration was performed for prep. number 7 and dialysis was performed for prep. number 10. To ensure sterility of TPP LONDs the samples were incubated with culture media to check for the presence of contaminants such as bacteria. If bacteria were present the LOND sample was discarded and not used for any further analyses, the LONDs presented in this study were all free from contaminants. The total concentration of CA4 in the LOND solution measured by UV-VIS spectroscopy was 733 *μ*g/mL, 1270 *μ*g/mL and 1700 *μ*g/mL for prep. numbers 7, 8 and 10 respectively by LC-MS/MS the concentration of CA4 was 720 *μ*g/mL, 1300 *μ*g/mL and 935 *μ*g/mL for prep. numbers 7, 8 and 10 respectively (Table 4.1). The calibration curves used to extrapolate the concentration of CA4 in TPP LONDs by LC-MS/MS in prep. numbers 7, 8 and 10 are shown in Appendix B, Figure B.1. It should be noted that the concentration of CA4 measured by LC-MS/MS was used for any drug related calculations.

The difference in CA4 concentration measured by UV-VIS spectroscopy and LC-MS/MS in prep. number 10 was assumed to be a loss through dialysis. The %EE of CA4 for prep. numbers 7, 8 and 10 was 41%, 74% and 53% respectively (Table 4.1). The stability of CA4 TPP LONDs was assessed by measuring size changes over time. It was observed that the LONDs were stable over six weeks when stored at 4°C (Mico *et al.*, 2017). CA4 TPP LONDs were incubated at 37°C for 2 h and no significant size changes were observed indicating the stability of these at physiological temperatures (Mico *et al.*, 2017). This is particularly important *in vivo*, as it indicates that CA4 TPP LONDs will have sufficient time to travel to the target site without destabilisation and premature release of CA4 (Mico *et al.*, 2017).

Table 4.1 Characterisation of TPP LONDs: Physical and chemical properties and drug encapsulation.

Prep. number	Lipids	Solvent	CA4 Stock used μg/mL	Concentration of LONDs x10^{14}/mL	Mean size (nm) DLS	Mean Size (nm) NanoSight	CA4 UV-VIS (μg/mL)	CA4 LC-MS/MS (μg/mL)	%EE	Purification technique	Evaluation (*in vitro/ in vivo*)
7	75mol% DSPC + 20mol% Cholesterol + 5mol% DSPE-BPEG$_{2000}$+ 0.1mol% Atto590 DOPE	Tripropionin	1750	1.7	86	99	733	720	41	N/D	*In vitro/ in vivo*
8			1750	1.2	89	77	1270	1300	74	Cross-filtration	
9			N/A	1.1	105	91	N/A	N/A	N/A	N/D	
10			1750	2	104	N/D	1700	935	53	Dialysis	
Mean				1.5 x10^{14}	96	89	1234	985	56		
SD				4.3 x10^{13}	10	11	485	293	17		

Four preparations of TPP LONDs, three encapsulating CA4 (prep. number 7, 8 and 10) were produced for *in vitro* and *in vivo* evaluation. 75mol% DSPC with 20mol% cholesterol, 5mol% DSPE-Biotinylated PEG$_{2000}$ and 0.1mol% Atto590 DOPE were used to produce the TPP LOND lipid monolayer shell. 0.1mol% Atto590 DOPE was incorporated for subsequent fluorescent tracing. CA4 was dispersed in TPP. The concentration of LONDs/mL and size was measured by NanoSight. The size was also measured by DLS for comparison. CA4 concentration in the TPP LOND solution were measured by UV-VIS and LC-MS/MS which was considered more accurate. % EE was calculated by dividing the concentration of CA4 provided by UV-VIS by the initial CA4 stock concentration x 100. Dialysis and cross-filtration were used for purification for the removal of excess lipid and/or unencapsulated CA4. All prep. were evaluated *in vitro* and *in vivo*. N/A: not applicable; N/D: no data. All data used to compile this table except for LC-MS/MS were provided by Dr Victoria Mico (School of Physics and Astronomy, University of Leeds).

4.3 CA4 TPP LONDs disrupt endothelial and CRC cell MTs *in vitro*

CA4 TPP LONDs were assessed for the ability of the CA4 payload to cause MT disruption as an indicator of drug release and/or uptake. This was performed in two endothelial cell lines SVR and EA.hy926 and in SW480 human CRC cells. SW480 cells were used to assess the efficacy of CA4 TPP LONDs to cause MT disruption in a cancer cell line, as it has been observed that some cancer cells are more sensitive to CA4 treatment than endothelial cells (Ahmed *et al.*, 2003). All cell lines were treated for 2 h to allow potential slow release and/or uptake of CA4 TPP LONDs.

IF staining of *β*-tubulin in untreated SVR, EA.hy926 and SW480 cells Figure 4.2 A, Figure 4.3 A and Figure 4.4 A respectively showed filamentous MTs spreading throughout the cytoplasm. In contrast, the results shown in Figure 4.2 B, Figure 4.3 B and Figure 4.4 B for SVR, EA.hy926 and SW480 cells respectively confirmed MT disruption following treatment with 10 *μ*M of CA4 TPP LONDs. MT disruption was characteristic of a uniformly stained cytoplasm from tubulin that had dispersed as a result of MT depolymerisation. 10 *μ*M CA4 dissolved in DMSO or TPP was used as a free drug control, and resulted in MT disruption in all three cell lines tested, characterised by the same uniformly stained pattern observed with 10 *μ*M CA4 TPP LONDs (Figure 4.2 C & D, Figure 4.3 C & D and Figure 4.4 C & D for SVR, EA.hy926 and SW480 respectively).

The observed *β*-tubulin staining pattern in Figure 4.3 B of tubulin dispersed throughout the cytoplasm as a result of MT depolymerisation in EA.hy926 cells however had a “star-like” pattern at the cell periphery. Touil *et al.,* (2009) observed a “star-like” pattern when EA.hy926 were treated with an inhibitor of actin polymerisation (Touil *et al.*, 2009). A similar pattern referred to as bleb or blebbing was reported for actin cell surface protrusions observed in endothelial cells treated with CA4P (Tozer *et al.*, 2002). This pattern was also evident in SW480 cells (Figure 4.4 B and C).

TPP alone did not cause any MT disruption in any of the three cell lines tested and showed the normal pattern of MTs filaments spreading throughout the cytoplasm (Figure 4.2 E, Figure 4.3 E and Figure 4.4 E, SVR, EA.hy926 and SW480 respectively). The no primary antibody controls had minimal background fluorescence in all three cell lines, which validated the specificity of the *β*-tubulin

primary antibody (Figure 4.2 F, Figure 4.3 F and Figure 4.4 F for SVR, EA.hy926 and SW480 respectively).

CA4 TPP LONDs caused MT disruption within the 2 h treatment time frame used. However, previous reports have shown that the effect of CA4P on MTs occurs within 30 min of drug exposure (Kanthou & Tozer, 2002). Therefore, the next stage of the CA4 TPP LOND *in vitro* evaluation process was to assess the time taken for CA4 TPP LONDs to cause MT disruption.

IF staining of β-tubulin after 30 min exposure of SVR cells to 10 μM CA4 TPP LONDs caused MT disruption with depolymerised MTs staining the cytoplasm in a perforated pattern (Figure 4.5 B, white open arrows). Free CA4 in TPP at 10 μM caused the same perforated pattern in SVR cells with some residual MTs still present following the 30 min exposure (Figure 4.5 C, white arrows). Subsequent experiments with different CA4 TPP LONDs prep. numbers 8 and 10 showed that these retained the ability to cause MT disruption after 30 min of exposure even at the lower concentration of 0.1 μM used with prep. number 10, without any evidence of a perforated staining pattern, suggesting that this was unrelated to treatment (Figure 4.6).

4.4 CA4 TPP LONDs cause a concentration dependent MT disruption

10 μM and 0.1 μM CA4 TPP LONDs caused MTs to depolymerise and tubulin to disperse throughout the cytoplasm giving a uniform staining pattern on IF, which was evident within 30 min of treatment. To assess if CA4 TPP LONDs had a concentration dependent effect on MT disruption SVR cells were treated with escalating concentrations of CA4 TPP LONDs for 2 h. Lower than 10 nM concentrations were used as CA4P has been shown to cause a decrease in polymerised tubulin and/or begin to depolymerise at concentrations as low as 1 nM (Galbraith *et al.*, 2001; Kanthou & Tozer, 2002).

Morphological assessment of the IF stained β-tubulin images showed that 2, 4 and 8 nM of CA4 TPP LONDs did not cause any change to the filamentous structure of MTs when compared to untreated SVR cells (Figure 4.7 A-C). As the same pattern of β-tubulin staining was observed for 2, 4 and 8 nM CA4 TPP LONDs only 2 and 8 nM representative images are shown, for the 4 nM CA4 TPP LONDs representative image see Appendix B, Figure B.2.

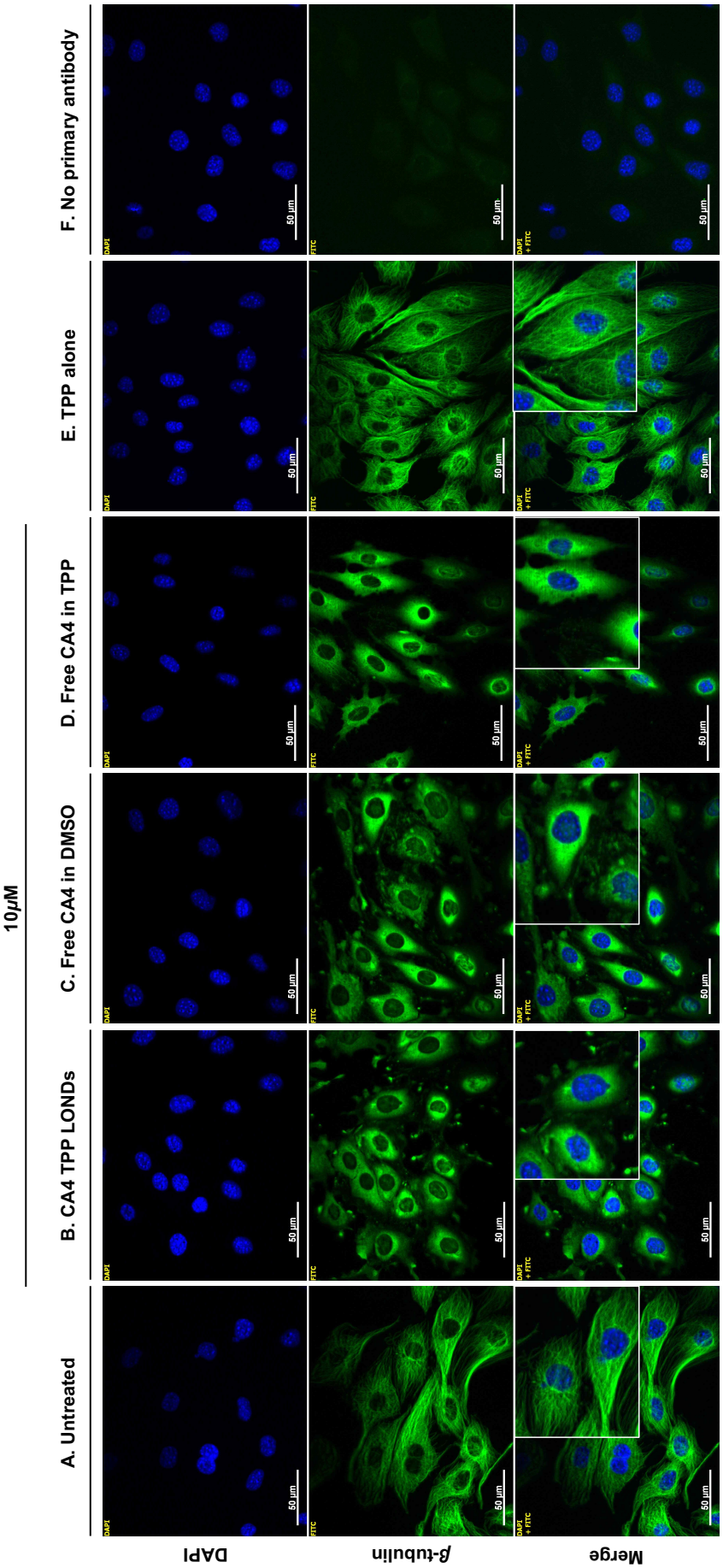
10μM
A. Untreated
B. CA4 TPP LONDs
C. Free CA4 in DMSO
D. Free CA4 in TPP
E. TPP alone
F. No primary antibody
DAPI
β-tubulin
Merge
50 μm

Figure 4.2 CA4 TPP LONDs cause MT disruption in SVR cells.

To assess the efficacy of CA4 TPP LONDs at causing MT disruption SVR cells cultured in *μ*-slides (ibidi) were treated with 10 *μ*M of CA4 TPP LONDs, 10 *μ*M of CA4 dissolved in DMSO as a positive control, 10 *μ*M of CA4 dissolved in TPP was also used as second free drug control and to control for CA4 in TPP without the LOND shell. Free TPP alone was used as a control of the oil without CA4. All treatment groups were compared to untreated control cells. Following the 2 h at 37°C, cells were fixed, immunostained for *β*-tubulin using a mouse monoclonal anti-*β*-tubulin antibody and visualised using a biotinylated rabbit anti-mouse and FITC-labelled avidin. The slides were mounted with prolong Gold containing DAPI. (A) Untreated cells with long MT filaments. (B) 10 *μ*M of CA4 TPP LONDs resulted in MT disruption caused by the CA4 payload inhibiting tubulin polymerisation and subsequently causing MTs to depolymerise. The tubulin from depolymerised MTs appeared evenly dispersed throughout the cytoplasm leading to a uniformly stained pattern. (C) 10 *μ*M free CA4 in DMSO resulted in the same pattern described for CA4 TPP LONDs. (D) 10 *μ*M free CA4 in TPP also resulted in tubulin inhibition and depolymerised MTs stained uniformly throughout the cytoplasm. (E) No MT disruption observed for SVR cells treated with TPP alone. Inset images show magnified cells in panels A-E. (F) No primary antibody control showed minimal background indicating the specificity of the anti-*β*-tubulin antibody. Scale bars indicate 50 *μ*m. Prep. number 7 was used.

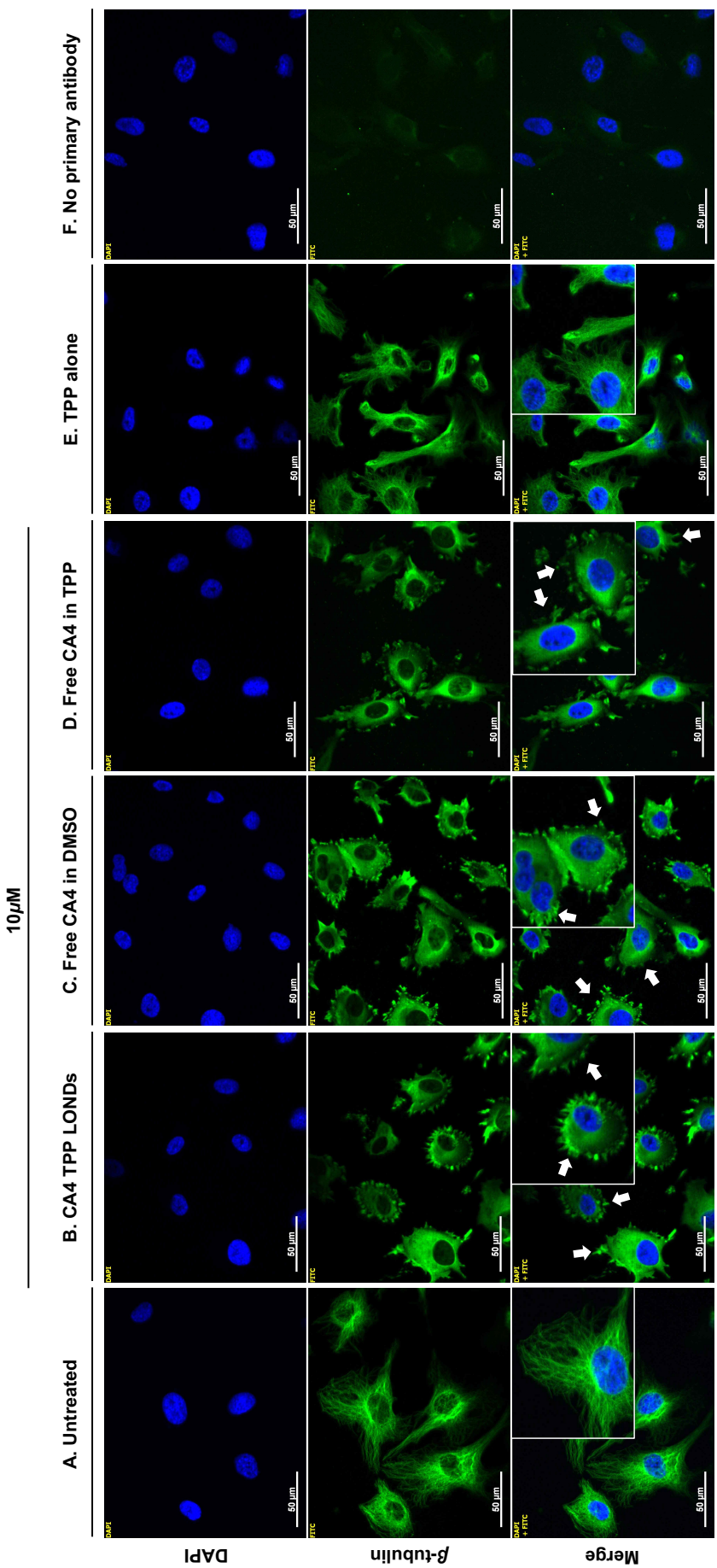
10μM
A. Untreated
B. CA4 TPP LONDs
C. Free CA4 in DMSO
D. Free CA4 in TPP
E. TPP alone
F. No primary antibody
DAPI
β-tubulin
Merge
50 μm

Figure 4.3 CA4 TPP LONDs cause MT disruption in EA.Hy926 cells.
To assess the efficacy of CA4 TPP LONDs at causing MT disruption, EA.hy926 cells were cultured in *μ*-slides (ibidi) and treated with 10 *μ*M CA4 TPP LONDs and 10 *μ*M of CA4 dissolved in DMSO as a positive control. 10 *μ*M of CA4 dissolved in TPP was also used as second free drug control and to control for CA4 in TPP without the LOND shell. Free TPP alone was used as a control of the oil without CA4. All treatment groups were compared to untreated control cells. Following the 2 h at 37°C, cells were fixed, immunostained for *β*-tubulin using a mouse monoclonal anti-*β*-tubulin antibody and visualised using a biotinylated rabbit anti-mouse and FITC-labelled avidin. The slides were mounted with prolong Gold containing DAPI. (A) Untreated EA.Hy926 cells with normal MT filaments. (B) 10 *μ*M CA4 TPP LONDs resulted in MT disruption caused by the CA4 payload inhibiting tubulin polymerisation and subsequently causing MTs to depolymerise. The tubulin from depolymerised MTs had dispersed throughout the cytoplasm and at the cell periphery formed “star-like” structures shown by the white arrows in the inset image of magnified cells (C) 10 *μ*M free CA4 in DMSO resulted in the same “star-like” pattern caused by inhibition of tubulin polymerisation and subsequent depolymerisation (white arrows, inset image of magnified cells). (D) 10 *μ*M free CA4 in TPP also resulted in the same patterns described for CA4 TPP LONDs and CA4 in DMSO (white arrows, inset image of magnified cells). (E) No MT disruption observed for EA.hy926 cells treated with TPP alone. (F) No primary antibody, with minimal background indicating the specificity of the anti-*β*-tubulin antibody. Scale bars indicate 50 *μ*m. Prep. number 7 was used.

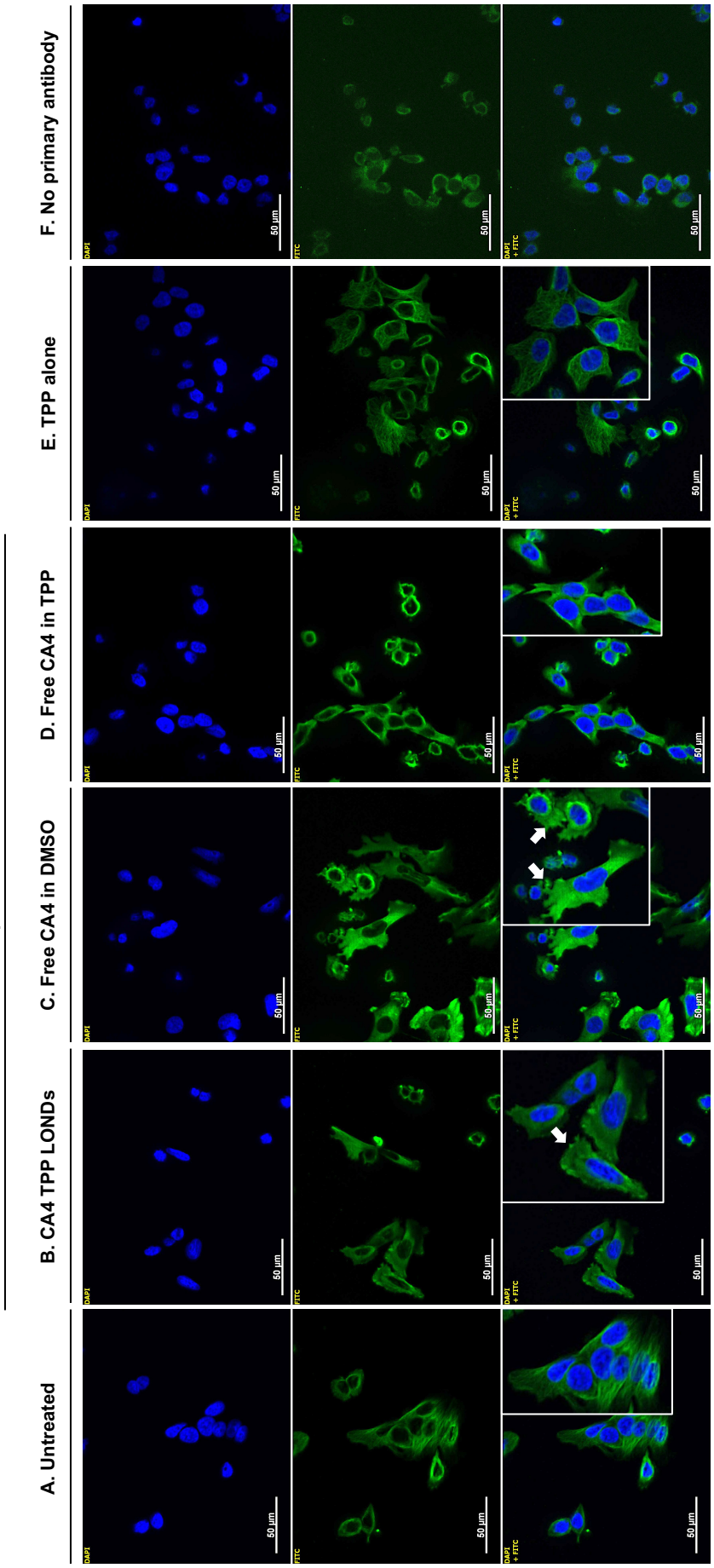
10μM
A. Untreated
B. CA4 TPP LONDs
C. Free CA4 in DMSO
D. Free CA4 in TPP
E. TPP alone
F. No primary antibody
DAPI
β-tubulin
Merge
50 μm

Figure 4.4 CA4 TPP LONDs cause MT disruption in SW480 cells.

To assess the efficacy of CA4 TPP LONDs at causing MT disruption, SW480 cells were cultured in *μ*-slides (ibidi) and treated with 10 *μ*M CA4 TPP LONDs and 10 μM of CA4 dissolved in DMSO as a positive control. 10 *μ*M of CA4 dissolved in TPP was also used as second free drug control and to control for CA4 in TPP without the LOND shell. Free TPP alone was used as a control of the oil without CA4. All treatment groups were compared to untreated control cells. Following the 2 h at 37°C, cells were fixed, immunostained for *β*-tubulin using a mouse monoclonal anti-*β*-tubulin antibody and visualised using a biotinylated rabbit anti-mouse and FITC-labelled avidin. The slides were mounted with prolong Gold containing DAPI. (A) SW480 control cells with MT filaments, the inset image shows magnified cells with this. (B) 10 *μ*M of CA4 TPP LONDs resulted in MT disruption caused by the CA4 payload inhibiting tubulin polymerisation. The staining pattern showed tubulin dispersed throughout the cytoplasm as a result of MT depolymerisation and formed “star-like” structures at the cell periphery, white arrow in inset image shows a cell with this pattern as an example. (C) 10 *μ*M free CA4 in DMSO resulted in the same “star-like” pattern caused by inhibition of tubulin polymerisation and subsequent depolymerisation (inset image, magnified cells, arrows showing the “star-like” pattern). (D) 10 *μ*M free CA4 in TPP caused MT disruption characteristic by a uniform staining fluorescence by tubulin dispersed in the cytoplasm as a result of MT depolymerisation. (E) No MT disruption observed for SW480 cells treated with TPP alone. (F) No primary antibody, showing minimal background from the secondary antibody. Scale bars indicate 50 *μ*m. Prep. number 7 was used.

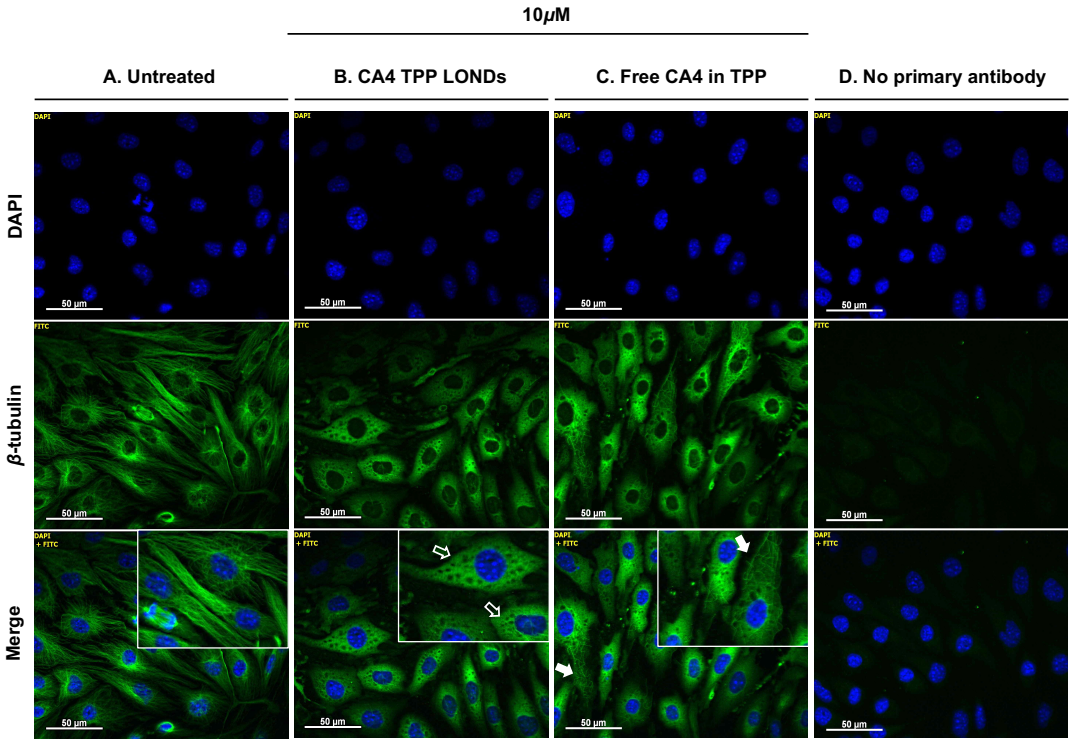

Figure 4.5 CA4 TPP LONDs cause MT disruption in SVR cells within 30 min of exposure.

To investigate the time at which CA4 TPP LONDs caused MT disruption, SVR cells cultured in *μ*-slides (ibidi) were treated with 10 *μ*M CA4 TPP LONDs for 30 min and with 10 *μ*M free CA4 in TPP as the positive control. SVR untreated were used as controls. Following 30 min at 37°C, cells were fixed, immunostained for *β*-tubulin using a mouse monoclonal anti-*β*-tubulin antibody and visualised using a biotinylated rabbit anti-mouse and FITC-labelled avidin. The slides were mounted with prolong Gold containing DAPI. (A) SVR control cells with untreated MTs. Inset image shows magnified cells. (B) 10 *μ*M of CA4 TPP LONDs resulted in MT disruption. A perforated pattern of depolymerised MTs with tubulin dispersed in the cytoplasm was observed as a result of tubulin inhibition (white open arrows, inset image of magnified cells). (C) Free CA4 in TPP caused MT disruption evident by the uniform stained cytoplasm by depolymerised MTs. Residual MTs were also observed (white arrows, inset image of magnified cells). (D) No primary antibody control, showing very minimal background staining, validating the specificity of the anti-*β*-tubulin antibody. Scale bars indicate 50 *μ*m. Prep. number 7 was used.

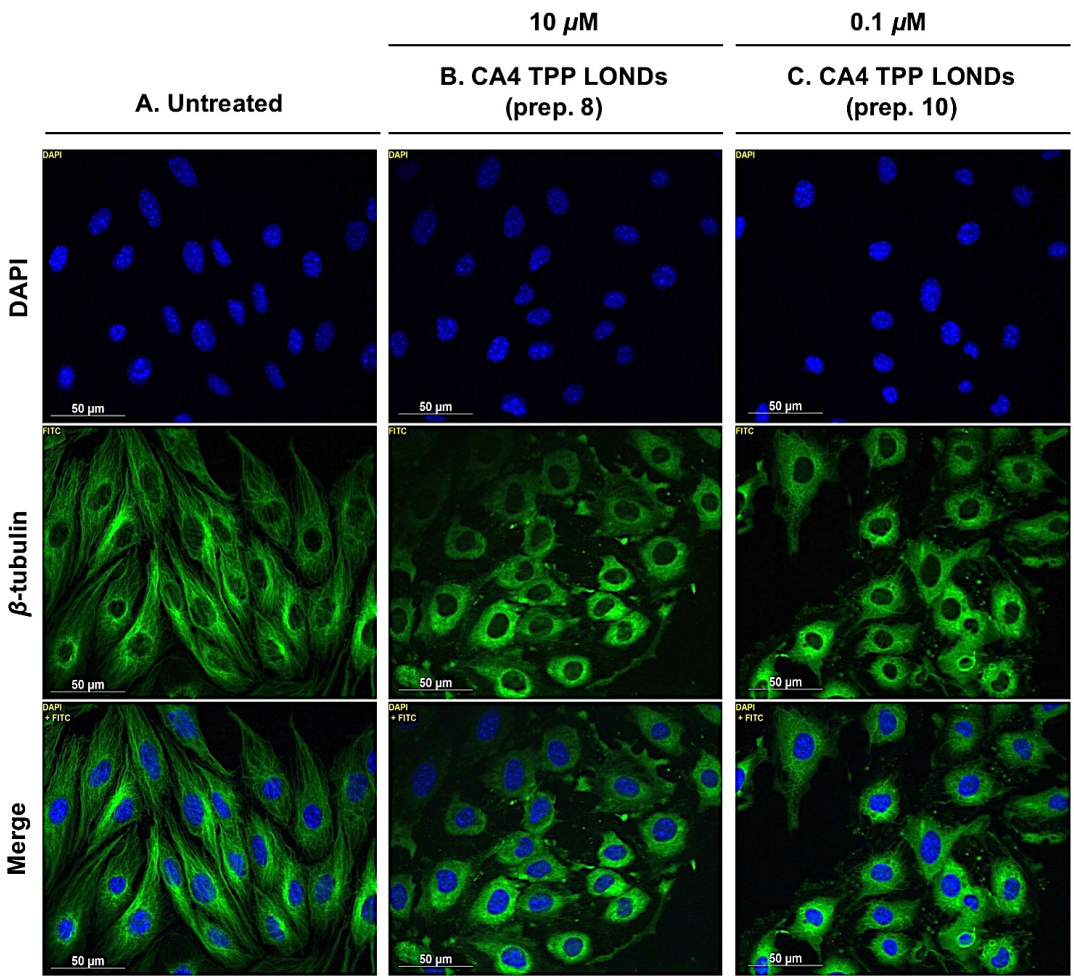

Figure 4.6 MT disruption within 30 min by different preparations of CA4 TPP LONDs.

SVR cells cultured in *μ*-slides (ibidi) were treated with 10 *μ*M of CA4 TPP LONDs for 30 min at 37°C. SVR untreated were used as controls. Following 30 min at 37°C, cells were fixed, immunostained for *β*-tubulin using a mouse monoclonal anti-*β*-tubulin antibody and visualised using a biotinylated rabbit anti-mouse and FITC-labelled avidin. The slides were mounted with prolong Gold containing DAPI. (A) SVR control untreated cells with normal MTs. (B) 10 *μ*M of CA4 TPP LONDs prep. number 8 resulted in MT disruption. (C) 0.1 *μ*M of CA4 TPP LONDs, prep. number 10 caused MT disruption. This MT disruption results in MT depolymerisation and tubulin dispersion throughout the cytoplasm uniformly staining it. Scale bars indicate 50 *μ*m.

At 20 and 10 nM, CA4 TPP LONDs caused the MTs to lose the radial filamentous structure and were tangled around the nuclei, a representative image of this pattern is shown in Figure 4.7 D (for 10 nM representative image see Appendix B, Figure B.2). Complete MT depolymerisation evident by the uniformly stained cytoplasm was caused after treatment of SVR cells with 40, 60 and 100 nM of CA4 TPP LONDs (Figure 4.7 E, white open arrows and Appendix B, Figure B.2 for 60 and 100 nM). SVR cells were also treated with free CA4 in TPP at 2 and 8 nM, morphological assessment of these showed no MT disruption (Figure 4.7 F and G).

To quantitate the response to CA4 TPP LONDs, MT lengths were measured using *Image J* (Figure 4.8 A). A total of 250 MTs were measured for untreated SVR cells and those treated with 2 and 8 nM CA4 TPP LONDs or free CA4 in TPP. 225 MTs were measured for 20 nM CA4 TPP LONDs, as 40 nM of CA4 TPP LONDs caused complete MT depolymerisation in SVR cells no MT filaments were measured and 0 *μ*m was used for graphical and statistical analysis. Although, SVR cells treated with 2 and 8 nM CA4 TPP LONDs did not show qualitatively any difference (Figure 4.7 B and C) a statistically significant reduction or abrogation of MT lengths was observed after treatment of SVR cells with 2, 8, 20 and 40 nM CA4 TPP LONDs ($p=0.024$ and $p<0.0001$, Mann-Whitney U test, two-tailed).

Free CA4 in TPP LONDs at 2 nM did not cause a significant reduction in MT lengths of treated SVR cells, however 8 nM did ($p<0.0001$, Mann-Whitney U test, two-tailed). Significant differences were also observed between the different concentrations of CA4 TPP LONDs and free CA4 in TPP (Figure 4.8 B). Using Spearman's correlation, a negative but statistically insignificant correlation was observed between CA4 TPP LONDs concentrations and MT lengths of SVR cells ($r=-1$, $p=0.083$) (Figure 4.8 C).

4.5 MT recovery following transient treatment with CA4 TPP LONDs

CA4 rapidly binds and dissociates from tubulin with a dissociation rate of 3.6 min at 37°C (Lin *et al.*, 1989). As a result of this rapid binding and dissociation, MT disruption and cellular disruption have been shown to recover following transient treatment with CA4P for 30 min with a 24 h recovery period (Galbraith *et al.*, 2001).

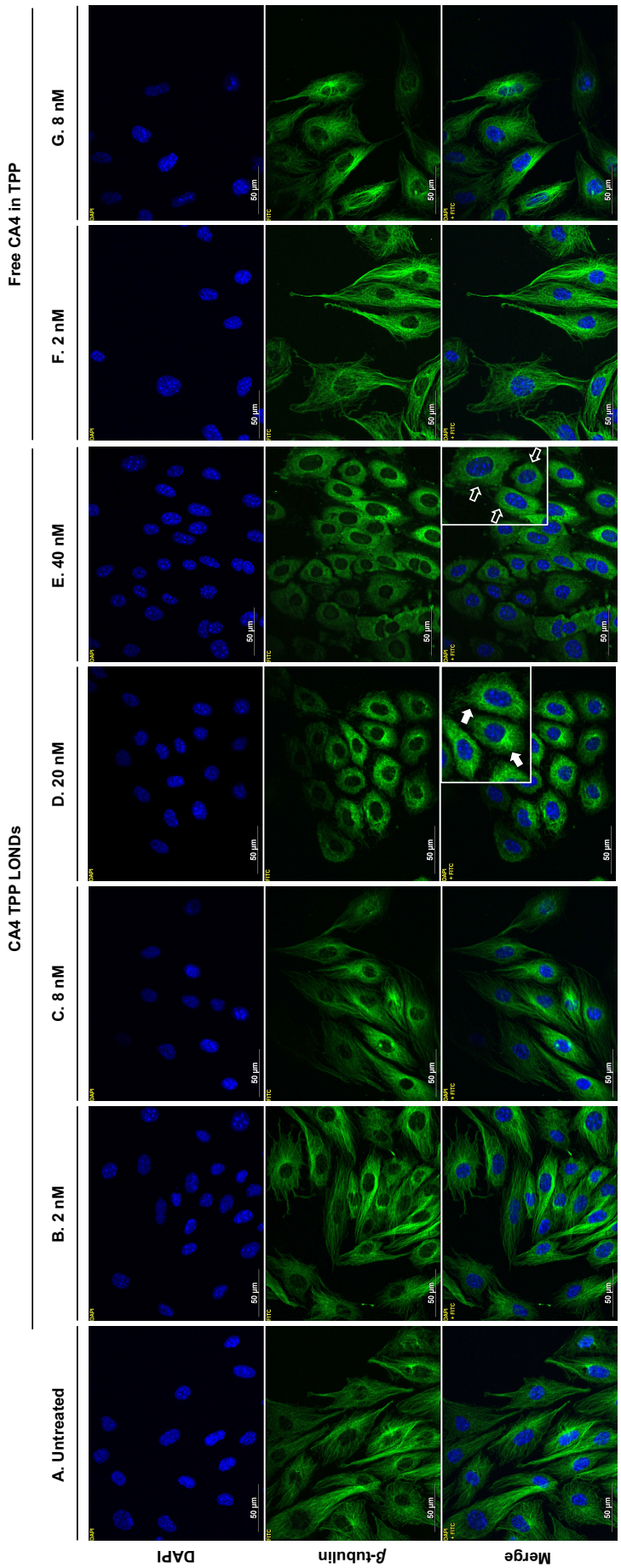
CA4 TPP LONDs
Free CA4 in TPP
A. Untreated
B. 2 nM
C. 8 nM
D. 20 nM
E. 40 nM
F. 2 nM
G. 8 nM
DAPI
β-tubulin
Merge
50 µm

Figure 4.7 CA4 TPP LONDs and Free CA4 in TPP MT disruption in SVR cells. SVR cells were treated with escalating concentrations of CA4 TPP LONDs, 2, 8, 20 and 40 nM and 2 and 8 nM of free CA4 in TPP for 2 h at 37°C. Following, cells were fixed, immunostained for *β*-tubulin using a mouse monoclonal anti-*β*-tubulin antibody and visualised using a biotinylated rabbit anti-mouse and FITC-labelled avidin. The slides were mounted with prolong Gold containing DAPI. (A) Untreated SVR cells with filamentous MTs. (B) SVR cells treated with 2 nM of CA4 TPP LONDs, MTs appeared to have MT filaments similar to untreated SVR cells. (C) SVR cells treated with 8 nM of CA4 TPP LONDs showed MTs with long filament structures as in untreated SVR cells. (D). Treatment with 20 nM of CA4 TPP LONDs showed evidence of shortening of the filamentous MTs at the distal ends at the cell periphery and tangled around the nuclei (white arrows). (E) 40 nM CA4 TPP LONDs had a uniformly stained cytoplasm from the tubulin dispersing as a consequence of depolymerised MTs (open white arrows). (F) SVR cells treated with 2 nM of free CA4 in TPP, appeared to have undisrupted MTs. (G) SVR cells treated with 8 nM of free CA4 in TPP did not show any evidence of MT disruption, as the MTs appeared as untreated. Scale bars indicate 50 *μ*m. Prep. number 8 was used.

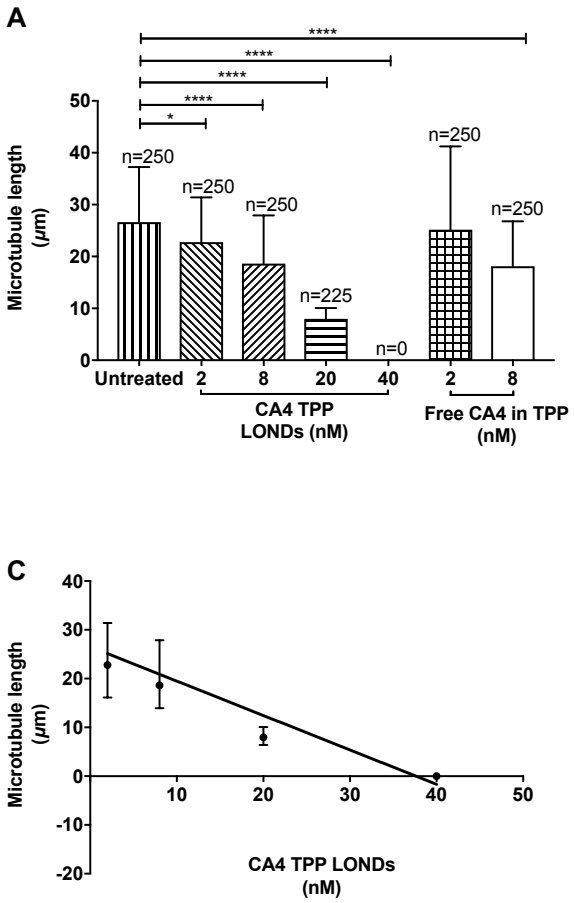

B

Statistical results: Mann-Whitney U test (two-tailed)		
Groups	Significant	P value
2 nM CA4 TA LONDs vs.		
8 nM CA4 TA LONDs	yes	p=0.0002
20 nM CA4 TA LONDs	yes	p<0.0001
40 nM CA4 TA LONDs	yes	p<0.0001
2 nM Free CA4 in TPP	yes	p=0.020
8 nM Free CA4 in TPP	yes	p<0.0001
8 nM CA4 TA LONDs vs.		
20 nM CA4 TA LONDs	yes	p<0.0001
40 nM CA4 TA LONDs	yes	p<0.0001
2 nM Free CA4 in TPP	yes	p<0.0001
8 nM Free CA4 in TPP	no	p=0.420
20 nM CA4 TA LONDs vs.		
40 nM CA4 TA LONDs	yes	p<0.0001
2 nM Free CA4 in TPP	yes	p<0.0001
8 nM Free CA4 in TPP	yes	p<0.0001
40 nM CA4 TA LONDs vs.		
2 nM Free CA4 in TPP	yes	p<0.0001
8 nM Free CA4 in TPP	yes	p<0.0001

Figure 4.8 CA4 TPP LONDs cause a concentration-dependent reduction in MT lengths.

(A) Fluorescent images were used to quantitate the MT disruption caused by treatment with escalating concentrations of CA4 TPP LONDs for 2 h at 37°C. The lengths of 250 MTs (10 MTs/cell in 5 cells per FOV, five FOV in total per condition) were measured using *Image J* from untreated SVR cells and SVR cells treated with 2 and 8 nM of CA4 TPP LONDs or SVR cells treated with 2 and 8 nM of free CA4 in TPP. A total of 225 MT lengths were measured from SVR cells treated with 20 nM CA4 TPP LONDs. 40 nM of CA4 TPP LONDs caused MTs to depolymerise and tubulin to disperse throughout the cytoplasm uniformly staining it, therefore no MT lengths were measured and 0 *μ*m was used to plot the graph. Data represent the median value from the measured MTs (n=1 biological replicate) and the error bars represent the interquartile range. * p=0.024. **** p<0.0001 calculated by Mann-Whitney U test (two-tailed). (B) Tabulated format of statistical analyses from comparing the different concentrations. (C) The relationship between MT lengths and CA4 TPP LOND concentration using Spearman's correlation showed a negative but statistically insignificant correlation between the two (r=-1, p=0.083, two-tailed). Data shows the median value and error bars interquartile range.

This recovery has also been observed *in vivo* as demonstrated by the rapid recovery of blood flow 24 h post-treatment (Dark *et al.*, 1997; Maxwell *et al.*, 1998; Murata, Overgaard & Horsman, 2001; Liu, Mason & Gimi, 2015). Concentrations > 40 nM CA4 TPP LONDs caused complete MT depolymerisation characterised by a uniformly stained cytoplasm within 30 min to 2 h of transient treatment (Figure 4.5 and Figure 4.7). The next stage in this work therefore focused on the ability of MTs to recover following a 2 h transient treatment with CA4 TPP LONDs followed by a 24 h recovery period. It was important to know if delivery of CA4 in a hydrophobic DDS such as LONDs delayed the recovery period of MTs as *in vivo* repeated injections could be administered prior to recovery to enhance the anti-tumour activity of CA4 TPP LONDs.

Qualitative analysis of IF stained *β*-tubulin images showed no differences in MT structures of untreated control SVR cells (Figure 4.9 A) and SVR cells treated with 55 and 100 nM of CA4 TPP LONDs for 2 h and then followed by recovery in drug-free media for 24 h (Figure 4.9 B and C, respectively). MT structures from SVR cells treated with free CA4 in TPP at 55 and 100 nM (Figure 4.9 D and E, respectively) appeared similar to untreated control SVR cells. These data point towards recovery of MTs from the disruptive effects of CA4 delivered by LONDs.

4.6 CA4 TPP LONDs cause cell cycle changes

The above data showed that transient treatment of endothelial cells and SW480 cells with CA4 TPP LONDs caused MT disruption. However, this MT disruption was reversible in SVR cells. Intratumoural retention of CA4 TPP LONDs through the EPR effect *in vivo* however, could potentially lead to a prolonged exposure of the tumour cells to CA4. Therefore, the next stages focused on a continuous exposure of cells to CA4 TPP LONDs and the ability of these to induce mitotic catastrophe and cell cycle changes.

IF staining of *β*-tubulin showed that cells treated for 24 h with 55 nM and 100 nM CA4 TPP LONDs or free CA4 in TPP had disrupted MTs characterised by dispersed tubulin throughout the cytoplasm as a result of MT depolymerisation and some cells also had residual MTs (Figure 4.10). Treated cells also showed characteristics of mitotic catastrophe, giant multinucleated cells and enlarged nuclei (Figure 4.10).

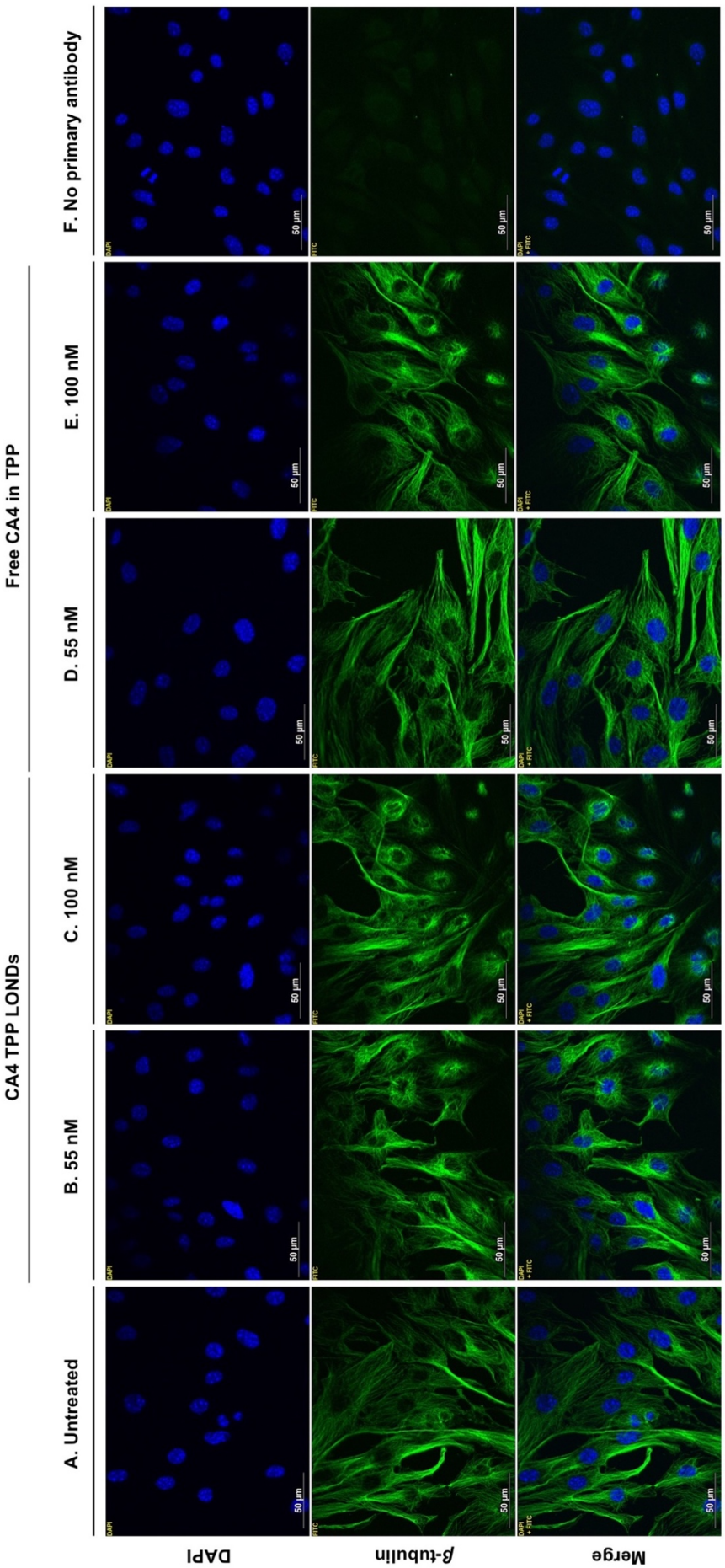
CA4 TPP LONDs
Free CA4 in TPP
A. Untreated
B. 55 nM
C. 100 nM
D. 55 nM
E. 100 nM
F. No primary antibody
DAPI
β-tubulin
Merge
50 µm

Figure 4.9 MT recovery following transient treatment with CA4 TPP LONDs.
To investigate the potential of MTs to recover following treatment with CA4 TPP LONDs, SVR cells were treated with 55 and 100 nM of CA4 TPP LONDs for 2 h at 37°C. After the 2 h treatment, cells were washed and incubated in drug-free media for 24 h. Untreated SVR cells were used as a control, while SVR cells treated with 55 and 100 nM of free CA4 in TPP were used as a positive control. Following 24 h recovery period at 37°C, cells were fixed, immunostained for β-tubulin using a mouse monoclonal anti-β-tubulin antibody and visualised using a biotinylated rabbit anti-mouse and FITC-labelled avidin. The slides were mounted with prolong Gold containing DAPI. (A) SVR untreated cells with filamentous MTs. (B) SVR cells treated with 55 nM of CA4 TPP LONDs (C) SVR cells treated with 100 nM of CA4 TPP LONDs. (D) SVR cells treated with 55 nM of free CA4 in TPP. (E) SVR cells treated with 100 nM of free CA4 in TPP. All treated SVR cells had MT filaments similar to untreated control SVR cells in A. (F) No primary antibody control. Scale bars indicate 50 μm. Prep. number 10 was used.

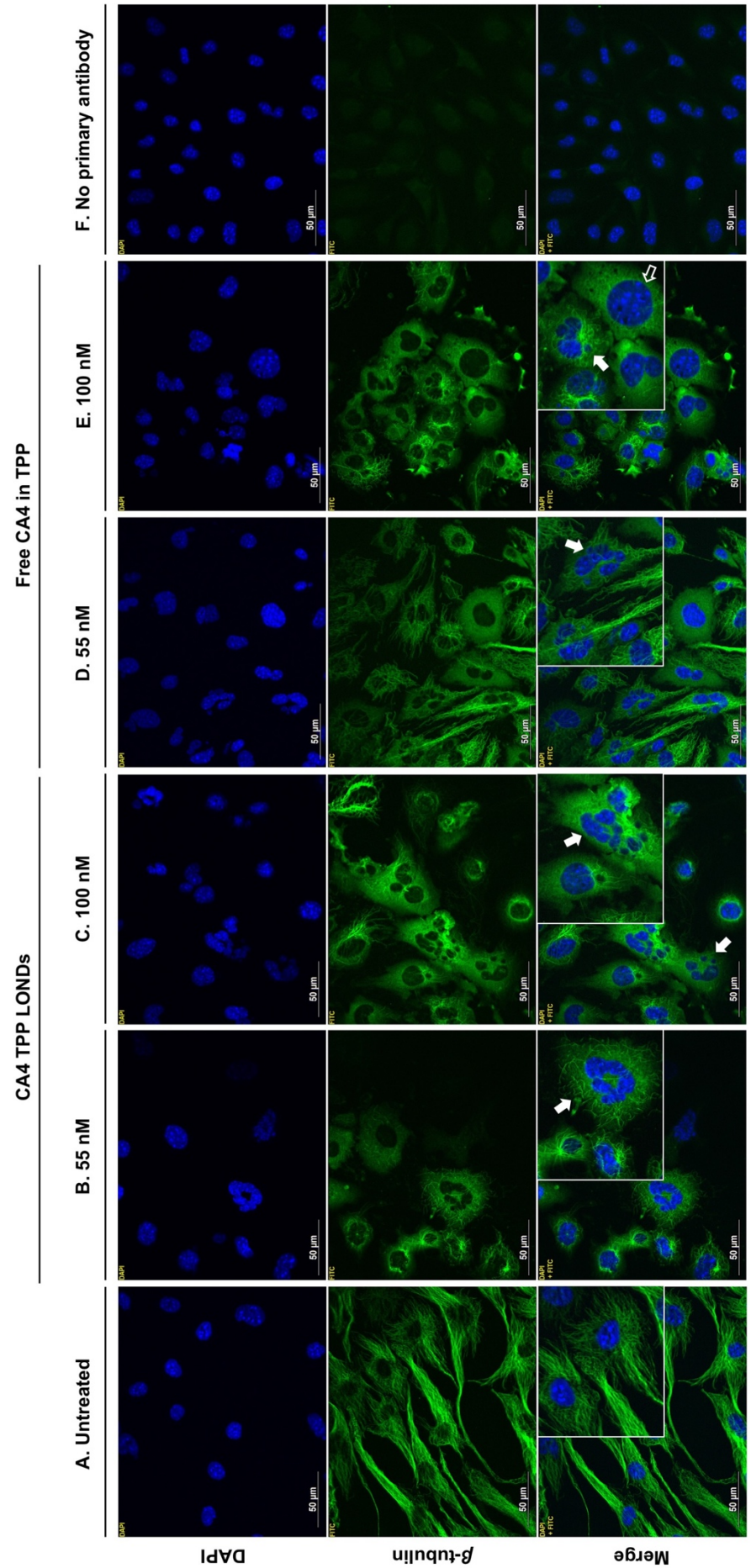
CA4 TPP LONDs
Free CA4 in TPP
A. Untreated
B. 55 nM
C. 100 nM
D. 55 nM
E. 100 nM
F. No primary antibody
DAPI
β-tubulin
Merge
50 µm

Figure 4.10 CA4 TPP LONDs cause cells to enter mitotic catastrophe.
To investigate the potential of CA4 TPP LONDs at causing mitotic catastrophe (cell death pathway, characterised by giant multinucleated cells), SVR cells were treated with 55 and 100 nM of CA4 TPP LONDs for 24 h at 37°C. Untreated SVR cells were used as a control, while SVR cells treated with 55 and 100 nM of free CA4 in TPP were used as a positive control. Following 24 h at 37°C, cells were fixed, immunostained for *β*-tubulin using a mouse monoclonal anti-*β*-tubulin antibody and visualised using a biotinylated rabbit anti-mouse and FITC-labelled avidin. The slides were mounted with prolong Gold containing DAPI. (A) SVR untreated cells with filamentous MTs and undisrupted nuclei. Inset image shows magnified cell. (B) SVR cells treated with 55 nM of CA4 TPP LONDs for 24 h, lead to disrupted MTs, tangled around the nuclei and giant multinucleated cells (white arrow, inset image of magnified cell). (C) 100 nM of CA4 TPP LONDs caused disrupted MTs, with tubulin dispersing in the cytoplasm and uniformly staining it as a result of MT depolymerisation. Some of these cells were giant with multiple nuclei (white arrows, inset image of magnified cell). Residual MTs were also observed. (D) 55 nM of free CA4 in TPP caused MT disruption in SVR cells with a number of residual MTs present, multiple nuclei were also observed in cells (white arrow, inset image of magnified cell). (E) SVR cells treated with 100 nM of free CA4 in TPP resulted in MT disruption (tubulin dispersing as a result of MT depolymerisation and forming a uniform fluorescence around the cells nuclei). Cells also had multiple nuclei (white arrows, inset image of magnified cell) and enlarged nuclei (white open arrow, inset image of magnified cell) characteristic of cells that have entered mitotic catastrophe. (F) No primary antibody, showed minimal background indicating the specificity of the anti-*β*-tubulin antibody. Scale bars indicate 50 *μ*m. Prep. number 10 was used.

Flow cytometry was used to examine the effect of CA4 TPP LONDs on the SVR cell cycle. As shown in Figure 4.11 A and Figure 4.12 A, CA4 TPP LONDs and free CA4 in DMSO both at 55 nM and 100 nM caused a statistically significant effect on the cell cycle, a G2/M phase arrest was induced. ≥ 78% of treated SVR cells were in the G2/M phase compared to 10% in the control group ($p<0.0001$, unpaired t-test). A G2/M phase arrest was not observed when SVR cells were treated with TPP LONDs alone. Statistical analyses are tabulated in Figure 4.12 B. Diploid analysis of the DNA content (Figure 4.11 A) showed that a proportion of cells treated with CA4 TPP LONDs or free CA4 in DMSO had entered a second cell cycle and were tetraploid (4N DNA). These were subsequently analysed using the polyploidy mode in the ModFitLT V3.2 software (Figure 4.11 B). ≥ 12% of SVR treated cells at both concentrations were tetraploid (4N DNA) (Figure 4.12 C).

Flow cytometry of SW480 cells showed that CA4 TPP LONDs and free CA4 in DMSO both at 55 nM and 100 nM continuous exposure for 24 h caused a G2/M phase arrest (Figure 4.13 A and Figure 4.14 A). Over 80% of SW480 cells treated with CA4 TPP LONDs and free CA4 in DMSO were in the G2/M phase compared to 25% in free drug control cells ($p<0.0001$, unpaired t-test). TPP LONDs alone did not cause any changes to the cell cycle. Statistical analyses are tabulated in Figure 4.14 B. Diploid analysis of the DNA content (Figure 4.13 A) showed that a proportion of cells treated with CA4 TPP LONDs or free CA4 in DMSO had entered a second cell cycle and were tetraploid (4N DNA). These were subsequently analysed using the polyploidy mode in the ModFitLT V3.2 software (Figure 4.13 B). The % of cells which were tetraploid (in the second G2/M phase) was determined and graphed in Figure 4.14 C. There was a statistically significant higher % of tetraploid SW480 cells following treatment with 100 nM CA4 TPP LONDs compared to 55 nM CA4 TPP LONDs ($p=0.0002$, unpaired t-test). In contrast, a higher % of tetraploid cells were observed in SW480 cells treated with 55 nM free CA4 in DMSO compared to 100 nM CA4 in DMSO ($p=0.0005$, unpaired t-test).

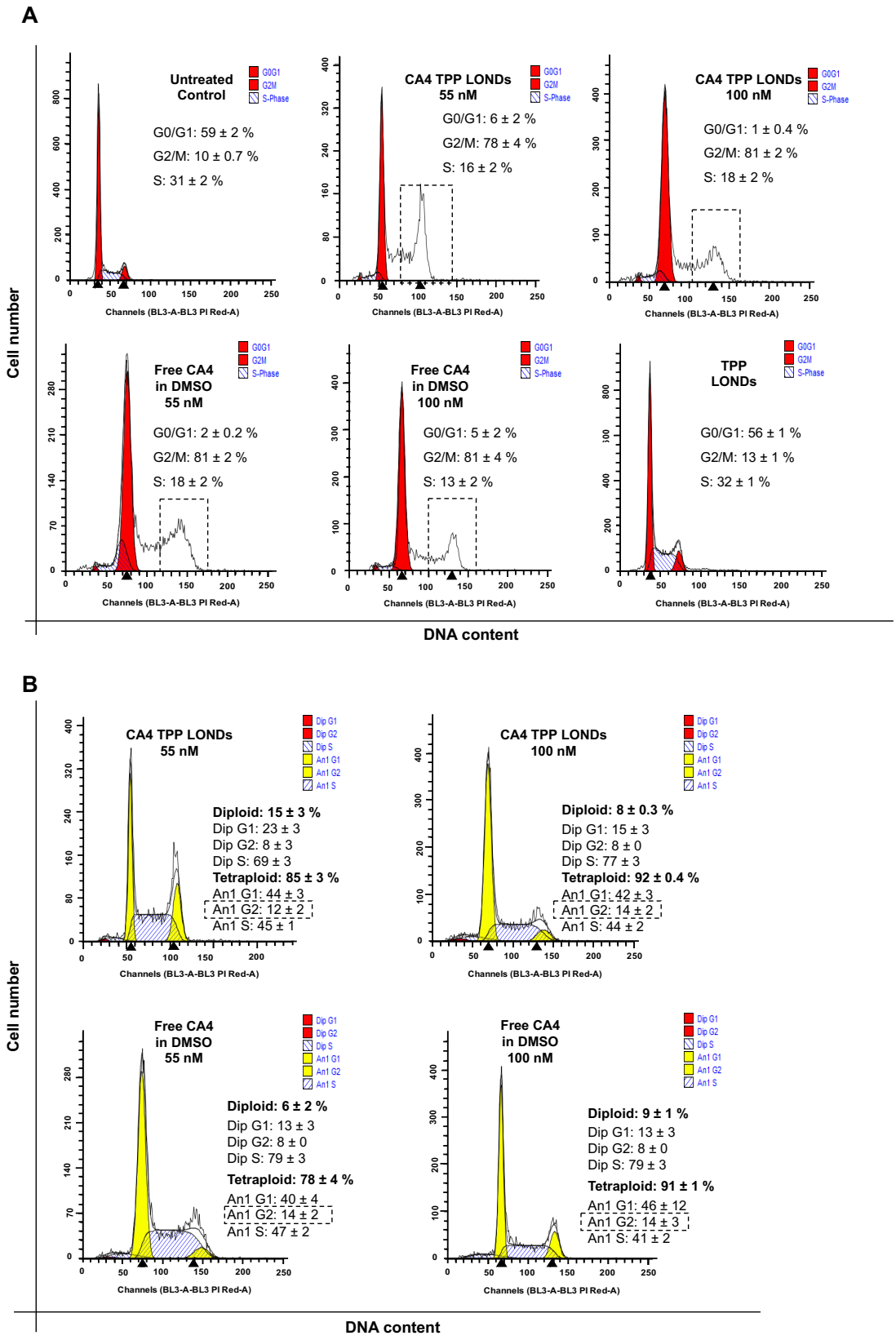
A
Cell number
DNA content
Untreated Control
G0/G1: 59 ± 2 %
G2/M: 10 ± 0.7 %
S: 31 ± 2 %
CA4 TPP LONDs 55 nM
G0/G1: 6 ± 2 %
G2/M: 78 ± 4 %
S: 16 ± 2 %
CA4 TPP LONDs 100 nM
G0/G1: 1 ± 0.4 %
G2/M: 81 ± 2 %
S: 18 ± 2 %
Free CA4 in DMSO 55 nM
G0/G1: 2 ± 0.2 %
G2/M: 81 ± 2 %
S: 18 ± 2 %
Free CA4 in DMSO 100 nM
G0/G1: 5 ± 2 %
G2/M: 81 ± 4 %
S: 13 ± 2 %
TPP LONDs
G0/G1: 56 ± 1 %
G2/M: 13 ± 1 %
S: 32 ± 1 %
G0G1
G2M
S-Phase
Channels (BL3-A-BL3 PI Red-A)
B
Cell number
DNA content
CA4 TPP LONDs 55 nM
Diploid: 15 ± 3 %
Dip G1: 23 ± 3
Dip G2: 8 ± 3
Dip S: 69 ± 3
Tetraploid: 85 ± 3 %
An1 G1: 44 ± 3
An1 G2: 12 ± 2
An1 S: 45 ± 1
CA4 TPP LONDs 100 nM
Diploid: 8 ± 0.3 %
Dip G1: 15 ± 3
Dip G2: 8 ± 0
Dip S: 77 ± 3
Tetraploid: 92 ± 0.4 %
An1 G1: 42 ± 3
An1 G2: 14 ± 2
An1 S: 44 ± 2
Free CA4 in DMSO 55 nM
Diploid: 6 ± 2 %
Dip G1: 13 ± 3
Dip G2: 8 ± 0
Dip S: 79 ± 3
Tetraploid: 78 ± 4 %
An1 G1: 40 ± 4
An1 G2: 14 ± 2
An1 S: 47 ± 2
Free CA4 in DMSO 100 nM
Diploid: 9 ± 1 %
Dip G1: 13 ± 3
Dip G2: 8 ± 0
Dip S: 79 ± 3
Tetraploid: 91 ± 1 %
An1 G1: 46 ± 12
An1 G2: 14 ± 3
An1 S: 41 ± 2
Dip G1
Dip G2
Dip S
An1 G1
An1 G2
An1 S
Channels (BL3-A-BL3 PI Red-A)

Figure 4.11 Cell cycle distribution of SVR cells following treatment with CA4 TPP LONDs and free CA4 in DMSO.

(A) ModFitLT V3.2 software results from diploid analysis, to obtain the % of cells in G2/M phase. SVR cells cultured in 12-well plates and treated with 55 and 100 nM CA4 TPP LONDs and 55 and 100 nM free CA4 in DMSO as a positive control. Control SVR cells with <0.01% DMSO were used as a free drug control, while TPP LONDs without CA4 were used to control for the CA4 TPP LONDs. Following a continuous treatment for 24 h at 37°C, SVR cells were fixed with 70% (v/v) EtOH, stained with PI and analysed by flow cytometry. Values (%) represent the mean ± SEM of n=21 for control, n=18 for TPP LONDs, n=12 for 100 nM free CA4 in DMSO, n=9 for 55 nM free CA4 in DMSO and n=9 for both concentrations of CA4 TPP LONDs (n=3 replicates for each experimental repeat). (B) Rectangles in A showed a proportion of cells in a second G2/M phase (4N DNA content) these were analysed using a polyploidy mode in ModFitLT V3.2 software and the % of cells in the second G2/M phase was determined.

A

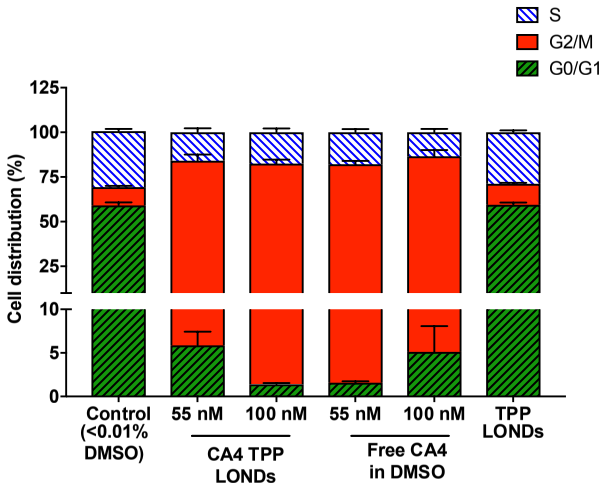

B

Statistical results: unpaired t-test								
Groups – G0/G1 phase			**Groups – G2/M phase**			**Groups – S phase**		
Control (<0.01% DMSO) vs.	Significant	P value	**Control (<0.01% DMSO) vs.**	Significant	P value	**Control (<0.01% DMSO) vs.**	Significant	P value
55 nM CA4 TPP LONDs	yes	p<0.0001	55 nM CA4 TPP LONDs	yes	p<0.0001	55 nM CA4 TPP LONDs	yes	p<0.0001
100 nM CA4 TPP LONDs	yes	p<0.0001	100 nM CA4 TPP LONDs	yes	p<0.0001	100 nM CA4 TPP LONDs	yes	p=0.0002
55 nM CA4 in DMSO	yes	p<0.0001	55 nM CA4 in DMSO	yes	p<0.0001	55 nM CA4 in DMSO	yes	p<0.0001
100 nM CA4 in DMSO	yes	p<0.0001	100 nM CA4 in DMSO	yes	p<0.0001	100 nM CA4 in DMSO	yes	p<0.0001
TPP LONDs	no	p=0.14	TPP LONDs	yes	p=0.013	TPP LONDs	no	p=0.90

Groups – G0/G1 phase			**Groups – G2/M phase**			**Groups – S phase**		
TPP LONDs vs.	Significant	P value	**TPP LONDs vs.**	Significant	P value	**TPP LONDs vs.**	Significant	P value
55 nM CA4 TPP LONDs	yes	p<0.0001	55 nM CA4 TPP LONDs	yes	p<0.0001	55 nM CA4 TPP LONDs	yes	p<0.0001
100 nM CA4 TPP LONDs	yes	p<0.0001	100 nM CA4 TPP LONDs	yes	p<0.0001	100 nM CA4 TPP LONDs	yes	p<0.0001
55 nM CA4 in DMSO	yes	p<0.0001	55 nM CA4 in DMSO	yes	p<0.0001	55 nM CA4 in DMSO	yes	p<0.0001
100 nM CA4 in DMSO	yes	p<0.0001	100 nM CA4 in DMSO	yes	p<0.0001	100 nM CA4 in DMSO	yes	p<0.0001
55 nM CA4 TPP LONDs vs.								
100 nM CA4 TPP LONDs	yes	p=0.012						
55 nM CA4 in DMSO	yes	p=0.015						

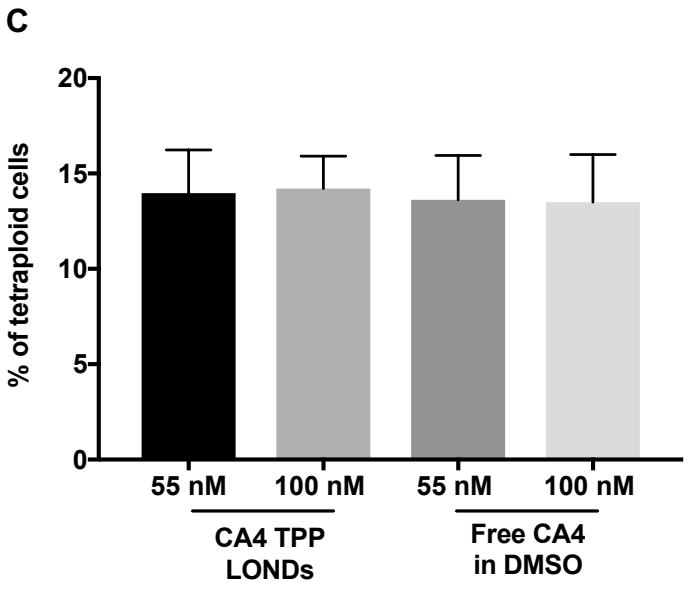

Figure 4.12 Effect of CA4 TPP LONDs and free CA4 in DMSO on SVR cell cycle distribution.

(A) To assess the ability of CA4 TPP LONDs to modulate the cell cycle, SVR cells were treated with 55 and 100 nM CA4 TPP LONDs and 55 and 100 nM free CA4 in DMSO as a positive control. Control SVR cells with <0.01% DMSO were used as a free drug control, while TPP LONDs without CA4 were used to control for the CA4 TPP LONDs. Following, a continuous treatment for 24 h at 37°C, SVR cells were fixed with 70% (v/v) EtOH, stained with PI and analysed by flow cytometry. The results were subsequently analysed using ModFitLT V3.2 software. Values (%) represent the mean and the error bars the SEM of n=21 for control, n=18 for TPP LONDs, n=12 for 100 nM free CA4 in DMSO, n=9 for 55 nM free CA4 in DMSO and n=9 for both concentrations of CA4 TPP LONDs (n=3 biological replicates for each experimental repeat). Treatment with CA4 TPP LONDs or free CA4 in DMSO at both concentrations resulted in significant increase in the cells in G2/M phase when compared to control and TPP LONDs. (B) Results from statistical analyses which were carried out using unpaired t-tests. (C) % of tetraploid cells: A proportion of cells treated with CA4 TPP LONDs and/or free CA4 in DMSO were able to escape G2/M phase block and enter another cell division subsequently leading to tetraploid cells (4N DNA). Prep. number 10 was used.

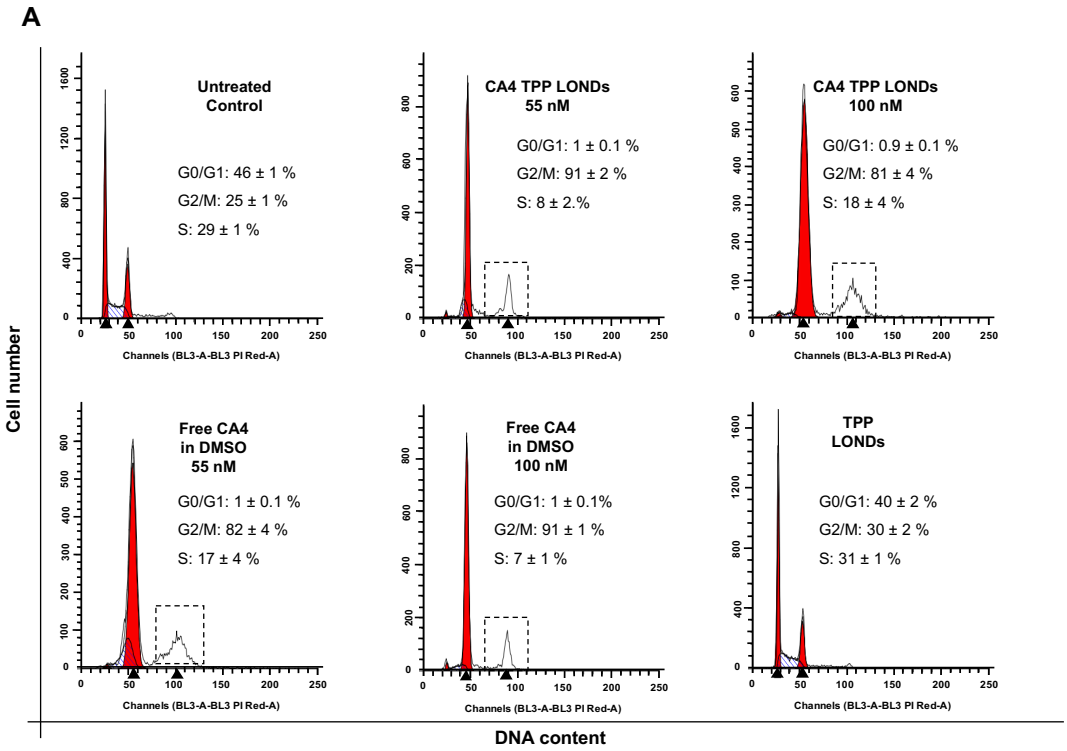
A
Untreated Control
G0/G1: 46 ± 1 %
G2/M: 25 ± 1 %
S: 29 ± 1 %
CA4 TPP LONDs 55 nM
G0/G1: 1 ± 0.1 %
G2/M: 91 ± 2 %
S: 8 ± 2.%
CA4 TPP LONDs 100 nM
G0/G1: 0.9 ± 0.1 %
G2/M: 81 ± 4 %
S: 18 ± 4 %
Free CA4 in DMSO 55 nM
G0/G1: 1 ± 0.1 %
G2/M: 82 ± 4 %
S: 17 ± 4 %
Free CA4 in DMSO 100 nM
G0/G1: 1 ± 0.1%
G2/M: 91 ± 1 %
S: 7 ± 1 %
TPP LONDs
G0/G1: 40 ± 2 %
G2/M: 30 ± 2 %
S: 31 ± 1 %
Channels (BL3-A-BL3 PI Red-A)
Cell number
DNA content

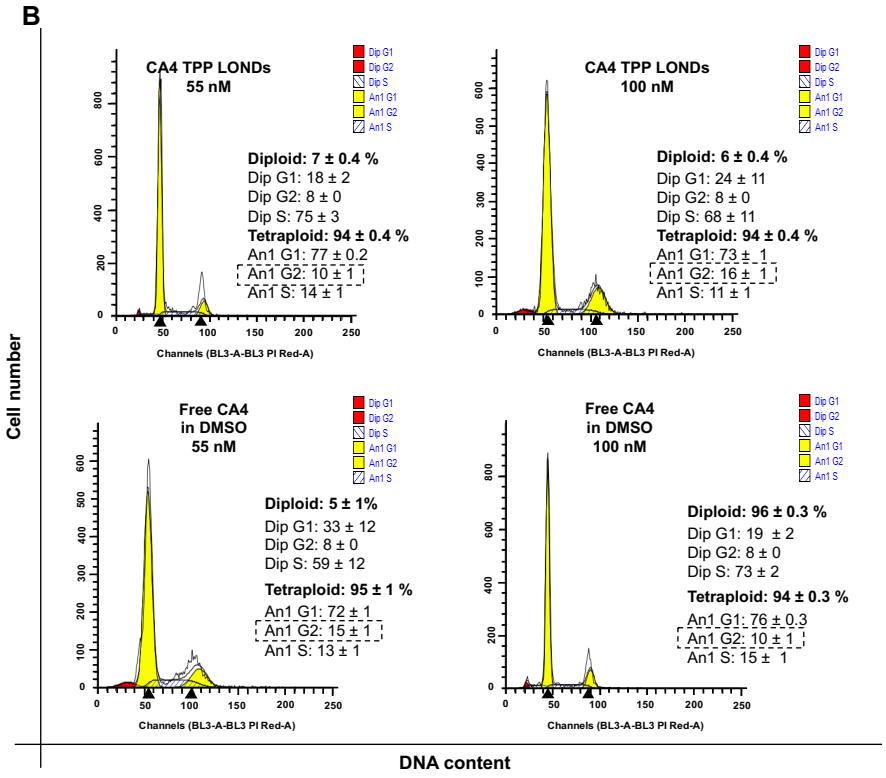
B
CA4 TPP LONDs 55 nM
Diploid: 7 ± 0.4 %
Dip G1: 18 ± 2
Dip G2: 8 ± 0
Dip S: 75 ± 3
Tetraploid: 94 ± 0.4 %
An1 G1: 77 ± 0.2
An1 G2: 10 ± 1
An1 S: 14 ± 1
CA4 TPP LONDs 100 nM
Diploid: 6 ± 0.4 %
Dip G1: 24 ± 11
Dip G2: 8 ± 0
Dip S: 68 ± 11
Tetraploid: 94 ± 0.4 %
An1 G1: 73 ± 1
An1 G2: 16 ± 1
An1 S: 11 ± 1
Free CA4 in DMSO 55 nM
Diploid: 5 ± 1%
Dip G1: 33 ± 12
Dip G2: 8 ± 0
Dip S: 59 ± 12
Tetraploid: 95 ± 1 %
An1 G1: 72 ± 1
An1 G2: 15 ± 1
An1 S: 13 ± 1
Free CA4 in DMSO 100 nM
Diploid: 96 ± 0.3 %
Dip G1: 19 ± 2
Dip G2: 8 ± 0
Dip S: 73 ± 2
Tetraploid: 94 ± 0.3 %
An1 G1: 76 ± 0.3
An1 G2: 10 ± 1
An1 S: 15 ± 1
Dip G1
Dip G2
Dip S
An1 G1
An1 G2
An1 S
Channels (BL3-A-BL3 PI Red-A)
Cell number
DNA content

Figure 4.13 Cell cycle distribution of SW480 cells following treatment with CA4 TPP LONDs and free CA4 in DMSO.

(A) ModFitLT V3.2 software results from diploid analysis, to obtain the % of cells in G2/M phase. SW480 cells cultured in 12-well plates and treated with 55 and 100 nM CA4 TPP LONDs and 55 and 100 nM free CA4 in DMSO as a positive control. Control SW480 cells with <0.01% DMSO were used as a free drug control, while TPP LONDs without CA4 were used to control for the CA4 TPP LONDs. Following a continuous treatment for 24 h at 37°C, SW480 cells were fixed with 70% (v/v) EtOH, stained with PI and analysed by flow cytometry. Values (%) represent the mean ± SEM of n=18 for control, n=18 for TPP LONDs, n=9 for 100 nM free CA4 in DMSO, n=9 for 55 nM free CA4 in DMSO and n=9 for both concentrations of CA4 TPP LONDs (n=3 replicates for each experimental repeat). (B) Rectangles in A showed a proportion of cells in a second G2/M phase (4N DNA content) these were analysed using a polyploidy mode in ModFitLT V3.2 software and the % of cells in the second G2/M phase was determined.

A

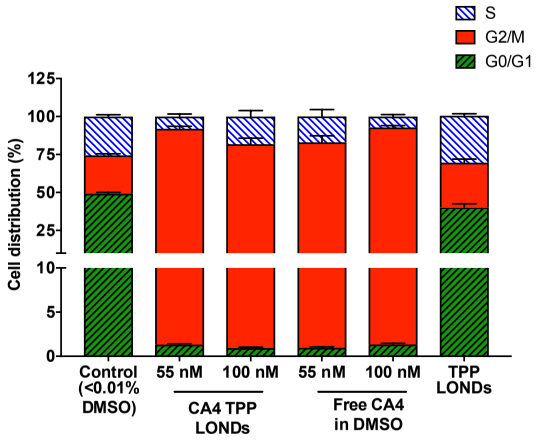

B

Statistical results: unpaired t-test

Groups – G0/G1 phase	Significant	*P* value	Groups – G2/M phase	Significant	P value	Groups – S phase	Significant	P value
Control (<0.01% DMSO) vs.			**Control (<0.01% DMSO) vs.**			**Control (<0.01% DMSO) vs.**		
55 nM CA4 TPP LONDs	yes	p<0.0001	55 nM CA4 TPP LONDs	yes	p<0.0001	55 nM CA4 TPP LONDs	yes	p<0.0001
100 nM CA4 TPP LONDs	yes	p<0.0001	100 nM CA4 TPP LONDs	yes	p<0.0001	100 nM CA4 TPP LONDs	yes	p=0.003
55 nM CA4 in DMSO	yes	p<0.0001	55 nM CA4 in DMSO	yes	p<0.0001	55 nM CA4 in DMSO	yes	p=0.003
100 nM CA4 in DMSO	yes	p<0.0001	100 nM CA4 in DMSO	yes	p<0.0001	100 nM CA4 in DMSO	yes	p<0.0001
TPP LONDs	yes	p=0.021	TPP LONDs	no	p=0.090	TPP LONDs	no	p=0.24

Groups – G0/G1 phase	Significant	P value	Groups – G2/M phase	Significant	P value	Groups – S phase	Significant	P value
TPP LONDs vs.			**TPP LONDs vs.**			**TPP LONDs vs.**		
55 nM CA4 TPP LONDs	yes	p<0.0001	55 nM CA4 TPP LONDs	yes	p<0.0001	55 nM CA4 TPP LONDs	yes	p<0.0001
100 nM CA4 TPP LONDs	yes	p<0.0001	100 nM CA4 TPP LONDs	yes	p<0.0001	100 nM CA4 TPP LONDs	yes	p=0.001
55 nM CA4 in DMSO	yes	p<0.0001	55 nM CA4 in DMSO	yes	p<0.0001	55 nM CA4 in DMSO	yes	p=0.001
100 nM CA4 in DMSO	yes	p<0.0001	100 nM CA4 in DMSO	yes	p<0.0001	100 nM CA4 in DMSO	yes	p<0.0001
55 nM CA4 TPP LONDs vs.			**55 nM CA4 TPP LONDs vs.**			**55 nM CA4 TPP LONDs vs.**		
100 nM CA4 TPP LONDs	yes	p=0.010	100 nM CA4 TPP LONDs	yes	p=0.040	100 nM CA4 TPP LONDs	yes	p=0.030
55 nM CA4 in DMSO	yes	p=0.034						
100 nM CA4 TPP LONDs vs.			**100 nM CA4 TPP LONDs vs.**			**100 nM CA4 TPP LONDs vs.**		
100 nM CA4 in DMSO	yes	p=0.020	100 nM CA4 in DMSO	yes	p=0.022	100 nM CA4 in DMSO	yes	p=0.020
55 nM CA4 in DMSO vs.						**55 nM CA4 in DMSO vs.**		
100 nM CA4 in DMSO	yes	p=0.050				100 nM CA4 in DMSO	yes	p=0.050

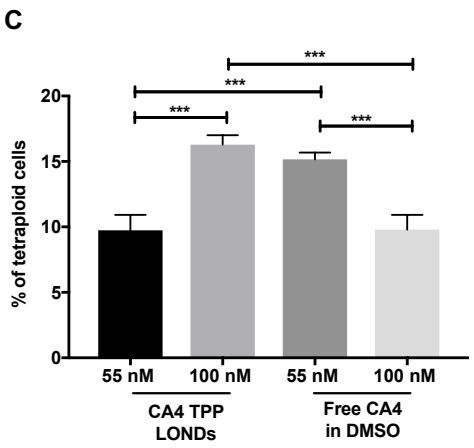

Figure 4.14 Effect of CA4 TPP LONDs and free CA4 in DMSO on SW480 cell cycle distribution.

(A) To assess the ability of CA4 TPP LONDs to modulate the cell cycle, SW480 cells were treated with 55 and 100 nM CA4 TPP LONDs and 55 and 100 nM free CA4 in DMSO as a positive control. Control SW480 cells with <0.01% DMSO were used as a free drug control, while TPP LONDs without CA4 were used to control for the CA4 TPP LONDs. Following a continuous treatment for 24 h at 37°C, SW480 cells were fixed with 70% (v/v) EtOH, stained with PI and analysed by flow cytometry. The results were subsequently analysed using ModFitLT V3.2 software. Values (%) represent the mean and the error bars the SEM of n=18 for control and TPP LONDs and n=9 for CA4 TPP LONDs and free CA4 in DMSO at both concentrations (n=3 biological replicates for each experimental repeat). CA4 TPP LONDs and free CA4 in DMSO cause a statistically significant increase in the % of cells in G2/M phase compared to control and TPP LONDs treated cells. (B) Results from statistical analyses which were carried out using unpaired t-tests. (C) % of tetraploid cells: A proportion of cells treated with CA4 TPP LONDs and/or free CA4 in DMSO were able to escape G2/M phase block and enter another cell division subsequently leading to tetraploid cells (4N DNA). SW480 cells treated with 100 nM CA4 TPP LONDs had a higher % of tetraploid cells compared to SW480 cells treated with 55 nM CA4 TPP LONDs (***, p=0.0002). A higher % of tetraploid cells was observed in SW480 cells treated with 55 nM free CA4 in DMSO compared to 100 nM free CA4 in DMSO (***, p=0.0005). A significant difference was also observed between 55 nM CA4 TPP LONDs and 55 nM free CA4 in DMSO with a higher % of tetraploid cells in the free CA4 in DMSO group (***, p=0.0007). A higher % of tetraploid cells was observed in SW480 cells treated with 100 nM CA4 TPP LONDs compared to 100 nM free CA4 in DMSO (***, p=0.0002). Significance was calculated using an unpaired t-test. Prep number. 10 was used.

4.7 Intracellular localisation of CA4 TPP LONDs in endothelial cells

Using IF and cell cycle analysis, it was evident that CA4 TPP LONDs were capable of delivering CA4 to both endothelial cells and CRC cells *in vitro.* To investigate whether drug release and/or uptake of intact LONDs contributed to drug delivery, LOND distribution in SVR cells was investigated using IF to locate the fluorescence from the lipid shell (Atto590-DOPE) of the LONDs. Co-registered IF images from the CA4 TPP LOND shell and *β*-tubulin showed a potential co-localisation with disrupted MTs 24 h post-treatment with 0.5 *μ*M CA4 TPP LONDs (Figure 4.15). As MTs were disrupted (Figure 4.15 B) this indicated that CA4 from TPP LONDs had been released into the cells and that the red fluorescence present was potentially lipids from the LOND shell following disassembly. TPP LONDs or LOND lipids were located around the nuclei and also co-localised with MTs (Figure 4.15 C).

4.8 Discussion

4.8.1 Development of CA4 TPP LONDs

TPP LONDs were developed for the hydrophobic delivery of CA4 following the issues of solubility and retention/leaking inherent to TA LONDs. High pressure homogenisation produced TPP LONDs with a mean diameter of < 100 nm in contrast to the previously prepared TA LONDs which were > 250 nm. The decrease in size was due, in part, to the presence of cholesterol which induced the dense packing of the phospholipids (Bozzuto & Molinari, 2015). The concentration of particles produced was also increased compared to TA LONDs from 10^9 particles/mL to 10^{14} particles/mL. The %EE of CA4 was the same in TA LONDs. However, it was assumed that due to the use of a less water soluble oil TPP (*logP* 1.7 vs TA *logP* 0.1), and the increase in shell stability and rigidity by the addition of cholesterol and DSPC that CA4 retention in the LOND would be improved. TPP LONDs were observed to be stable for six weeks at storage temperature 4°C and 2 h at 37°C.

4.8.2 *In vitro* evaluation of MT disruption by CA4 TPP LONDs

CA4 TPP LONDs caused MT disruption in both endothelial cell lines tested and SW480 cells within the 2 h treatment indicating successful release and/or uptake of CA4 from the LONDs. MT disruption was observed when free CA4 was dissolved in TPP further indicating that the oil was not inhibiting and/or changing the activity of CA4, as TPP alone did not cause any MT disruption.

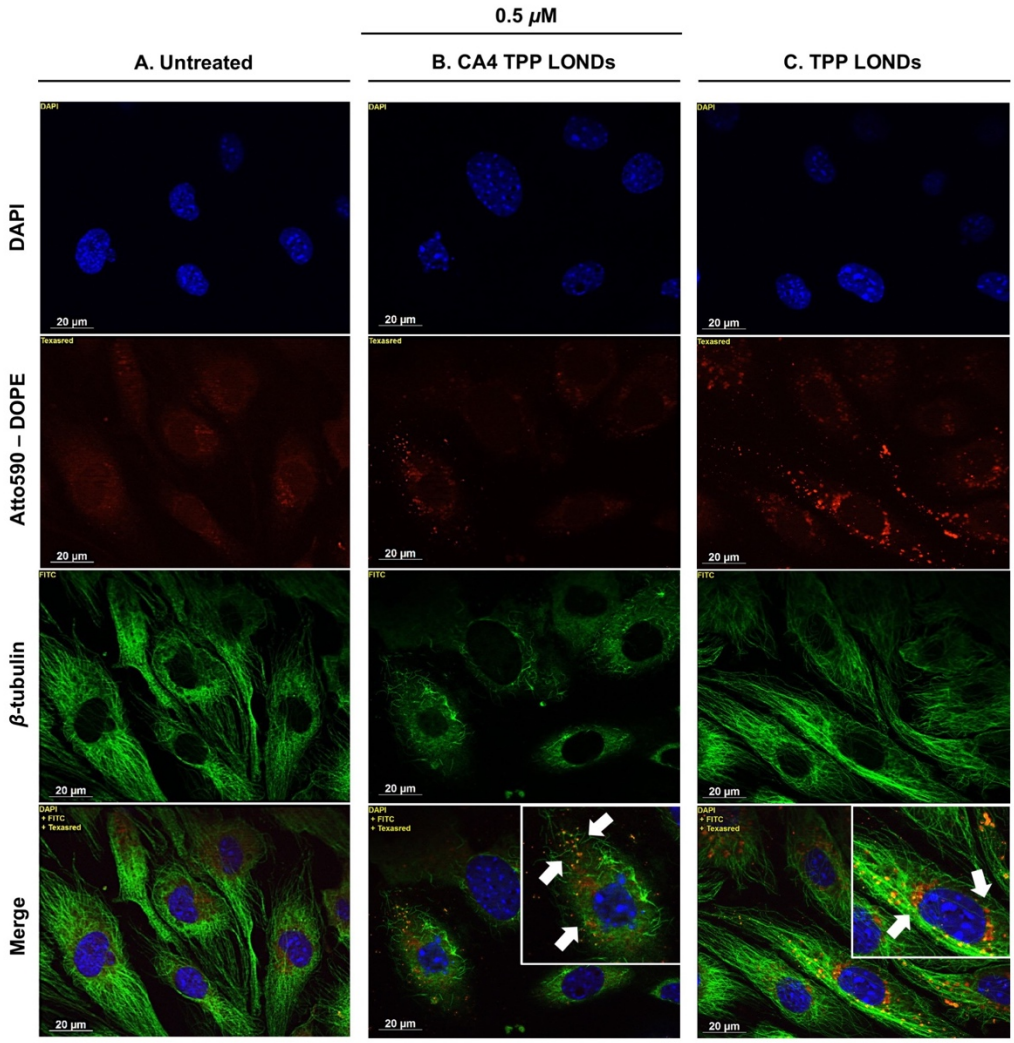

Figure 4.15 Intracellular localisation of CA4 TPP LONDs.

To investigate the localisation of LONDs in SVR cells, SVR cells cultured in *μ*-slides (ibidi) were treated for 24 h at 37°C with 0.5 *μ*M CA4 TPP LONDs, incorporating a red fluorescence Atto590-DOPE in their shell. Untreated SVR cells and SVR cells treated with TPP LONDs were used as control. Following 24 h at 37°C, cells were fixed and immunostained for *β*-tubulin using a mouse monoclonal anti-*β*-tubulin antibody and visualised using a biotinylated rabbit anti-mouse and FITC-labelled avidin. Slides were mounted with prolong Gold containing DAPI. (A) Untreated control SVR cells showing filamentous MTs with no evidence of red fluorescence. (B) SVR cells treated with 0.5 *μ*M CA4 TPP LONDs, showing a red fluorescence (white arrows) presumably from the LOND shell. The red fluorescence co-localised with the disrupted MTs (formed a uniform fluorescence in the cytoplasm, residual MTs were also present). (C) SVR cells treated with TPP LONDs, also showing co-localisation of red fluorescence from the LOND lipid shell and MTs. Scale bars indicate 20 *μ*m. Prep. number 8 was used.

The release and/or uptake of CA4 from TPP LONDs was observed to occur within 30 min of treatment of SVR cells, as MTs were disrupted when treated with 10 μM CA4 TPP LONDs from prep. numbers 7, 8 and when tested at the lower concentration of 0.1 μM CA4 TPP LONDs with prep. number 10. The data therefore, showed the rapidity of release and/or uptake of CA4 TPP LONDs and that this was reproducible with a different preparation of CA4 TPP LONDs and at a lower concentration.

The ability of CA4 TPP LONDs to cause MT disruption in SVR cells at escalating concentrations was investigated compared to free CA4 in TPP. CA4 TPP LONDs caused a significant disruption to the MTs at the lowest concentration 2 nM compared to untreated SVR cells, without causing any qualitative changes to the appearance of the cells. Free CA4 in TPP showed no significant MT disruption at 2 nM, pointing towards an enhanced in effect when CA4 was encapsulated and delivered by TPP LONDs. However, at 8 nM no differences were observed between free CA4 and CA4 TPP LONDs.

Although, CA4 *in vitro* and *in vivo* causes very rapid effects the ability of MTs to reassemble and tumours to recover hinders the anti-tumour activity of this agent. The results presented in this study showed that the shape of MTs in SVR cells treated for 2 h with CA4 TPP LONDs recovered within 24 h post drug washout. CA4 is a reversible inhibitor of MT assembly (Lin *et al.*, 1989). Quan *et al.,* (2008) investigated the reversibility of microtubule disassembly in hepatocellular carcinoma cells. Their results showed that microtubule disruption or disassembly resulted in the activation of ERK1/2 and p38 MAPK in hepatocellular carcinoma cells < 2 h followed by reassembly within a few hours. Inhibition of p38 MAPK blocked the MT reassembly in hepatocellular carcinoma and p38 MAPK inhibitors potentiated the cytotoxicity of CA4. The authors suggested that under shorter exposure times (less than 2 h) and low concentrations below 1 μM, CA4 is able to stimulate p38 MAPK but is not able to induce apoptosis, and therefore p38 MAPK protects cells against CA4 treatment as it enables reassembly (Quan, Xu & Lou, 2008). Here, the precise underlying mechanism involved in SVR MT reassembly is not currently known, activation of p38 MAPK may be involved.

4.8.3 Ability of CA4 TPP LONDs to modulate the cell cycle

Prolonged exposure of cells to CA4 leads to mitotic arrest which results in a number of outcomes including apoptosis, mitotic catastrophe and polyploidy (Greene, Meegan & Zisterer, 2015). Mitotic catastrophe is characterised by cells with enlarged, fragmented and multiple nuclei. Following a 24 h exposure, CA4 TPP LONDs caused

SVR cells to enter mitotic catastrophe as confirmed by DNA content analysis using flow cytometry. A G2/M phase block was observed after treatment of SVR and SW480 cells with CA4 TPP LONDs but not TPP LONDs indicating that the effect was driven by the CA4 payload consistent with previous reports (Nabha *et al.*, 2000, 2002; Kanthou *et al.*, 2004).

It can be speculated from previous reports that the cellular mechanism involved in this G2/M arrest caused by the release of CA4 from TPP LONDs is through the accumulation of cyclin B in the nucleus followed by the sustained activation of $p34^{cdc2}$ preventing the progression to anaphase and subsequent exit from mitosis which has been demonstrated in both endothelial and cancer cells (Nabha *et al.*, 2002; Kanthou *et al.*, 2004). The cells then die without exiting mitosis ("mitotic death") either through caspase-dependent or independent pathways (Kanthou *et al.*, 2004; Vitale *et al.*, 2007, 2011). It is evident from the above results that a proportion of both SVR and SW480 cells have escaped mitosis *i.e.* mitotic slippage and have entered polyploidy. One of the events potentially driving this mitotic slippage is the slow proteasomal degradation of cyclin B which after a prolonged arrest occurs (Vakifahmetoglu, Olsson & Zhivotovsky, 2008). Another, potential mechanism of mitotic slippage described in bladder cancer cells and cervical cancer cells is the activation of caspase 3 which cleaves a member of the spindle assembly checkpoint BubR1 leading to multinucleation and polyploidy (Shen *et al.*, 2010; Greene *et al.*, 2011). The release from G2/M block in CRC cells (CT26 and Caco-2) following exposure to CA4P at 50 nM for 48 h results in approximately 30% of polyploidy followed by cell death (Greene *et al.*, 2012).

4.8.4 Cellular localisation

IF imaging of the fluorescent lipid shell (via the Atto590-DOPE) showed that the lipids from the LONDs were located near the nuclear membrane and co-localised with MTs. At this stage the mechanism of intracellular release and/or uptake was not required in developing and translating the LONDs as a hydrophobic DDS.

Fusogenic lipids natural or helper lipids like DOPE as well as provide stabilisation can also promote the endosomal escape of NPs from endosomes due to structural transition when exposed to low pH of the endosomal compartment (Biswas & Torchilin, 2014; Selby *et al.*, 2017). The presence of the PEG which is used a steric stabiliser and improves *in vivo* circulation time however, can interfere with this fusion of DOPE and the cellular/endosomal membrane (Remaut *et al.*, 2007; Selby *et al.*, 2017). Hak *et al.,* (2012 and 2015) studied the potential of DSPE-$BPEG_{2000}$ to affect

intracellular uptake of nanoemulsions with a similar size, approximately 100 nm and phospholipid-stabilised shell which including DSPC, cholesterol and at a 2.5 or 5:62:33 molar ratio % respectively, the oil core was soybean oil. Their results showed intracellular uptake of the nanoemulsions via caveolae-dependent pathways and other clathrin- and caveolae-independent pathways within 2 h of incubation. Intact and disassembled nanoemulsions were co-localised with lysosomes, indicating the uptake of intact nanoemulsions followed by an immediate disassembly, the authors also concluded that once internalised the 5mol% DSPE-BPEG$_{2000}$ did not affect nanoemulsion stability and disassembly (Hak *et al.*, 2012, 2015).

From previous data it can be speculated that fusion is unlikely to occur due to the low molar concentration of DOPE which was used as a fluorescent marker and the potential inhibitory effects of PEG preventing this. However, from the data collected by Hat *et al.,* (2012 and 2015), it can be hypothesised that LONDs behave in a similar manner, rapid uptake by endocytosis into cells followed by a rapid release of CA4, as an effect on MTs is observed within 30 min and remaining lipids from LOND disassembly could potentially be localised in various intracellular compartments such as endosomes, lysosomes, Golgi or endoplasmic reticulum after 24 h of exposure. Although, the potential of LOND disassembly outside the cell prior to CA4 uptake through diffusion for example or LOND disassembly in an endosome followed by degradation and subsequent release of CA4 cannot be excluded.

4.8.5 Conclusion

Overall the initial *in vitro* results with CA4 TPP LONDs showed the successful and rapid release and/or uptake and subsequent release of CA4 into endothelial and human CRC cells. Encapsulating CA4 in TPP LONDs retained the MT disruption activity of CA4 with minor differences with free CA4. It was observed that SVR cells recover following transient treatment, however, both SVR and SW480 cells during prolonged treatment with CA4 TPP LONDs or free CA4 enter mitotic catastrophe which eventually can lead to cell death. This is particularly important as *in vivo* the potential retention of CA4 TPP LONDs by the EPR effect may lead to prolonged exposure of tumour cells to CA4 and subsequent cell-death.

Chapter 5

In vivo delivery of CA4 TPP LONDs

5.1 Introduction

As shown in the previous chapter, CA4 TPP LONDs appeared stable and demonstrated effects consistent with drug uptake and/or release in both endothelial cells and SW480 cells *in vitro*. Next, the potential of LONDs as a hydrophobic DDS was assessed *in vivo* using mice bearing SW480 human CRC xenografts. *In vivo* evaluation is key to the development of any DDS. A novel DDS such as LONDs needs to be stable enough to prolong circulation time without rapid clearance in order to reach the target site, accumulate at the target site and release the payload. During the initial stages of development, the PK of the proposed delivery system following systemic administration is therefore required.

Delivery of encapsulated CA4 has been reported for both targeted and untargeted NPs (Wang *et al.*, 2013; Li *et al.*, 2015). Specifically delivery of CA4 in untargeted NPs resulted in an increase of CA4 intratumoral delivery due to the EPR effect, however CA4 was also found in a number of normal tissues such as the liver, heart and spleen (Wang *et al.*, 2013). Others have shown that targeting CA4 NPs to VEGFR2 or RGD greatly improved tumour growth inhibition when compared to untargeted NPs, however it did not prevent the unspecific uptake in normal tissues (Su *et al.*, 2014; Li *et al.*, 2015). Pattillo *et al.,* (2009) showed that multiple dosing of targeted CA4 liposomes was required for a significant growth inhibition (Pattillo *et al.*, 2009). These studies of CA4 NPs also co-delivered other agents such as DOX or used radiation in order to observed a tumour growth inhibition (Pattillo *et al.*, 2009; Li *et al.*, 2015).

The first pilot studies with untargeted CA4 TPP LONDs specifically aimed to investigate intratumoral delivery and tumour pharmacodynamic (PD) responses following a single dose. Following this the aim was to investigate any potential tumour growth inhibition in human CRC xenografts following multiple doses of CA4 TPP LONDs.

5.2 Delivery of CA4 TPP LONDs to mice bearing SW480 human CRC xenografts

The first stage of *in vivo* evaluation of CA4 TPP LONDs focused on the pharmacological responses in terms of tumour PD and tumour, plasma and liver PK. Mice (32-33 g) bearing SW480 xenografts on day 10 of tumour growth were sorted according to body weight into 3 groups (n=6 per group). To achieve the highest

possible concentration of CA4 TPP LONDs, a dose of 0.1 mL per 10 g of body weight was used, resulting in a dose of 12.8 mg/kg (or 4 mM per injection) which was well below the commonly used dose of 100 mg/kg. The other two groups were TPP LONDs at 0.1 mL per 10 g of body weight or free CA4 as a positive control at a 50 mg/kg dose in 10% DMSO/peanut oil. 3.8 x 10^{13} CA4 TPP LONDs and 3.3 x 10^{13} TPP LONDs were administered i.v. through the tail vein (slow bolus delivery). In contrast, free CA4 in 10% DMSO/peanut oil was administered i.p.. Peanut oil was chosen as the vehicle carrier for free CA4 as the i.p. injection of TPP was not well tolerated.

At 1 and 24 h post-injection, three mice from each group were sacrificed and tumour, liver and plasma samples were harvested. All information including experimental cohorts, mouse body weight on day 10 and tumour volumes on day 7 are shown in Figure 5.1. The CA4 TPP LONDs dose per mouse including the number of LONDs per injection for CA4 TPP LONDs and TPP LONDs are summarised in Table 5.1.

5.2.1 Pharmacodynamic response of SW480 xenografts to CA4 TPP LONDs

Tumour PD responses to CA4 TPP LONDs were assessed using biomarkers for haemorrhage, necrosis, mitoses and blood vessels (MVD). Tumour histology 1 h post-injection of CA4 TPP LONDs showed evidence of peripheral haemorrhage in 1/3 tumours which was associated with large areas of viable tumour cells (Figure 5.2 A). Evidence of potential haemorrhage was observed in 1/3 tumours treated with TPP LONDs, although this might have resulted from the inherent leaky tumour vasculature (Figure 5.2 B). In contrast, 2/3 tumours 1 h post-injection with free CA4 in DMSO/peanut oil showed evidence of central haemorrhage in the necrotic areas and peripheral haemorrhage (Figure 5.2 C).

At 24 h post-injection of CA4 TPP LONDs, 3/3 tumours showed evidence of haemorrhage, one showed extensive central haemorrhage (Figure 5.3 A). Evidence of haemorrhage was also observed in 2/3 tumours, 24 h post-injection of free CA4 in DMSO/peanut oil (Figure 5.3 B). In contrast, no haemorrhage was observed in tumours with TPP LONDs, 24 h post-injection (Figure 5.3 C).

The % area of tumours with evidence of haemorrhage (Figure 5.4 A) and necrosis (Figure 5.4 B) was determined. No statistically significant differences in % haemorrhage or necrosis were observed at any time point between the groups (Mann-Whitney U test, two-tailed).

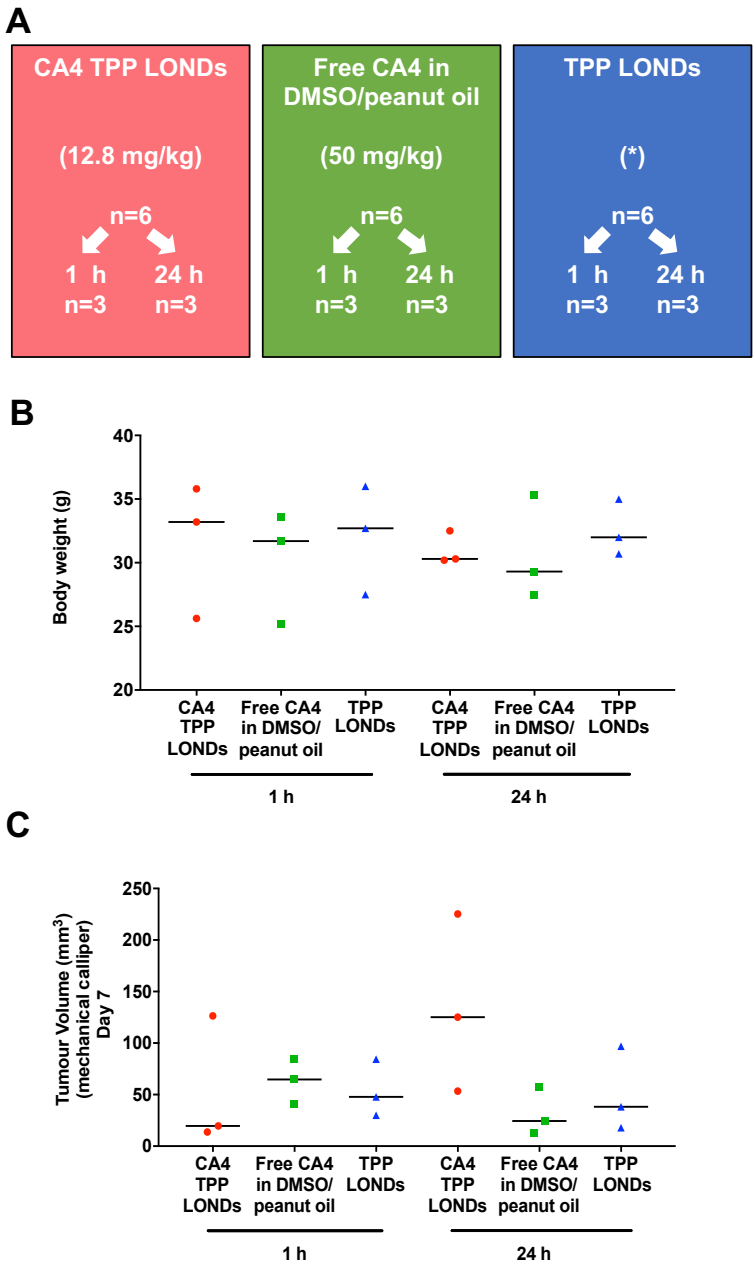

Figure 5.1 Delivery of CA4 TPP LONDs to mice bearing human CRC xenografts. (A) Experimental cohorts: n=6 per group these were further sub-divided into n=3 for 1 and 24 h time points post-injection for PD and PK analysis; CD-1® nude male mice bearing SW480 xenografts received i.v. injection through the tail vein of a dose of 12.8 mg/kg CA4 TPP LONDs or TPP LONDs (* 0.1 mL per 10 g of body weight) or i.p. 50 mg/kg free CA4 in DMSO (10%)/peanut oil on day 10 of tumour growth. A mean number of 3.8 x 10^{13} CA4 TPP LONDs and a mean number of 3.3 x 10^{13} TPP LONDs were administered per injection. (B) Body weight in grams (g) post randomisation into sub-groups on day 10 prior to injections. Straight lines (–) represent the median. (C) Tumour volumes measured by mechanical callipers in mm^3 on day 7 of tumour growth. Straight lines (–) represent the median value.

Table 5.1 Dose and number of LONDs/injection for individual mice.

Group	Weight (g)	Dose (mg)/ injection	Dose (mM)/ injection	Number of LONDs/ injection	Dose (mg/kg)
1 h CA4 TPP LONDs					
Mouse 1	33.2	0.4	3.8	4×10^{13}	12
Mouse 2	25.6	0.3	3.7	3.1×10^{13}	12
Mouse 3	35.9	0.5	4.4	4.3×10^{13}	14
24 h CA4 TPP LONDs					
Mouse 1	30.2	0.4	4.2	3.6×10^{13}	13.2
Mouse 2	32.5	0.4	4	3.9×10^{13}	12.3
Mouse 3	30.3	0.4	4.2	3.6×10^{13}	13.2
Mean ± SD	31.3 ± 3.5	0.4 ± 0.06	4.1 ± 0.3	$3.8 \times 10^{13} \pm 4.6 \times 10^{12}$	12.8 ± 0.8
1 h TPP LONDs					
Mouse 1	31.7			3.5×10^{13}	
Mouse 2	33.6	N/A	N/A	3.7×10^{13}	N/A
Mouse 3	25.2			2.7×10^{13}	
24 h TPP LONDs					
Mouse 1	35.3			3.9×10^{13}	
Mouse 2	27.5	N/A	N/A	3×10^{13}	N/A
Mouse 3	29.3			3.2×10^{13}	
Mean ± SD	30.4 ± 3.8			$3.3 \times 10^{13} \pm 4.5 \times 10^{12}$	

N/A: not applicable.

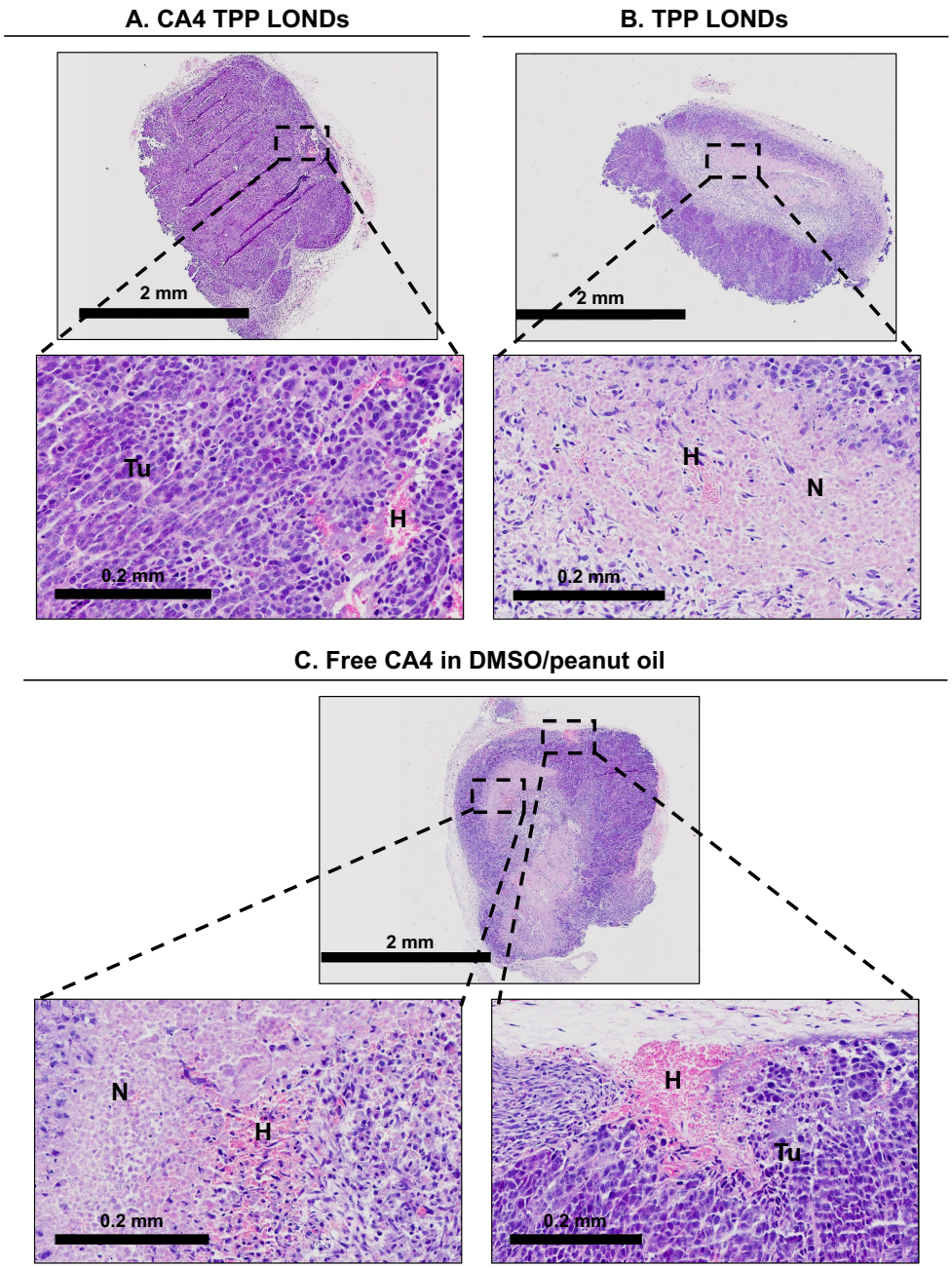

Figure 5.2 Tumour histology 1 h post-injection with CA4 TPP LONDs, TPP LONDs or free CA4 in DMSO/peanut oil.

Histological images of tumours stained with H & E 1 h post-injection. (A) CA4 TPP LONDs treated tumour showing some evidence of haemorrhage (H) surrounded by viable tumour cells (Tu). Top image show the entire tumour section and square box or boxes show the area of the bottom image or images. (B) Tumour post-injection with TPP LONDs showing potential haemorrhage in the necrotic area (N). (C) Tumour post-injection with free CA4 DMSO/peanut oil showing areas of central haemorrhage in the necrotic areas of the tumour and peripheral haemorrhage. Scale bars indicate 2 mm and 0.2 mm. Prep. numbers 8 and 9 were used.

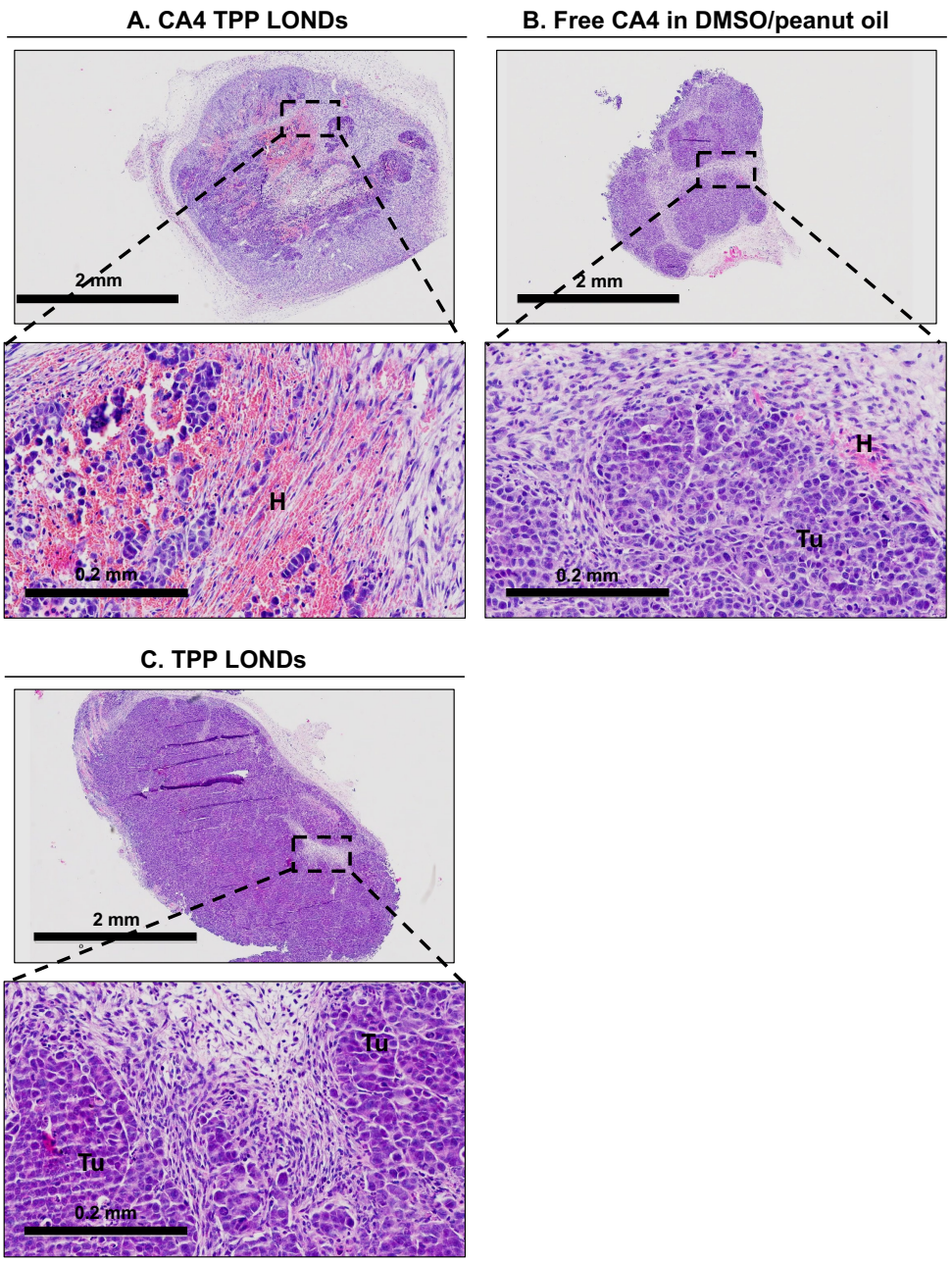

Figure 5.3 Tumour histology 24 h post-injection with CA4 TPP LONDs, TPP LONDs or free CA4 in DMSO/penaut oil.

Histological images of tumours stained with H & E 24 h post-injection. (A) Tumour post-injection with CA4 TPP LONDs showing extensive central haemorrhage (H). (B) Tumour post-injection with free CA4 DMSO/peanut oil. Haemorrhage was observed near viable tumour cells (Tu). (C) Large areas of viable tumour cells were observed in tumour post-injection with TPP LONDs. Top image show the entire tumour section and square box shows the area of the bottom image. Scale bars indicate 2 mm and 0.2 mm. Prep. numbers 8 and 9 were used.

The results however, showed that at 1 h post-injection there was higher % of haemorrhage in 1/3 (7%) tumours with free CA4 compared to TPP LONDs. Interestingly, substantial haemorrhage was only observed 24 h after administration of CA4 TPP LONDs in 1/3 tumours (9%). This result points towards a potentially delayed PD response from the CA4 TPP LONDs. Less than 0.5% haemorrhage was observed in 1/3 tumours in the TPP LONDs group following 1 h post-injection, indicating that anything ≤ 0.5% haemorrhage could be considered as the background level. There was no correlation between the % area with haemorrhage and % area with necrosis using Spearman's correlation coefficients (Figure 5.4 C).

It was shown previously (section 4.6) that extended exposure (24 h) of SW480 cells to CA4 *in vitro* resulted in the accumulation of SW480 cells in G2/M phase of the cell cycle. To investigate the effect of CA4 TPP LONDs on cell cycle regulation *in vivo*, the number of mitoses in tumour tissues from CA4 TPP LONDs and control animals were determined (Figure 5.4 D). Although an increase in mitoses was observed 24 h post-injection with CA4 TPP LONDs and free CA4 in DMSO/peanut oil, these were not significantly different from control TPP LONDs (Mann-Whitney U test, two-tailed).

Haemorrhage is often associated with a reduction in the number of blood vessels as shown previously with CA4P (Nabha *et al.*, 2001). As CA4 delivered by TPP LONDs and free CA4 showed some evidence of haemorrhage 1 h and 24 h post-injection, MVD was determined in tumour tissues. The immunostained CD31 pattern 1 h and 24 h post-injection in all experimental cohorts appeared very similar (Figure 5.5 A I-IV) with no significant differences in MVD between the groups at any time point tested (Figure 5.5 C).

5.2.2 Biodistribution of CA4 and its main metabolite CA4G following a single dose of CA4 TPP LONDs

No statistically significant differences were observed in tumour PD response post-injection with CA4 TPP LONDs, free CA4 in DMSO/peanut oil or TPP LONDs. To determine if delivering CA4 by TPP LONDs altered drug PK, the concentrations of CA4 and its main metabolite, CA4G, in tumour, liver and plasma were determined from all experimental groups harvested 1 h post-injection using LC-MS/MS (sections 2.6 and 3.6.2 for method development details).

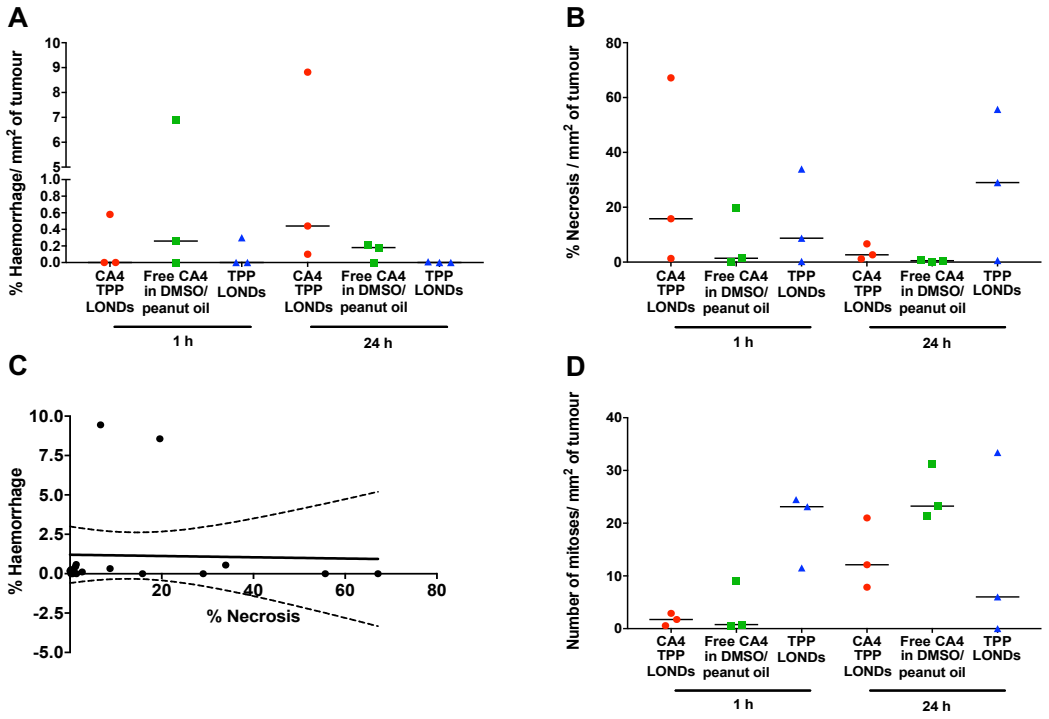

Figure 5.4 % haemorrhage, necrosis and number of mitoses per mm^2 of tumour post-injection with CA4 TPP LONDs, free CA4 in DMSO/penaut oil and TPP LONDs.

(A) % area with haemorrhage per mm^2 of tumour. (B) % area with necrosis per mm^2 of tumour. (C) The relationship between % area with necrosis and % area with haemorrhage using Spearman's correlation showed no correlation between the two variables (r=-0.04, p=0.9, 95% confidence interval -0.5 to 0.4, two-tailed). The solid line denotes line of best fit and the dotted lines indicate the 95% confidence band. (D) Number of mitoses per mm^2 of tumour was determined. No statistically significant differences were observed between the experimental cohorts in terms of % haemorrhage, necrosis and mitoses (Mann-Whitney U test, two-tailed). Straight lines (–) represent the median. Prep. numbers 8 and 9 were used.

The results in Figure 5.6 A showed detectable/or above LOD (10 ng) CA4 in tumour tissues from 2/3 mice in the CA4 TPP LONDs group and 2/3 mice in the free CA4 in DMSO/peanut oil group. Interestingly, the concentration of CA4 measured (median 1380 ng/g) from CA4 TPP LONDs treated tumours was not significantly different from that in tumours of the free CA4 in DMSO/peanut oil group (median 2389 ng/g) which received approximately four times the dose of CA4. CA4 was not detected in any liver or plasma samples from the CA4 TPP LONDs group. In contrast, it was detected in 1/3 livers and 1/3 plasma samples with free CA4 in DMSO/peanut oil.

Due to the lack of a CA4G standard, the presence and PA of CA4G could be recorded but not quantified (Figure 5.6 B) and therefore the LOD for CA4G is unknown. CA4G was present in 5/6 liver samples analysed and was only detected in tumour samples and plasma from mice receiving free CA4 DMSO/peanut oil. This suggested that CA4 when free was rapidly glucuronidated. The ratio of the CA4 PA and CA4G PA was determined where possible (Figure 5.6 C). This showed that CA4 was mainly converted to CA4G in the liver and plasma and to a lesser extent in the tumour (Figure 5.6 C). Due to technical issues, the 24 h post-injection PK samples were unable to be analysed.

5.3 Multiple dosing of SW480 xenografts with CA4 TPP LONDs

Following, confirmation of intratumoural delivery of CA4 by CA4 TPP LONDs (section 5.2), the potential of CA4 TPP LONDs to improve the therapeutic index and therefore, anti-tumour activity of CA4 was investigated using a multiple dosing schedule. Mice bearing SW480 human CRC xenografts were sorted into three experimental cohorts receiving CA4 TPP LONDs (n=4), free CA4 in DMSO/peanut oil (n=6) or DMSO/peanut oil (n=6) according to tumour volume (Figure 5.7 A and B). On days 11, 14 and 18 of tumour growth mice were i.v. injected with 2×10^{13} CA4 TPP LONDs which equated to a 3 mg/kg dose or i.p. free CA4 in DMSO (10%)/peanut oil at the same 3 mg/kg dose or an equivalent volume of DMSO (10%)/peanut oil (Figure 5.7 B). Tumour volumes measured by HFUS were recorded the day before each treatment (Tx) and body weights were also monitored throughout the study as an indicator of wellbeing.

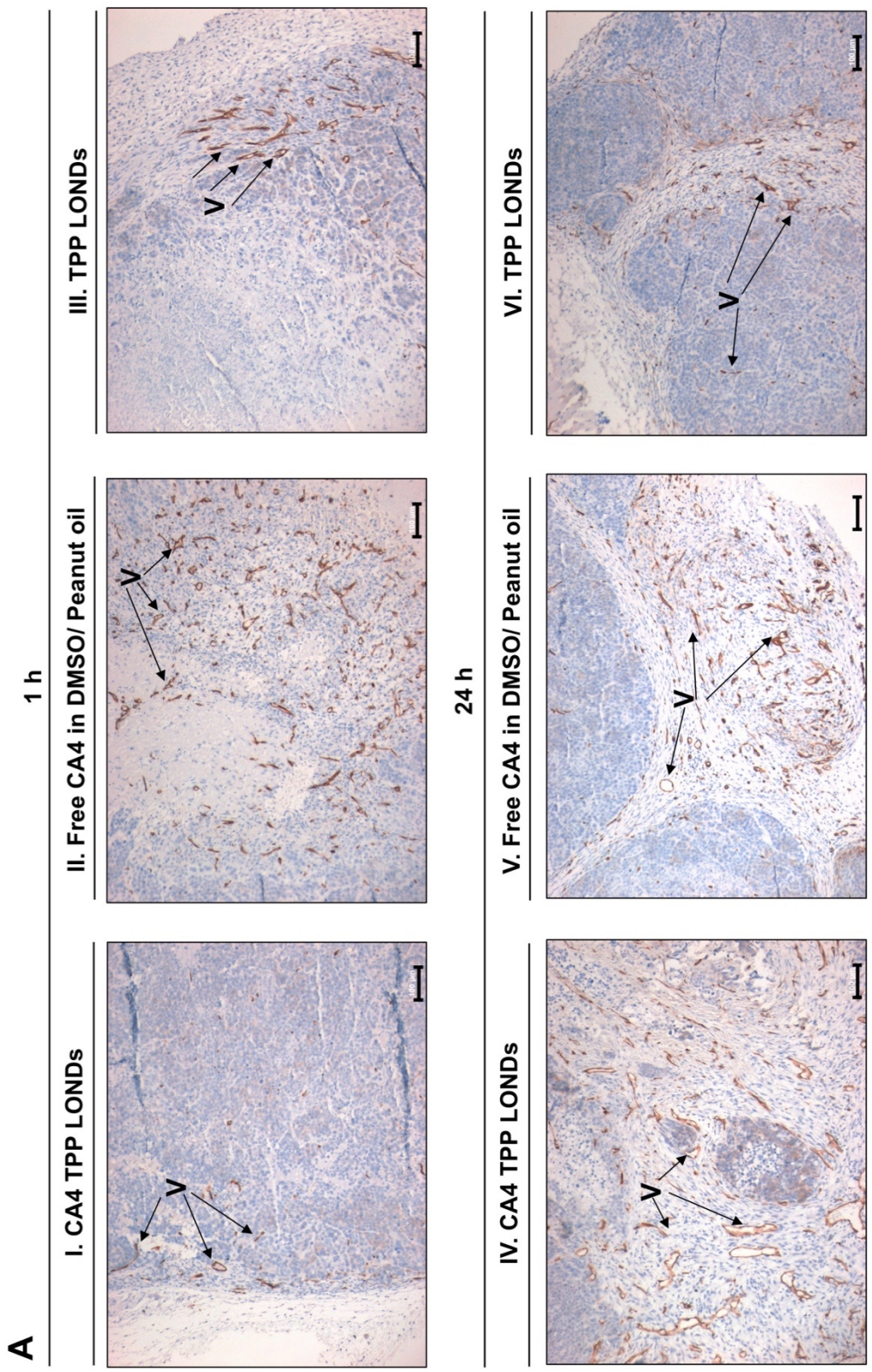
A
1 h
24 h
I. CA4 TPP LONDs
II. Free CA4 in DMSO/ Peanut oil
III. TPP LONDs
IV. CA4 TPP LONDs
V. Free CA4 in DMSO/ Peanut oil
VI. TPP LONDs
V

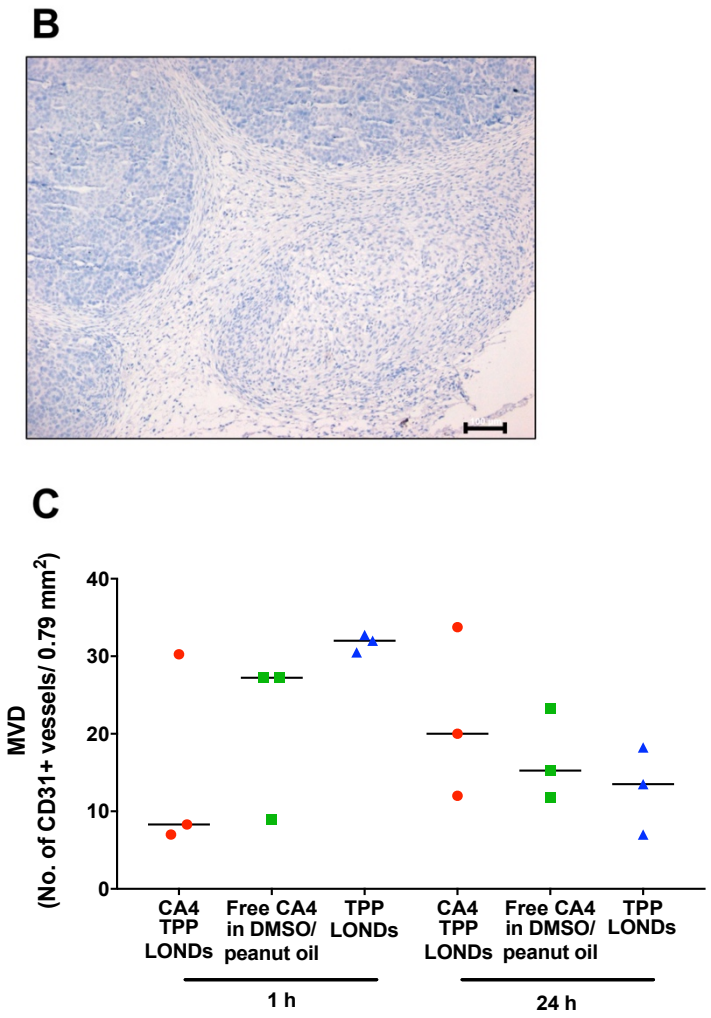

Figure 5.5 MVD 1 h and 24 h post-injection with CA4 TPP LONDs, free CA4 in DMSO/peanut oil and TPP LONDs.

Immunohistochemical images of tumours stained with a rat anti-mouse CD31 antibody and CD31 + vessels were visualised with DAB. (A-I) Tumour section 1 h post-injection with CA4 TPP LONDs showing CD31 positive vessels (V) (arrows, representative vessels). (A-II) Tumour section 1 h post-injection with free CA4 in DMSO/peanut oil, areas with a number of CD31 + vessels were observed. (A-III) Tumour section 1 h post-injection with TPP LONDs, CD31 + vessels were observed. (A-IV) 24 h post-injection with CA4 TPP LONDs. (A-V) 24 h post-injection with free CA4 in DMSO/peanut oil. (A-VI) 24 h post-injection with TPP LONDs. CD31+ vessels were observed in all experimental cohorts. Scale bars indicate 100 μm. (B) No primary control. (C) MVD: number of CD31+ blood vessels per 0.79 mm^2 of tumour (n=4 hot spots). Straight lines (–) represent the median. No statistically significant differences were observed (Mann-Whitney U test, two-tailed). Prep. numbers 8 and 9 were used.

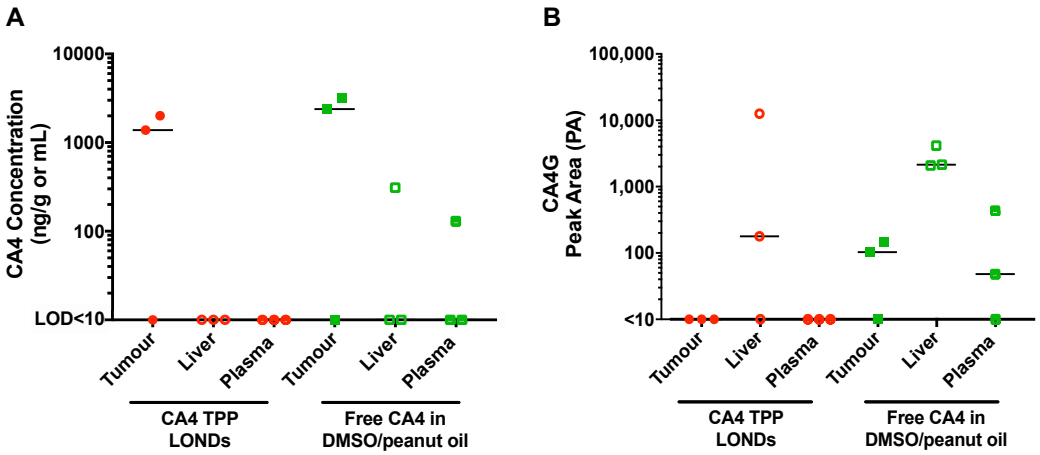

C

1 h Biodistribution										
		Tumour			Liver			Plasma		
Mouse	Group	CA4 (PA)	CA4G (PA)	Ratio (CA4:CA4G)	CA4 (PA)	CA4G (PA)	Ratio (CA4:CA4G)	CA4 (PA)	CA4G (PA)	Ratio (CA4:CA4G)
1	CA4 TPP LONDs	239	< 10	-	< LOD	< 10	-	< LOD	< 10	-
2		< LOD	< 10	-	< LOD	178	-	< LOD	< 10	-
3		357	< 10	-	< LOD	12591	-	< LOD	< 10	-
1	Free CA4 in DMSO/ Peanut oil	426	148	2.9	47	4153	0.01	27	435	0.06
2		< LOD	< 10	-	< LOD	2079	-	< LOD	< 10	-
3		572	103	5.6	< LOD	2140	-	< LOD	48	-

Figure 5.6 *In vivo* concentrations of CA4 and its major metabolite CA4G, 1 h post-injection with CA4 TPP LONDs and free CA4 in DMSO/peanut oil.
SW480 tumour xenografts were established in CD-1® nude male mice. On day 10 of tumour growth, mice were injected i.v. through the tail vein with a dose of 12.8 mg/kg CA4 TPP LONDs or i.p. with 50 mg/kg CA4 DMSO/peanut oil. After 1 h and tumour, liver tissue were excised and blood for plasma collected (n=3 per group). The samples were homogenised, dried, reconstituted in MeOH and analysed by LC-MS/MS for CA4 and CA4G detection. (A) Concentration of CA4 in ng/g of tumour, liver and ng/mL of plasma. The LOD for CA4 on LC-MS/MS was 10 ng. (B) PA of CA4G in tumour, liver and plasma samples. (C) Conversation of CA4 to CA4G ratio. Straight lines (–) in A and B show the median. Using a Mann-Whitney U test (two-tailed) no statistically significant differences were observed.

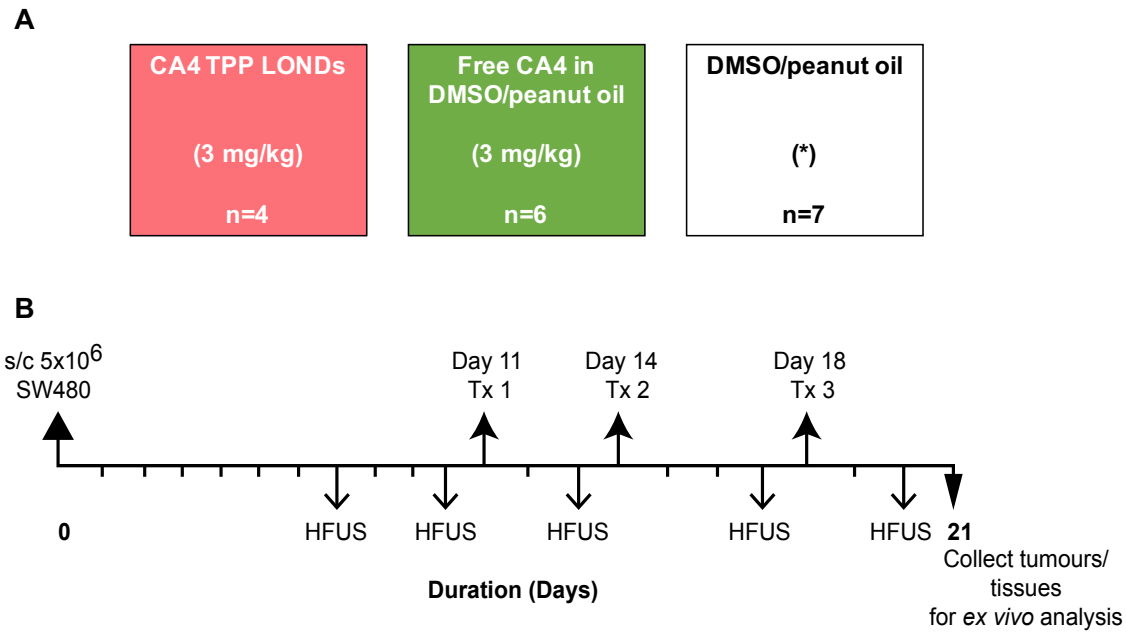

Figure 5.7 Treatment of SW480 human CRC xenografts with CA4 TPP LONDs. (A) SW480 human CRC xenografts were established in BALB/c nude male mice by s.c. injection of 5 x 10^6 cells on day 0. On day 7 of tumour growth mice were sorted according to tumour volume into three experimental cohorts: CA4 TPP LONDs (3 mg/kg), Free CA4 in DMSO/peanut oil (3 mg/kg) or DMSO/peanut oil at the equivalent volume of free CA4 in DMSO/peanut oil (*). (B) Treatment schedule: Treatments (Tx) began on day 11 of tumour growth where mice received 2 x 10^{13} CA4 TPP LONDs i.v. through the tail vein, free CA4 DMSO/peanut oil and DMSO/peanut oil i.p. Further treatments were performed on days 14 and 18. Tumour volume was monitored by HFUS. On day 21, 72 h after the final treatment mice were sacrificed and tumours and tissues were collected for *ex vivo* analysis. CA4 TPP LONDs prep. number 7 was used.

5.3.1 Anti-tumour activity following multiple dosing with CA4 TPP LONDs

CA4 TPP LONDs inhibited tumour growth compared with DMSO/peanut oil control however, this failed to reach a statistical significance (Figure 5.8). The CA4 TPP LONDs group and free CA4 in DMSO/peanut oil group showed similar growth rates (Figure 5.8). Free CA4 in DMSO/peanut oil treatment significantly inhibited tumour growth of SW480 xenografts after the first treatment when compared to control DMSO/peanut oil ($p=0.01$, Mann-Whitney U test, two-tailed) and CA4 TPP LONDs ($p=0.04$, Mann-Whitney U test, two-tailed) (Figure 5.8). Actual tumour volumes from HFUS and individual mice tumour volume data for each group are shown in Appendix C, Figure C.1. A modest increase in tumour doubling time was observed in CA4 TPP LONDs (median tumour doubling time 4.9 days) and free CA4 in DMSO/peanut oil (median tumour doubling time 4.4 days) treated groups however, these were not significantly different compared to control DMSO/peanut oil (median tumour doubling time 3.7 days) (Figure 5.9 A).

72 h after the final treatment, mice were sacrificed, tumours harvested and weighed (Figure 5.9 B). The median tumour weights were 0.8 g, 0.9 g and 1.1 g for CA4 TPP LONDs, free CA4 in DMSO/peanut oil and DMSO/peanut oil respectively. It should be noted that tumour mass was not recorded for 1/4 animals in the CA4 TPP LONDs group. These data support the increased tumour doubling time and growth delay in tumours from mice treated with either CA4 TPP LONDs or free CA4 DMSO/peanut oil as they weighed less than control DMSO/peanut oil treated tumours. The % tumour mass to body weight ratio was also calculated the median % of tumour/body weight ratio for mice treated with CA4 TPP LONDs and free CA4 DMSO/peanut oil was 4% in both cases, compared to 5% in DMSO/peanut oil mice (Figure 5.9 C).

As an indication of wellbeing mouse body weight was monitored and the % change in body weight throughout the treatment was calculated (Figure 5.9 D). Although not statistically significant from control mice treated with DMSO/peanut oil, a mild loss in weight (0.4%) was observed in mice treated with CA4 TPP LONDs after the second treatment (Figure 5.9 D). Individual mouse weights throughout the treatment regime are shown Appendix C, Figure C.2.

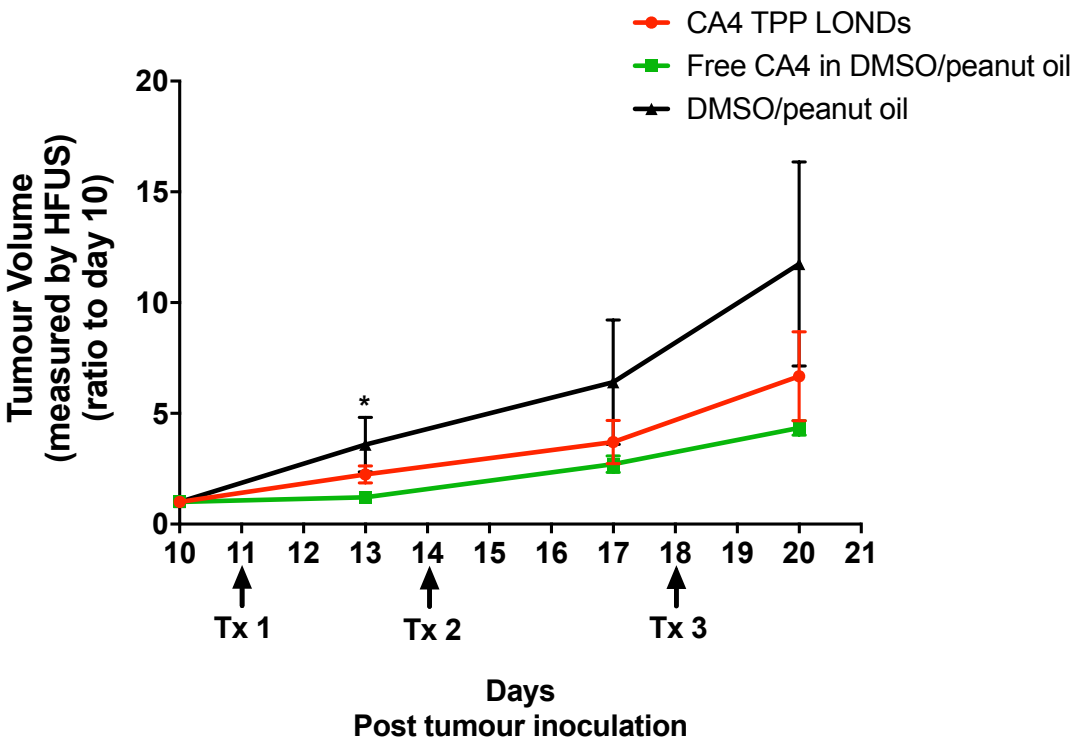

Figure 5.8 Tumour growth during multiple dosing with CA4 TPP LONDs, free CA4 in DMSO/peanut oil and DMSO/peanut oil.

Tumour volume ratios to day 10 are shown for each group. Tumour growth in the free CA4 DMSO/peanut oil group was significantly inhibited on day 13 compared to control DMSO/peanut oil (*, $p = 0.01$) and CA4 TPP LONDs (*, $p = 0.04$). Data represent the mean and error bars the SEM, p values were determined by Mann-Whitney U test, two-tailed. The absence of error bars indicates that the errors were smaller than the size of the symbol.

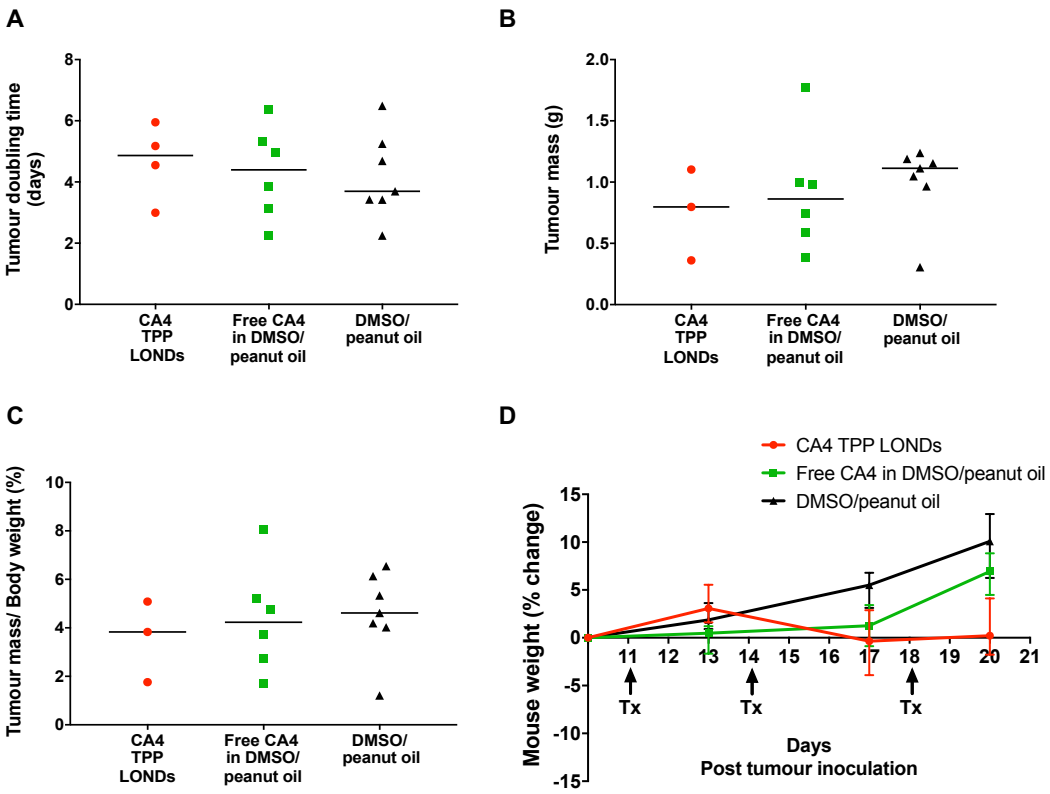

Figure 5.9 Analysis of tumour response and mouse wellbeing during multiple treatments with CA4 TPP LONDs, free CA4 in DMSO/peanut oil and DMSO/peanut oil.

(A) Tumour volumes doubling time in days: Although not significantly different (Mann-Whitney U test, two-tailed) treated tumours with CA4 TPP LONDs and free CA4 DMSO/peanut oil had higher doubling times compared to control DMSO/peanut oil. Straight lines (–) represent the median. (B) Tumour mass (g) on excision following three treatments. Tumours were smaller in the two treatment groups, however these were not statistically significantly different from DMSO/peanut oil control (Mann-Whitney U test, two-tailed). Straight lines (–) represent the median. (C) % Tumour mass/Body weight ratio. Straight lines (–) represent the median. (D) % change in mouse body weight throughout the treatment regime. This was calculated by dividing the weight gained or lost at each measurement by the starting weight x 100. Mice treated with CA4 TPP LONDs had a mild loss in body weight after the first and second treatment on days 11 and 17. Data represents the median and error bars the interquartile range.

5.3.2 Tumour histology following multiple dosing with CA4 TPP LONDs

Treatment with CA4 or CA4P leads to extensive haemorrhage evident within the first few hours post-injection followed by severe secondary necrosis (Dark *et al.*, 1997; Grosios *et al.*, 1999; Malcontenti-Wilson *et al.*, 2001). Perfusion (Table 1.1) in tumours treated with CA4 or CA4P begins to recover 24 h post-injection (Maxwell *et al.*, 1998; Zhao *et al.*, 2005a; Liu, Mason & Gimi, 2015). This is particularly relevant for this study, as tumours were excised 72 h after the final treatment and these would potentially be sufficient time for vascular recovery.

Examination of CA4 TPP LOND treated tumour sections showed areas of central haemorrhagic necrosis surrounded by viable tumour rim (Figure 5.10 A-I). In contrast, another tumour section from the same group was almost completely necrotic with only very small areas of viable tumour cells (Figure 5.10 A-II). These results suggest intratumoural delivery of CA4 from the TPP LONDs. Extensive central necrosis with a viable tumour rim was also observed after treatment with CA4 in DMSO/peanut oil, a large area of haemorrhage was seen at the tumour periphery (Figure 5.10 B). Areas of haemorrhage were also observed in tumours from mice treated with control DMSO/peanut oil (Figure 5.10 C). Suggesting that some haemorrhage was unrelated to treatment and was potentially associated with leaky vasculature.

To quantitate the degree of haemorrhage and necrosis in each group, the % area of tumour per mm^2 with haemorrhage and necrosis were determined (Figure 5.11). Interestingly, the higher % of haemorrhage was observed in the control DMSO/peanut oil group compared to CA4 TPP LONDs and free CA4 in DMSO/peanut oil (Figure 5.11 A). However, no statistically significant differences were observed between the groups (Mann-Whitney U test, two-tailed). This further supported the assumption that the extent of haemorrhage observed was related to the inherently leaky tumour vasculature.

As seen in Figure 5.8 and Figure 5.9 B, tumours treated with DMSO/peanut oil were among the largest in terms of size (mm^3) and mass (g) from the treatment cohorts. Therefore, a correlation between tumour size and % haemorrhage was next determined for all groups combined and a weak positive correlation was observed using Spearman's correlation coefficient ($r=0.6$, $p=0.03$, Figure 5.11 B). No significant differences were observed between the groups in terms of % necrosis (Mann-Whitney U test, two- tailed) (Figure 5.11 C). Moreover, no significant correlation was

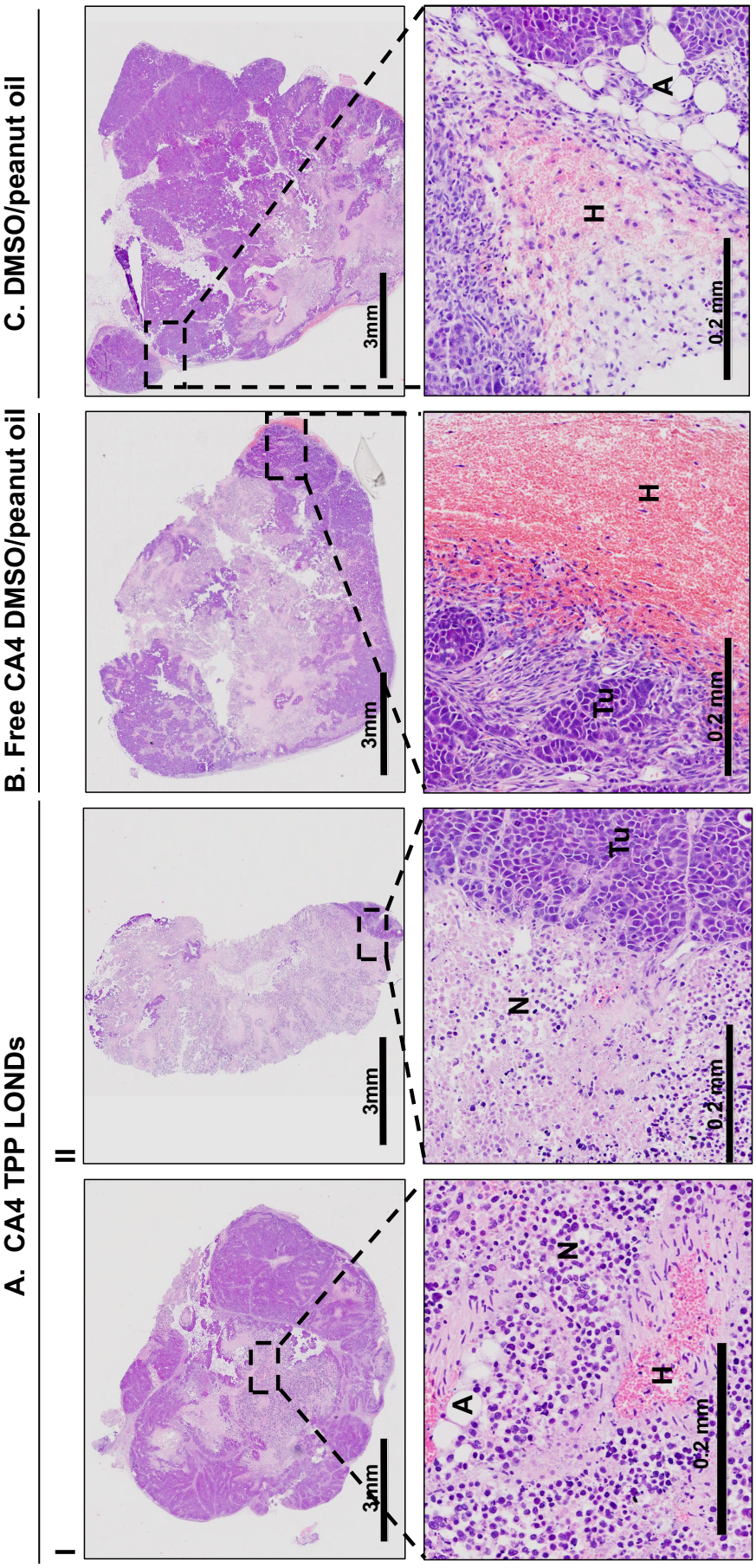
A. CA4 TPP LONDs
B. Free CA4 DMSO/peanut oil
C. DMSO/peanut oil
I
II
3mm
0.2 mm
A
N
H
Tu

Figure 5.10 Tumour histology after multiple treatments with CA4 TPP LONDs, free CA4 in DMSO/peanut oil and DMSO/peanut oil.

Histological images of tumours stained with H & E. (A- I) Tumour tissue 72 h post-treatment with CA4 TPP LONDs, showing areas of central haemorrhagic necrosis (haemorrhage labelled as H and necrosis labelled as N). (A-II) Additionally a different tumour from the CA4 TPP LONDs treatment group was completely necrotic with only small areas of viable tumour cells (labelled as Tu). (B) Tumour tissue 72 h post-treatment with free CA4 DMSO/peanut oil showing extensive central necrosis (N) with viable tumour cells (Tu) and a large area of haemorrhage at the tumour periphery. (C) Tumour tissue 72 h post-treatment with control DMSO/peanut oil showing areas of haemorrhage (H), extensive necrosis (N) and viable tumour cells (Tu). Adipocytes labelled as A in images. Top image show the entire tumour section and square box shows the area of the bottom image. Scale bars indicate 3 mm and 0.2 mm. CA4 TPP LONDs prep. number 7.

observed between % necrosis and tumour volume (Figure 5.11 D) or % haemorrhage and % necrosis (Figure 5.11 E) using Spearman's correlation coefficient.

MVD was determined to investigate any potential differences in the number of blood vessels (Figure 5.12 A and B). The immunostained pattern appeared very similar between the two treatment groups and control DMSO/peanut oil. No statistically significant differences were observed in MVD between the groups (Mann-Whitney U test, two-tailed).

5.3.2.1 Assessment of heart tissue for cardiovascular toxicity

A major concern associated with the use of CA4P is cardiovascular toxicity with a number of clinical trials reporting such toxicities (Dowlati *et al.*, 2002; Rustin *et al.*, 2003; Mooney *et al.*, 2009). Previous *in vivo* work with CA4P in rats at doses ≤ 60 mg/kg revealed after histopathological examinations of heart tissue, infiltration of inflammatory cells around capillaries, pyknosis of the capillary endothelial cells and oedema around the capillaries while at a 120 mg/kg dose severe necrosis of the myocardium was observed (Tochinai *et al.*, 2016).

Longitudinal sections of the myocardium from treated animals are shown in Figure 5.13. The presence of infiltrating inflammatory cells around capillaries, pyknosis around the endothelial cells of capillaries or necrosis of the myocardium were not observed in any of the cohorts assessed (Figure 5.13 B-D for CA4 TPP LONDs, free CA4 DMSO/peanut oil and DMSO/peanut oil respectively).

5.4 Discussion

5.4.1 Single dose of CA4 TPP LONDs, free CA4 in DMSO/peanut oil and TPP LONDs

Tumour histology showed that CA4 TPP LONDs caused extensive central haemorrhage 24 h post-injection, in contrast, free CA4 in DMSO/peanut oil had extensive haemorrhage in the central and peripheral regions of the tumour 1 h post-injection. As CA4 TPP LONDs are untargeted particles and their average size is <100 nm it would be plausible to assume that one of the main mechanism of intratumoural uptake is the EPR effect. The EPR effect is where NPs ≤ 200 nm such as LONDs passively accumulate in tumours due to leaky vasculature. This may explain why there is a delayed response in terms of haemorrhage. Another possibility is that CA4 TPP LONDs are being retained in the tumour where the CA4 payload is slowly released. A study with a untargeted NPs carrying both methotrexate and CA4 showed

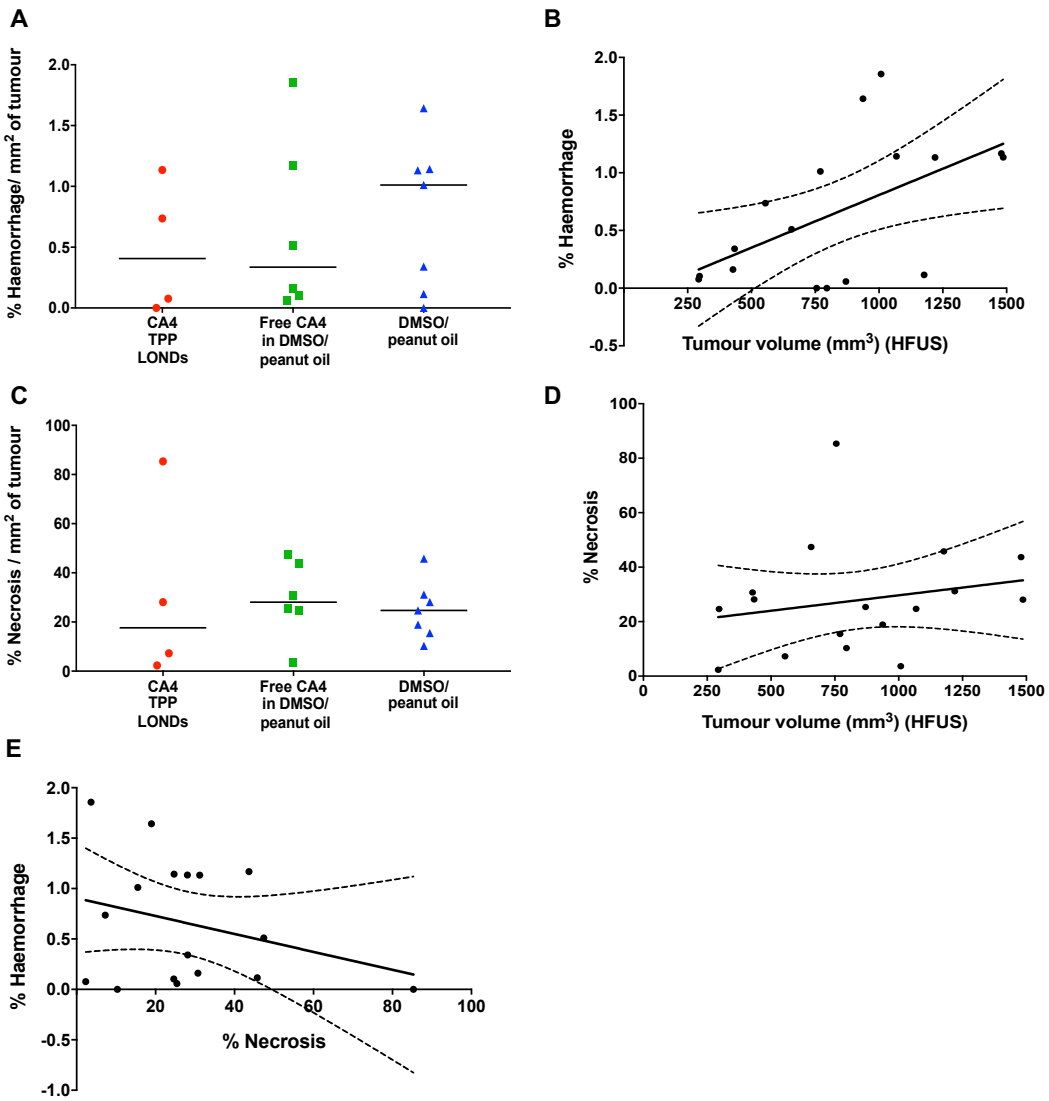

Figure 5.11 Quantitative analysis of tumour histology following multiple treatments with CA4 TPP LONDs, free CA4 in DMSO/peanut oil and DMSO/peanut oil.

(A) % are of haemorrhage per mm^2 of tumour. Straight lines (–) indicate the median value. (B) The relationship between % area with haemorrhage and tumour volume using Spearman's correlation showed a weak positive correlation between the two variables (r=0.6, * p=0.03, 95% confidence interval 0.07 to 0.8, two-tailed). (C) % necrosis per mm^2 of tumour. Straight lines (–) indicate the median value. (D) Relationship between necrosis and tumour size using Spearman's correlation showed no correlation between the two variables (r=0.3, p=0.31, 95% confidence interval -0.3 to 0.7, two tailed). (E) Relationship between % haemorrhage with % necrosis. Spearman's correlation showed no correlation between the two variables (r=-0.12, p=0.63, 95% confidence interval -0.6 to 0.4, two tailed). The solid line denotes line of best fit and the dotted lines indicate the 95% confidence band in B, D and E. CA4 TPP LONDs prep. number 7 was used.

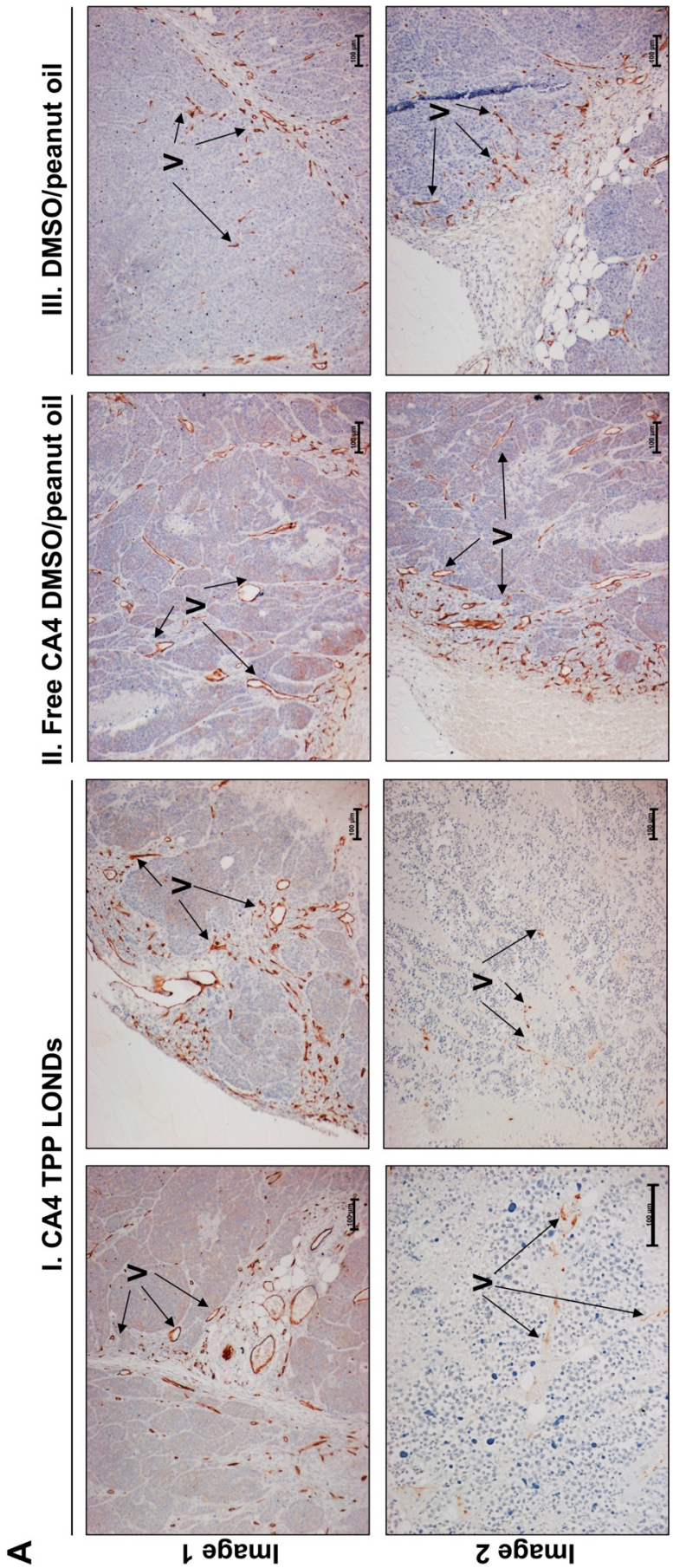
A
I. CA4 TPP LONDs
II. Free CA4 DMSO/peanut oil
III. DMSO/peanut oil
Image 1
Image 2
V
100 um

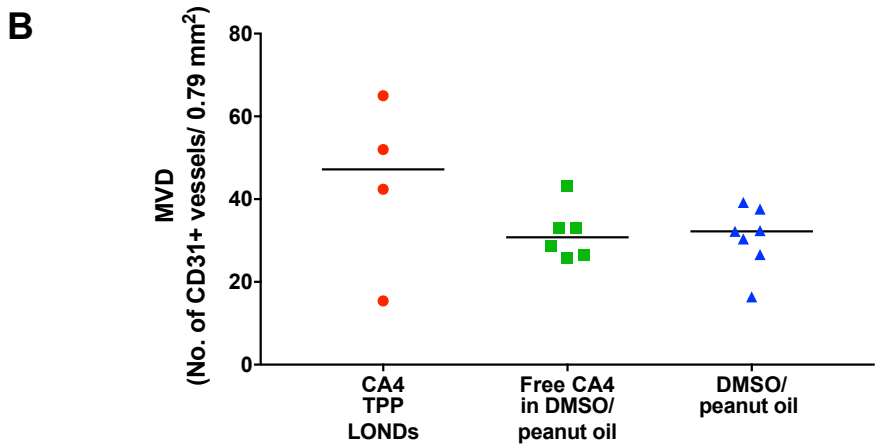

Figure 5.12 MVD following multiple treatments with CA4 TPP LONDs, free CA4 in DMSO/peanut oil and DMSO/peanut oil.

Immunohistochemical images of tumours stained with a rat anti-mouse CD31 antibody and CD31 + vessels were visualised with DAB. (A-I) Tumour section from CA4 TPP LOND treatment showing a number of CD31 positive + vessels (labelled as V and arrows show some representative vessels). (A-II) Tumour section from free CA4 DMSO/peanut oil treatment showing a number of CD31 + vessels. (A-III) Tumour section from DMSO/peanut oil treatment group, also showing a number of CD31 + vessels. Scale bars indicate 100 μm. Image 1 and 2 represent two different FOV from the same tumour section. (B) MVD: number of CD31+ blood vessels per 0.79 mm^2 of tumour (n=5 hot spots). Straight lines (–) represent the median. No statistically significant differences were observed by Mann-Whitney U test, two-tailed. CA4 TPP LONDs prep. number 7 was used.

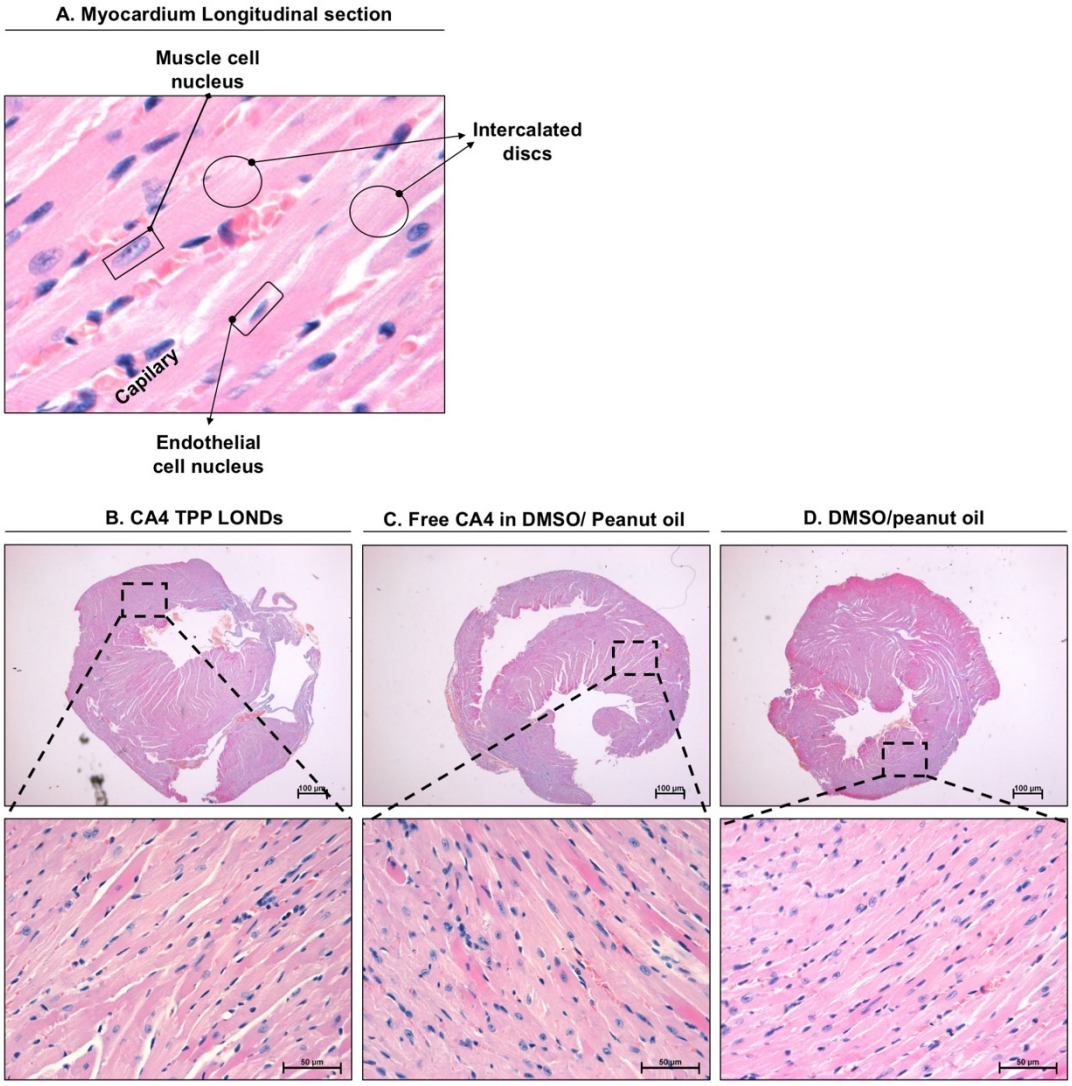

Figure 5.13 Histological examination of heart tissue following multiple treatments with CA4 TPP LONDs, free CA4 in DMSO/peanut oil and DMSO/peanut oil.

Histological images of hearts stained with H & E. (A) Myocardium longitudinal section. (B) CA4 TPP LONDs treated heart tissue section. (C) Free CA4 DMSO/peanut oil treated heart tissue. (D) DMSO/peanut oil treated heart tissue. No evidence of endothelial cell pyknosis around the capillaries or myocardium necrosis, or infiltrating inflammatory cells were observed. Scale bars indicate 100 μm and 50 μm. CA4 TPP LONDs prep. number 7 was used.

a longitudinal increase in CA4 tumour concentration compared to free drug due to the EPR effect (Wang *et al.*, 2013). TPP LONDs caused a < 0.5% haemorrhage, the low level presumably is due to the inherent leaky architecture of the tumour vasculature. Tumour vessels are predominantly thin-walled capillaries or sinusoids with more often just an endothelial lining stabilised by a basement membrane (Vincent *et al.*, 2005). These are prone to spontaneous haemorrhage (Vincent *et al.*, 2005).

Secondary to the haemorrhage effect of CA4 is extensive, central necrosis with a characteristic viable tumour rim usually 24 h post-treatment (Grosios *et al.*, 2000). CA4 TPP LONDs (12.8 mg/kg) and free CA4 in DMSO/peanut oil (50 mg/kg) did not cause any significant central necrosis post-injection. A single i.p. dose of 100 mg/kg in murine adenocarcinoma NT tumours and human breast cancer (MDA-MB-231) tumours showed the characteristic haemorrhagic necrosis with less than 5% viable tumour cells around the rim (Dark *et al.*, 1997). Similar data was reported for SW1222 tumour xenografts where a single 200 mg/kg dose of CA4P i.p. showed no morphological changes after 1 h but at 24 h the centre of the tumour was necrotic with only a small viable rim (El-Emir *et al.*, 2005). Another study on SW1222 tumours showed that at 30 mg/kg, CA4P produced patchy haemorrhagic necrosis 24 h after treatment, whereas 100 mg/kg and 200 mg/kg produced extensive necrosis with only a viable rim present consistent with previous reports (Lankester *et al.*, 2007). 24 h post-treatment with CA4P (150 mg/kg) in MAC29 tumours caused 90.4% central haemorrhagic necrosis within a viable tumour rim (Holwell *et al.*, 2002). 100 mg/kg CA4P used in KHT sarcoma xenografts also showed extensive central necrosis and a viable rim 24 h after treatment (Li, Rojiani & Siemann, 1998). There was an increase in the cell killing effect in KHT sarcomas and this was dose dependent (Li, Rojiani & Siemann, 1998).

Although treatment with free CA4 and CA4 TPP LONDs showed evidence of haemorrhage suggesting extravasation of RBCs from vessels, the MVD was not affected. A single dose of 100 mg/kg CA4P was found to significantly reduce vessel density after 1 h in a mouse model of colorectal cancer metastases (Malcontenti-Wilson *et al.*, 2001). The same study also reported on the heterogeneity that occurs within the tumour after CA4P treatment as some areas of the tumour were affected more or differently hence the presence of a viable rim (Malcontenti-Wilson *et al.*, 2001). The vasculature and endothelial structures in the periphery and central core of tumours are different, the vasculature in the periphery being composed of larger vessels with faster flowing blood compared to the central vessels with any changes

to blood flow at the tumour periphery are less damaging (Tozer *et al.*, 2001). It should be noted that lack of significant reduction in MVD does not necessarily point towards treatment failure as the functional biology of the tumour, the perfused vasculature, maybe altered. Studies using Hoechst 33342 as a marker of perfusion showed that blood vessels were still distributed throughout the tumour after a 1 h i.p. dose of 200 mg/kg but perfusion was confined to the tumour rim (El-Emir *et al.*, 2005). The study presented here measured the total number of CD31+ vessels of tumours rather than the CD31+ vessels that were actually functional.

Another histological feature that was examined following single treatment with CA4 TPP LONDs, TPP LONDs and free CA4 was mitosis. CA4 causes G2/M block following 24 h of *in vitro* exposure therefore, the ability of CA4 to cause G2/M block was assumed to lead to increased numbers of mitoses *in vivo*. This block occurs in metaphase during the M phase of the cell cycle (Kanthou *et al.*, 2004) .The results 1 h post-treatment showed similar numbers of mitoses whereas at 24 h free CA4 and CA4 TPP LONDs, showed a trend to a higher number of mitoses compared to the control. G2/M arrest was not observed in non-Hodgkin's lymphoma following treatment with 800 mg/kg of CA4P, the authors suggested that the levels of CA4 in plasma did not reach the necessary level to cause G2M arrest *in vivo* as *in vitro* which may be the case here (Nabha *et al.*, 2001).

Conventional delivery of free drugs requires very high circulating doses to achieve the desired bioavailability in tumour tissue. This then produces high concentrations of drug circulating throughout the body leading to harmful side effects to other tissues. However, NP PK may be very different and the initial stages of NP development require insight into tissue biodistribution following systemic administration (Sanhai *et al.*, 2008). This work showed that CA4 TPP LONDs at approximately four times lower the dose of free CA4 (12.8 mg/kg vs 50 mg/kg), following 1 h post-injection delivered similar amounts of CA4 intratumourally. As CA4 was not detected in liver or plasma of CA4 TPP LOND treated mice, the levels present might have been below the LOD (10 ng). The EPR effect and the LONDs structure, PEG on the surface to increase circulation time and improve uptake, small size to allow cellular uptake, may promote accumulation in tumour. CA4G was found in the liver of CA4 TPP LONDs treated mice suggesting release from the LONDs that were distributed in the liver, this would eventually be excreted.

In contrast, CA4 was found in liver and plasma samples of free CA4 treated mice demonstrating non-specific distribution/uptake. Although most of the drug in both

cases was in the inactive glucuronide form CA4G suggesting the rapid metabolism of CA4 when administered free. CA4G was also detected in the tumour of free CA4 treated mice, drugs injected i.p. could undergo hepatic metabolism before even entering the bloodstream however, this may have escaped from the liver or direct intratumoural metabolism.

Glucuronidation is a key metabolic process involved in CA4 clearance and is catalysed by UDP glucosyltransferases, specifically UGT1A9 and UGT1A6 mainly expressed in the liver (Aprile, Del Grosso & Grosa, 2010). Previous reports have shown that normal colon also expresses UGT1A, including UGT1A9 isoform (Strassburg, Manns & Tukey, 1998; Strassburg *et al.*, 1999), possibly as a first-pass metabolism before compounds reach the liver. It is therefore not surprising that some CRCs have maintained the ability to express some of these UGT1As (Landmann *et al.*, 2014). SW480 were found to express low levels of UGT1A, enabling tumour cells to directly metabolise drugs (Landmann *et al.*, 2014). This tumour cell direct metabolism severely impairs the efficacy of anti-cancer drugs and promotes cancer cell resistance. This may also explain the presence of CA4G in tumour samples from mice treated with free CA4 in DMSO/peanut oil. CA4G was not detected in tumour samples from mice treated with CA4 TPP LONDs, the levels were either below the LOD for CA4G (unknown) as CA4 TPP LONDs were slowly releasing CA4 into the tumour or CA4 was potentially still trapped in an intracellular compartment (endosomes) and not yet released into the tumour cells. However, the former is more plausible as extensive haemorrhage is also only observed after 24 h post-injection with CA4 TPP LONDs.

5.4.2 Multiple treatments with CA4 TPP LONDs, free CA4 in DMSO/peanut oil and DMSO/peanut oil

Single doses of CA4P or CA4 are known to either cause no or very modest tumour growth delays at doses ranging between 50-500 mg/kg, in contrast, to repeated dosing schedules which cause significant growth delays (Grosios *et al.*, 1999; Hill *et al.*, 2002). The anti-tumour activity of CA4 TPP LONDs was therefore, evaluated following multiple treatments (three in total). Tumour doubling time was insignificantly increased in both the CA4 TPP LONDs and free CA4 in DMSO/peanut oil compared to DMSO/peanut oil control. Although, tumour volumes were significantly lower in mice treated with free CA4 in DMSO/peanut oil than those treated with CA4 TPP LONDs and DMSO/peanut oil control after the first treatment. Despite, tumour histology showing extensive central necrosis (85% in 1/4) and evidence of

haemorrhage after multiple treatments with CA4 TPP LONDs, these observations were not statistically different from free CA4 in DMSO/peanut oil and DMSO/peanut oil.

Vincent *et al.,* (2005) treated B16 melanoma tumours with CA4P every 2 days and monitored tumour growth for a total of 8 days (four treatments in total) (Vincent *et al.*, 2005). They used a dose of 5 mg/kg and showed a significant growth delay which was associated with extensive necrosis and a reduction in MVD (Vincent *et al.*, 2005). In contrast, tumour growth inhibition in colorectal liver metastases was only observed after daily dosing of 15 mg/kg for a consecutive 21 days, lower doses were tested and, although were all well tolerated, had no effect (Malcontenti-Wilson *et al.*, 2001). A significant growth delay was reported in lung cancer xenografts following daily doses of 50 mg/kg CA4P for a total of 21 days, this effect was not associated with any changes in MVD (Boehle *et al.*, 2001). Another study in non-Hodgkin's lymphoma xenografts investigated the antitumor and anti-angiogenic activity of CA4P (Nabha *et al.*, 2001). Different dose ranges were studied; a single dose of 800 mg/kg, two doses of 400 mg/kg, four doses of 200 mg/kg and eight doses of 100 mg/kg. Interestingly the maximum antitumor activity was observed when CA4P was given at 200 mg/kg every day for 4 days (Nabha *et al.*, 2001). This further demonstrates that CA4 activity is greatly enhanced when administered at lower doses and more often. The same paper demonstrated that 24 h after treatment there was a significant reduction in blood vessel % (in the 800 mg/kg or 100mg/kg x8 dose), however after 48 h the vessel number started to return (Nabha *et al.*, 2001). Here, no statistically significant difference in MVD was observed 72 h after the last treatment potentially this was due to recovery such as in the lymphoma xenograft model.

Collectively, previous work with CA4P show the heterogeneity in tumour response between the different types of tumours and the dosing required to cause a significant growth delay. Tumour size also affects tumour response to CA4 treatment. A single i.p. injection of 25 mg/kg in rhabdomyosarcomas xenografts in rats showed significant growth delay in large tumours >7000 mm^3 and no growth delay was observed in small tumours <1000 mm^3 (Landuyt *et al.*, 2000). Interestingly this tumour growth delay or antitumor activity following single treatment was not permanent as tumours resumed tumour growth (Landuyt *et al.*, 2000).

NP formulations of CA4 have also been used in preclinical work. Wakaskar *et al.,* (2005) used polymer micelles to encapsulate CA4. *In vivo*, they investigated the PK of the polymer micelles compared to CA4P 2 and 24 h post-injection with 1 mg/kg

and also monitored breast tumour growth after a single 1 mg/kg dose for 5 days. Their results showed that the polymer micelles enhanced the potency of CA4 by increasing intratumoural uptake and retention compared to CA4P therefore causing a significant growth delay (Wakaskar *et al.*, 2015). However, CA4 from the polymer micelles was also present in liver, spleen, lungs and kidney tissue 2 h post-injection (Wakaskar *et al.*, 2015). A liposome formulation (approximately 100 nm in size) with a derivative of CA4 was produced and the group studied their anti-tumour activity in Wnt-1 breast cancer xenografts (22 and 40 mg/kg) (Moiseeva *et al.*, 2012). Following four treatments once a week the liposome formulation did not cause any significant growth inhibition (Moiseeva *et al.*, 2012). The lack of anti-tumour activity might have been due to the timings between the treatments as this would allow tumour recovery.

Systemic administration of non-targeted NPs can preferentially accumulate in tumour due to the EPR effect and poor lymphatic drainage however, they can also escape from the circulation through vascular openings known as fenestrations into other organs (Gaumet *et al.*, 2008). The low dose used 3 mg/kg was well tolerated and did not cause any severe toxicities in terms of weight loss or cardiac toxicities when assessing heart histology as previously reported in rats treated with 120 mg/kg CA4P (Tochinai *et al.*, 2016).

5.4.3 Conclusions

The single dose experiment had some limitations, firstly the small numbers of animals per group, made it difficult to distinguish any statistical significant differences between the groups. Due to equipment issues, the acquisition of 24 h biodistribution data from single treatment with CA4 TPP LONDs was not possible. This might have shown an increase in CA4 uptake to support the assumption of a slow release of drug from CA4 TPP LONDs or longer retention in the tumour.

However, in contrast, a longer retention of CA4 TPP LONDs in tumour should therefore equate to an enhanced anti-tumour activity, which is not the case following multiple treatments with low dose CA4 TPP LONDs. This might be explained by PK, non-targeted particles such CA4 TPP LONDs are assumed to have a longer blood circulation therefore there is an accumulation of drug in the tumour as shown by the 1 h biodistribution data (early PK response), however because they are non-targeted and not bound to any part of the tumour they can be easily washed out back to the blood circulation (late PK response) (Durymanov, Rosenkranz & Sobolev, 2015). Figure 5.14 summarises some of these key points. From the literature on CA4P tumour resumes growth between 24 and 48 h post-treatment, therefore the timings

between the treatments in this study possibly allowed the tumour enough time to clear CA4 and begin regrowth. Moreover, the mode of action of CA4 itself might hinder the activity of CA4 TPP LONDs. An initial release and/or uptake of a number of CA4 TPP LONDs in the tumour could potential cause rapid vascular shutdown preventing any further uptake of remaining CA4 TPP LONDs circulating. A full PK time course would be required to fully understand the kinetics of intratumoural delivery and/or retention.

In conclusion, CA4 TPP LONDs were able to successfully deliver drug intratumourally and cause some initial histopathological changes indicating drug release. The multiple dosing schedules pointed towards poor retention in the tumour, indicating the need for some form of targeting or potentially a more frequent dosing schedule <48 h.

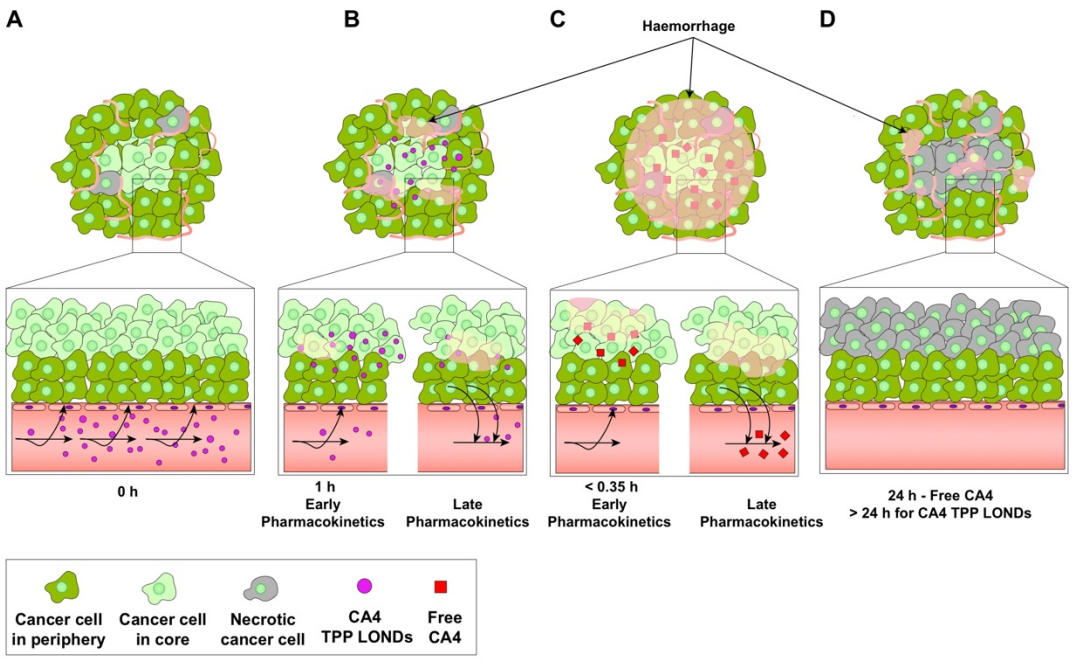

Figure 5.14 Schematic showing potential mechanisms for PK and tumour histopathological responses following administration of CA4 TPP LONDs.
(A) It is assumed that untargeted CA4 TPP LONDs preferentially accumulate in the tumour region of the vasculature following intravenous administration. (B) Uptake and initial over accumulation of CA4 TPP LONDs in the tumour due to the leaky vasculature and poor lymphatic drainage (EPR effect) (early pharmacokinetics). Because CA4 TPP LONDs are untargeted some fail to remain in the tumour and are extravasated back out and washout out through the circulation due to high interstitial pressures (late pharmacokinetics). Any trapped CA4 TPP LONDs in the tumour result in slow release of CA4 over time and the cause of haemorrhage. (C) Delivery of CA4 at a high enough dose > 50 mg/kg via the circulation occurs within the first 0.35 h (plasma half-life of CA4, Kirwan *et al.,* 2004) of administration resulting in extensive haemorrhage due to the rapid effects of CA4. CA4 is then cleared from tumour and the circulation. (D) 24 h post-injection of high dose CA4 (free) most of the tumour core is necrotic with patchy areas of haemorrhage and the periphery of the tumour remains viable. In the case of slow release of CA4 from trapped CA4 TPP LONDs the histopathological response would be higher % of haemorrhage and subsequent necrosis with a viable rim at a > 24 h time point. The tumour can resume growth from this viable rim as it can acquire oxygen and nutrients from nearby normal vessels.

Chapter 6

CA4 ThMBs for US triggered targeted delivery of CA4

6.1 Introduction

Delivery of CA4 TPP LONDs *in vitro* leads to extensive changes to the endothelial cell cytoskeleton whilst *in vivo* the results suggested that there is an initial accumulation of CA4 TPP LONDs in tumour due to the EPR effect, while the histology results suggested that any retained CA4 TPP LONDs lead to the slow release of CA4 over time into the tumour. However, as CA4 TPP LONDs were untargeted and delivered systemically it does not eliminate the potential of unspecific uptake into other organs through vessel fenestrations.

To further improve drug delivery CA4 TPP LONDs were attached to thMBs and targeted to VEGFR2 to produce CA4 thMBs as performed for CA4 TA LONDs, although, these were produced using a two-step method to avoid the destabilisation of the LONDs. The rationale for developing the MBs-LOND construct and using an external US trigger as performed for CA4 TA LONDs was to enable the controlled release of CA4 at a specific target region thereby minimizing drug release in areas not exposed to US. This approach of direct attachment to MBs is preferred over co-delivery for example, as it will increase the local concentration of drug where US is applied and reduces systemic concentrations (Kooiman *et al.*, 2014).

Significant changes to tumour histology were not observed early post-injection with low doses of CA4 TPP LONDs alone, indicating that assessment of tumour histology was not sufficient to detect any subtle changes caused by CA4 TPP LONDs. CA4P treatment has been shown in a number of studies to cause significant changes to the functional vasculature of tumours with the rapid reduction in blood flow caused by vasoconstriction or vascular occlusion (Table 1.1. and Figure 1.4). The reduction in blood flow was dose-dependent and maximal blood flow shutdown was observed within 1-6 h post-injection and was sustained for 24 to 48 h (Siemann, 2011).

The fluorescent dye, Hoechst 33342, can be used to identify and quantify the functional vasculature of tumours in frozen tissue sections when viewed under ultraviolet light (Smith *et al.*, 1988). Following, i.v. injection of Hoechst 33342, cells surrounding blood vessels are the first to incorporate the dye (Smith *et al.*, 1988). Although, not specific for endothelial cells, the rapidity of intracellular uptake of Hoechst 33342 in combination with its poor diffusion across cell layers make it a useful and easy imaging tool for measuring tumour perfusion *in situ* (Smith *et al.*, 1988; Goertz *et al.*, 2002). Measurements of tumour perfusion by Hoechst 33342 have been correlated with measurements of perfusion by High Frequency Doppler US imaging (Goertz *et al.*, 2002). Detection of total Hoechst 33342 in the tumour can

act as a relative global index of the whole tumour perfusion (Wildiers *et al.*, 2003). Hoechst 33342 has been extensively used to study perfusion in CA4P and CA4-treated tumours, with results showing a significant reduction within the first few hours post-injection (Dark *et al.*, 1997; Grosios *et al.*, 1999; Chaplin & Hill, 2002; El-Emir *et al.*, 2005; Salmon & Siemann, 2007).

Following, production of ThMBs with CA4 TPP LONDs (CA4 thMBs), the aim of this work was to test potential release of CA4 from US-triggered thMBs *in* vitro and to assess, using Hoechst 33342, changes in tumour blood flow as an indicator of drug release and/or uptake from CA4 *in vivo*.

6.2 CA4 ThMBs *in vitro*

To enable the controlled delivery, retention and release of CA4 from LONDs, they were attached to thMBs which are targeted to VEGFR2. CA4 thMBs were produced on-chip using a two-step process (methods section 2.4.1.2). Briefly, MBs were formed prior to LOND attachment. The NeutrAvidin functionalised LONDs were introduced into the chip via a different inlet channel further downstream from MB production. MBs and LONDs were then allowed to mix along a serpentine channel and assemble via NeutrAvidin-biotin binding (Figure 1.8). The duration of LOND MB mixing along the serpentine was approximately 1.14 s. (Mico, 2017).

To investigate delivery of CA4 via thMBs with and without the US trigger, +/- T, *in vitro,* assessment of MT disruption using IF was performed. 5 x 10^4 CA4 thMBs which equated to a 100 nM CA4 concentration were used to treat VEGFR2 expressing SVR cells for 2 h at 37°C. An US trigger was applied to the SVR cells using the specifically designed UARP, four minutes after the CA4 thMBs were added to the SVR cells which allowed for optimal binding. The trigger was tone burst and results in thMB destruction (McLaughlan *et al.*, 2017). The results in Figure 6.1, showed untreated SVR cells exposed to the US trigger alone with MT filaments spreading throughout the cytoplasm (Figure 6.1 A), indicating that the trigger alone did not cause any apparent morphological changes to the cells. In contrast, SVR cells treated with CA4 TPP LONDs + T and CA4 thMBs + T showed MT disruption characteristic of the uniformly stained pattern of dispersed tubulin throughout the cytoplasm as a result of depolymerised MTs (Figure 6.1 B and C).

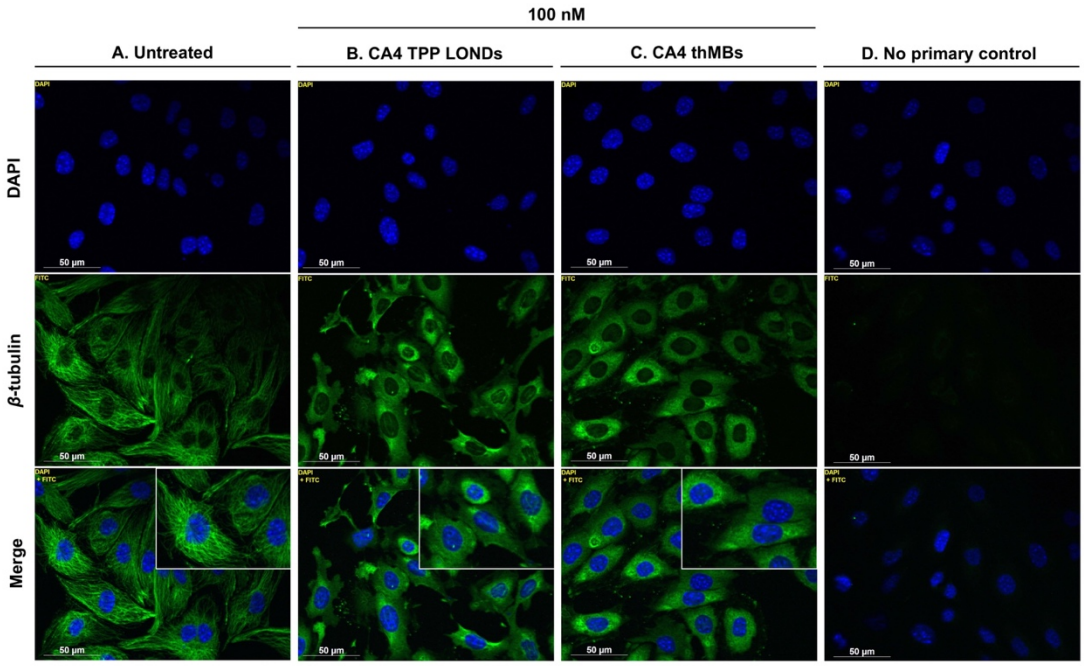

Figure 6.1 CA4 thMBs with an US trigger *in vitro.*

To assess delivery of CA4 by US-triggered thMBs, SVR cells were treated with CA4 thMBs followed by an US trigger (+ T) and MT disruption was investigated by IF. CA4 thMBs (targeted to VEGFR2) were produced on-chip using a two-step process, with the slow mixing and attachment of NeutrAvidin functionalised CA4 TPP LONDs downstream of MB production. 3.4 x 10^7/mL CA4 thMBs were produced with a mean size of 2.4 ± 1.5 μm. 5 x 10^4 CA4 thMBs were added onto the SVR cells which equated to a 100 nM CA4 concentration. CA4 thMBs were allowed four minutes to bind to VEGFR2 on SVR cells and then were burst by an US using the specifically designed UARP (10 μs, tone burst, PRF 1 kHz with a peak negative pressure of 260 kPa). Following, US the cells were incubated for 2 h at 37°C, cells were subsequently fixed, immunostained for β-tubulin using a mouse monoclonal anti-β-tubulin antibody and visualised using a biotinylated rabbit anti-mouse and FITC-labelled avidin. The slides were mounted with prolong Gold containing DAPI. (A) Untreated control SVR cells + T, showed filamentous MTs spreading throughout the cytoplasm. (B) SVR cells exposed to 100 nM CA4 TPP LONDs + T, caused MT disruption characteristic of tubulin dispersed throughout the cytoplasm as a result of MT depolymerisation. (C) SVR cells treated with 5 x 10^4 thMBs with CA4 TPP LONDs at 100 nM + T showed disrupted MTs, characterised by complete depolymerisation with a subsequent tubulin dispersion throughout the cytoplasm. Inset images show magnified cells in panels A-C. (D) No primary antibody, with minimal background indicating the specificity of the anti-β-tubulin antibody. Scale bars indicate 50 μm. Prep. number 8 was used.

IF staining of *β*-tubulin from untreated SVR cells without T, showed long filamentous MTs spreading throughout the cytoplasm (Figure 6.2 A). Treatment with CA4 TPP LONDs which were used as a positive control at 100 nM caused MT disruption and this was characterised by tubulin dispersed throughout the cytoplasm as a result of MT depolymerisation and uniformly stained it and with tangled MTs around nuclei (Figure 6.2 B). Interestingly, 100 nM CA4 thMBs – T also caused MT disruption with the same pattern as observed for CA4 TPP LONDs (Figure 6.2 C). This suggested that CA4 was released from the thMBs construct and entered into SVR cells in the absence of an US trigger. The 2 h incubation time presumably resulted in dissolution of thMBs whereby the gas core was lost and CA4 TPP LONDs were free to be internalised into SVR cells.

6.3 Delivery of CA4 thMBs *in vivo*

To investigate delivery of CA4 via US-triggered thMBs *in vivo* for the first time a small-scale pilot study was conducted and measurements of tumour and tissue perfusion using Hoechst 33342 as a marker of perfusion were performed. Mice bearing SW480 human CRC xenografts on day 11 of tumour growth were sorted into three groups according to HFUS tumour volume measurements (Figure 6.3). On day 14 of tumour growth one group (n=4) received a 200 µL i.v. infusion (0.1 mL/min) of 1.65 x 10^6 thMBs with CA4 TPP LONDs at a dose of 0.001 mg/kg. The concentration, diameter and CA4 loading of the CA4 thMBs solution measured by LC-MS/MS was 8.25 x 10^6/mL, 2.6 ± 1.5 *µ*m and 0.0001 mg/mL respectively (Appendix D, Figure D.1). It should be noted that this dose is the maximum possible dose that can be delivered by CA4 thMBs when using prep. number 10 (Table 4.1) for production as this needed to be diluted by 2000 to 10^{11} LONDs/mL which is further diluted by 2. The second group (n=3) received a 100 *µ*L i.v. infusion (0.1 mL/min) of CA4P in PBS at 50 mg/kg as a positive control as this dose has been shown to cause reduction in perfusion and also to enable i.v. administration (Chaplin, Pettit & Hill, 1996). The third group (n=3) received a 100 *µ*L i.v. infusion (0.1 mL/min) of PBS. The i.v. infusion was well tolerated with no immediate adverse reactions. 1 h post-injection all mice received a 15 mg/kg i.v. injection of Hoechst 33342 and were sacrificed 1 min later and tumour, liver and heart tissue were harvested. To assess tumour perfusion 1 h post-injection was chosen as previous studies using CA4P in both colon and mammary carcinoma cells have shown this to be the time of maximal perfusion reduction (Murata, Overgaard & Horsman, 2001; El-Emir *et al.*, 2005).

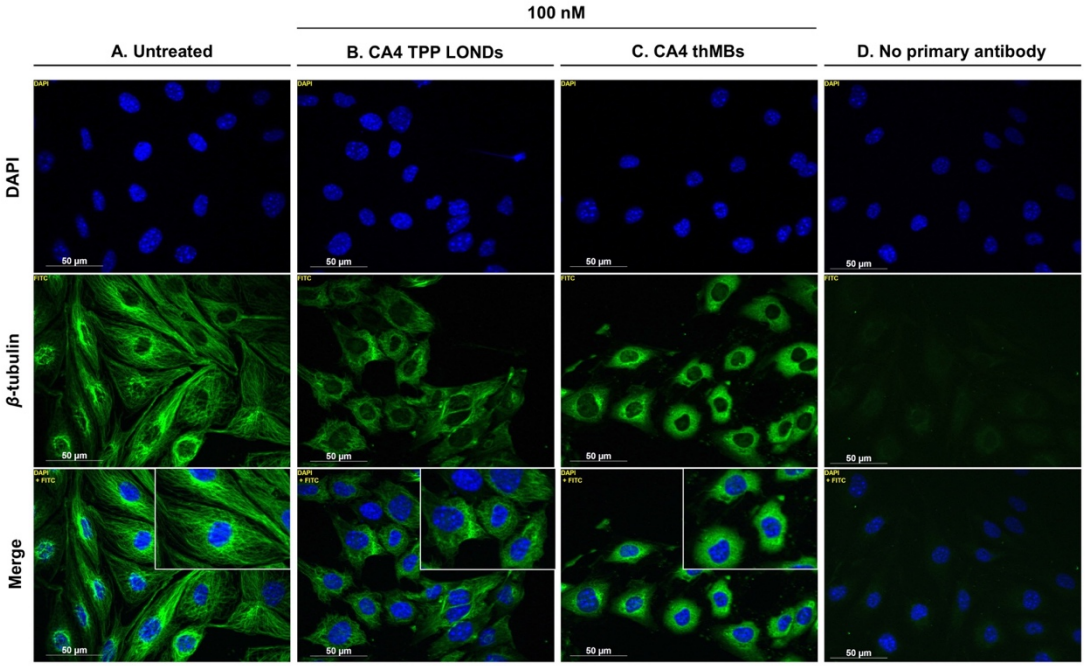

Figure 6.2 CA4 thMBs without an US trigger *in vitro.*

To assess delivery of CA4 thMBs *in vitro*, MT disruption was investigated. CA4 TPP LONDs were used as a positive control at the same concentration. CA4 thMBs were produced on-chip using a two-step process, with the slow mixing and attachment of NeutrAvidin functionalised CA4 TPP LONDs downstream of MB production. 3.4 x 10^7/mL CA4 thMBs were produced with a mean size of 2.4 ± 1.5 μm. 5 x 10^4 CA4 thMBs were added onto the SVR cells which equated to a 100 nM CA4 concentration. Cells were incubated for 2 h at 37°C. Following 2 h at 37°C, cells were fixed, immunostained for β-tubulin using a mouse monoclonal anti-β-tubulin antibody and visualised using a biotinylated rabbit anti-mouse and FITC-labelled avidin. The slides were mounted with prolong Gold containing DAPI. (A) Untreated SVR cells with long MT filaments. (B) 100 nM CA4 TPP LONDs resulted in MT disruption, with some tangled MTs around the nuclei and some that had depolymerised and tubulin dispersed throughout the cytoplasm. (C) 5 x 10^4 CA4 thMBs at 100 nM, caused MT disruption characteristic of depolymerised MTs uniformly staining the cytoplasm of cells. Inset images show magnified cells in panels A-C. (D) No primary antibody, with minimal background indicating the specificity of the anti-β-tubulin antibody. Scale bars indicate 50 μm. Prep. number 8 was used.

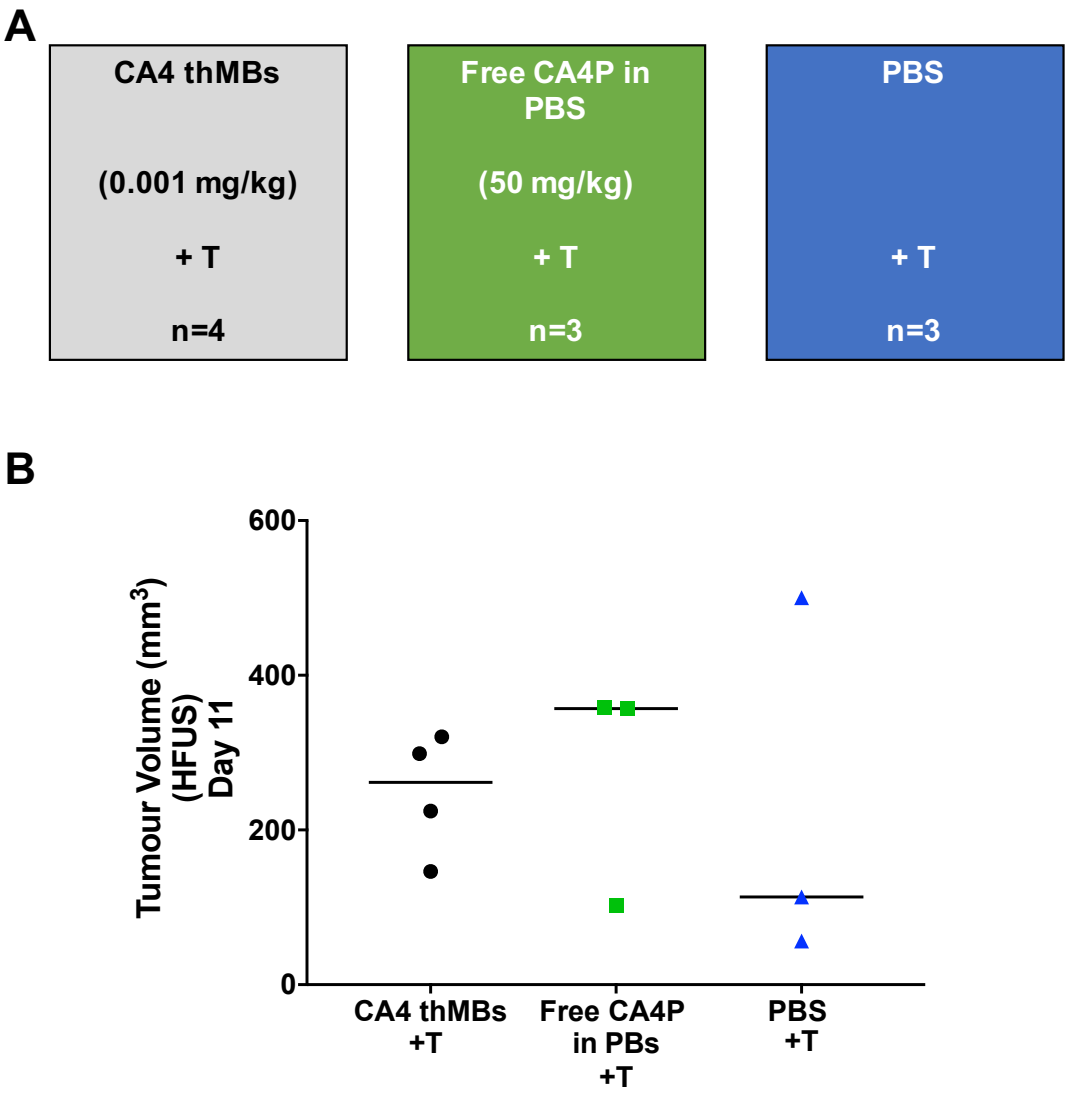

Figure 6.3 Delivery of CA4 by US triggered thMBs *in vivo.*

(A) Schematic showing the experimental cohorts: Briefly, SW480 tumour xenografts were established in CD-1® nude mice by s.c. injection of 5 x10^5 cells on day 0. On day 11 of tumour growth tumour volumes were measured by HFUS and mice were sorted into three groups accordingly: CA4 thMBs (0.001 mg/kg) + T (n=4); Free CA4P in PBS (50 mg/kg) + T (n=3); PBS (* equivalent volume to CA4P) + T (n=3). All were administered via i.v. infusion through the tail vein (0.1 mL/min). (B) Tumour volumes on day 11 used for randomisation. Straight lines (–) represent the median value. No statistically significant differences were observed between the tumour volumes of the three experimental cohorts (Mann-Whitney U test, two tailed). Prep. number 10 was used.

6.3.1 Tumour histology 1 h post-injection with CA4 thMBs, CA4P and PBS

The morphology of SW480 xenografts 1 h post-injection with very low dose CA4 thMBs was assessed. The results shown in Figure 6.4 A-C for CA4 thMBs + T, free CA4P + T and PBS control + T respectively, showed that tumour morphology was similar between the groups. Although, areas with haemorrhage, especially in the CA4 thMB + T group and CA4P + T treated xenografts were observed, this was also observed in the PBS + T group suggesting that this was the background level of the inherent leaky tumour vasculature.

6.3.2 Tumour perfusion 1 h post-injection with CA4 thMBs, CA4P and PBS

In vivo functional vasculature was assessed by *in-situ* staining with Hoechst 33342. CD31 staining was also used as a marker of endothelial cells (blood vessels). Co-registration of fluorescence labelling for Hoechst 33324 and CD31 showed that tumour perfusion in the tumour core was reduced in SW480 xenografts 1 h post-injection with CA4 thMBs + T and free CA4P + T compared to PBS + T controls (Figure 6.5). The reduction in perfusion was evident by the very weak intensity of Hoechst 3342 staining. Occasionally, within the same tumour at a different FOV in both CA4 thMBs and free CA4P, well perfused vessels and surrounding cell nuclei were observed (Figure 6.5). In the CA4 thMB + T and free CA4P + T groups in contrast to the tumour core, the periphery of the same tumours was well perfused similar to the PBS + T group (Figure 6.6) suggesting, that the tumour core was more susceptible to the effects of CA4 thMBs + T and CA4P + T.

To quantitate the reduction in perfusion observed, fluorescent images from tumour core were scored as described in section 2.5.10.1. Hoechst 33342 intensity was scored as an index of tumour perfusion, using a scale from 0 to 3, with 0 being the least perfused with no Hoechst 33342 staining and 3 being the highest score (Figure 6.7). Although the median score values for Hoechst 33342 intensity were lower in the treated groups (CA4 thMBs + T and CA4P + T) compared to PBS these did not reach statistical significance (Figure 6.7 B). This was potentially due to the small animal numbers used per group. A no Hoechst 33342 perfusion marker tumour control is shown in Appendix D, Figure D.2.

6.3.3 Perfusion in heart and liver tissue 1 h post-injection with CA4 thMBs, free CA4P and PBS

To investigate potential off-target toxicity and release of CA4 from thMBs, perfusion in heart and liver tissues was assessed using Hoechst 33342. Heart was chosen due to the cardiovascular toxicities associated with CA4 and liver because it is the main organ responsible for metabolising CA4 (Rustin *et al.*, 2003; Aprile *et al.*, 2007).

The results for liver and heart tissue are shown in Figure 6.8 and Figure 6.9 respectively. Qualitative assessment of the fluorescent images between the three experimental groups in both liver and heart tissue did not show any significant differences in the staining pattern of Hoechst 33342 and hence tissue perfusion.

6.4 Discussion

6.4.1 Production of CA4 thMBs

External triggering of NP loaded MBs through US enhances drug uptake, while targeting enhances the accumulation and attachment to the target side (Lentacker, De Smedt & Sanders, 2009). The initial aim of the study was to produce CA4 thMBs using a two-step method, which resulted in a concentration of thMBs of approximately 10^7/mL. The concentration produced in this two-step microspray regime was significantly lower than previously reported for the single step regime used for production of thMBs carrying liposomes (approximately 10^9 bubbles/mL) (Peyman *et al.*, 2012). The lower CA4 thMB/mL concentrations were due to the addition of CA4 TPP LONDs downstream of MB production, which increasing the overall liquid volume produced and diluting the final CA4 thMB concentration/mL by 2. The low CA4 drug concentration is due to the initial dilution of CA4 TPP LONDs to a concentration of 10^{11}/mL. Moreover, this low concentration of CA4 thMBs/mL also hinders their use for imaging the hydrophobic delivery of CA4 as a bolus of at least 10^7 MBs is required for contrast (Lyshchik *et al.*, 2007).

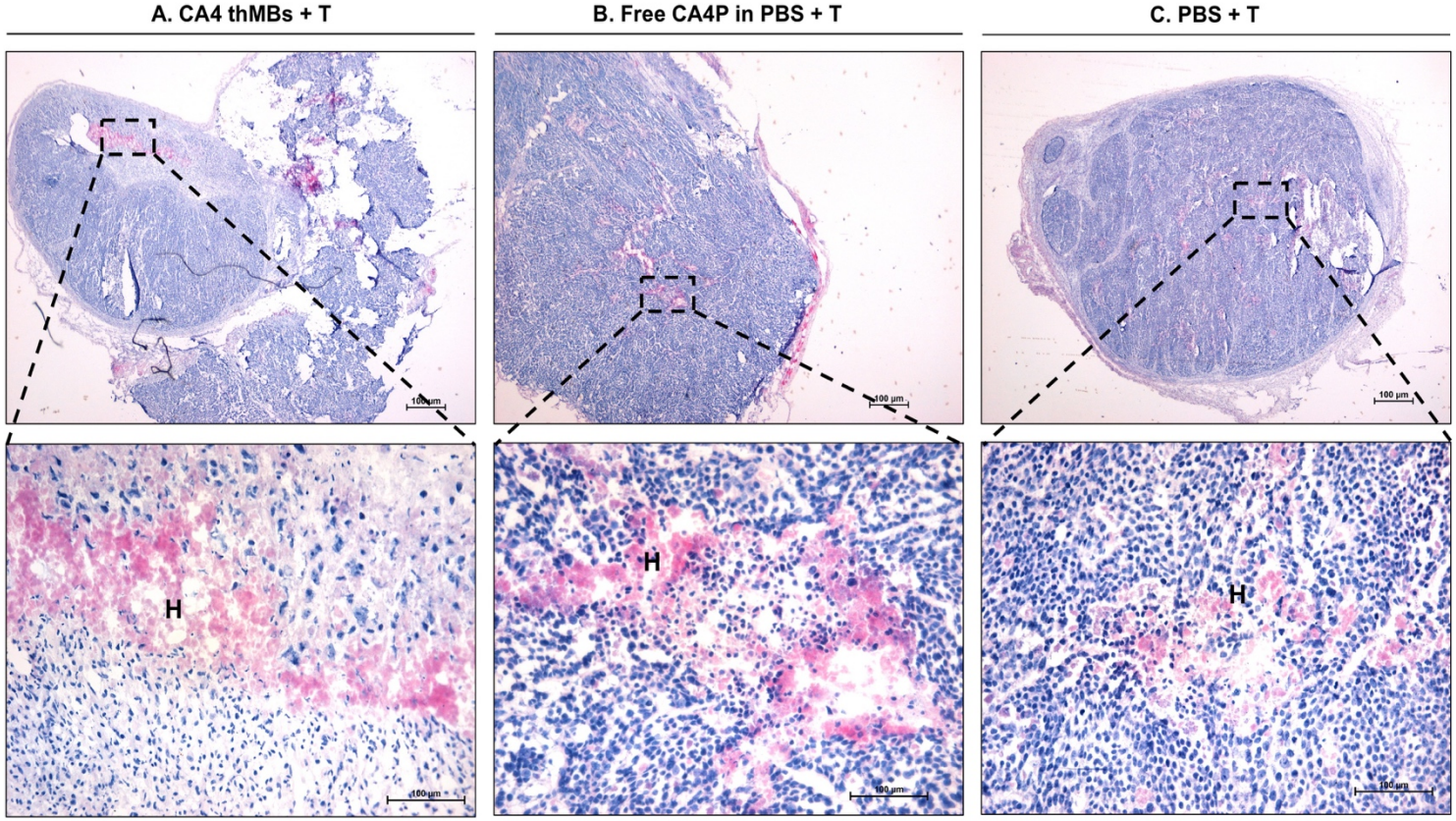

Figure 6.4 SW480 tumour morphology following 1 h post-injection with CA4 thMBs.

H & E 10 μm frozen sections from tumours treated with 1.65 x 10^6 CA4 thMBs (0.001 mg/kg) + T, CA4P (50 mg/kg) + T and PBS (equivalent volume to CA4P). (A). (A) 1 h post-injection with CA4 thMBs + T, the tumour showing areas of central haemorrhage (H). (B) 1 h post-injection with free CA4P + T, the tumour showing areas of extensive central H. (C) 1 h post-injection with PBS + T, tumour showing areas of central H. Squares indicate the area of the bottom images. Scale bars indicate 100 μm. Prep. number 10 was used.

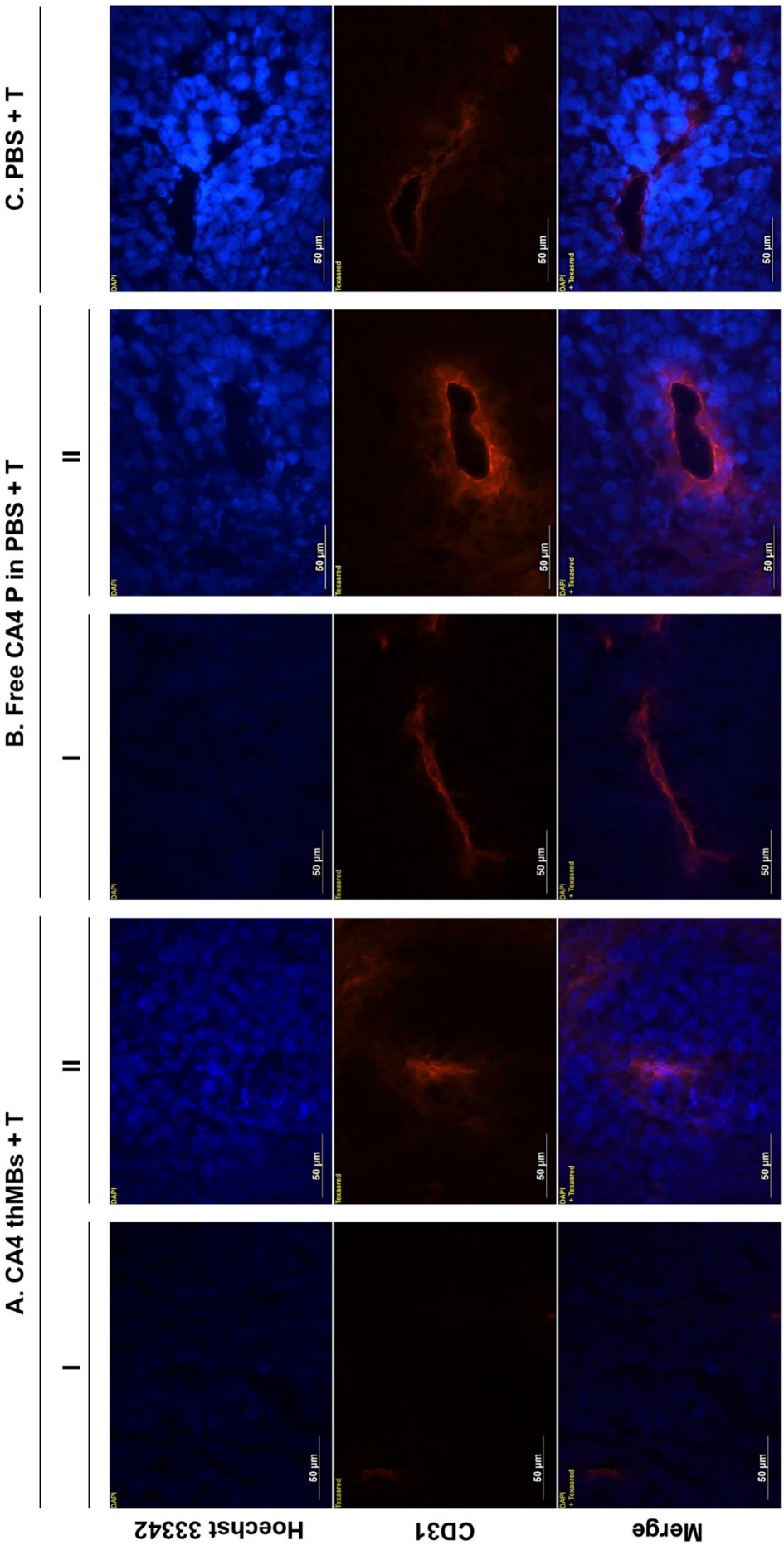
A. CA4 thMBs + T
B. Free CA4 P in PBS + T
C. PBS + T
I
II
I
II
Hoechst 33342
CD31
Merge
DAPI
Texasred
DAPI + Texasred
50 µm

Figure 6.5 SW480 tumour perfusion in the core, 1 h post-injection with CA4 thMBs, free CA4P and PBS.

Co-registered IF images with Hoechst 33342 and CD31 from frozen tumour sections 1 h post-injection with CA4 thMBs + T, free CA4P + T and PBS + T. Perfusion staining with Hoechst 33342 was performed *in-situ* while CD31 staining was performed *ex-vivo* using a rat monoclonal antibody against CD31 and visualised using a goat anti-rat secondary antibody Alexa Fluor 568. (A-I) Tumour core 1 h post-injection with 0.001 mg/kg CA4 thMBs + T showing central reduction in the intensity of Hoechst 33342 staining therefore, perfusion which was indicative of vascular shutdown. (A-II) Different FOV of the same tumour section treated with CA4 thMBs showing a well perfused area. (B-I) Tumour core 1 h post-injection with 50 mg/kg free CA4P in PBS + T used as a positive control, showing extensive central reduction in perfusion evident by the low intensity of Hoechst 33342. (B-II) Different field of view within the same tumour section treated with free CA4P showing a vessel that was well perfused. (C) Tumour core 1 h post-injection with PBS + T, showing intense staining of Hoechst 33342 suggesting good perfusion within the tumours. Scale bars indicate 50 μm. Prep. number 10 was used.

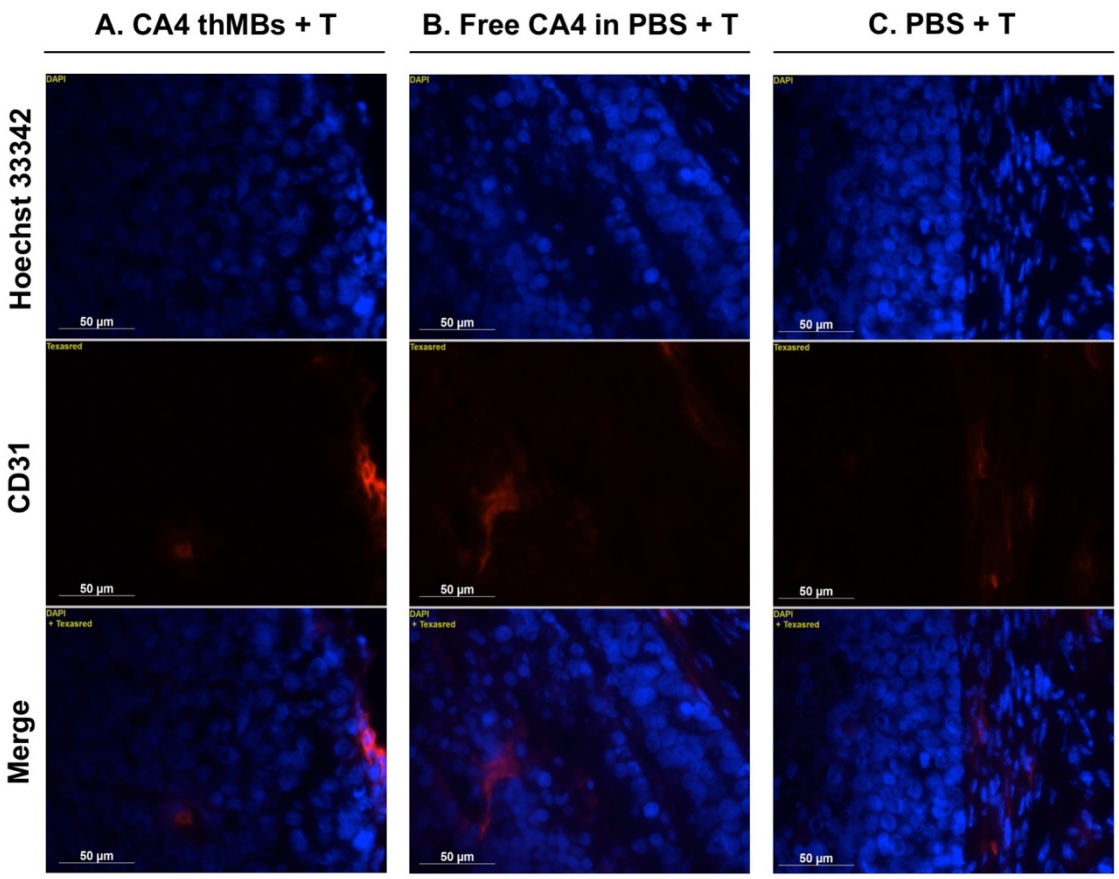

Figure 6.6 SW480 tumour perfusion in the periphery, 1 h post-injection with CA4 thMBs, free CA4P and PBS.

Co-registered IF images with Hoechst 33342 and CD31 from frozen tumour sections 1 h post-injection with CA4 thMBs + T, free CA4P + T and PBS + T. Perfusion staining with Hoechst 33342 was performed *in-situ* while CD31 staining was performed *ex-vivo* using a rat monoclonal antibody against CD31 and visualised using a goat anti-rat secondary antibody Alexa Fluor 568. (A) Tumour periphery 1 h post-injection with 0.001 mg/kg CA4 thMBs + T, had intense staining of Hoechst 33342 indicative of good perfusion. (B) Tumour periphery 1 h post-injection with 50 mg/kg free CA4P + T, showing intense staining of Hoechst 33342. (C) Tumour periphery 1 h post-injection with PBS + T, showing intense staining of Hoechst 33342. Scale bars indicate 50 *µ*m. Prep. number 10 was used.

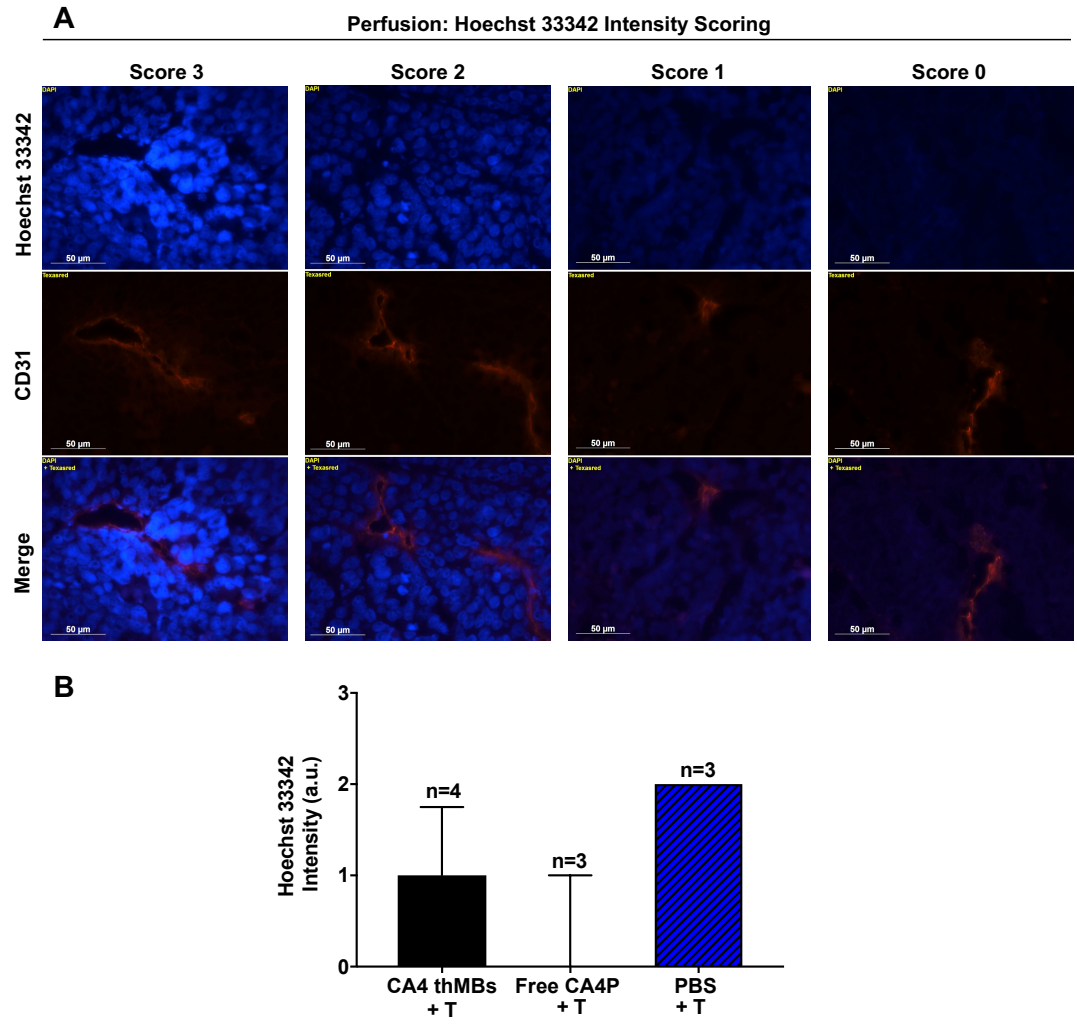

Figure 6.7 Semi-quantitative analysis of Hoechst 33342 intensity 1 h post-injection with CA4 thMBs, free CA4P and PBS .

(A) Representative fluorescence images of Hoechst 33342 and CD31 are shown to describe the perfusion intensity scoring system. The number 3 was given to the images with the highest Hoechst 33342 intensity, 2 was moderate Hoechst intensity 33342, 1 was low Hoechst 33342 intensity and 0 was very low intensity to no Hoechst 33342. Scale bars indicate 50 μm. (B) Results from the semi-quantitative analysis of Hoechst 33342 intensity. No statistically significant differences were observed between mice treated with PBS + T compared to CA4 thMBs + T ($p=0.14$, Mann-Whitney, U-test, two-tailed) or PBS + T compared to CA4P + T ($p=0.1$, Mann-Whitney, U-test, two-tailed) or CA4 thMBs + T compared to CA4P + T ($p=0.11$, Mann-Whitney, U test, two-tailed). The data represents the median and error bars the interquartile range. a.u.: arbitrary units.

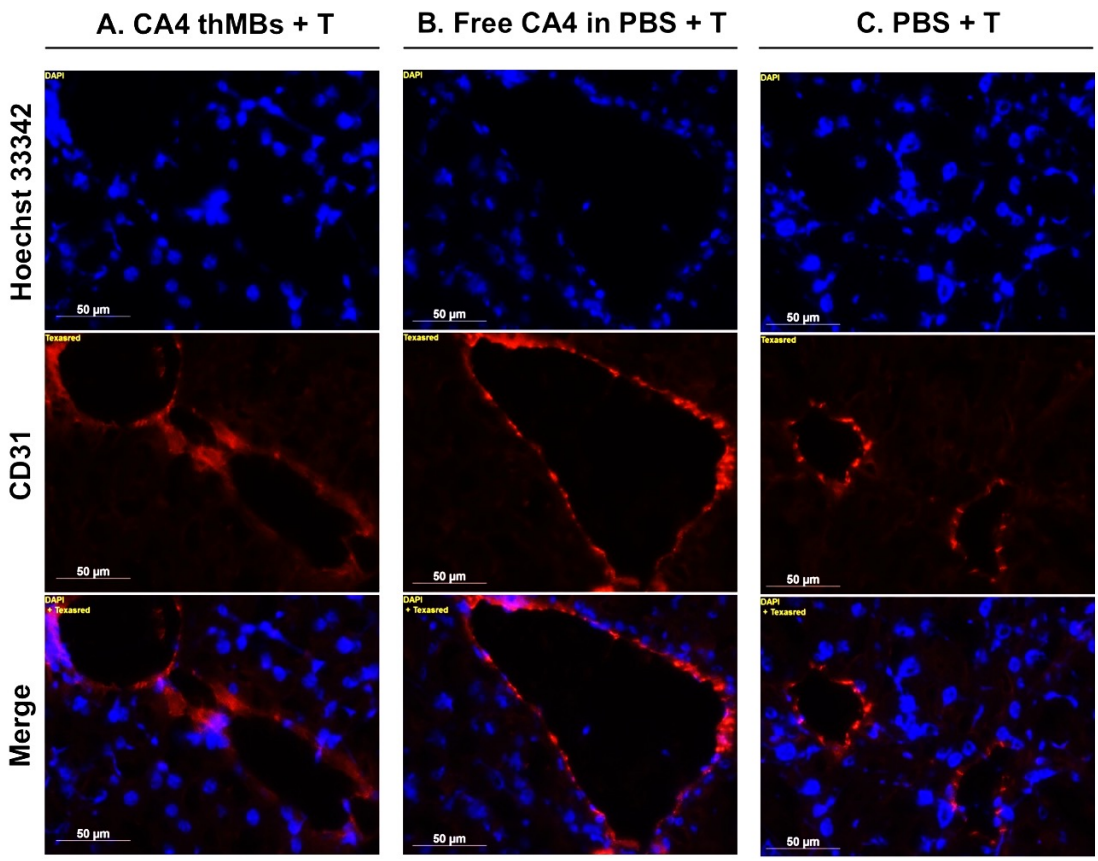

Figure 6.8 Perfusion of liver tissue 1 h post-injection with CA4 thMBs, free CA4P and PBS.

Co-registered IF images with Hoechst 33342 and CD31 from frozen liver sections 1 h post-injection with CA4 thMBs + T, free CA4P + T and PBS + T. Perfusion staining with Hoechst 33342 was performed *in-situ* while CD31 staining was performed *ex-vivo* using a rat monoclonal antibody against CD31 and visualised using a goat anti-rat secondary antibody Alexa Fluor 568. (A) Liver tissue section, 1 h post-injection with 0.001 mg/kg CA4 thMBs + T. (B) Liver tissue section 1 h post-injection with 50 mg/kg free CA4P + T. (C) Liver tissue section 1 h post-injection with PBS + T. In all three groups the liver tissue around the CD31 positive vessels appeared to be well perfused. Scale bars indicate 50 *µ*m. Prep. number 10 was used.

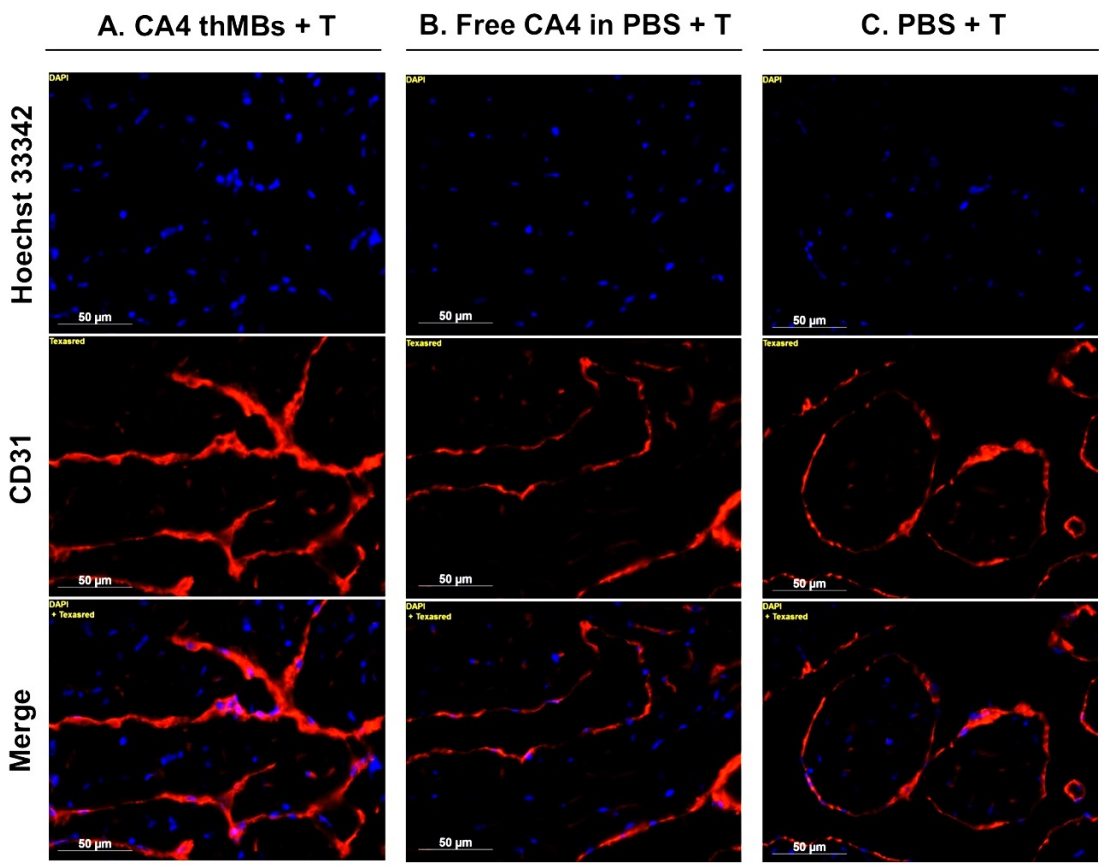

Figure 6.9 Perfusion of heart tissue 1 h post-injection with CA4 thMBs, free CA4P and PBS.

Co-registered IF images with Hoechst 33342 and CD31 from frozen heart sections 1 h post-injection with CA4 thMBs + T, free CA4P + T and PBS + T. Perfusion staining with Hoechst 33342 was performed *in-situ* while CD31 staining was performed *ex-vivo* using a rat monoclonal antibody against CD31 and visualised using a goat anti-rat secondary antibody Alexa Fluor 568. (A) Heart 1 h post-injection with 0.001 mg/kg CA4 thMBs + T. (B) Heart 1 h post-injection with 50 mg/kg free CA4P + T. (C) Heart 1 h post-injection with PBS + T. In all three groups the heart tissue around the CD31 positive vessels appeared to be well perfused. Scale bars indicate 50 *µ*m. Prep. number 10 was used.

6.4.2 *In vivo* evaluation of CA4 thMBs by assessing tumour and tissue perfusion

In vivo delivery of very low dose CA4 thMBs showed that there were no differences in tumour histology compared with free CA4P or PBS control group. However, there were differences in tumour perfusion in the central core shown by the reduce staining of Hoechst 33342 in certain FOV. These did not reach statistical significance potentially due to the small mouse numbers per group. 50 mg/kg CA4P caused a more severe reduction in perfusion than 0.001 mg/kg CA4 thMBs as the median score for Hoechst 33342 intensity was lower but not statistically significant, this was potentially due to the difference in dose. Reduction in perfusion has been shown previously to be dose-dependent in mammary carcinoma tumours (Murata, Overgaard & Horsman, 2001). Tumour periphery was unaffected by CA4 thMBs and CA4P as the Hoechst 33342 staining intensity was similar to PBS control.

Similar results with differences in response between the tumour core and periphery have been reported in a number of preclinical studies. For example, studies using CA4P at a much higher dose of ≥ 200 mg/kg in SW1222 CRC xenografts reported that tumour morphology was unaffected 1 h post-injection while tumour perfusion assessed using Hoechst 33342 was significantly reduced in the tumour core (approximately 85% reduction) and not the tumour periphery (Pedley *et al.*, 2001; El-Emir *et al.*, 2005). The same studies in SW1222 CRC xenografts also assessed tumour morphology and perfusion 24 h post-injection, they observed that treatment with CA4P caused extensive central necrosis with perfusion being reduced in the core, in contrast the periphery was composed of viable tumour cells which were well perfused (Pedley *et al.*, 2001; El-Emir *et al.*, 2005).

Salmon and Siemann (2007) assessed tumour perfusion in the periphery or the viable rim after CA4P treatment. They reported that following 4 h post-injection with 100 mg/kg CA4P, an 80% reduction in perfusion was observed in the tumour as a whole with a 50% reduction specifically at the tumour periphery assessed by Hoechst 33342 (Salmon & Siemann, 2007). However, after 48 h post-injection perfusion in the periphery had returned to normal levels while in the tumour core it was still significantly reduced (Salmon & Siemann, 2007).

DCE-MRI has also been used to study perfusion in CA4 treated tumours in both animal models and phase I human trials (Beauregard *et al.*, 1998; Maxwell *et al.*, 2002; Galbraith *et al.*, 2003; Stevenson *et al.*, 2003; Zhao *et al.*, 2005a). Initial results showed the same patterns as previously mentioned with Hoechst 33342 perfusion

staining, 3 h post-treatment with CA4P (100 mg/kg i.p.) there was a reduction in perfusion in the central regions of the tumour but not the periphery, perfusion in the periphery increased after treatment (Beauregard *et al.*, 1998). DCE-MRI was also used to study perfusion in rat breast carcinoma (Zhao *et al.*, 2005a). The results showed that a single dose of CA4P (30 mg/kg) caused a significant reduction in blood flow (indicative from the reduction in signal) 2 h post administration (Zhao *et al.*, 2005a). 24 h later, complete recovery was observed in the tumour periphery but not the central regions of the tumour (Zhao *et al.*, 2005a). The data from DCE-MRI was also confirmed by Hoechst 33342 staining (Zhao *et al.*, 2005a). A phase I clinical trial which was conducted in parallel with an *in vivo* study in rat P22 sarcomas showed significant reductions in blood flow measured by DCE-MRI in rats and humans at 4 to 6 h after administration of CA4P (30 mg/kg for rats, ≥ 52 mg/m^2 for humans) with no significant reduction in blood flow observed in kidney and muscle tissue (Galbraith *et al.*, 2003).

CEUS using SonoVue MBs has recently been used to quantitatively evaluate the efficacy of CA4P in a CT26 CRC model specifically the tumour periphery and core (Zhang *et al.*, 2018). Their results showed significant reduction in tumour perfusion in the central regions of the tumour compared to the periphery (between 2-12 h post-treatment), however they observed recovery to the whole tumour by 48 h (Zhang *et al.*, 2018).

There is a clear difference in susceptibility of the tumour to CA4 treatment in the core and the tumour periphery. The reason behind this is attributed to the difference in the vasculature of the two compartments. The vasculature in the periphery is composed of larger vessels with presumably faster flowing blood compared to the central vessels (Tozer *et al.*, 2001). Therefore, any changes to the blood flow at the tumour periphery are less damaging (Tozer *et al.*, 2001). Nguyen, *et al.,* (2012), investigated the differences in tumour vasculature in the periphery and the core of a mouse colorectal liver metastases model. They reported that vessels in the periphery due to a greater investiture of SMCs were more stable and mature than in the core (Nguyen *et al.*, 2012). Other differences include, low levels of hypoxia presumably due to the close proximity of normal vessels, higher expression of proangiogenic factors and receptors (VEGF) and immune cells in the periphery compared to the central region, all these contributed to resistance to treatment with Oxi4503 (Combretastatin A1) a derivative of CA4P (Nguyen *et al.*, 2012). It should however be noted that different types of tumours will have a different degree of vascularisation therefore, vessel morphology and maturity (Nguyen *et al.*, 2012).

CA4 thMBs and CA4P did not appear to cause any significant reduction in perfusion in heart or liver consistent with previous reports which have studied normal tissue perfusion after 1 h and 6 h post-injection with 250 mg/kg CA4P (Murata, Overgaard & Horsman, 2001).

6.4.3 Potential method of release and or uptake of CA4 TPP LONDs from thMBs

US can lead to MB cavitation and depending on the US parameters this can cause stable or inertial cavitation subsequently leading to drug uptake through several pathways including membrane pore formation-sonoporation, endocytosis and/or opening of cell-cell junctions (van Wamel *et al.*, 2006; Meijering *et al.*, 2009; Kooiman *et al.*, 2014). The US parameters used such as centre frequency, pulse repetition frequency, pulse length acoustic pressure and total exposure time of cells or tumour all influence the mechanism of drug uptake (De Cock *et al.*, 2015). It is difficult to compare and contrast uptake mechanisms induced by US exposed MBs as in the literature a variety of different US settings are used. *In vitro*, it has been demonstrated by De Cock *et al.,* (2015) that high acoustic pressures promote membrane pore formation through which drugs can passively diffuse, in contrast, low acoustic pressures promote endocytosis through the stimulation of the cytoskeleton (De Cock *et al.*, 2015).

Attached drug carriers such as liposome could also potentially rupture due to the applied US (Klibanov *et al.*, 2010). A study using DOX-liposome-loaded microbubbles and US (the US exposure settings MI 0.17) showed that these were able to improve the anti-tumour activity of DOX compared to DOX-liposomes alone and with US (Lentacker *et al.*, 2010). They proposed that US destroys the liposome coupled to the MB releasing free DOX near the cell membrane allowing free drug to enter more easily and that the resulting perforations on the cell membrane caused by the imploded MBs increased uptake of both free DOX and DOX-liposomes (Lentacker *et al.*, 2010). De Cock *et al.,* (2016) also studied the release of NPs (mRNA lipoplexes) from MBs following US exposure, and they observed two different release mechanisms the one being the previously reported local release of NPs and/or their contents in the cell surroundings followed be uptake through pores and endocytosis and the other mechanism which they termed sonoprinting this was direct deposition of the NPs onto the cell (De Cock *et al.*, 2016). Sonoprinting, occurs when the MB is close to the cells as the close contact is what promotes NP delivery and this can be ensured by targeting (De Cock *et al.*, 2016).

In this study VEGFR2 targeting promotes the close contact and binding of the CA4 thMBs to tumour vasculature, subsequently the US applied should lead to MB destruction as demonstrated in liposomes (McLaughlan *et al.*, 2017). The applied US could potentially also rupture the LONDs leading to the release of CA4, while the high forces, shock waves and microjets that are generated during the collapse of the MB could lead to the formations of pores and enhanced uptake of free CA4 or any remaining intact CA4 TPP LONDs. The proposed mechanism is also summarised in Figure 1.9.

6.4.4 Conclusion

In conclusion CA4 thMBs were successfully produced, however future work will require improvement of the production method to reduce the overall liquid required for production and increase the thMB concentrations. It was difficult to distinguish any differences in effect caused by CA4 thMBs compared to CA4 TPP alone *in vitro* using the IF assay and the 2 h time point.

Hoechst 33342 was shown to be a good initial indicator of tumour response to CA4 thMBs in contrast to the traditionally used methods of histology and tumour volume. Collectively the *in vivo* data presented in this study and previously reported show that the very early effects of CA4 treatment either as free drug or delivered by CA4 thMBs result in changes in the functional biology of tumours as an early indication of tumour response even though there is no evidence of morphological changes. Importantly, the very low dose of CA4 in thMBs were sufficient to cause a reduction in perfusion, potentially indicating the local release of CA4 via US which subsequently increased uptake into tumour cells eliminating the need for high circulating concentrations.

Chapter 7

Combination therapy using irinotecan and US triggered CA4 ThMBs

7.1 Introduction

Preclinical data with CA4P as a monotherapy report that despite the rapid reduction in tumour perfusion and extensive secondary central necrosis, only moderate effects on tumour growth are observed after multiple treatments (Nabha *et al.*, 2001; Hill *et al.*, 2002). Tumours regrow from the viable rim, which is a major cause of recurrence (Dark *et al.*, 1997; Chaplin & Hill, 2002). CA4P induced hypoxia through upregulation of hypoxia-inducible factor-1*α* (HIF-1*α*) expression and vascular mimicry can promote cell survival and angiogenesis (Yao *et al.*, 2015; Liang, Ni & Chen, 2016). Mobilisation of bone marrow derived circulating endothelial progenitor cells (CEPs) has also been described, and together with hypoxia represent two key factors in treatment resistance (Liang, Ni & Chen, 2016). Treatment with CA4P leads to the accumulation of CEPs, these home to sites of viable tumour cells in the rim, where they incorporate into the endothelial cells of tumour vessels and promote revascularisation (Shaked, 2006). An increase in CEPs after CA4P treatment has also been observed in a Phase I clinical trial (Nathan *et al.*, 2012). To control or prevent regrowth from the viable rim, VDAs such as CA4P have been used in combination with anti-angiogenic agents (e.g. bevacizumab) (Nathan *et al.*, 2012), chemotherapy (e.g. 5-FU and irinotecan) (Grosios *et al.*, 2000; Wildiers *et al.*, 2004), radiotherapy (Murata, Overgaard & Horsman, 2001; Ng *et al.*, 2012) and radio-immunotherapy *in vivo* and in clinical trials (Pattillo *et al.*, 2005; Meyer *et al.*, 2009).

Low dose US triggered CA4 thMBs caused a reduction in tumour core perfusion 1 h post-injection, indicating the release and subsequent intratumoural uptake of CA4 from the thMB construct (Chapter 6). CA4 thMBs could be used as a monotherapy, as the attachment to the thMB is hypothesised to enhance CA4 delivery and therefore, improve the therapeutic effect. However, previous data presented (Chapter 5), using CA4 TPP LONDs as a monotherapy showed a modest but insignificant tumour growth inhibition. Although, a better tumour response was anticipated with US triggered CA4 thMBs, the very low doses that can be achieved may limit its use as a monotherapy, CA4 thMBs were therefore evaluated as a combined therapy with the conventional chemotherapeutic agent, irinotecan (section 1.1.2.2). Irinotecan is a topoisomerase inhibitor used in the treatment of CRC and liver metastases and has been shown to have efficacy in low dose treatment schedules (Houghton *et al.*, 1995; Fioravanti *et al.*, 2009) and combined therapies (FOLFIRI) (Del Rio *et al.*, 2017).

7.2 Irinotecan and US triggered CA4 thMBs combination therapy

To determine the effect of combination therapy with irinotecan and US triggered CA4 thMBs on the growth of human CRC xenografts, mice bearing SW480 xenografts were sorted according to tumour volume into four experimental groups (Figure 7.1). Mice received an i.p injection of irinotecan at 10 mg/kg followed 1 h later by an i.v. injection through the tail vein of 0.001 mg/kg CA4 thMBs or CA4P at the same dose. Control mice were treated with 10 mg/kg irinotecan alone or PBS and all groups received an US trigger (+ T). Each group received two Tx per week for a total of five Tx. 1 h after the final treatment, mice were administered with 15 mg/kg Hoechst 33342 to image vascular perfusion *in situ* and sacrificed one minute later. Tumour and tissues were collected for *ex vivo* analysis (Figure 7.1). The injections were performed with the help of Dr Nicola Ingram and Dr Milene Volpato (School of Medicine, University of Leeds).

The mean concentration, diameter and CA4 loading of the thMBs used for the five treatments was $3.5 \times 10^7 \pm 3.5 \times 10^7$ MBs/mL, 4 ± 0.3 μm and 0.0001 ± 0.00006 mg/mL respectively (Table 7.1 and Appendix E, Figure E.1). Using a mean CA4 thMB bolus of 7×10^6 MBs this equated to the 0.001 mg/kg CA4 dose. Irinotecan was administered 1 h before CA4, as it was plausible that administering CA4 first would result in vascular collapse therefore, potentially hindering the penetration of irinotecan. The half-lives of irinotecan, SN38 and SN38G in mouse plasma following i.p. administration were determined as approximately 6 h for all three compounds (Guichard *et al.*, 1998).

7.2.1 Effect of irinotecan with US triggered CA4 thMBs on tumour growth

The combination therapy of irinotecan with CA4 thMBs significantly inhibited the growth of SW480 xenografts after the first three treatments compared to the PBS control group ($p=0.05$, Mann-Whitney U test, two-tailed, Figure 7.2). The combination therapy of irinotecan with CA4P significantly inhibited the growth of SW480 xenografts from day 17 onwards compared with irinotecan alone and PBS control ($p=0.04$, Mann-Whitney U test, two-tailed, Figure 7.2). The results indicated an enhanced effect when irinotecan was combined with CA4P. For pairwise comparisons of relative tumour volumes see Appendix E, Figure E.2. Tumour volume

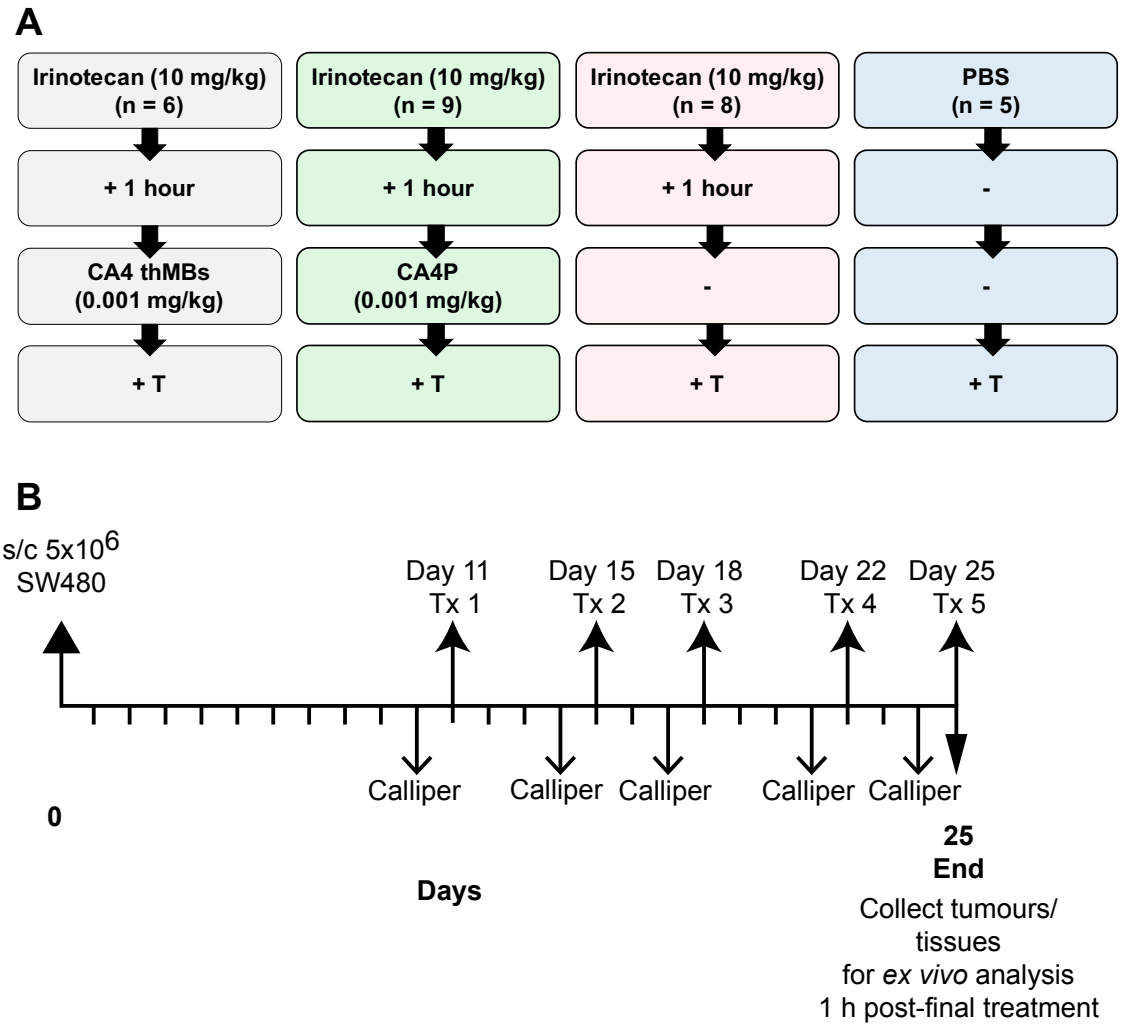

Figure 7.1 Treatment schedule for irinotecan and CA4 combined therapy in mice bearing SW480 human CRC xenografts.

(A) Schematic showing the experimental groups used: SW480 tumour xenografts were established in CD-1® nude male mice by s.c. injection of 5 x 10^5 cells on day 0. On day 10 of tumour growth tumour volumes were measured by mechanical callipers and mice were sorted into four groups according to tumour volume; Irinotecan followed 1 h later by CA4 thMBs plus US trigger (+T) (n=6); Irinotecan followed 1 h later by CA4P + T (n=9); Irinotecan followed 1 h later by T (n=8); PBS + T (n=5). Irinotecan was administered i.p. at a dose of 10 mg/kg, CA4 thMBs and CA4P were administered i.v. through the tail vein at a dose of 0.001 mg/kg. (B) Treatment schedule: Mice received five treatments (Tx) in total. Tumour volume was measured by mechanical callipers before each treatment. 1 h after the final treatment, mice received an i.v. injection of 15 mg/kg Hoechst 33342 and sacrificed 1 min later. Tissues were collected for *ex vivo* analysis.

Table 7.1 Characterisation of CA4 thMBs.

CA4 thMB prep.	ThMBs concentration x10^7/mL	Size μm ± SD	CA4 mg/mL	Dose mg/kg
1	9	4 ± 2.6	0.0002	0.001
2	5	4.4 ± 2.6	0.0001	0.001
3	2	3.7 ± 2.6	0.0001	0.001
4	0.7	4.2 ± 3.1	0.0002	0.001
5	1	3.6 ± 2.5	0.00006	0.0003
Mean	3.5	4	0.0001	0.001
SD	3.5	0.3	0.00006	0.0003

A total of five preparations of CA4 thMBs were prepared using CA4 TPP LONDs prep. number 10. The mean ± SD concentration, diameter and CA4 loading measured by LC-MS/MS of the thMBs used for the five treatments was 3.5 x 10^7 ± 3.5 x 10^7 MBs/mL, 4 ± 0.3 μm and 0.0001 ± 0.00006 mg/mL respectively. The mean dose administered based on the injection volume of 0.2 mL to a 32 g mouse (average weight) was 0.00002 mg which equates to a 0.001 mg/kg dose.

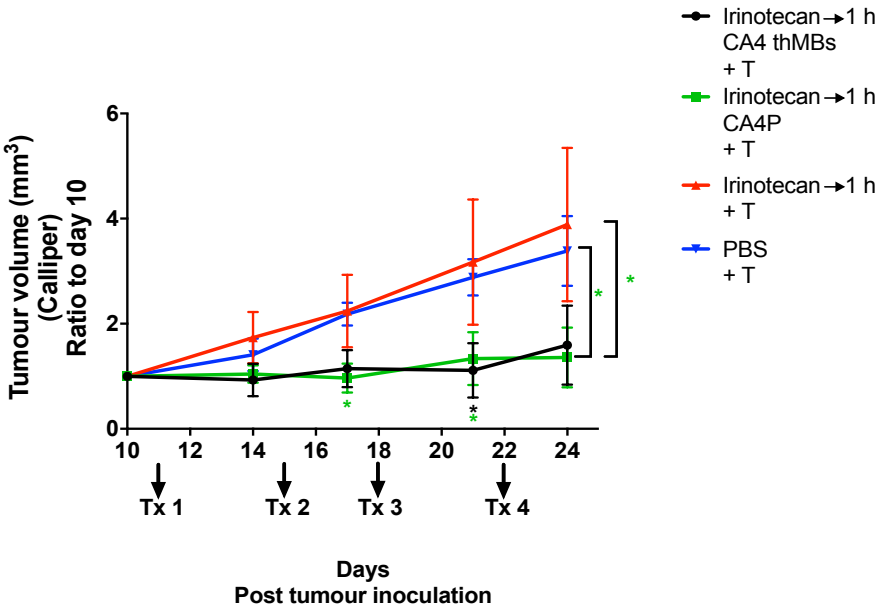

Statistical results: Mann-Whitney U test (two-tailed)			
Groups	Day	Significant	P value
PBS + T vs. Irinotecan ➜ 1 h CA4P + T	17	yes	p=0.01
PBS + T vs. Irinotecan ➜ 1 h CA4P + T	21	yes	p=0.02
PBS + T vs. Irinotecan ➜ 1 h CA4P + T	24	yes	p=0.04
Irinotecan ➜ 1 h + T vs. Irinotecan ➜ 1 h CA4P + T	24	yes	p=0.04
PBS + T vs. Irinotecan ➜ 1 h CA4 thMBs + T	21	yes	p=0.05

Figure 7.2 Effect of combination therapy with irinotecan and CA4 on tumour growth.

Tumour volume ratios to day 10 are shown for each group. Tumour growth in the irinotecan with CA4P + T group was significantly inhibited from day 17 onwards compared to PBS + T (p=0.01, p=0.02 and p=0.04 respectively). By day 24 after the fourth treatment, tumour growth in the combined irinotecan with CA4P + T group was inhibited when compared to irinotecan alone + T (*, p=0.04). Tumour growth was also significantly inhibited on day 21 in the irinotecan with CA4 thMBs + T group compared to PBS control (*, p=0.05). Data represents the mean ± SEM, p values were determined by Mann-Whitney U test, two-tailed.

data over the treatment course of individual mice from each experimental group are shown in Appendix E, Figure E.3.

After the final treatment, tumours were excised and weighed (Figure 7.3 A). Tumour masses were significantly lower in the irinotecan with CA4P group compared to PBS (p=0.02, Mann-Whitney U test, two-tailed). Although tumour masses in the irinotecan with CA4 thMBs were lower compared to control PBS (median values 0.06 g vs 0.15 g respectively) these did not reach statistical significance. Tumour mass relative to mouse body weight (%) was calculated (Figure 7.3 B) and these were significantly lower in the irinotecan with CA4P group compared to PBS (p= 0.03, Mann-Whitney U test, two-tailed). The median tumour doubling time in the irinotecan and CA4P group was insignificantly increased and tumour regression was observed in 5/9 mice. Tumour doubling time was not increased in the irinotecan with CA4 thMBs group compared to PBS however regression was observed in 3/6 mice. One tumour from the irinotecan alone group had regressed. Tumour doubling time data has been divided into two graphs for simplicity (Figure 7.3 C and D). No significant differences were observed in tumour doubling time between the groups.

During treatment, mouse body weight was monitored as an indicator of wellbeing and drug toxicity. The % change in body weight was determined (Figure 7.4) and mice in the irinotecan alone + T group showed a mild weight loss (< 2%) after the first treatment, before recovering by treatment three. Individual mouse body weights during the treatment course from day 10 prior to the first treatment are shown in Appendix E in Figure E.4.

7.2.2 Effects of combined therapy of irinotecan and CA4 on tumour perfusion

To assess mechanisms by which the combination therapy of irinotecan and CA4 thMBs or CA4P enhanced tumour growth inhibition, tumour perfusion was assessed by fluorescence microscopy for the perfusion marker, Hoechst 33324. It should be noted that 2/9 tumours from the irinotecan with CA4P + T group were not available for perfusion analysis due to them being too small as a result of tumour regression. Tumour sections were fixed and immunostained with a fluorescent anti-CD31 antibody to delineate the blood vessels. Co-registration of fluorescent images with Hoechst 33342 and CD31 showed that tumour tissue in the PBS and irinotecan alone groups was well perfused around areas with CD31 positive blood vessels (Figure 7.5 A and B). In contrast, perfusion in the core of tumours treated with irinotecan and CA4P or CA4 thMBs was almost abolished (Figure 7.5 C, I and D, I). This indicated

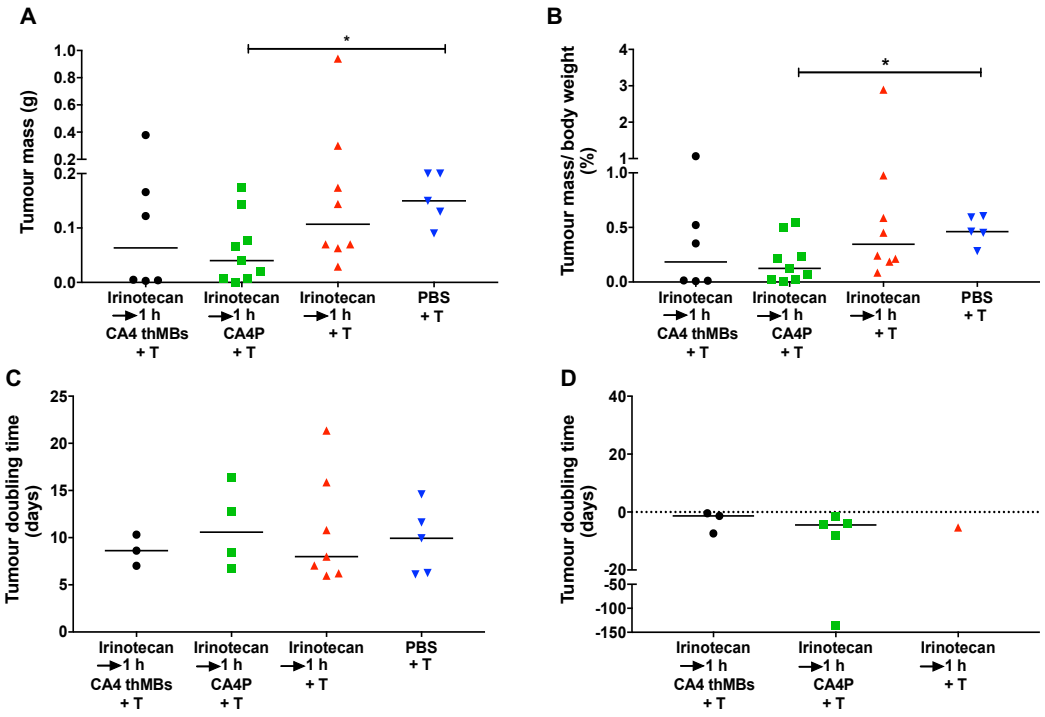

Figure 7.3 Tumour responses following combination therapy with irinotecan and CA4.

(A) Tumour mass (g) on excision following five treatments. Tumours were significantly smaller in the irinotecan with CA4P + T compared to PBS + T (*, p=0.02). (B) Tumour mass to body weight ratio (%). Mice in the irinotecan with CA4P + T group had a significantly smaller tumour mass to body weight ratio compared to PBS + T group (*, p=0.03). (C & D) Tumour doubling time in days divided in two graphs for simplicity. Negative values in D indicate tumour regression. Straight lines (–) in the data represent the median. Significance was determined using a Mann-Whitney U test, two-tailed.

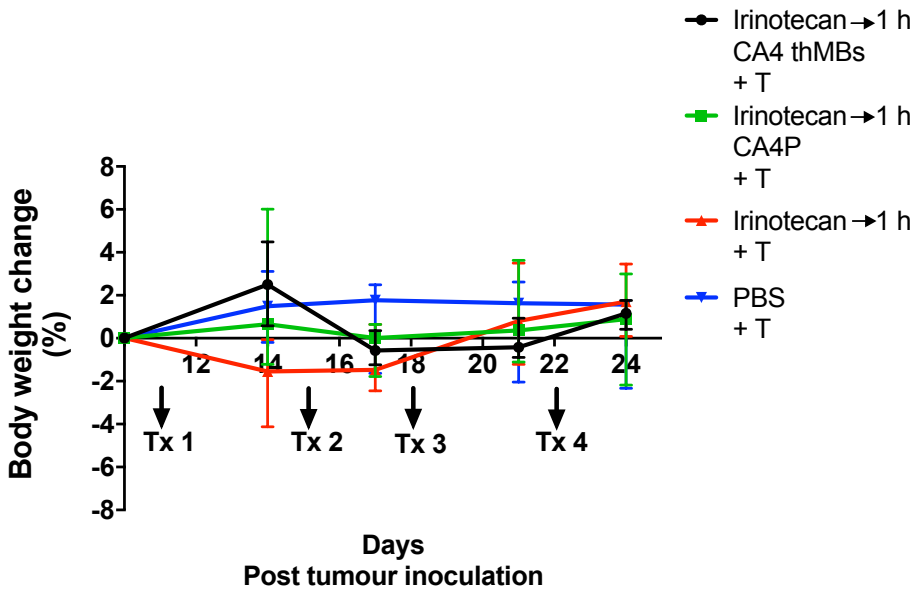

Figure 7.4 % body weight change during the treatment course with irinotecan and CA4.

CD-1® nude mice bearing SW480 human CRC xenografts were weighed one day before each treatment (Tx) and the % body weight change throughout the treatment course was determined. This was calculated by dividing the weight gained or lost at each measurement by the starting weight x 100. Although, mice in all treatment groups showed some mild body weight loss during the treatment course, these were not statistically significant (Mann-Whitney U test, two-tailed). Data represents the median value and error bars the interquartile range.

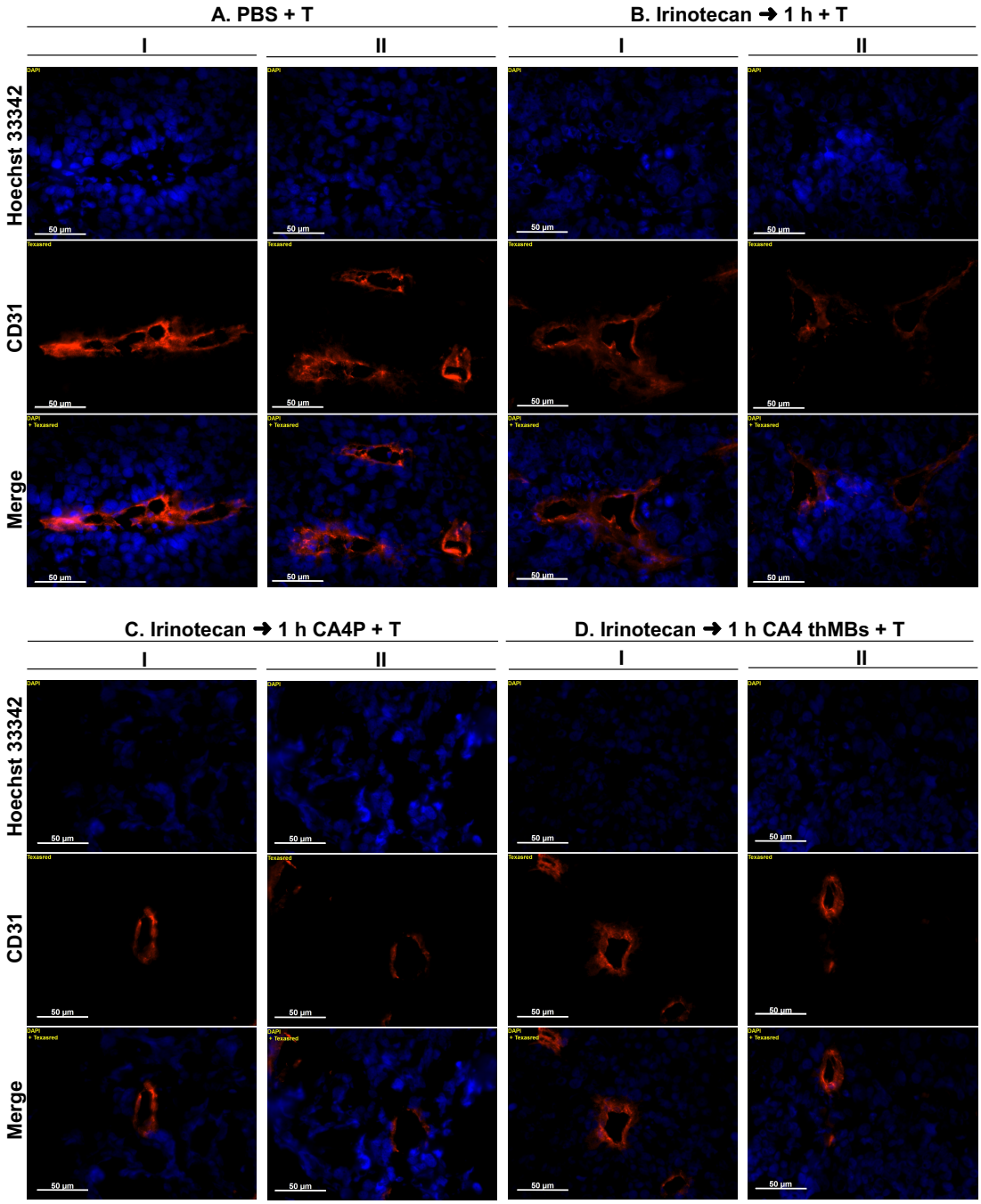

Figure 7.5 Effect of the combination therapy with irinotecan and CA4 on tumour core perfusion.

Mice bearing SW480 human CRC xenografts were treated twice weekly for a total of five treatments, 1 h after the fifth and final treatment, mice were injected with Hoechst 33342 and sacrificed 1 min later. 10 *µ*m frozen sections were cut from the centre of the tumour, fixed and immunostained with a fluorescent rat monoclonal antibody against CD31 and visualised using a goat anti-rat secondary antibody Alexa Fluor 568. Images I and II in each group are of different FOV from the same tumour section. (A I-II) Tumour post-treatment with PBS + T showing that the tumour cell nuclei

around the CD31 positive blood vessels were well perfused. (B I-II) Tumour post-treatment with irinotecan + T showing that the tumour cell nuclei around CD31 positive blood vessels were well perfused. (C – I) Tumour post-treatment with irinotecan and CA4P + T showing that perfusion was reduced around the tumour cell nuclei. (C – II) Tumour cell nuclei around a CD31 positive blood vessel that was well perfused. (D – I) Tumour post-treatment with irinotecan and CA4 thMBs + T where perfusion around the CD31 positive blood vessels was almost completely abolished. (D – II) An area of a tumour which was not as affected as D – I. Scale bars indicate 50 μm.

a reduction in functional vasculature suggesting that tumour microenvironmental changes may promote the enhanced effect. Occasionally, in both the experimental groups treated with irinotecan and CA4P or CA4 thMBs, areas with CD31 positive vessels within the same tumour section were more perfused, indicating heterogeneity in tumour response to treatment (Figure 7.5 C, II and D, II). Perfusion was also assessed in the tumour periphery. Compared to the tumour core, perfusion in the periphery was retained in all experimental groups in a manner similar to the PBS control group (Figure 7.6 A-D).

To quantify the reduction in perfusion, different FOV acquired from co-registered fluorescent images with Hoechst 33342 and CD31 from the tumour core were scored by two blinded independent assessors (the author and Dr Nicola Ingram, School of Medicine, University of Leeds). Using a pre-determined scoring system, Hoechst 33342 intensity was given a score on a scale from 0 to 3, with 0 being the FOV with no Hoechst 33342 and 3 being the most intense staining (Figure 7.7 A). Results are shown in Figure 7.7 B. Despite changes in Hoechst 33342 intensity when assessing the co-registered fluorescence images and the lower median Hoechst 33342 intensity scores in the combination groups these failed to reach statistical significance (Figure 7.7 B). The data however suggested that there was a greater reduction in perfusion in the combination group indicating that this was due to CA4 either from CA4 thMBs or CA4P.

Tumour cell morphology with adjacent immunostained CD31 sections were examined to see if the reduction in perfusion observed with Hoechst 33342 intensity was associated with necrosis (Figure 7.8). Morphologically, tumours treated with irinotecan alone had extensive necrosis (Figure 7.8 B) compared to the other tumours which were mainly viable tumour cells (Figure 7.8). The correlation between necrosis and perfusion was not formally scored as only a few of the tumours from each group were available for histopathological examinations as the tumour tissue available was used for perfusion and PK analysis.

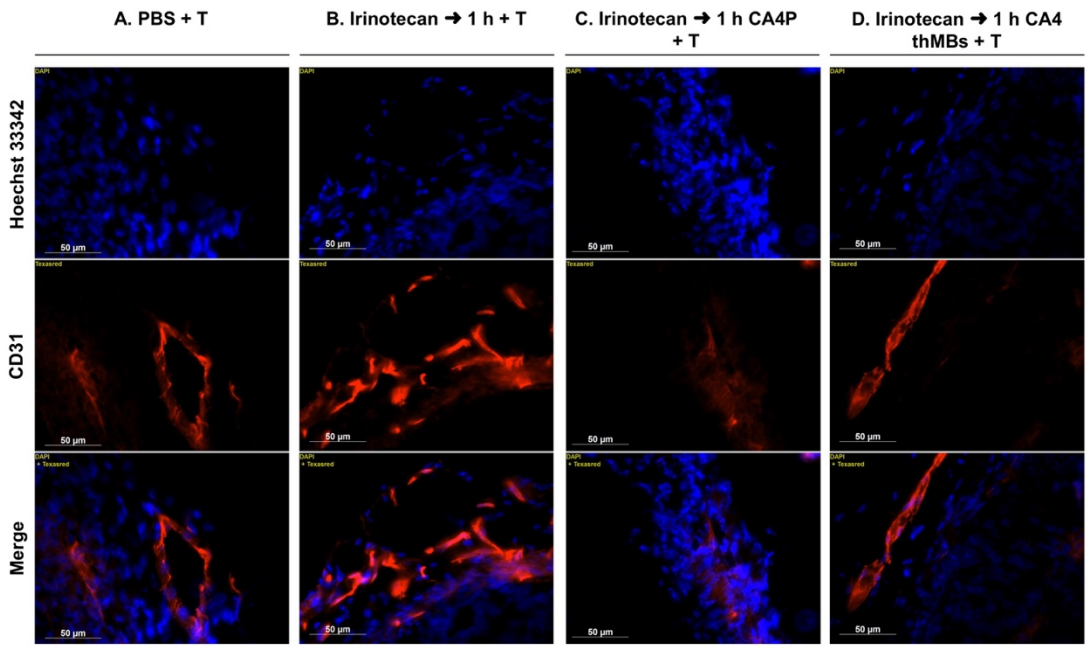

Figure 7.6 Effect of the combination therapy with irinotecan and CA4 on tumour periphery perfusion.

Mice bearing SW480 human CRC xenografts were treated twice weekly for a total of five treatments, 1 h after the fifth and final treatment, mice were injected with Hoechst 33342 and sacrificed 1 min later. 10 *µ*m frozen sections were cut from the centre of the tumour, fixed and immunostained with a fluorescent rat monoclonal antibody against CD31 and visualised using a goat anti-rat secondary antibody Alexa Fluor 568. (A) Tumour post-treatment with PBS + T. (B) Tumour post-treatment with irinotecan + T. (C) Tumour post-treatment with irinotecan and CA4P + T. (D) Tumour post-treatment with irinotecan and CA4 thMBs + T. The tumour periphery in all groups was well perfused, indicative of the Hoechst 33342 staining intensity. Scale bars indicate 50 *µ*m.

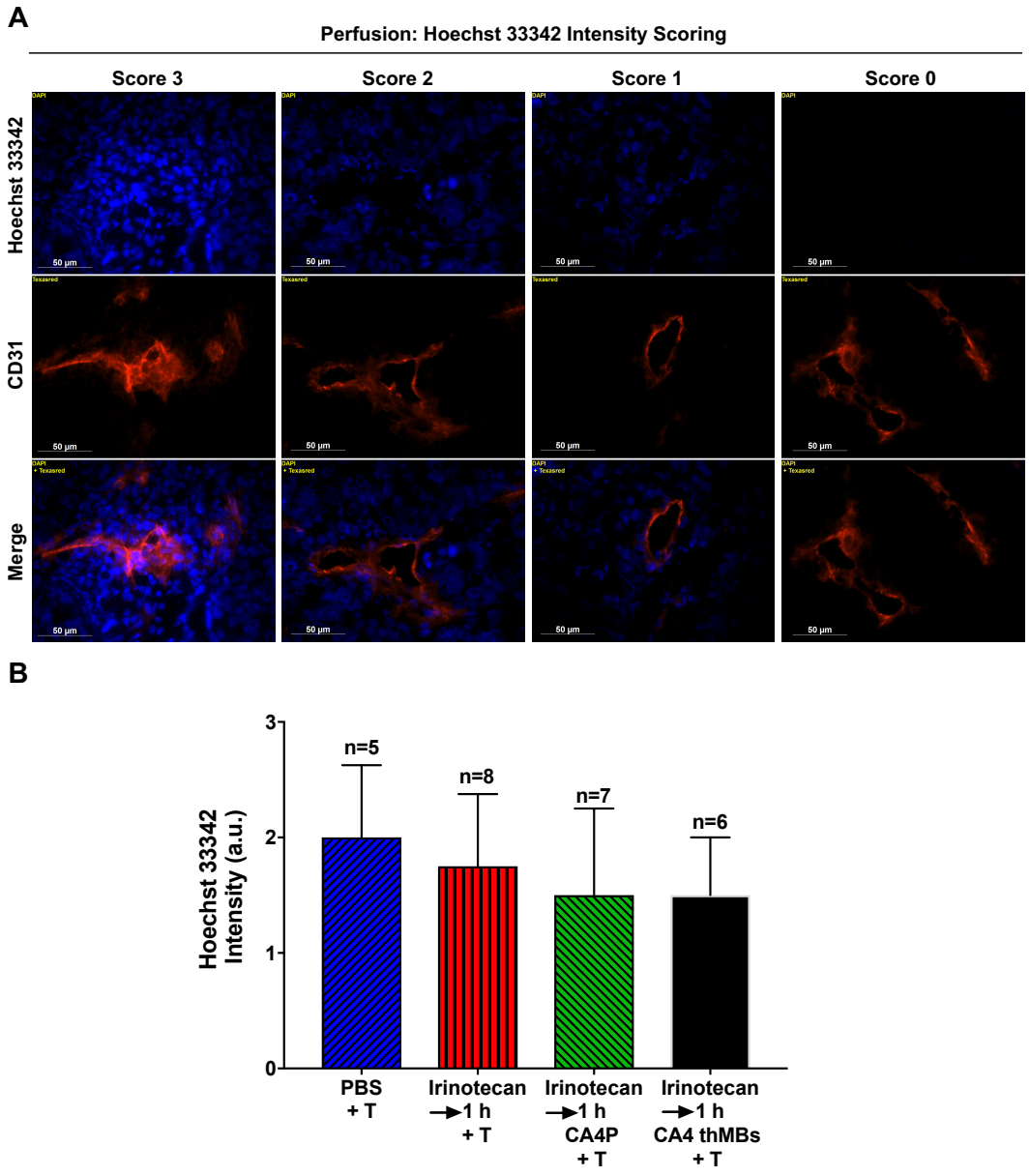

Figure 7.7 Semi-quantitative analysis of tumour core perfusion using Hoechst 33342 intensity.

(A) Representative fluorescence images of Hoechst 33342 and CD31 are shown to describe the perfusion intensity scoring system. A score of 3 was given to the image with the highest Hoechst 33342 intensity, 2 was moderate, 1 was low and 0 was very low or no Hoechst 33342 staining across the FOV. Scale bars indicates 50 μm. (B) FOV from the tumour core were scored from two assessors (the author and Dr Nicola Ingram, School of Medicine, University of Leeds) blinded to the treatment groups. No statistically significant differences were observed between PBS + T compared to irinotecan + T (p=0.3), irinotecan and CA4P + T (p=0.2) or irinotecan and CA4 thMBs + T (p=0.05). No statistically significant differences between irinotecan + T compared to irinotecan and CA4P + T (p=0.7) or irinotecan and CA4 thMBs + T (p=0.5) were

observed. Hoechst 33342 intensity in the irinotecan and CA4P + T was not significantly different from irinotecan and CA4 thMBs + T ($p=0.7$). The data represents the median score from the two assessors and the error bars denote the interquartile range. Significance was calculated using a Mann Whitney U test, two tailed. a.u. arbitrary units.

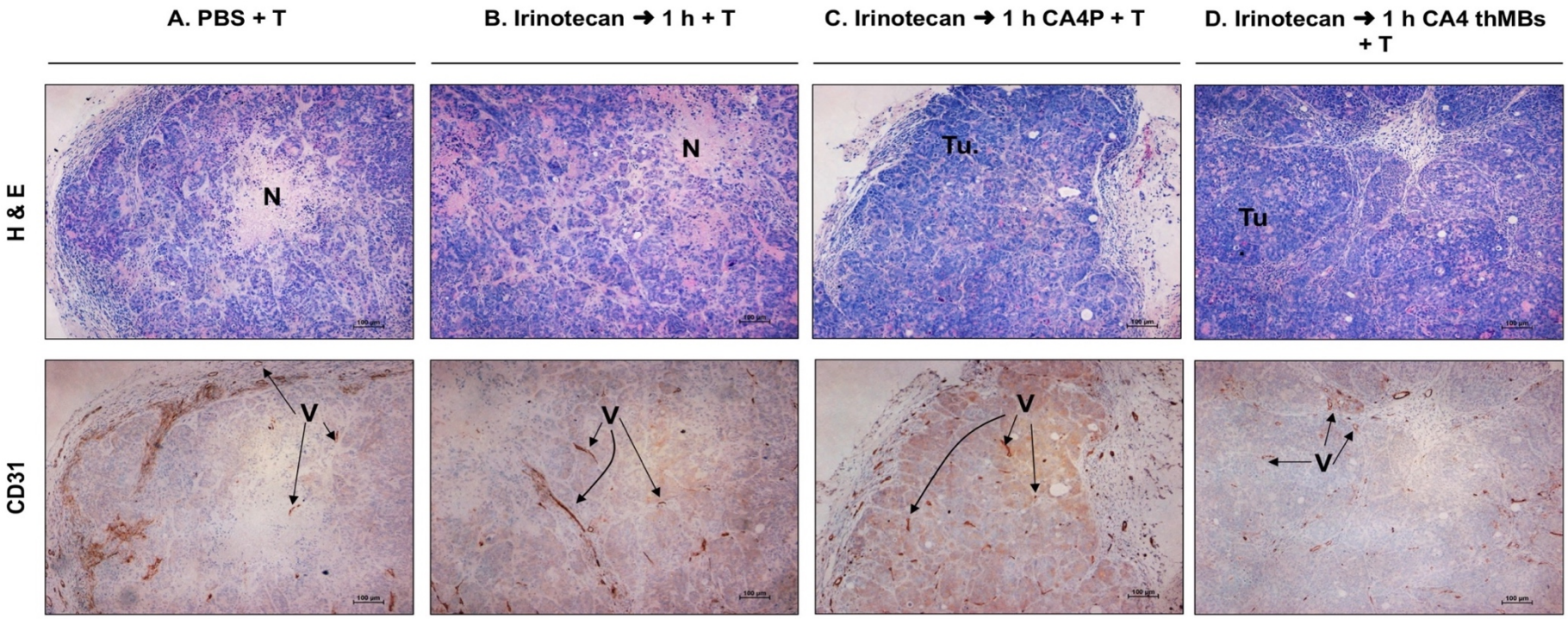

Figure 7.8 Tumour histology and vasculature following combination therapy with irinotecan and CA4.

Top images: Histological images of tumours stained with H & E. Bottom images: Immunohistochemical images of adjacent tumour sections stained with a rat anti-mouse CD31 antibody and CD31 + vessels were visualised with DAB. (A) Tumour section, treated with PBS + T. (B) Tumour treated with irinotecan + T. (C) Tumour treated with Irinotecan + CA4P + T. (D) Tumour section treated with irinotecan and CA4 thMBs + T. In the H & E images necrosis is labelled as N while viable tumour cells are labelled as Tu and blood vessels are labelled as V. Scale bars indicate 100 μm.

7.2.3 Assessment of liver toxicity following combination therapy of irinotecan with CA4

In rare cases, irinotecan is associated with drug induced steatohepatitis mainly characterised by steatosis (when the cytoplasm of the hepatocyte is occupied by fat) and lobular inflammation (Ramachandran & Kakar, 2009). Liver histology on H and E sections was assessed for these drug-induced toxicities. Perivascular inflammation characterised by mononuclear inflammatory cells was observed in all the groups (Figure 7.9). Specifically it was observed in 2/5 mice from the PBS group, 3/6 mice treated with irinotecan and CA4 thMBs + T, 4/9 mice treated with irinotecan and CA4P + T and 3/8 mice treated with irinotecan alone + T. Inflammatory cells in the control PBS group may represent normal resident inflammatory cells that are present in healthy livers. The inflammation was considered very mild as it was also observed in the PBS group and was only observed in small areas of liver.

7.2.4 Tumour and tissue metabolism of irinotecan after combination therapy with CA4

To investigate whether or not the metabolism of irinotecan when administered 1 h prior to CA4 thMBs or CA4P was altered, concentrations of irinotecan and its active and inactive metabolites SN38 and SN38G respectively were determined in tumour samples. The concentrations of irinotecan and its metabolites were also determined in liver, kidney, spleen, colon, lung, heart and plasma samples to investigate if CA4 thMBs or CA4P altered the metabolism and/or biodistribution of irinotecan in these tissues.

The LC-MS/MS method used for irinotecan, SN38 and SN38G detection was developed by Dr Laura McVeigh (School of Medicine, University of Leeds) and Ms Antonia Wierzbicki (Institute of Cancer Therapeutics, University of Bradford) with supervision by Prof. Paul Loadman (Institute of Cancer Therapeutics, University of Bradford). The concentration of CA4 and the presence of CA4G were also determined using the previously described method in sections 2.6 and 3.6.2.

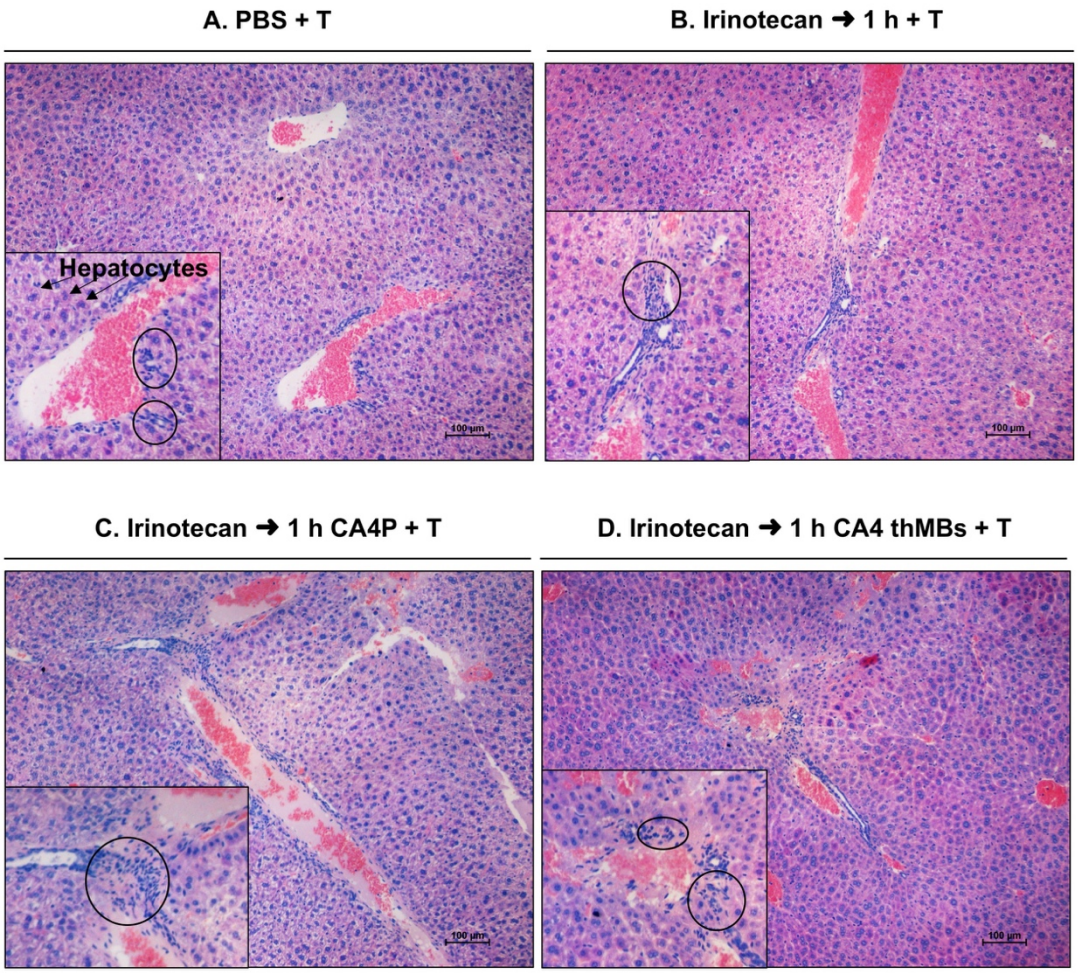

Figure 7.9 Liver histology following combination therapy with irinotecan and CA4.

Histological images of liver stained with H & E. (A) Liver from a mouse treated with PBS + T. Hepatocytes are shown by the black arrows. (B) Liver from a mouse treated with irinotecan +T. (C) Liver tissue from a mouse treated with irinotecan and CA4P + T. (D) Liver tissue from a mouse treated with irinotecan and CA4 thMBs + T. Mononuclear inflammatory cells are circled in the inset images and were observed in all the groups. Scale bars indicate 100 μm.

Tumour and tissue drug concentrations are shown in Figure 7.10 and summarised in tabulated format in Table 7.2. Irinotecan, SN38 and SN38G calibration curves used to extrapolated the data are shown in Appendix E, Figure E.5. Some tumour samples were too small to be cut in half and were used for perfusion analysis only. For LC-MS/MS analysis these were 8/8 tumours from the irinotecan + T, 6/9 tumours from the irinotecan with CA4P + T and 3/6 tumours from the irinotecan with CA4 thMBs + T. Not all tumours or tissues analysed had detectable levels of compounds (Irinotecan, SN38, SN38G or CA4), potentially due to levels being below the LOD. The LOD of all three compounds irinotecan, SN38 and SN38G was 100 pg/mL (Information provided by Dr Laura McVeigh, School of Medicine, University of Leeds). The LOD of CA4 was 10 ng/mL (Figure 3.16).

The rationale for administrating irinotecan 1 h prior to CA4P or CA4 thMBs was that following intratumoural delivery of irinotecan/SN38/SN38G, CA4 would disrupt the vessels causing a reduction in vascular perfusion and subsequently “trapping” the compounds in the tumour. The 1 h post-treatment tumour data however, showed no significant change in the median concentrations of irinotecan or its two metabolites when CA4 was administered either as CA4P or in CA4 thMBs (Figure 7.10 A). CA4 was not detected in any tumour tissue analysed from the two groups with CA4 suggesting that this was below the LOD.

The biodistribution of irinotecan/SN38/SN38G and CA4 was analysed in liver, kidney, spleen, colon, lung, heart and plasma samples (Figure 7.10). A significantly higher concentration of irinotecan was detected in both liver and heart tissue in the irinotecan + T group compared to the irinotecan and CA4 thMBs + T group ($p=0.02$ and $p=0.04$, respectively, Mann-Whitney U test, two-tailed) (Figure 7.10 B and G).

A significantly higher concentration of SN38G in colon was observed in the irinotecan and CA4P + T group compared to the irinotecan + T group ($p=0.03$, Mann-Whitney U test, two-tailed, Figure 7.10 E). The irinotecan + T group had significantly higher concentration of SN38 in lung and plasma compared to irinotecan and CA4P + T ($p=0.04$ and $p=0.01$ respectively, Mann-Whitney U test, two-tailed, Figure 7.10 F and H). The concentration of SN38 in plasma of irinotecan + T group was also significantly higher than in the irinotecan and CA4 thMBs group ($p=0.001$, Mann-Whitney U test, two-tailed, Figure 7.10 H). CA4 was detected in liver (1/9), kidney (1/9) and spleen (2/9) from the irinotecan and CA4P + T group and in the kidney (1/6) and spleen (1/6) from the irinotecan and CA4 thMBs + T (Figure 7.10 B-D). Detectable levels of CA4 in the liver, kidney and spleen are not surprising as CA4 is glucuronidated in the liver

and excreted via the kidneys and is consistent with previous biodistribution studies in rats (section 1.2.1.10 and Figure 1.5). Moreover, detection of CA4 in one kidney and one spleen sample from different mice in the CA4 thMBs + T group suggested that CA4 thMBs were present in these tissue, however due to the fact that LC-MS/MS measures the total concentration of drug present in a tissue homogenate, it was unclear if CA4 was still encapsulated or free.

The relative % of irinotecan, SN38 and SN38G in each tissue analysed from each groups are shown in Figure 7.11. The data shows that the highest levels of conversion of irinotecan to SN38 and SN38G are in plasma and liver. Irinotecan, SN38 and SN38G were widely distributed in the various tissues. This is presumably due to the fact that irinotecan is subject to extensive metabolic conversion by various enzymes mainly UGT1A1 which mediates the conversion of SN38 to SN38G and cytochrome P-450 isoform 3A (CYP3A4) which gives rise to a number of inactive metabolites. (Mathijssen *et al.*, 2001).

The data showed that the highest % of conversation of irinotecan was in the plasma, however, irinotecan was administered i.p. and previous work has shown that following i.p. administration, a small fraction of irinotecan can be metabolised in the peritoneal space to SN38 via carboxylesterase which have crossed the peritoneal membrane from plasma into the peritoneal space (Ahn *et al.*, 2010). Irinotecan is subsequently absorbed into the plasma for further metabolism, explaining the highest relative % of conversation of irinotecan in the plasma. Irinotecan can be converted to SN38 in a number of tissues including lungs, colon, stomach, uterus, pancreas and as previously mentioned the liver (Guichard *et al.*, 1998).

7.3 Discussion

7.3.1 Anti-tumour activity of combination therapy with irinotecan and CA4

Combined therapies of free CA4P or encapsulated CA4 in targeted NPs with conventional chemotherapeutic agents or radiation have shown enhanced tumour growth inhibition (Wildiers *et al.*, 2004; Pattillo *et al.*, 2005; Su *et al.*, 2014). In order to improve drug delivery of CA4 TPP LONDs and avoid non-specific uptake and release into normal tissues, CA4 thMBs were produced. To further enhance therapeutic efficacy of CA4 thMBs these were combined with irinotecan. Escoffre *et. al.,* (2013) delivered US-triggered MBs 1 h after irinotecan (20 mg/kg) and showed an enhanced delivery and tumour growth inhibition. Therefore, delivery of CA4 thMBs

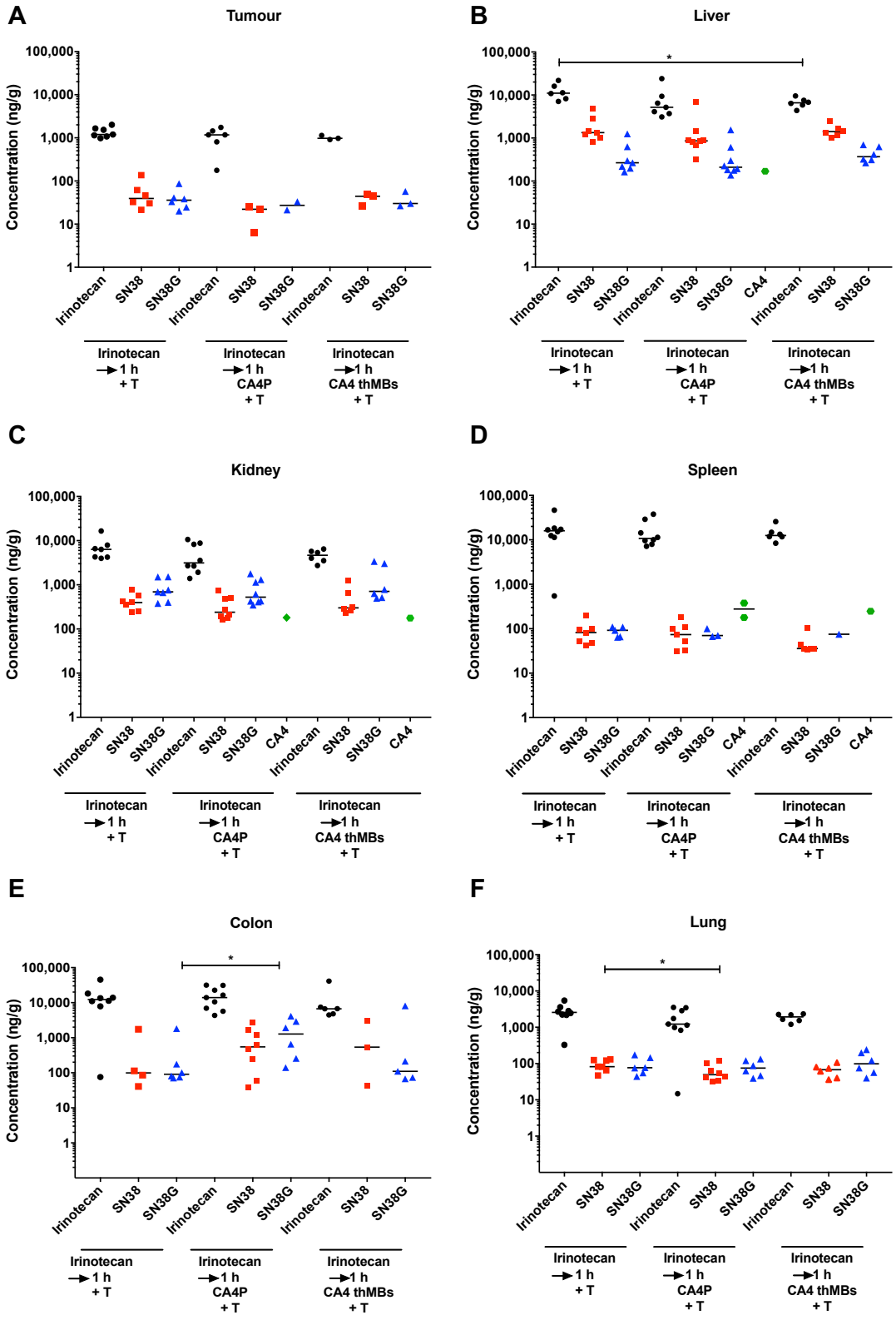
A
Tumour
B
Liver
C
Kidney
D
Spleen
E
Colon
F
Lung
Concentration (ng/g)
100,000
10,000
1,000
100
10
1
Irinotecan
SN38
SN38G
CA4
*
Irinotecan → 1 h + T
Irinotecan → 1 h CA4P + T
Irinotecan → 1 h CA4 thMBs + T

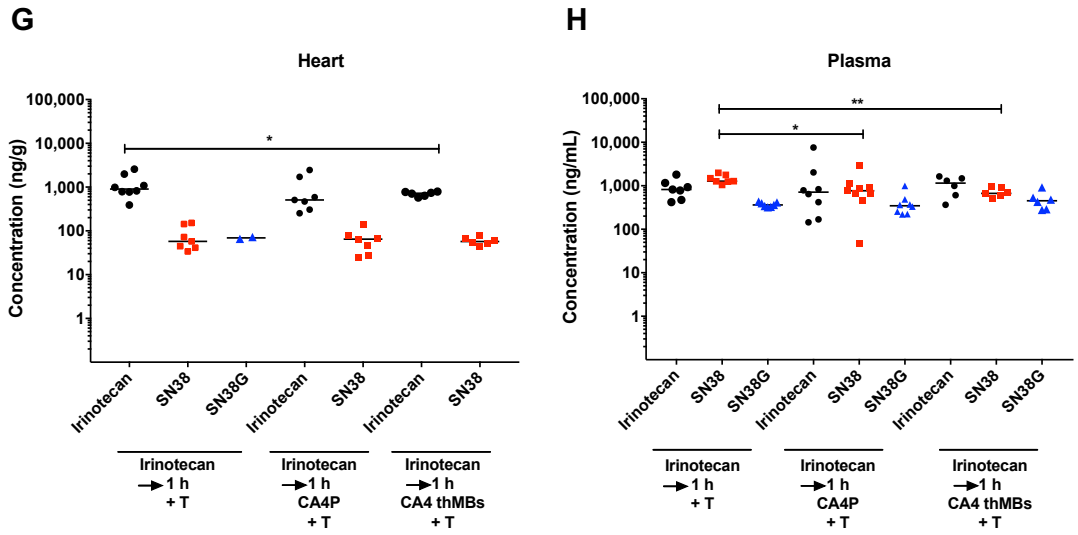

Figure 7.10 *In vivo* biodistribution of irinotecan, SN38, SN38G and CA4.
Tumour, Liver, kidneys, spleen, colon, heart, lungs and plasma were harvested and snap-frozen for LC-MS/MS analysis. (A) Tumour tissue concentrations of irinotecan/SN38 and SN38G in ng/g of tissue. 8/8 tumours from the irinotecan + T; 6/9 tumours from the irinotecan and CA4P + T; 3/6 tumours from the irinotecan and CA4 thMBs + T were available for analysis. (B) Liver tissue concentrations of irinotecan, SN38, SN38G and CA4 in ng/g of tissue. A significantly higher concentration of irinotecan was observed in the irinotecan alone group compared to irinotecan with CA4 thMBs (*, p=0.02). (C) Kidney tissue concentrations of irinotecan, SN38, SN38G and CA4 in ng/g of tissue. (D) Spleen tissue concentrations of irinotecan, SN38, SN3 G and CA4 in ng/g of tissue. (E) Colon tissue concentrations of irinotecan, SN38 and SN38G in ng/g of tissue. A significantly higher concentration of SN38G was observed in the irinotecan with CA4P group compared to irinotecan alone (*, p=0.03). (F) Lung tissue concentrations of irinotecan, SN38 and SN38G in ng/g of tissue. Irinotecan + T showed a higher concentration of SN38 compared to SN38 in the irinotecan with CA4P + T group (*, p=0.04). (G) Heart tissue concentrations of irinotecan, SN38 and SN38G in ng/g of tissue. A higher median concentration of irinotecan was observed in heart tissue in mice treated with irinotecan + T compared to irinotecan with CA4 thMBs + T (*, p=0.04). (H) Plasma tissue concentrations of irinotecan, SN38, SN38G in ng/g of tissue. A higher median concentration of SN38 was observed in the irinotecan + T group compared to irinotecan with CA4P + T group and CA4 thMBs (*, p=0.01, **, p=0.001 respectively). Straight lines (–) represent the median value. Significance was determined using a Mann-Whitney U test, two-tailed.

Table 7.2 Concentrations of irinotecan, SN38, SN38G and CA4 in tissue samples.

Tissue	Irinotecan, SN38, SN38G and CA4 concentration (ng/g or mL of tissue or plasma, median ± SD, n)										
	Irinotecan ➔ 1 h + T			Irinotecan ➔ 1 h CA4P + T				Irinotecan ➔1 h CA4 thMBs + T			
	Irinotecan	SN38	SN38G	Irinotecan	SN38	SN38G	CA4	Irinotecan	SN38	SN38G	CA4
Tumour	1198 ± 373.6, n=7	39.35 ± 54.9, n=6	35.86 ± 40.7, n=6	1174 ± 544.5, n=6	22.1 ± 10.1, n=3	27.22 ± 8.3, n=2	-	975.3 ± 115.6, n= 3	44.31 ± 11.8, n=3	29.98 ± 16.9, n= 3	-
Liver	11039 ± 5489, n=6	1338 ± 1411, n= 7	266.7 ± 391.3, n=7	5191 ± 7391, n=7	860.2 ± 2221, n=8	209.5± 478.2, n=8	168.9, n=1	6589 ± 1722, n=6	1412 ± 522.1, n=6	369.7 ± 181.2, n=6	-
Kidney	6338 ± 4391, n=7	397.2 ± 431.2 n=7	693.5 ± 477.9, n=7	3137 ± 3624, n=8	240.5 ± 209.6, n=8	524.7 ± 535.6, n=8	181.3, n=1	4680 ± 1435, n=6	300.4 ± 404.3, n=6	710.2 ± 1353, n=6	176.1, n=1
Spleen	16003 ± 13154, n=8	82.18 ± 54.6, n=7	92.1 ± 22.2, n=5	10738 ± 11260, n=8	73.7 ± 54.5, n=7	70.4 ± 18.5, n=3	278.4 ± 141.2, n= 2	12576 ± 5958, n=6	35.92 ± 27.3, n=6	75.3, n=1	247.3, n=1
Colon	12357 ± 13253, n=8	99.25 ± 832.7, n= 4	90.6 ± 704, n=6	14003 ± 10438, n=9	546.6 ± 924.7, n=8	1280 ± 1606, n=6	-	6701 ± 14345, n=6	538 ± 1590, n=3	110.2 ± 3570, n=5	-
Lung	2564 ± 1437, n=8	81.9 ± 32.7, n=7	76.7 ± 52.3, n=6	1219 ± 1246, n=9	49.4 ± 32.8, n=8	75.21 ± 38.9, n=6	-	1924 ± 463.5, n=6	67.72 ± 26.5, n=6	98.49 ± 81.5, n=6	-
Heart	903.7 ± 724.7, n=8	57.6 ± 49.4, n=7	69.1 ± 5, n=2	508 ± 846.6, n=7	64.9 ± 40.1, n=7	-	-	722.9 ± 82.8, n=6	57.08 ± 12.9, n=6	-	-
Plasma	818.4 ± 469.3, n=7	1273 ± 334.5, n=7	363.5 ± 43.9, n=7	714.6 ± 2500, n=8	770.4 ± 820.7, n=9	346.8 ± 253.6, n=8	-	1150 ± 501.3, n=6	665.5 ± 184.3, n=6	453.7 ± 234.5, n=6	-

The concentrations of irinotecan, SN38, SN38G and CA4 in tumour, Liver, kidneys, spleen, colon, heart, lungs and plasma. 8/8 tumours from the irinotecan + T; 6/9 tumours from the irinotecan and CA4P + T; 3/6 tumours from the irinotecan and CA4 thMBs + T were available for analysis. Data shows the median ± SD values. N/A: not applicable. N number of samples with detectable levels.

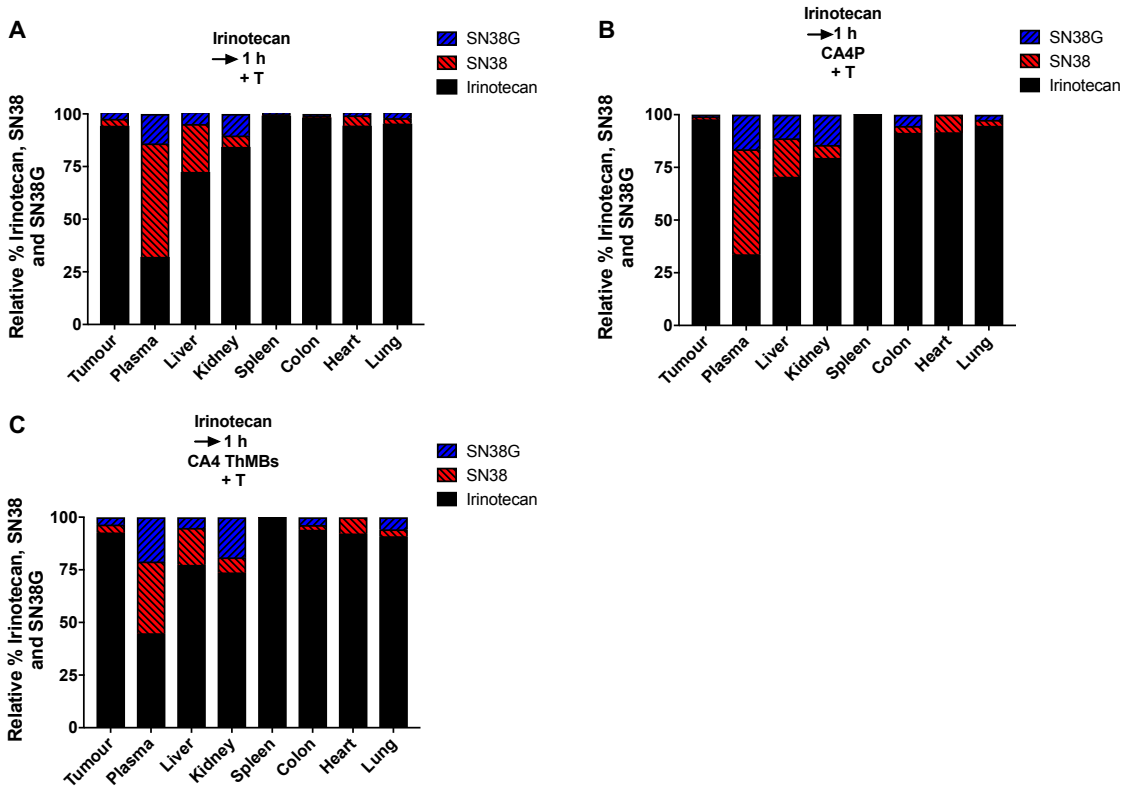

Figure 7.11 Relative % of irinotecan, SN38 and SN38G in tissue samples. Tumour, Liver, kidneys, spleen, colon, heart, lungs and plasma were collected for LC-MS/MS after five treatments and the relative % of irinotecan/SN38/SN38G was determined. (A) Relative % of irinotecan, SN38 and SN38G in tissue samples from mice treated with irinotecan + T. (B) Relative % of irinotecan, SN38 and SN38G in tissue samples from mice treated with irinotecan and CA4P + T. (C) Relative % of irinotecan, SN38 and SN38G in tissue samples from mice treated with irinotecan and CA4 thMBs + T.

was anticipated to improve drug delivery of irinotecan and also enhance its efficacy by the presence of CA4 through microenvironmental changes.

The schedule of administration and tumour type are particularly important for effective anti-tumour activity. In this study irinotecan was administered 1 h before CA4, because of potential tumour microenvironmental changes hindering the penetration of irinotecan following CA4 treatment. A previous study with irinotecan and CA4P in a sarcoma model demonstrated that enhanced tumour growth inhibition was independent of the administration sequence due to the already increased sensitivity of the model to CA4P (Wildiers *et al.*, 2004). Tumour responses have been enhanced when CA4P was administered 1 h after cisplatin in rodent and human tumour xenografts (Siemann *et al.*, 2002). Triple drug combinations including CA4P, paclitaxel and carboplatin have also been conducted in preclinical animal models of anaplastic thyroid cancer (Yeung *et al.*, 2007). This study administered CA4P a day before carboplatin followed 1 h later by paclitaxel, the triple combination showed a significant tumour growth inhibition against anaplastic thyroid cancer (Yeung *et al.*, 2007). In contrast, another studied in liver tumours showed that if CA4 was administered 2 h prior to gemcitabine it significantly decreased the uptake of gemcitabine (Fruytier *et al.*, 2016). Work conducted with CA4 in combination with radiation in two different mammary carcinoma models KHT and C3H demonstrated the importance of scheduling in terms of tumour type (Murata, Overgaard & Horsman, 2001). Administration of CA4 after or concurrently with radiation in C3H enhanced cell killing but not if it was administered before radiation, in contrast, in the KHT model, the enhanced activity was independent of sequence (Murata, Overgaard & Horsman, 2001). Therefore, generally the greatest anti-tumour activity is observed when CA4 or CA4P is administered after or concurrently with a chemotherapeutic agent.

The growth of tumours treated with irinotecan and CA4 thMBs was moderately delayed when compared to PBS control xenografts, only reaching statistical significance on day 17 after the first two treatments. In contrast, the combination of irinotecan with CA4P resulted in significant tumour growth inhibition as well as tumour regression. This was also significantly different from irinotecan administered alone. The data support the hypothesis that CA4 enhances the anti-tumour activity of irinotecan or irinotecan is potentially potentiating the anti-tumour activity of CA4. There are at least three mechanisms that can explain the potential in enhanced activity: (i) trapping, (ii) different cell targets or (ii) microenvironmental changes.

7.3.1.1 The trapping effect

The potential of trapping chemotherapeutic agents in tumours through vascular collapse caused by CA4 and therefore prolonging the exposure time of tumour cells to the chemotherapeutic agent, is one of the key features initiating combination studies (Siemann *et al.*, 2002; Siemann, 2011).

The results in the present study did not demonstrate a trapping effect with the 1 h time point following the final treatment. The addition of CA4 thMBs or CA4P did not appear to alter the early tumour and tissue metabolism of irinotecan as the concentrations of irinotecan, SN38 and SN38G were similar between the three experimental groups. However, this does not rule out the possibility of trapping. Wildiers *et al.,* (2004) administered irinotecan 1 h before CA4P and observed a significant increase in the intratumoural concentration of SN38 measured by HPLC from 1 h to 5 h, suggesting the potential trapping of SN38 (Wildiers *et al.*, 2004). Morinaga *et al.,* (2003) demonstrated that a CA4 derivative administered at the same time as cisplatin, increased the concentrations of cisplatin over time, with the highest concentration observed after 96 h (Morinaga *et al.*, 2003). Therefore, in the present study it is plausible that either the time point for collection was too soon to observe a trapping effect or potentially the amount of CA4 was insufficient to trap effectively.

The trapping effect of CA4 has been demonstrated using a NP system, the nanocell, encapsulating both CA4 and DOX (Sengupta *et al.*, 2005). The work conducted with the nanocell demonstrated a timely release of CA4 in the tumour causing vascular collapse followed, by the release and subsequent trapping of DOX in the tumour, enhancing anti-tumour effects and reducing toxicity (Sengupta *et al.*, 2005). Gao *et al.,* (2015) used MRI to study the trapping of GdDTPA by CA4P, when these two agents were co-administered. Their results showed that CA4P prolonged the retention time of GdDTPA in tumour, as there was an enhanced contrast signal over time without a rapid decline and therefore, concluded that this was due to effective trapping (Gao *et al.*, 2015).

7.3.1.2 Different cell targets

In a mouse colon adenocarcinoma model (MAC 29) the administration of 5-FU (125 mg/kg), 20 min prior to CA4P (125 mg/kg) caused a significant growth delay, without any evidence of trapping of 5-FU in tumours (Grosios *et al.*, 2000). The study therefore, demonstrated that trapping of drugs does not fully explain the enhanced anti-tumour activity when CA4 is used in combination (Grosios *et al.*, 2000). The 20 min time point used was potentially due to the plasma half-life of 5-FU being 15 min

in mice (Chadwick & Rogers, 1972). Analysis of the PK parameters in tumour tissue using HPLC 4 h post administration of 5-FU with CA4P, showed that 5-FU was rapidly cleared from tumours in the combined group vs 5-FU alone (Grosios *et al.*, 2000). This was explained by increased metabolism of 5-FU, although the concentrations of 5-FU in the tumours were lower in the combined group, theoretically the severe necrosis caused by CA4P left only a small proportion of target cells for example the viable rim for therapy (Grosios *et al.*, 2000). Therefore, irinotecan was potentially able to target and eliminate the remaining or CA4 resistant cells in the viable rim.

The studies described previously investigated the combination of CA4 or CA4P with chemotherapeutic agents after a single treatment. In the present work, irinotecan was administered using a frequent low dose treatment schedule followed by CA4 thMBs or CA4P. CEPs are a major cause for tumour resistance to CA4 as they are recruited to the viable rim (Nathan *et al.*, 2012). Frequent low dose administration of chemotherapy can exhibit anti-angiogenic properties (Kerbel & Kamen, 2004). Low dose irinotecan administered at 10 mg/kg twice a week for a total of four weeks, as well as demonstrating an enhanced anti-tumour activity also showed anti-angiogenic effects (Murakami *et al.*, 2011). Specifically, low dose irinotecan administered in this frequent dosing schedule decreased and continuously suppressed CEPs in a colon cancer model (Murakami *et al.*, 2011). This anti-angiogenic activity of low dose irinotecan could also explain the potential in enhanced activity when CA4 thMBs or CA4P are combined.

7.3.1.3 Microenvironmental changes

Tumour microenvironmental changes caused by CA4P or CA4 thMBs may have also contributed to the potential enhanced activity. After the final treatment measurements of perfusion using Hoechst 33342 showed that both CA4P and CA4 thMBs caused a reduction in perfusion compared to PBS control when qualitatively assessing the images. However following quantitative assessment despite the lower median Hoechst 33342 intensity scores in the combination groups these did not reach statistical significance compared to PBS or irinotecan alone (Figure 7.5 and 7.7).

A previous study reported that a 75 mg/kg single dose of irinotecan alone did not cause any reduction in perfused vasculature (Chaplin & Hill, 2002). It should also be noted, that a reduction in perfusion is also expected as after the five treatments over a two week period of growth, central areas of tumour would be necrotic due to both the irinotecan and the fast growth characteristics of tumour xenografts that outstrip the growth of corresponding vasculature to feed it. However, in this case the

reduction in perfusion was observed qualitatively to be greater than the control groups which does indicate an additional effect from CA4 release. Demonstrating both the release of CA4 from the CA4 thMB construct and the changes in tumour microenvironment in terms of blood flow. Therefore, trapping may have occurred as perfusion was reduced, however was not observed as mentioned at the time point analysed.

Wildiers *et al.,* (2004) also suggested that CA4P was directly influencing the intratumoural metabolism of irinotecan, caused indirectly due to the tumour microenvironmental changes induced by CA4 such as reduction in oxygen levels, perfusion or alterations in pH (Wildiers *et al.*, 2004). Irinotecan can be metabolised to SN38 in tumour tissue (Atsumi, Okazaki & Hakusui, 1995; Guichard *et al.*, 1999). Previous studies have demonstrated that changes in interstitial fluid pressure caused by CA4P enhance the retention and uptake of paclitaxel NPs in breast cancer (Gao *et al.*, 2016). CA4P was administered 1 h prior to paclitaxel NPs and reduced the overall interstitial fluid pressure, providing the ideal tumour microenvironment that lead to enhanced paclitaxel NP uptake in tumour, compared to paclitaxel NPs alone (Gao *et al.*, 2016).

7.3.1.4 Toxicity and dosing

Very mild perivascular inflammation in the liver was observed in this study in all the treatment groups involving irinotecan, indicating no additional change in toxicity from the combination therapy. Also inflammation was observed in the PBS group indicating that resident inflammatory cells were also potentially present in healthy livers. Other studies have used much higher doses of CA4 than are currently able to encapsulated in LONDs. However, this study suggested that high doses may not be required to cause reduction in perfusion, but the timing for effective chemotherapy trapping may potentially need refining or the method of delivery e.g. with thMBs.

7.3.2 Potential mechanism of action of CA4 delivery by thMBs compared to CA4P

The difference in anti-tumour activity between the group that received CA4P and the group that received CA4 thMBs was potentially attributed to the different delivery routes, although, tumour growth was not significantly different between the two groups. This may be due to a number of plausible reasons: firstly delivery of CA4 via thMBs has altered the PK of CA4 and secondly the US alone was enhancing the delivery of the two free drugs.

The US trigger caused MB destruction, which may have cause LOND rupture and subsequent release of CA4 near the tumour region, however, release of intact CA4 TPP LONDs near the tumour region would have potentially led to uptake of these and subsequent entrapment in endosomal compartments, leading to a slow release of the drug. Therefore, the levels of CA4 required to work in combination with irinotecan were potentially not as high as CA4P delivered unencapsulated at the desired time. Chapter 5 discusses in detail the potential of slow release, followed by a delayed response when CA4 TPP LONDs are delivered as a monotherapy. Data presented in Chapter 6 suggested that CA4 thMBs caused a reduction in tumour perfusion 1 h post-injection, demonstrating that there is a release of CA4 intratumourally from LOND thMB structures, however the concentration required to cause a change in perfusion may not necessarily correlate with the concentration required to entrap irinotecan.

However, it could also be argued that a slow release of CA4 would be beneficial for additional anti-tumour effects when administered after irinotecan, due to the sustained reduction in tumour perfusion leading to a decrease in oxygen and nutrient content that would eventually lead to necrosis of tumour cells. The compounds in this case could potentially be administered at the same time.

Choijmants *et al.,* (2011) have shown that US alone enhanced the delivery of low dose irinotecan and caused a significant tumour growth reduction in a human uterine sarcoma xenograft model (Choijamts *et al.*, 2011). The US trigger, may therefore be enhancing the intratumoral delivery of both irinotecan and CA4P leading to an enhanced efficacy.

7.3.3 Conclusion

In conclusion the above study findings support the hypothesis that CA4 thMBs have the potential to enhance the anti-tumour activity of a conventional chemotherapeutic agent such as irinotecan. Further optimisation and refinement of the treatment schedule is required to determine the optimal timing of delivery of CA4 thMBs and US to achieve the greatest anti-tumour response. The results demonstrated that the combination of irinotecan with CA4P and US enhanced the anti-tumour response compared to irinotecan alone and US. However, the exact mechanism of action leading to this enhanced efficacy is not clear although microenvironmental changes such as reduction in perfusion may be occurring as suggested by the data presented. Later, PK data would also be required to potentially identify any trapping or retention of irinotecan, SN38 and SN38G in the tumour.

Chapter 8
Final discussion

8.1 Towards clinical translation of a novel drug delivery system

CRC is the fourth most common cause of cancer related deaths worldwide, surgery is the first line treatment in early stage CRC and following surgical resection most patients and particularly patients with advance disease undergo chemotherapy. However, conventional delivery of anti-cancer drugs is an inefficient process caused by low bioavailability, rapid metabolism and elimination and poor solubility. This project was undertaken to assess LONDs as a novel hydrophobic DDS. LONDs can be used as a generic particle to aid the delivery of poorly soluble compounds to a number of cancers or diseases, however this study was focused on the treatment of CRC.

Drug delivery via passively and actively targeted NPs has a number of advantages including drug solubilisation, protection from rapid degradation, rapid metabolism and elimination and it also enables the control release into target tissues (Öztürk-Atar, Eroğlu & Çalış, 2017). Limitations of this technology include unspecific uptake into normal tissue due to the small size of NPs, potential aggregation of particles during storage and limitations in drug loading depending on the particle properties (Öztürk-Atar, Eroğlu & Çalış, 2017).

There is a substantial amount of research ongoing on the use of NPs for drug delivery, currently approximately 50 NPs are approved for use clinically by the FDA, from these 34% are polymer NPs, 30% are nanocrystals, 20% are liposomes (Doxil® and Onivyde®), 10% inorganic NPs, 4% are protein NPs (Abraxane) and 2% are micelles (Ventola, 2017). Doxil® and Abraxane have also been approved for cancer treatment including metastatic breast cancer and pancreatic cancer by the European Medicines Agency (EMA) (Tran *et al.*, 2017). To receive approval, the FDA has issued some guidelines regarding assessment of nano-formulations for clinical use (U.S. Department of Health and Human Services Food and Drug Administration, 2017). A full physical and chemical characterisation of the nano-formulations is required, including information on size, surface charge, shape, morphology, concentration, *in vitro* release kinetics, at least 85% release of drug from the particle is required, capacity of loading, stability, sterility and endotoxin levels. Thorough investigations need to be conducted in terms of the PK and PD responses of the released compound as well as the PK of the particle which acts as the carrier for the active compound. Most importantly nano-formulations intended for clinical use need to be produced in accordance with the current good manufacturing practice (CGMP)

regulations (U.S. Department of Health and Human Services Food and Drug Administration, 2017).

8.1.1 Physiochemical properties of LONDs and *in vitro evaluation*

The multidisciplinary nature of this project permitted development and evaluation of different LOND particles and this was the first study describing their *in vitro* and *in vivo* evaluation. CA4 was encapsulated in LONDs and used in proof-of-concept drug delivery studies during the course of the project. It was shown that the first LOND structure using TA to produce CA4 TA LONDs were unsuitable for use as drug delivery vehicles. This was due to issues with stability in terms of the shell and the solubility of the TA oil, leading to rapid leakage of CA4. These issues were overcome by replacing the TA oil with TPP and improving the shell rigidity by incorporating DSPC and cholesterol to produce CA4 TPP LONDs. The highest %EE of CA4 achieved in CA4 TPP LONDs was > 70%, these were stable for over 6 weeks at 4ºC (Mico, 2017; Mico *et al.*, 2017).

In order to advance LONDs as hydrophobic drug delivery vehicles their stability and physiochemical properties and loading capacity need further investigation. Unlike liposomes for example, which rely on the incorporation of hydrophobic drugs in the lipid bilayer and are restricted in the amount of drug that can be encapsulated (Nallamothu *et al.*, 2006a), nanoemulsion such as LONDs have a higher loading capacity as hydrophobic compounds are encapsulated in their oil core. However, further optimisation in LOND production is required to achieve a higher loading.

Stability of LONDs over time is currently assessed through the evaluation of size changes and further experiments potentially using dialysis techniques are required to study drug leakage from CA4 TPP LONDs consistent with size reduction. Dialysis could also be used to study the *in vitro* release kinetics of CA4 from the LONDs over time at 37ºC by measuring the concentration of CA4 released at different time intervals by LC-MS/MS. This technique is routinely used to study the release kinetics of drugs from NPs (Nallamothu *et al.*, 2006a, 2006b; Wang *et al.*, 2010).

The surface charge of LONDs was not determined in this project, however as surface charge is another factor that determines delivery efficacy of NPs (Wilhelm *et al.*, 2016) measurement in LONDs should be evaluated. DLS has been used previously to measure surface charge of polymeric CA4P NPs (Poojari, Srivastava & Panda, 2015).

The first *in vitro* results with CA4 TPP LONDs in this study showed the rapid release and/or potential uptake of CA4 from LONDs within 30 min of exposure of endothelial and human CRC cells. CA4 released from the TPP LONDs following transient treatments resulted in the characteristics of MT disruption, while prolonged treatments resulted in a mitotic block in G2/M phase and mitotic catastrophe.

8.1.2 CA4 thMB production, optimisation and upscaling

LONDs are nanosized drug delivery vehicles and similar to liposomes may suffer from non-specific uptake and distribution *in vivo*. In order to target drug delivery and increase the concentration of drug delivered at the target site, LONDs were attached to thMBs in this study and their release was triggered by an external US destruction pulse designed to destroy the MBs and further enhance the uptake of LONDs and/or free drug to tumour cells.

Production of thMBs with LONDs was initiated using a single step method based on previous results with liposomes (Peyman *et al.*, 2012). However, production of thMBs with CA4 TA LONDs using the single step method resulted in the destabilisation of the LONDs and the release of oil in the solution affecting MB production and stability (Mico, 2017). Further, optimisation resulted in the design of the two-step on-chip system whereby LONDs were attached to MBs after production. CA4 thMBs were produced in this manner and used *in vitro* and *in vivo*. This study showed that using the on-chip two-step method for production of CA4 thMBs, 10^7 MBs/mL were produced, this needs further optimisation to reduce the initial volume and potentially increase the concentration of MBs/mL. This would subsequently increase the number of LONDs per thMB and the concentration of CA4 delivered. To enable contrast imaging of hydrophobic delivery of drugs via LONDs and thMBs, concentrations of 10^8 MBs/mL would be required at production, this would result in a 10^7 bolus injection of MBs which is normally used for contrast imaging (Lyshchik *et al.*, 2007).

Alternative conjugation to NeutrAvidin-biotin for attachment of LONDs to thMBs or targeting antibodies to the surface of LONDs or thMBs need to be explored in the future. NeutrAvidin could potentially bind to physiological biotin in the human body which is needed for fatty acid synthesis and gluconeogenesis therefore, may lead to unanticipated non-specific binding (Kaufmann, 2009). Another potential issue is that the binding of NeutrAvidin to biotin through a multivalent manner may induce cross-linking of the CA4 thMB components. To overcome these potential issues, alternative conjugation approaches are being explored such as maleimide-thiol linkages, which have been used previously (Eloy *et al.*, 2017). A maleimide-PEG-lipid (DSPE) would

replace the DSPE-BPEG$_{2000}$ lipid on the LOND and thMB shell, following a thiol-carrying antibody would be able to react with maleimide forming a thioether bond (Klibanov, 2005). Preliminary work has been conducted by Dr Victoria Mico (School of Physics and Astronomy, University of Leeds) using maleimide-thiol as an alternative conjugation approach.

To scale-up, simplify and improve reproducibility of the normal on-chip production of thMBs, progress has been made by the Leeds Microbubble Consortium at the University of Leeds with the development of the Horizon Microbubble Maker for the on-demand production of MBs. This approach may well be adapted in future for the production of thMBs with LONDs.

The combination of NPs-attached to MBs and US has not yet been performed in a clinical trial setting. However, co-delivery of a commercially available MB with gemcitabine and combined with US improved gemcitabine efficacy and showed an increase survival of patients with pancreatic cancer (Kotopoulis *et al.*, 2013; Dimcevski *et al.*, 2016). Demonstrating the potential of clinical translation of this novel approach of thMBs with LONDs. Encapsulation of a drug in a NP and direct attachment to MB is anticipated to further enhance efficacy and reduce systemic concentrations of toxic drugs.

8.1.3 *In vivo* evaluation of LONDs and CA4 thMBs

To further progress the use of LONDs and LONDs with thMBs as DDS, more investigations of PK, PD responses and drug penetration will be required prior to further translation of this technology towards clinical trials. This may involve the introduction of new techniques to measure the early response to therapy and methodologies to measure drug penetration into tissues as methods like LC-MS/MS used in this project measure the total drug concentration in a tissue homogenate and therefore, do not provide an image of the heterogeneity of drug distribution within the tissues and specifically within the complex microenvironment of a solid tumour (Giordano *et al.*, 2016).

8.1.3.1 Measuring early response to therapy

This study showed by using CA4 TPP LONDs as a monotherapy and assessing tumour responses after 1 and 24 h post-injection, that tumour histology in terms of haemorrhage, necrosis and mitoses was not sensitive enough when using small cohort numbers and low doses. Therefore, despite minor differences such as higher % of haemorrhage 24 h post-injection these were insignificant when compared to

control and free CA4 tumours. Staining of tumour perfusion using Hoechst 33342 was then developed as an assay to assess tumour response to CA4 thMBs, as a significant reduction in blood flow is reported after CA4P treatment (El-Emir *et al.*, 2005). The fluorescent images with Hoechst 33342 showed a reduction in tumour perfusion 1 h post-injection with CA4 thMBs however, these did not reach statistical significance due to the small animal numbers used per group. Although Hoechst 33342 was a better marker for detecting early responses to CA4 and provided some semi-quantitative data, future work will involve using CEUS. Xie and co-workers (2018), used CEUS to measure the early changes in tumour perfusion after CA4P in the core and periphery (Zhang *et al.*, 2018).

8.1.3.2 PK and drug penetration

An LC-MS/MS method was developed for the specific detection of CA4 in LOND and tissue samples. The LOD for CA4 was 10 ng, further optimisation and validation to potentially improve the method will be required. Following this, further PK studies in the future will be conducted using LC-MS/MS to measure total drug concentration in various tissue samples, however in order to obtain more information about drug penetration and particularly distribution within solid tumours, methods like Mass Spectrometry Imaging (MSI) will be performed. MSI is a technique that can be used to visualise the localisation and distribution of parent drug and its metabolites in tissues, which is important for ADMET and PK studies (Prideaux & Stoeckli, 2012). Briefly, the basic steps in MSI start by obtaining a tissue specimen via snap-freezing and cryo-sectioning, followed by tissue section mounting, spectra are then collected from a tissue in a raster pattern creating a grid of points where molecules have been ionised and detected according to their m/z (Lietz, Gemperline & Li, 2013).

One of the most widely used MSI techniques is Matrix-Assisted Laser Desorption/Ionisation MSI (MALDI-MSI). MALDI-MSI allows molecular imaging and profiling of compounds such as lipids, peptides and drugs in tissue sections, specifically it acquires an array of single mass spectra across a tissue sections at a predefined resolution (20-200 μm), these are then combined to generate a molecular image (or map) of the position, distribution, abundance intensity of a specific ion signal within the tissue section (Cole *et al.*, 2011). However, it should be noted that MALDI-MSI has some drawbacks specifically when required for drug localisation. MALDI was specifically designed for molecules with high molecular weight and the matrix used is optimal for these, however most drugs have low molecular weight and therefore, there is a high background noise with a substantial amount of molecules

with similar molecular weights, also sensitivity is an issue when administering very low doses (Morosi *et al.*, 2013b).

As a “standard” Metrix is not available researchers have started to adapt protocols by using NPs as matrices to remove background noise, this has been carried out, and the visualisation of paclitaxel distribution in a number tumour xenografts was achieved and showed the heterogeneity in distribution and differences in paclitaxel penetration between the different tumour types (Morosi *et al.*, 2013a; Giordano *et al.*, 2016).

MALDI-MSI has also been used to study drug penetration of liposomal doxorubicin, irinotecan and their metabolites *in vitro* using spheroids (Liu, Weaver & Hummon, 2013; Lukowski, Weaver & Hummon, 2017). Spheroids are aggregates of tumour cells grown in tissue culture, these potentially have many properties of a solid tumour and are used to study drug penetrations (Minchinton & Tannock, 2006). Using patient-derived colorectal cancer organoids the drug response, distribution and metabolism of irinotecan was assessed using MALDI-MSI (Liu *et al.*, 2018). There is therefore, the potential to use MALDI-MSI to study drug penetration and distribution after treatment with LONDs or thMBs. The hypothesis in this study is that US through sonoporation is allowing the penetration of drug or LONDs deeper into the tumour core following thMB delivery.

8.1.4 US trigger optimisation for improved targeted drug delivery

Alternative US parameters could also be used and tested to identify the optimal conditions for drug delivery via CA4 thMBs. For example a longer 2.2 MHz tone burst could be tested or a 5 MHz chirp sequence. *In vitro* it has been shown that exposure of cells to a 5 MHz chirp pulse had a greater uptake of drug than a 2 min 2.2 MHz tone (McLaughlan *et al.*, 2013). Increasing the MI or more US cycles could also improve delivery of CA4 TPP LONDs by thMBs.

In the current studies an unfocused US transducer was used, as the nature of the pre-clinical setting permitted the direct placement of the US transducer onto the tumour-xenograft region it was assumed that there was minimal effect if any, on surrounding normal tissues. In the future alternatives to improve drug delivery such as a focused US maybe used. Focused US accumulates all of the acoustic energy to a specific region of interest inside the body with negligible effects on the surrounding tissue (Fan & Yeh, 2014). Using focused US, higher MI 0.4-0.5, higher duty cycles

2.5-3 % have been shown to improve NP uptake in tumours previously (Eggen *et al.*, 2014; Snipstad *et al.*, 2017).

8.1.5 Orthotopic model for CRC

Following pre-clinical studies in xenografts, the effectiveness of the CA4 TPP LONDs and CA4 thMBs would also be tested using an orthotopic model of CRC providing a more physiological relevant model to human disease (Evans *et al.*, 2016). This could be achieved by direct orthotopic implantation of CRC cells into the bowel wall, which is performed by surgery under general anaesthesia (Tseng, Leong & Engleman, 2007; Evans *et al.*, 2016). A laparotomy is performed to expose the cecum and then CRC previously grown in culture or small pieces of a tumour grown subcutaneously in another mouse and excised are injected into the cecal wall (Tseng, Leong & Engleman, 2007). However, surgery is invasive and can potentially lead to mortality and is complex and time consuming. Another less invasive technique is ultrasound-guided inoculation which has been employed in an orthotopic bladder cancer model, this is less invasive, rapid and reproducible (Jäger *et al.*, 2013). Ultrasound-guided inoculation could be used for direct injection into the bowel wall. Successful orthotopic models of CRC liver metastases have been already established using this technique (P.L.Coletta, personal communication).

8.1.6 The combination of irinotecan with CA4 thMBs and US

The combination of low dose irinotecan followed with CA4P or CA4 thMBs showed some interesting results in terms of anti-tumour activity. In particular the results, showed that high doses of these drugs are not required to cause a significant growth delay. To avoid any potential off-target effects of systemic irinotecan it could also be delivered in a liposomal formulation. Irinotecan has been encapsulated in liposomes and attached to thMBs using the single step method described previously (Peyman *et al.*, 2012) (P.L.Coletta, personal communication). Irinotecan liposomes attached to thMBs with the same US destruction pulse used in this study, have shown excellent results when compared to free irinotecan in CRC xenografts (work conducted by Dr Nicola Ingram, University of Leeds). CA4 TPP LONDs and irinotecan liposomes could potentially be attached on the same thMB and delivered simultaneously to tumours. Preliminary work has been conducted by Professor Steve Evans group at the University of Leeds showing that LONDs and liposomes could be attached on the same MB (Personal communication).

8.1.7 LONDs as generic vehicles for hydrophobic drug delivery

CA4 encapsulated in LONDs was used as a proof-of-concept, however the results are encouraging in terms of progressing and using this compound in the clinic as an alternative approach to CA4P, particularly in combination studies to enhance and potentiate the efficacy of other chemotherapeutic agents. The LOND technology, is generic and could be used for the encapsulation of other hydrophobic agents for cancer treatment. For example, Rapamycin (or Sirolimus) a hydrophobic drug with a *LogP* of 4.3, could be encapsulated in LONDs, rapamycin is an antibiotic used traditionally as an immunosuppressant, however, also has potent anti-tumour activity by inhibiting the mammalian target of rapamycin (mTOR) (Li, Kim & Blenis, 2009). Rapamycin has been used previously in nanoemulsions (Sobhani *et al.*, 2015). CPT, the parent compound of irinotecan, could also be tested for encapsulation in LONDs, it has strong anti-tumour activity against a variety of cancer however its use is hampered due to its poor solubility in aqueous solutions and toxicity (Gao, Li & Zhai, 2008).

8.2 Conclusion

The work presented in this thesis shows that LONDs are promising novel NP vehicles for hydrophobic drug delivery. Their use alone or in combination with US triggered VEGFR2 targeted thMBs suggest that this technology has the potential to greatly enhance drug delivery of highly potent but poorly soluble anti-cancer drugs, while significantly reducing the need for high circulating concentrations for therapeutic effect and subsequently reducing systemic toxicity. Further optimisation and preclinical evaluation is required prior to clinical translation.

Appendix A

Supplementary information to Chapter 3

A

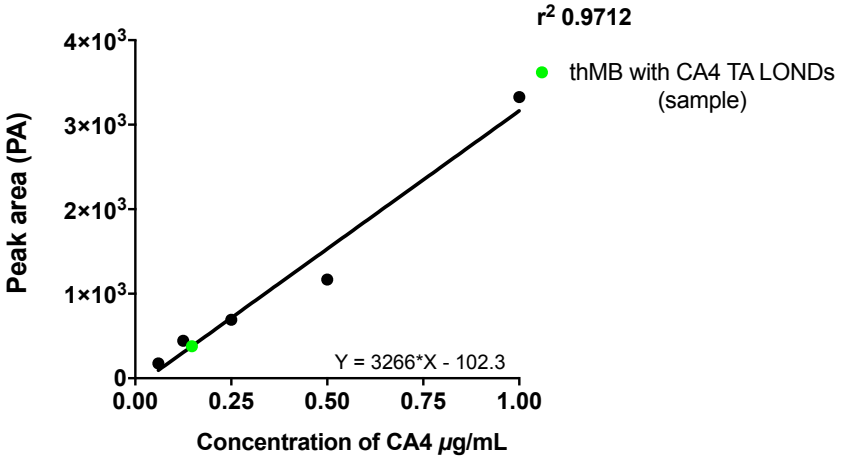

B

CA4 µg/mL	Peak Area (PA)
1	3328
0.5	1168
0.25	693
0.125	444
0.06	175
thMBs with CA4 TA LONDs (sample)	380

Figure A.1 Calibration curve of CA4 used to measure the concentration of CA4 in thMBs.

(A) Calibration curve of CA4. (B) Peak area (PA) data. The equation of the line was used to calculate the concentration of CA4 in the thMBs with CA4 TA LONDs. The concentration was 0.122 µg/mL x 4000 (dilution factor) = 488 µg/mL or 0.488 mg/mL.

Appendix B

Supplementary information to Chapter 4

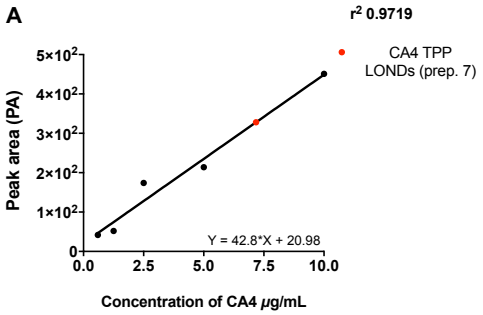

CA4 µg/mL STC	Peak Area (PA)
10	451
5	214
2.5	174
1.25	52
0.6	42
CA4 TPP LONDs (prep. 7)	328

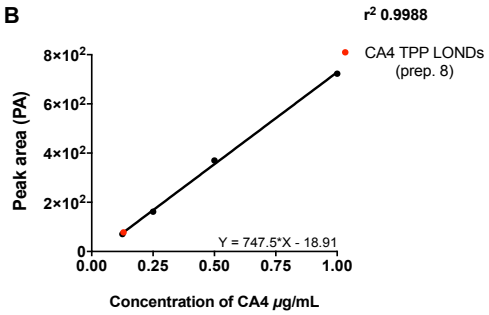

CA4 µg/mL STC	Peak Area (PA)
1	723
0.5	370
0.25	162
0.125	71
CA4 TPP LONDs (prep. 8)	78

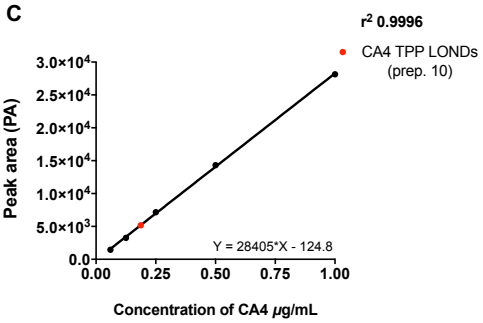

CA4 µg/mL STC	Peak Area (PA)
1	28136
0.5	14325
0.25	7172
0.125	3260
0.06	1446
CA4 TPP LONDs (prep. 10)	5180

Figure B.1 Calibration curves for CA4 used to measure the concentration of CA4 in TPP LONDs.

(A-C) Top images: Calibration of CA4 used to measure the concentration of CA4 in prep. numbers 7, 8 and 10 respectively. Bottom image: Tabulated peak area (PA) data. The equation of the line was used to calculate the concentration of CA4 in the different prep. samples. The concentration in prep. number 7. was 7.2 µg/mL x 100 (dilution factor) = 720 µg/mL. The concentration in prep. number 8 was 0.13 µg/mL x 10000 (dilution factor) = 1300 µg/mL. The concentration in prep. number 10 was 0.187 µg/mL x 5000 (dilution factor) = 935 µg/mL.

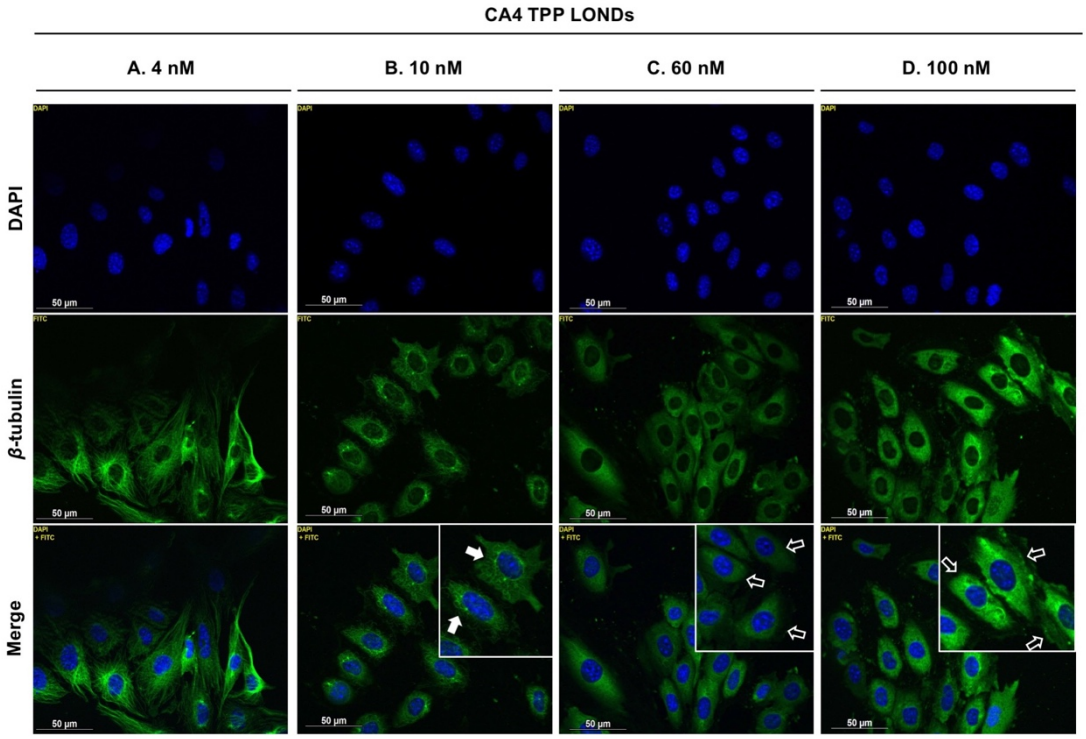

Figure B.2 CA4 TPP LONDs disruption in SVR cells.

SVR cells were treated with escalating concentrations of CA4 TPP LONDs, 4, 10, 60 and 100 nM for 2 h at 37°C. Following, cells were fixed and immunostained for *β*-tubulin using a mouse monoclonal anti-*β*-tubulin antibody. The slides were mounted with prolong Gold containing DAPI. (A) SVR cells treated with 4 nM of CA4 TPP LONDs, MTs appeared to have undisrupted MT filaments. (B) SVR cells treated with 10 nM of CA4 TPP LONDs showed evidence of shortening of the filamentous MTs at the distal ends at the cell periphery and tangled around the nuclei (white arrows). (C-D) 60 and 100 nM CA4 TPP LONDs had a uniformly stained cytoplasm from the dispersed tubulin caused by the depolymerisation of the MTs (open white arrows). Scale bars indicate 50 *µ*m. Prep. number 8 was used.

Appendix C

Supplementary information to Chapter 5

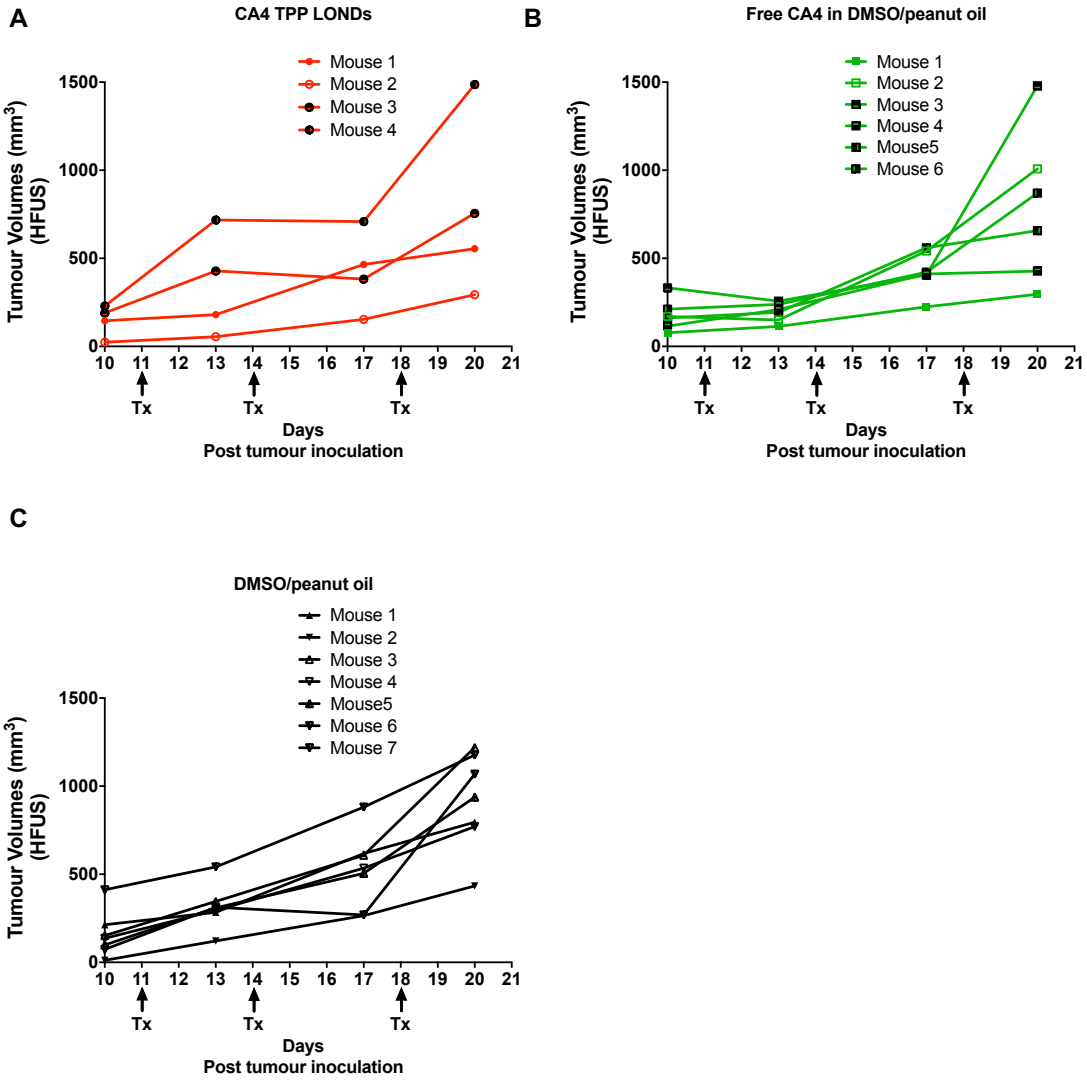

Figure C.1 Tumour volumes measured by HFUS per treatment group.

Individual tumour volumes measured by HFUS in mm^3 from BALB/c nude male mice treated with three treatments (Tx) of (A) CA4 TPP LONDs or (B) Free CA4 in DMSO/peanut oil or (C) DMSO/peanut oil control.

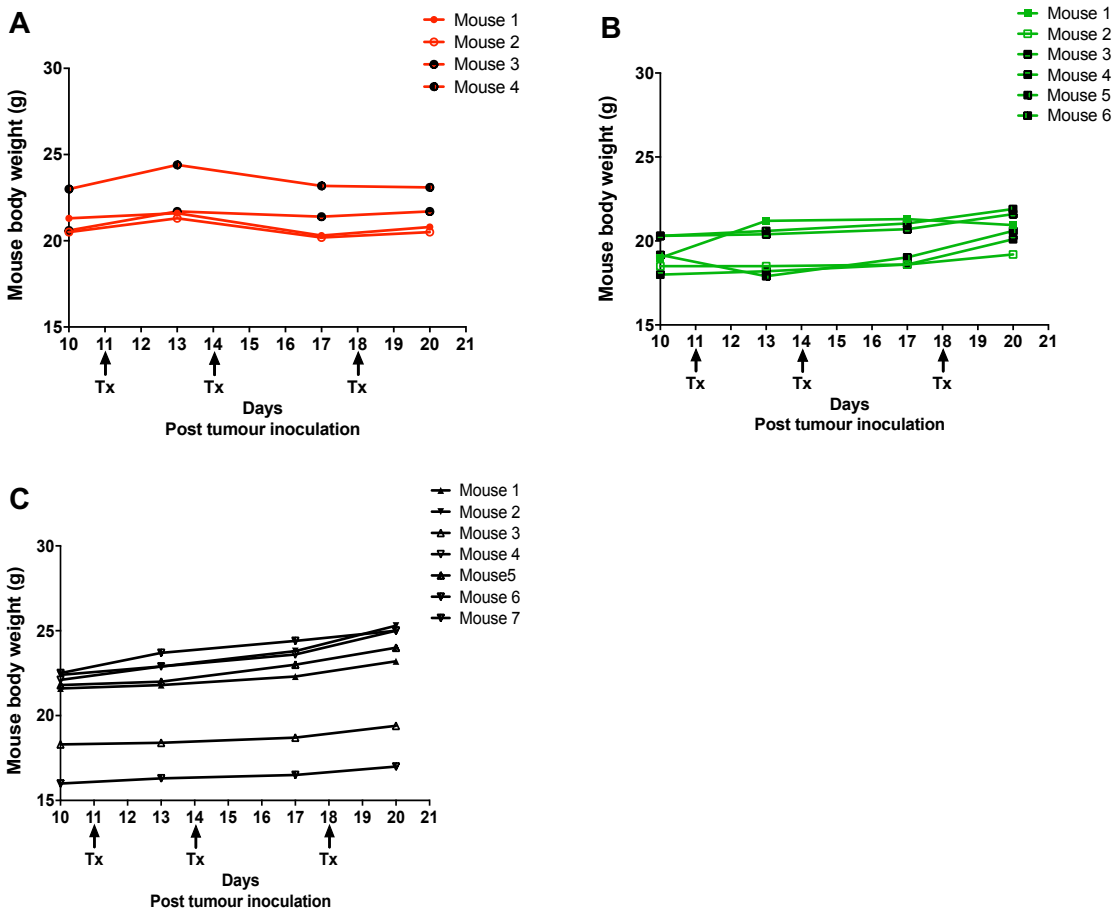

Figure C.2 Body weight during the treatment course of individual mice treated with CA4 TPP LONDs, free CA4 in DMSO/peanut oil and DMSO/peanut oil.

Mouse body weight in g of individual SW480 tumour bearing BALB/c nude male mice weighed one day before each treatment (Tx) on day 11, 14 and 18 of tumour growth. (A) Mice body weight (g) treated with 3 mg/kg CA4 TPP LONDs (n=4); (B) Mouse body weight (g) treated with 3 mg/kg free CA4 in DMSO (10%)/peanut oil (n=6); (C) Mouse body weight (g) treated with control DMSO/peanut oil (n=7).

Appendix D

Supplementary information to Chapter 6

A

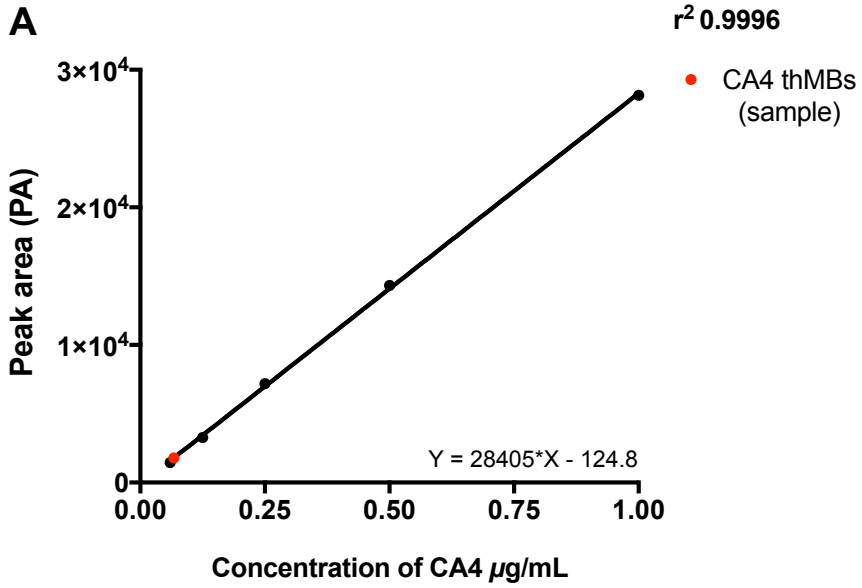

B

CA4 µg/mL STC	Peak Area (PA)
1	28136
0.5	14325
0.25	7172
0.125	3260
0.06	1446
CA4 thMBs (sample)	1785

Figure D.1 Calibration curve of CA4 used to measure the concentration of CA4 in thMBs by LC-MS/MS.

(A) Calibration curve of CA4. (B) Actual Peak area (PA) data. The equation of the line was used to calculate the concentration of CA4 in the thMB with CA4 TPP LONDs sample. The concentration was 0.063 µg/mL x 2 (dilution factor) = 0.126 µg/mL or 0.0001 mg/mL.

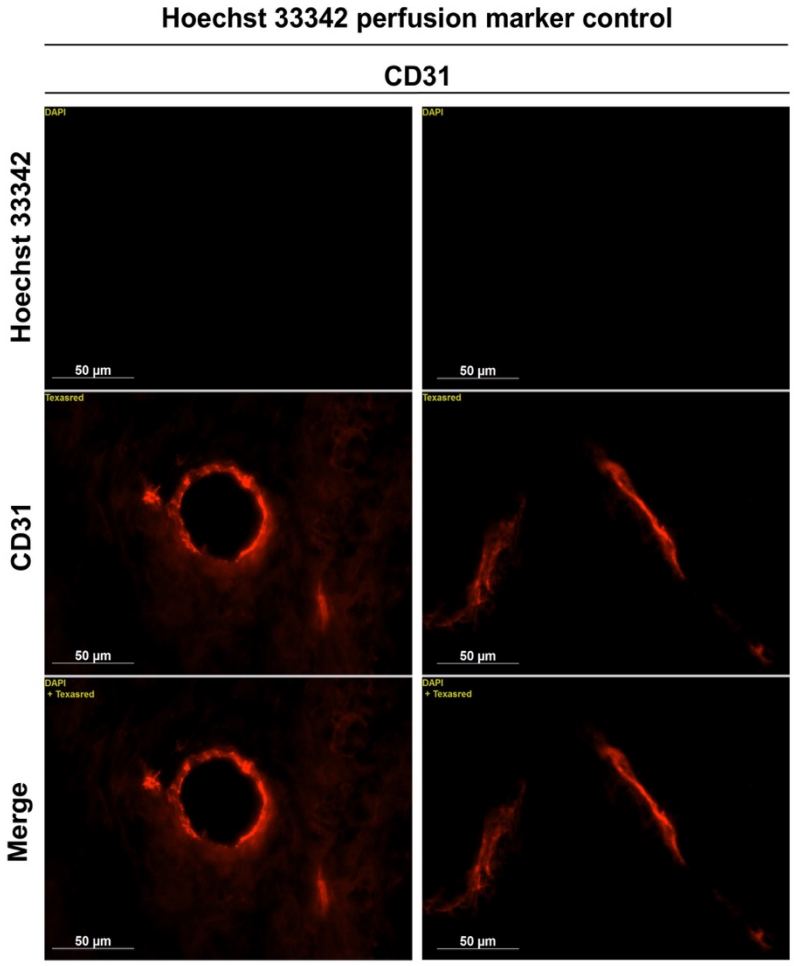

Figure D.2 Hoechst 33342 perfusion marker tumour control.

SW480 xenograft that was not stained *in situ* with the Hoechst 33342 perfusion marker. A 10 *µ*m frozen tumour section was fixed and immuno-labelled with a rat monoclonal antibody against CD31 and visualised using a goat anti-rat secondary antibody Alexa Fluor 568. Scale bars indicate 50 *µ*m.

Appendix E

Supplementary information to Chapter 7

A

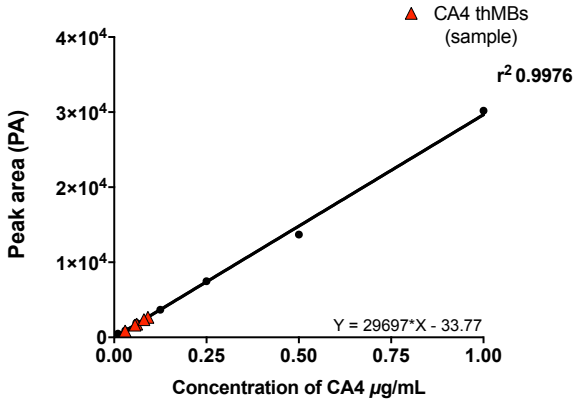

B

CA4 µg/mL	Peak Area (PA)
1	30190
0.5	13686
0.25	7471
0.125	3689
0.06	1954
0.03	921
0.01	505
thMBs with CA4 TPP LONDs (sample 1)	2679
ThMBs with CA4 TPP LONDs (sample 2)	1776
ThMBs with CA4 TPP LONDs (sample 3)	1642
ThMBs with CA4 TPP LONDs (sample 4)	2356
ThMBs with CA4 TPP LONDs (sample 5)	855

Figure E.1 Measurement of CA4 loading in thMBs using LC-MS/MS.
(A) CA4 thMBs were analysed by LC-MS/MS to determine the concentration of CA4 loading in the five different preparations. The equation of the line was used to calculate the concentration of CA4 thMBs. (B) Tabulated format of data presented in A.

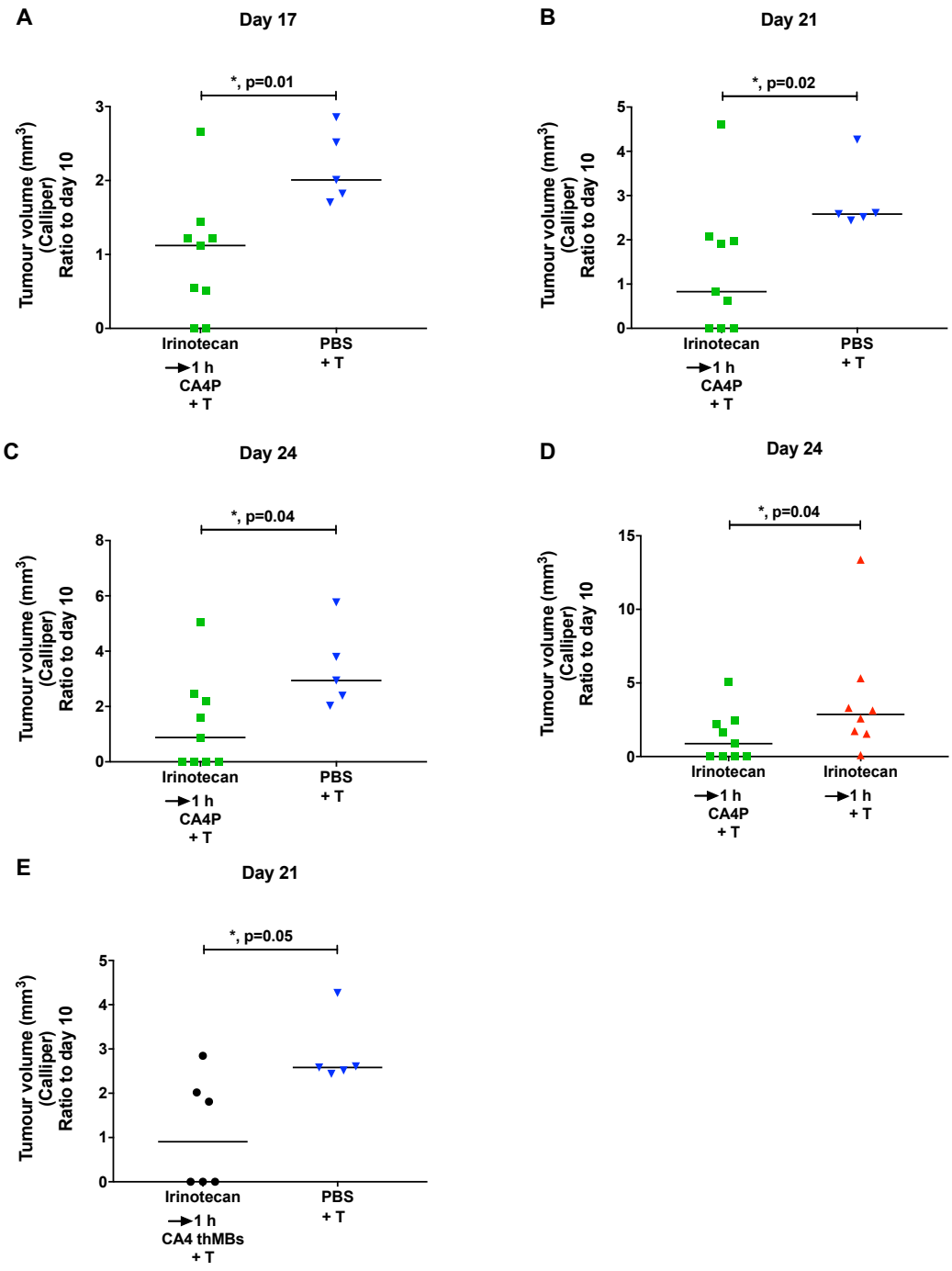

Figure E.2 Pairwise comparisons of tumour growth response following combination treatment of irinotecan and CA4.

(A-F) Straight lines (–) represent the median value. Statistical analysis was performed using a Mann-Whitney U-test, two-tailed.

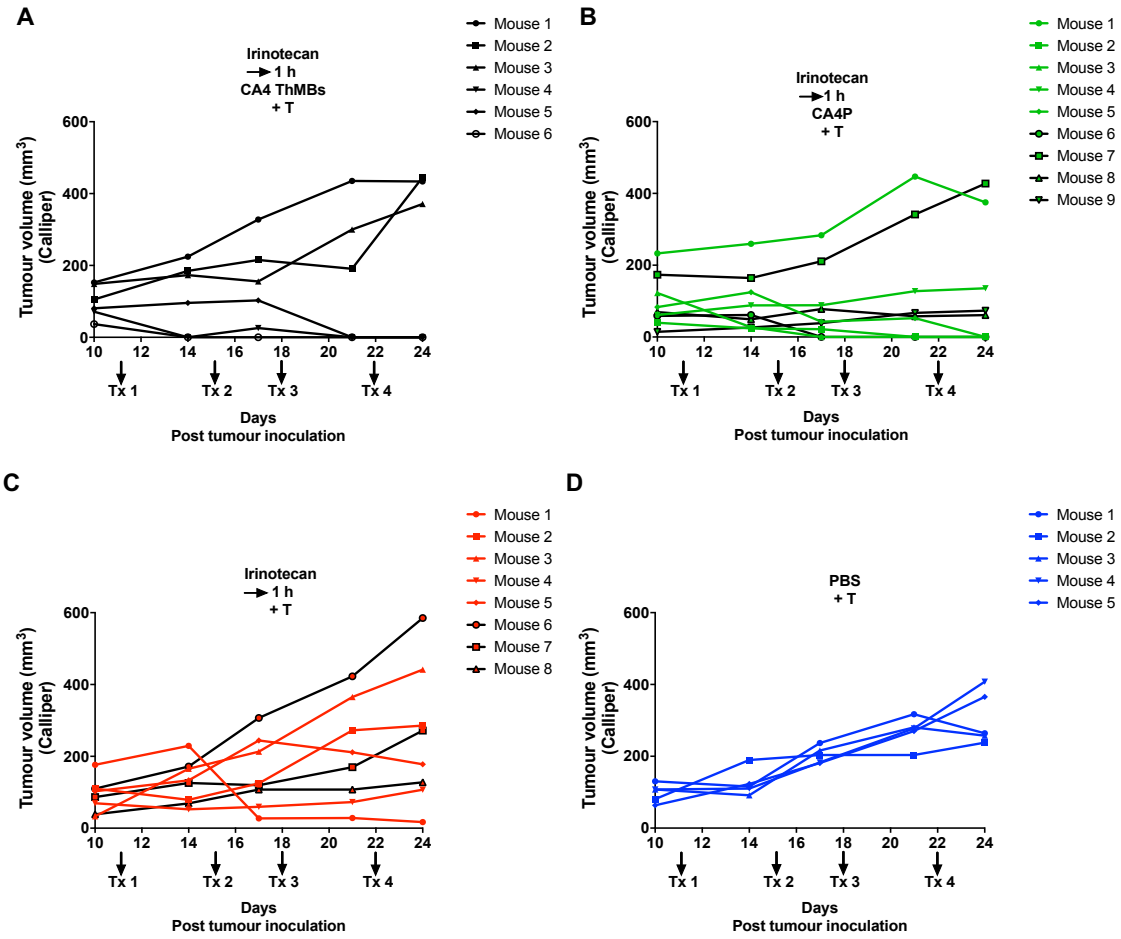

Figure E.3 Tumour volumes of individual mice per treatment group.

(A-D) Tumour size of individual SW480 tumour bearing mice measured by mechanical callipers treated with either (A) 10 mg/kg irinotecan i.p. followed 1 h later by CA4 thMBs plus US trigger (+T), or (B) CA4P +T at 0.001 mg/kg i.v., or (C) irinotecan + T alone i.p. or (D) PBS + T i.v. as control.

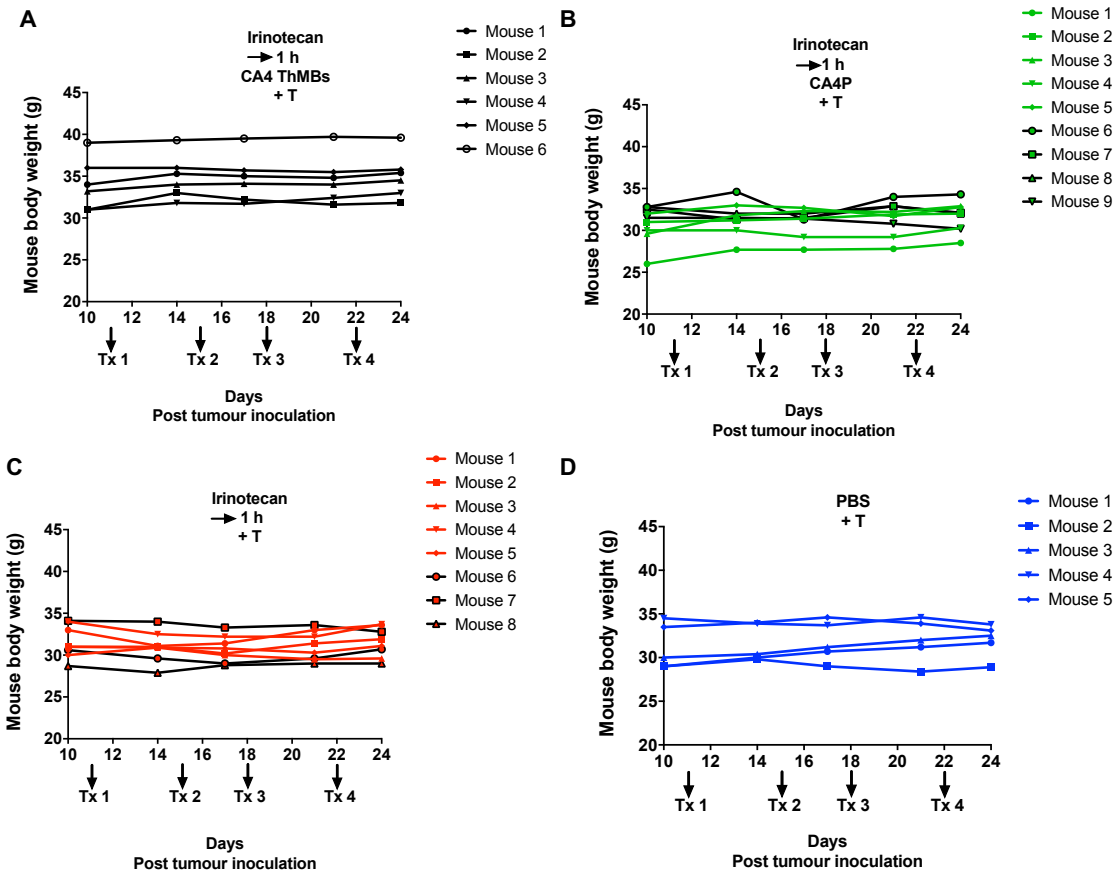

Figure E.4 Mouse body weights over time per treatment group.

(A-D) Mouse body weight in g of individual SW480 tumour bearing mice weighed one day before each of the four treatments (Tx) with (A) irinotecan i.p. followed 1 h later by CA4 thMBs plus US trigger (+T), or (B) CA4P +T at 0.001 mg/kg i.v., or (C) irinotecan + T alone i.p. or (D) PBS + T i.v.

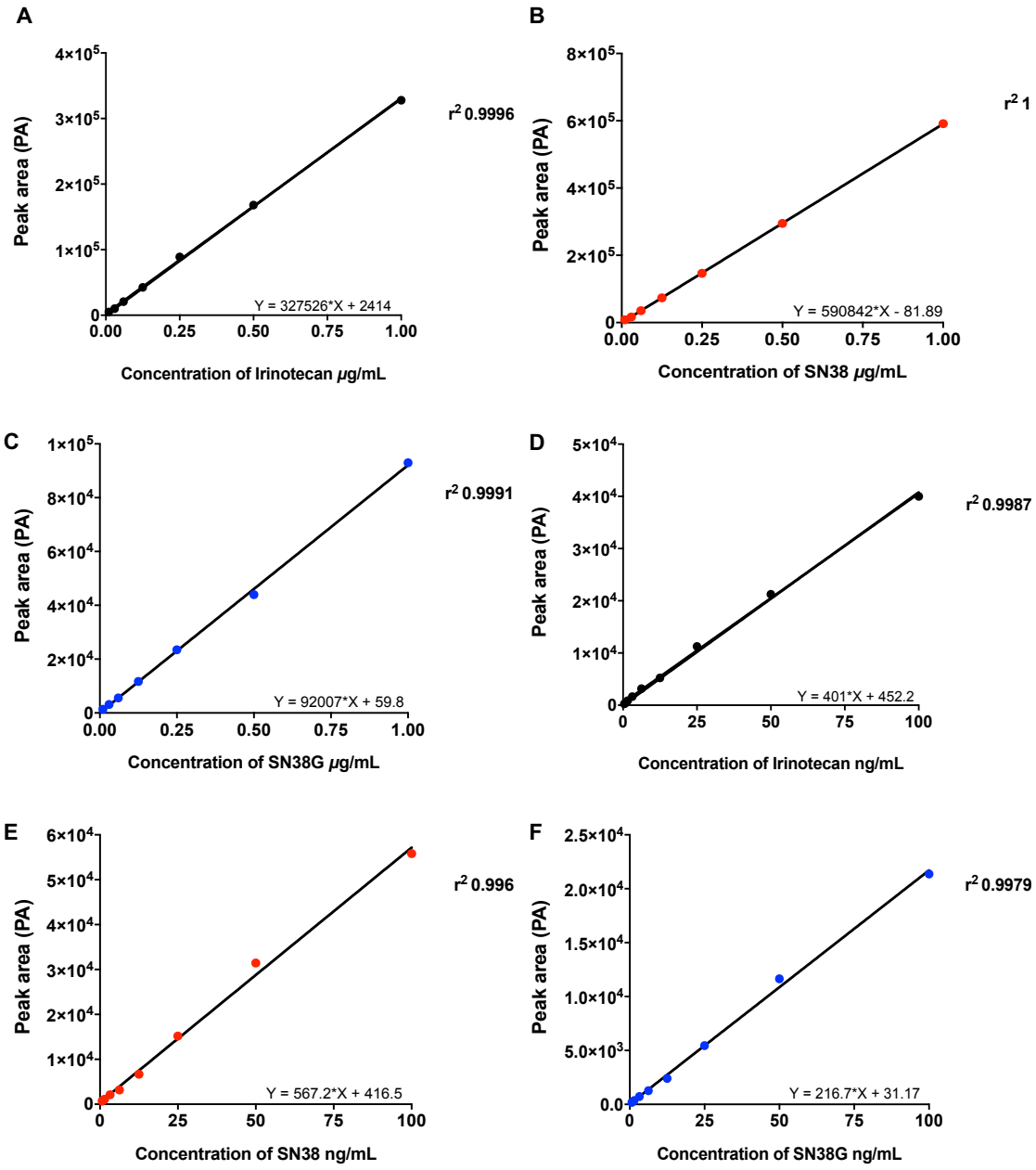

Figure E.5 Calibration curves for irinotecan, SN38 and SN38G.

(A-F) The equation of the line of individual calibration curves of irinotecan, SN38 and SN38G were used to calculate the concentration of the compounds in the different tissue samples.

References

Abdelrahman, M.A., Marston, G., Hull, M.A., Markham, A.F., Jones, P.F., Evans, J.A. and Coletta, P.L. 2012. High-Frequency Ultrasound for In Vivo Measurement of Colon Wall Thickness in Mice. *Ultrasound in Medicine and Biology*. **38**(3),pp.432–442.

Abou-Saleh, R.H., Peyman, S.A., Johnson, B.R.G., Marston, G., Ingram, N., Bushby, R., Coletta, P.L., Markham, A.F. and Evans, S.D. 2016. The influence of intercalating perfluorohexane into lipid shells on nano and microbubble stability. *Soft Matter*. **12**,pp.7223–7230.

Ahmed, B., Van Eijk, L.I., Bouma-ter Steege, J.C.A., Van Der Schaft, D.W.J., Van Esch, A.M., Joosten-Achjanie, S.R., Lambin, P., Landuyt, W. and Griffioen, A.W. 2003. Vascular targeting effect of combretastatin A-4 phosphate dominates the inherent angiogenesis inhibitory activity. *International Journal of Cancer*. **105**,pp.20–25.

Ahn, B.J., Choi, M.K., Park, Y.S., Lee, J., Park, S.H., Park, J.O., Lim, H.Y., Kang, W.K., Ko, J.W. and Yim, D.S. 2010. Population pharmacokinetics of CPT-11 (irinotecan) in gastric cancer patients with peritoneal seeding after its intraperitoneal administration. *European Journal of Clinical Pharmacology*. **66**,pp.1235–1245.

Akhmanova, A. and Steinmetz, M.O. 2008. Tracking the ends: A dynamic protein network controls the fate of microtubule tips. *Nature Reviews Molecular Cell Biology*. **9**,pp.309–322.

Anderson, H.L., Yap, J.T., Miller, M.P., Robbins, A., Jones, T. and Price, P.M. 2003. Assessment of pharmacodynamic vascular response in a phase I trial of combretastatin A4 phosphate. *Journal of Clinical Oncology*. **21**(15),pp.2823–2830.

Aoki, K. and Taketo, M.M. 2007. Adenomatous polyposis coli (APC): a multi-functional tumor suppressor gene. *Journal of Cell Science*. **120**,pp.3327–3335.

Aprile, S., Del Grosso, E. and Grosa, G. 2010. Identification of the human UDP-glucuronosyltransferases involved in the glucuronidation of combretastatin A-4. *Drug Metabolism and Disposition*. **38**(7),pp.1141–1146.

Aprile, S., Del Grosso, E. and Grosa, G. 2009. In vitro and in vivo phase II metabolism of combretastatin A-4: Evidence for the formation of a sulphate conjugate metabolite. *Xenobiotica*. **39**(2),pp.148–161.

Aprile, S., Del Grosso, E., Tron, G.C. and Grosa, G. 2007. In Vitro Metabolism Study of Combretastatin A-4 in Rat and Human Liver Microsomes. *Drug Metabolism and Disposition*. **35**(12),pp.2252–2261.

Aranda, E. and Owen, G.I. 2009. A semi-quantitative assay to screen for angiogenic compounds and compounds with angiogenic potential using the EA.hy926 endothelial cell line. *Biological Research*. **42**,pp.377–389.

Atsumi, R., Okazaki, O. and Hakusui, H. 1995. Metabolism of irinotecan to SN-38 in a tissue-isolated tumor model. *Biological & pharmaceutical bulletin*. **18**(7),pp.1024–1026.

Avanti Polar Lipids Inc. 2016. Phase Transition Temperatures for

Glycerophospholipids. [Accessed 17 May 2018]. Available from: https://avantilipids.com/tech-support/physical-properties/phase-transition-temps/.

Baluk, P., Hashizume, H. and McDonald, D.M. 2005. Cellular abnormalities of blood vessels as targets in cancer. *Current Opinion in Genetics and Development*. **15**,pp.102–111.

Banerjee, T., Mitra, S., Kumar Singh, A., Kumar Sharma, R. and Maitra, A. 2002. Preparation, characterization and biodistribution of ultrafine chitosan nanoparticles. *International Journal of Pharmaceutics*. **243**,pp.93–105.

Beauregard, D.A., Hill, S.A., Chaplin, D.J. and Brindle, K.M. 2001. The susceptibility of tumors to the antivascular drug combretastatin A4 phosphate correlates with vascular permeability. *Cancer Research*. **61**(18),pp.6811–6815.

Beauregard, D.A., Pedley, R.B., Hill, S.A. and Brindle, K.M. 2002. Differential sensitivity of two adenocarcinoma xenografts to the anti-vascular drugs combretastatin A4 phosphate and 5,6-dimethylxanthenone-4-acetic acid, assessed using MRI and MRS. *NMR in Biomedicine*. **15**,pp.99–105.

Beauregard, D.A., Thelwall, P.E., Chaplin, D.J., Hill, S.A., Adams, G.E. and Brindle, K.M. 1998. Magnetic resonance imaging and spectroscopy of combretastatin A4 prodrug-induced disruption of tumour perfusion and energetic status. *British journal of cancer*. **77**(11),pp.1761–1767.

Berg, K.C.G., Eide, P.W., Eilertsen, I.A., Johannessen, B., Bruun, J., Danielsen, S.A., Bjørnslett, M., Meza-Zepeda, L.A., Eknæs, M., Lind, G.E., Myklebost, O., Skotheim, R.I., Sveen, A. and Lothe, R.A. 2017. Multi-omics of 34 colorectal cancer cell lines - a resource for biomedical studies. *Molecular Cancer*. **16**(116),pp.1–16.

Bertrand, N., Wu, J., Xu, X., Kamaly, N. and Farokhzad, O.C. 2014. Cancer nanotechnology: The impact of passive and active targeting in the era of modern cancer biology. *Advanced Drug Delivery Reviews*. **66**,pp.2–25.

Bhal, S.K. n.d. LogP — Making Sense of the Value. *Advanced Chemistry Development Inc.* [Online]. [Accessed 14 April 2018]. Available from: http://www.acdlabs.com/download/app/physchem/making_sense.pdf.

Bilenker, J.H., Flaherty, K.T., Rosen, M., Davis, L., Gallagher, M., Stevenson, J.P., Sun, W., Vaughn, D., Giantonio, B., Zimmer, R., Schnall, M. and O'Dwyer, P.J. 2005. Phase I trial of combretastatin A-4 phosphate with carboplatin. *Clinical Cancer Research*. **11**(4),pp.1527–1533.

Biswas, S. and Torchilin, V.P. 2014. Nanopreparations for organelle-specific delivery in cancer. *Advanced Drug Delivery Reviews*. **66**,pp.26–41.

Blanco, E., Shen, H. and Ferrari, M. 2015. Priniciples of nanoparticle design for overcoming biological barriers to drug delivery. *Nature biotechnology*. **33**(9),pp.941–951.

Boehle, A.S., Sipos, B., Kliche, U., Kalthoff, H. and Dohrmann, P. 2001. Combretastatin A-4 prodrug inhibits growth of human non-small cell lung cancer in a murine xenotransplant model. *The Annals of thoracic surgery*. **71**,pp.1657–1665.

Boissenot, T., Bordat, A., Fattal, E. and Tsapis, N. 2016. Ultrasound-triggered drug delivery for cancer treatment using drug delivery systems: From theoretical considerations to practical applications. *Journal of Controlled Release*. **241**,pp.144–163.

Bozzuto, G. and Molinari, A. 2015. Liposomes as nanomedical devices. *International Journal of Nanomedicine*. **10**,pp.975–999.

Brouhard, G.J. and Rice, L.M. 2014. The contribution of αβ-tubulin curvature to microtubule dynamics. *Journal of Cell Biology*. **207**(3),pp.323–334.

Cabral, H., Matsumoto, Y., Mizuno, K., Chen, Q., Murakami, M., Kimura, M., Terada, Y., Kano, M.R., Miyazono, K., Uesaka, M., Nishiyama, N. and Kataoka, K. 2011. Accumulation of sub-100 nm polymeric micelles in poorly permeable tumours depends on size. *Nature Nanotechnology*. **6**,pp.815–823.

Cancer Research UK 2015. Bowel Cancer. *Cancer Research UK*. [Online]. [Accessed 15 May 2018]. Available from: http://www.cancerresearchuk.org/sites/default/files/cstream-node/surv_5yr_stage_mw_bowel_1.pdf.

Capek, I. 2004. Degradation of kinetically-stable o/w emulsions. *Advances in Colloid and Interface Science*. **107**,pp.125–155.

Cenciarelli, C., Tanzarella, C., Vitale, I., Pisano, C., Crateri, P., Meschini, S., Arancia, G. and Antoccia, A. 2008. The tubulin-depolymerising agent combretastatin-4 induces ectopic aster assembly and mitotic catastrophe in lung cancer cells H460. *Apoptosis*. **13**,pp.659–669.

Chadwick, M. and Rogers, W.I. 1972. The Physiological Disposition Of 5-Fluorouracil In Mice Bearing Solid L1210 Lymphocytic Leukemia. *Cancer Research*. **32**,pp.1045–1056.

Chan, Andrew, T., Ogino, S. and Fuchs, C.S. 2007. Aspirin and the risk of colorectal cancer in rela- tion to the expression of COX-2. *The New England Journal of Medicine*. **356**(21),pp.2131–2142.

Chaplin, D.J. and Hill, S.A. 2002. The development of combretastatin A4 phosphate as a vascular targeting agent. *International Journal of Radiation Oncology Biology Physics*. **54**(5),pp.1491–1496.

Chaplin, D.J., Pettit, G.R. and Hill, S.A. 1996. Anti-vascular approaches to solid tumour therapy: Evaluation of combretastatin A4 phosphate. *British journal of cancer*. **74**,pp.S86–S88.

Chase, D.M., Chaplin, D.J. and Monk, B.J. 2017. The development and use of vascular targeted therapy in ovarian cancer. *Gynecologic Oncology*. **145**(2),pp.393–406.

Chauhan, V.P., Popović, Z., Chen, O., Cui, J., Fukumura, D., Bawendi, M.G. and Jain, R.K. 2011. Fluorescent nanorods and nanospheres for real-time in vivo probing of nanoparticle shape-dependent tumor penetration. *Angewandte Chemie - International Edition*. **50**,pp.11417–11420.

Che-Ming, J.H., Zhang, L., Aryal, S., Cheung, C., Fang, Ronnie, H. and Zhang, L. 2011. Erthythrocyte membrane-camouflaged polymeric nanoparticles as a

biomimetic delivery platform. *Proceedings of the National Academy of Sciences*. **108**(27),pp.10980–10985.

Choi, H.S., Liu, W., Misra, P., Tanaka, E., Zimmer, J.P., Itty Ipe, B., Bawendi, M.G. and Frangioni, J. V. 2007. Renal clearance of quantum dots. *Nature Biotechnology*. **25**(10),pp.1165–1170.

Choijamts, B., Naganuma, Y., Nakajima, K., Kawarabayashi, T., Miyamoto, S., Tachibana, K. and Emoto, M. 2011. Metronomic irinotecan chemotherapy combined with ultrasound irradiation for a human uterine sarcoma xenograft. *Cancer Science*. **102**(2),pp.452–459.

Chowdhury, S.M., Lee, T. and Willmann, J.K. 2017. Ultrasound-guided drug delivery in cancer. *Ultrasonography*. **36**(3),pp.171–184.

De Cock, I., Lajoinie, G., Versluis, M., De Smedt, S.C. and Lentacker, I. 2016. Sonoprinting and the importance of microbubble loading for the ultrasound mediated cellular delivery of nanoparticles. *Biomaterials*. **83**,pp.294–307.

De Cock, I., Zagato, E., Braeckmans, K., Luan, Y., de Jong, N., De Smedt, S.C. and Lentacker, I. 2015. Ultrasound and microbubble mediated drug delivery: acoustic pressure as determinant for uptake via membrane pores or endocytosis. *Journal of Controlled Release*. **197**,pp.20–28.

Cohen, M.H., Gootenberg, J., Keegan, P. and Pazdur, R. 2007. FDA Drug Approval Summary: Bevacizumab Plus FOLFOX4 as Second-Line Treatment of Colorectal Cancer. *The Oncologist*. **12**,pp.356–361.

Cole, L.M., Djidja, M.C., Bluff, J., Claude, E., Carolan, V.A., Paley, M., Tozer, G.M. and Clench, M.R. 2011. Investigation of protein induction in tumour vascular targeted strategies by MALDI MSI. *Methods*. **54**(4),pp.442–453.

Cooney, M.M., Radivoyevitch, T., Dowlati, A., Overmoyer, B., Levitan, N., Robertson, K., Levine, S.L., DeCaro, K., Buchter, C., Taylor, A., Stambler, B.S. and Remick, S.C. 2004. Cardiovascular Safety Srofile of Combretastatin A4 phosphate in a Single-Sose Shase I Study in Patients with Advanced Cancer. *Clinical Cancer Research*. **10**,pp.96–100.

Cutsem, E. Van, Nordlinger, B. and Cervantes, A. 2010. Advanced colorectal cancer: ESMO clinical practice guidelines for treatment. *Annals of Oncology*. **21**,pp.v93–v97.

Dai, W., Jin, W., Zhang, J., Wang, X., Wang, J., Zhang, X., Wan, Y. and Zhang, Q. 2012. Spatiotemporally controlled co-Delivery of anti-Vasculature agent and cytotoxic drug by octreotide-Modified stealth liposomes. *Pharmaceutical Research*. **29**,pp.2902–2911.

Danhier, F., Lecouturier, N., Vroman, B., Jérôme, C., Marchand-Brynaert, J., Feron, O. and Préat, V. 2009. Paclitaxel-loaded PEGylated PLGA-based nanoparticles: In vitro and in vivo evaluation. *Journal of Controlled Release*. **133**,pp.11–17.

Dark, G.G., Hill, S.A., Prise, V.E., Tozer, G.M., Pettit, G.R. and Chaplin, D.J. 1997. Combretastatin A-4, an agent that displays selective toxicity towards tumour vasculature. *Cancer Research*. **57**,pp.1829–1834.

Desgrosellier, J.S. and Cheresh, D.A. 2010. Integrins in cancer: Biological

implications and therapeutic opportunities. *Nature Reviews Cancer*. **10**,pp.9–22.

Dhankar, R., Rathee, P., Jain, A.K., Arora, S., Kumar, M.S., Rath, G., Saxena, A.K., Sharma, P.R., Chashoo, G. and Goyal, A.K. 2011. HER-2 targeted immunonanoparticles for breast cancer chemotherapy. *Journal of Applied Pharmaceutical Science*. **1**(3),pp.132–139.

Dienstmann, R., Vermeulen, L., Guinney, J., Kopetz, S., Tejpar, S. and Tabernero, J. 2017. Consensus molecular subtypes and the evolution of precision medicine in colorectal cancer. *Nature Reviews Cancer*. **17**,pp.79–92.

Dimcevski, G., Kotopoulis, S., Bjånes, T., Hoem, D., Schjøt, J., Gjertsen, B.T., Biermann, M., Molven, A., Sorbye, H., McCormack, E., Postema, M. and Gilja, O.H. 2016. A human clinical trial using ultrasound and microbubbles to enhance gemcitabine treatment of inoperable pancreatic cancer. *Journal of Controlled Release*. **243**,pp.172–181.

Dorr, R.T., Dvorakova, K., Snead, K., Alberts, D.S., Salmon, S.E. and Pettit, G.R. 1996. Antitumor activity of combretastatin-A4 phosphate, a natural product tubulin inhibitor. *Investigational new drugs*. **14**,pp.131–137.

Dowlati, A., Robertson, K., Cooney, M., Petros, W.P., Stratford, M., Jesberger, J., Rafie, N., Overmoyer, B., Makkar, V., Stambler, B., Taylor, A., Waas, J., Lewin, J.S., McCrae, K.R. and Remick, S.C. 2002. A phase I pharmacokinetic and translational study of the novel vascular targeting agent combretastatin A-4 phosphate on a single-dose intravenous schedule in patients with advanced cancer. *Cancer Research*. **62**,pp.3408–3416.

Du, Z., Munye, M.M., Tagalakis, A.D., Manunta, M.D.I. and Hart, S.L. 2014. The Role of the helper lipid on the DNA transfection efficiency of lipopolyplex formulations. *Scientific Reports*. **4**(7107),pp.1–6.

Duan, Y.T., Man, R.J., Tang, D.J., Yao, Y.F., Tao, X.X., Yu, C., Liang, X.Y., Makawana, J.A., Zou, M.J., Wang, Z.C. and Zhu, H.L. 2016. Design, Synthesis and Antitumor Activity of Novel link-bridge and B-Ring Modified Combretastatin A-4 (CA-4) Analogues as Potent Antitubulin Agents. *Scientific Reports*. **6**(25387),pp.1–13.

Duck, F.A. 2007. Medical and non-medical protection standards for ultrasound and infrasound. *Progress in Biophysics and Molecular Biology*. **93**(1–3),pp.176–191.

Durymanov, M.O., Rosenkranz, A.A. and Sobolev, A.S. 2015. Current approaches for improving intratumoral accumulation and distribution of nanomedicines. *Theranostics*. **5**(9),pp.1007–1020.

Eberhart, Charles, E., Coffey, R.J., Radhika, A., Giardiello, Francis, M., Ferrenbach, S. and Dubois, R.N. 1994. Up-regulation of Cyclooxygenase 2 Gene Expression in Human Colorectal Adenomas and Adenocarcinomas. *Gastroenterology*. **107**,pp.1183–1188.

Eggen, S., Fagerland, S.M., Mørch, Ý., Hansen, R., Søvik, K., Berg, S., Furu, H., Bøhn, A.D., Lilledahl, M.B., Angelsen, A., Angelsen, B. and De Lange Davies, C. 2014. Ultrasound-enhanced drug delivery in prostate cancer xenografts by nanoparticles stabilizing microbubbles. *Journal of Controlled Release*. **187**,pp.39–49.

Eisenhauer, E.A., Therasse, P., Bogaerts, J., Schwartz, L.H., Sargent, D., Ford, R., Dancey, J., Arbuck, S., Gwyther, S., Mooney, M., Rubinstein, L., Shankar, L., Dodd, L., Kaplan, R., Lacombe, D. and Verweij, J. 2009. New response evaluation criteria in solid tumours: Revised RECIST guideline (version 1.1). *European Journal of Cancer*. **45**,pp.228–247.

El-Emir, E., Boxer, G.M., Petrie, I.A., Boden, R.W., Dearling, J.L.J., Begent, R.H.J. and Pedley, R.B. 2005. Tumour parameters affected by combretastatin A-4 phosphate therapy in a human colorectal xenograft model in nude mice. *European Journal of Cancer*. **41**,pp.799–806.

Elmore, S. 2007. Apoptosis: A Review of Programmed Cell Death. *Toxicologic Pathology*. **35**(4),pp.495–516.

Eloy, J.O., Petrilli, R., Chesca, D.L., Saggioro, F.P., Lee, R.J. and Marchetti, J.M. 2017. Anti-HER2 immunoliposomes for co-delivery of paclitaxel and rapamycin for breast cancer therapy. *European Journal of Pharmaceutics and Biopharmaceutics*. **115**,pp.159–167.

European Medicines Agency 2005. Avastin bevacizumab. *European Medicines Agency*. [Online]. [Accessed 10 April 2018]. Available from: http://www.ema.europa.eu/ema/index.jsp?curl=pages/medicines/human/medicines/000582/human_med_000663.jsp&mid=WC0b01ac058001d124.

Evans, J.P., Sutton, P.A., Winiarski, B.K., Fenwick, S.W., Malik, H.Z., Vimalachandran, D., Tweedle, E.M., Costello, E., Palmer, D.H., Park, B.K. and Kitteringham, N.R. 2016. From mice to men: Murine models of colorectal cancer for use in translational research. *Critical Reviews in Oncology/Hematology*. **98**,pp.94–105.

Fan, C.H. and Yeh, C.K. 2014. Microbubble-enhanced focused ultrasound-induced blood-brain barrier opening for local and transient drug delivery in central nervous system disease. *Journal of Medical Ultrasound*. **22**(4),pp.183–193.

Farook, U., Zhang, H.B., Edirisinghe, M.J., Stride, E. and Saffari, N. 2007. Preparation of microbubble suspensions by co-axial electrohydrodynamic atomization. *Medical Engineering and Physics*. **29**,pp.749–754.

FDA 2004. AVASTIN REFERENCE GUIDE. *FDA*. [Online]. [Accessed 2 March 2018]. Available from: https://www.accessdata.fda.gov/drugsatfda_docs/label/2014/125085s301lbl.pdf.

Fearon, E.F. and Vogelstein, B. 1990. A Genetic Model for Colorectal Tumorigenesis. *Cell*. **61**,pp.759–767.

Fearon, E.R. 2011. Molecular Genetics of Colorectal Cancer. *Annual Review of Pathology: Mechanisms of Disease*. **6**,pp.479–507.

Fioravanti, A., Canu, B., Alì, G., Orlandi, P., Allegrini, G., Di Desidero, T., Emmenegger, U., Fontanini, G., Danesi, R., Del Tacca, M., Falcone, A. and Bocci, G. 2009. Metronomic 5-fluorouracil, oxaliplatin and irinotecan in colorectal cancer. *European Journal of Pharmacology*. **619**,pp.8–14.

Fiume, M.Z. 2003. Final Report on the Safety Assessment of Triacetin 1. *International Journal of Toxicology*. **22**,pp.1–10.

Folkman, J. 1971. Tumour Angiogenesis: Therapeutic implications. *The New England Journal of Medicine*. **285**(21),pp.1182–1186.

Folkman, J. 1990. What is the evidence that tumors are angiogenesis-dependent? *Journal National Cancer Institute*. **82**(23),pp.4–6.

Friedman, A., Claypool, S. and Liu, R. 2013. The Smart Targeting of Nanoparticles. *Current Pharmaceutical Design*. **19**(35),pp.6315–6329.

Fruytier, A.-C., Le Duff, C.S., Po, C., Magat, J., Bouzin, C., Neveu, M.-A., Feron, O., Jordan, B.F. and Gallez, B. 2016. The Blood Flow Shutdown Induced by Combretastatin A4 Impairs Gemcitabine Delivery in a Mouse Hepatocarcinoma. *Frontiers in pharmacology*. **7**(506),pp.1–8.

Fuchs, C.S., Marshall, J., Mitchell, E., Wierzbicki, R., Ganju, V., Jeffery, M., Schulz, J., Richards, D., Soufi-Mahjoubi, R., Wang, B. and Barrueco, J. 2007. Randomized, controlled trial of irinotecan plus infusional, bolus, or oral fluoropyrimidines in first-line treatment of metastatic colorectal cancer: Results from the BICC-C study. *Journal of Clinical Oncology*. **25**(30),pp.4779–4786.

Galbraith, S.M., Chaplin, D.J., Lee, F., Stratford, M.R.L., Locke, R.J., Vojnovic, B. and Tozer, G.M. 2001. Effects of combretastatin A4 phosphate on endothelial cell morphology in vitro and relationship to tumour vascular targeting activity in vivo. *Anticancer Research*. **21**(1A),pp.93–102.

Galbraith, S.M., Maxwell, R.J., Lodge, M.A., Tozer, G.M., Wilson, J., Taylor, N.J., Stirling, J.J., Sena, L., Padhani, A.R. and Rustin, G.J.S. 2003. Combretastatin A4 phosphate has tumor antivascular activity in rat and man as demonstrated by dynamic magnetic resonance imaging. *Journal of Clinical Oncology*. **21**(15),pp.2831–2842.

Ganta, S., Talekar, M., Singh, A., Coleman, T.P. and Amiji, M.M. 2014. Nanoemulsions in Translational Research—Opportunities and Challenges in Targeted Cancer Therapy. *AAPS PharmSciTech*. **15**(3),pp.694–708.

Gao, M., Yao, N., Huang, D., Jiang, C., Feng, Y., Li, Y., Lou, B., Peng, F., Sun, Z., Ni, Y. and Zhang, J. 2015. Trapping effect on a small molecular drug with vascular-disrupting agent CA4P in rodent H22 hepatic tumor model: In vivo magnetic resonance imaging and postmortem inductively coupled plasma atomic emission spectroscopy. *Journal of Drug Targeting*. **23**(5),pp.436–443.

Gao, M., Zhang, D., Jin, Q., Jiang, C., Wang, C., Li, J., Peng, F., Huang, D., Zhang, J. and Song, S. 2016. Combretastatin-A4 phosphate improves the distribution and antitumor efficacy of albumin-bound paclitaxel in W256 breast carcinoma model. *Oncotarget*. **7**(36),pp.58133–58141.

Gao, Y., Li, L.B. and Zhai, G. 2008. Preparation and characterization of Pluronic/TPGS mixed micelles for solubilization of camptothecin. *Colloids and Surfaces B: Biointerfaces*. **64**(2),pp.194–199.

Garon, E.B., Neidhart, J.D., Gabrail, N.Y., de Oliveira, M.R., Balkissoon, J. and Kabbinavar, F. 2016. A randomized Phase II trial of the tumor vascular disrupting agent CA4P (fosbretabulin tromethamine) with carboplatin, paclitaxel, and bevacizumab in advanced nonsquamous non-small-cell lung cancer. *OncoTargets and Therapy*. **9**,pp.7275–7283.

Garstecki, P., Gitlin, I., Diluzio, W., Whitesides, G.M., Kumacheva, E. and Stone, H.A. 2004. Formation of monodisperse bubbles in a microfluidic flow-focusing device. *Applied Physics Letters*. **85**(13),pp.2649–2651.

Gaspari, R., Prota, A.E., Bargsten, K., Cavalli, A. and Steinmetz, M.O. 2017. Structural Basis of cis- and trans-Combretastatin Binding to Tubulin. *Chem*. **2**(1),pp.102–113.

Gaumet, M., Vargas, A., Gurny, R. and Delie, F. 2008. Nanoparticles for drug delivery: The need for precision in reporting particle size parameters. *European Journal of Pharmaceutics and Biopharmaceutics*. **69**,pp.1–9.

Gianella, A., Jarzyna, P.A., Mani, V., Ramachandran, S., Calcagno, C., Tang, J., Kann, B., Dijk, W.J.R., Thijssen, V.L., Griffioen, A.W., Storm, G., Fayad, Z.A. and Mulder, W.J.M. 2011. Multifunctional nanoemulsion platform for imaging guided therapy evaluated in experimental cancer. *ACS Nano*. **5**(6),pp.4422–4433.

Giordano, S., Zucchetti, M., Decio, A., Cesca, M., Fuso Nerini, I., Maiezza, M., Ferrari, M., Licandro, S.A., Frapolli, R., Giavazzi, R., Maurizio, D., Davoli, E. and Morosi, L. 2016. Heterogeneity of paclitaxel distribution in different tumor models assessed by MALDI mass spectrometry imaging. *Scientific Reports*. **6**,pp.1–12.

Goertz, D.E., Yu, J.L., Kerbel, R.S., Burns, P.N. and Foster, F.S. 2002. High frequency Doppler ultrasound monitors the effects of antivascular therapy on blood flow. *Cancer Res*. **62**,pp.6371–6375.

Goldberg, R.M., Sargent, D.J., Morton, R.F., Fuchs, C.S., Ramanathan, R.K., Williamson, S.K., Findlay, B.P., Pitot, H.C. and Alberts, S. 2006a. Randomized controlled trial of reduced-dose bolus fluorouracil plus leucovorin and irinotecan or infused fluorouracil plus leucovorin and oxaliplatin in patients with previously untreated metastatic colorectal cancer: A North American intergroup trial. *Journal of Clinical Oncology*. **24**(21),pp.3347–3353.

Goldberg, R.M., Tabah-Fisch, I., Bleiberg, H., De Gramont, A., Tournigand, C., Andre, T., Rothenberg, M.L., Green, E. and Sargent, D.J. 2006b. Pooled analysis of safety and efficacy of oxaliplatin plus fluorouracil/leucovorin administered bimonthly in elderly patients with colorectal cancer. *Journal of Clinical Oncology*. **24**(25),pp.4085–4091.

Gramont, Figer, A., Seymour, M., Homerin, M., Hmissi, A., Cassidy, J., Boni, C., Cortes-Funes, H., Cervantes, A., Freyer, G., Papamichael, D., Bail, N., Louvet, C., Hendler, D., Braud, F., Wilson, C., Morvan, F. and Bonetti, A. 2000. Leucovorin and fluorouracil with or without oxaliplatin as first-line treatment in advanced colorectal cancer. *Journal of Clinical Oncology*. **18**,pp.2938–2947.

Greene, F.L., Stewart, A.K. and Norton, H.J. 2002. A New TNM Staging Strategy for Node-Positive (Stage III) Colon Cancer. *Annals of Surgery*. **236**(4),pp.416–421.

Greene, L.M., Carr, M., Keeley, N.O., Lawler, M., Meegan, M.J. and Zisterer, D.M. 2011. BubR1 is required for the mitotic block induced by combretastatin-A4 and a novel cis-restricted β-lactam analogue in human cancer cells. *International Journal of Molecular Medicine*. **27**,pp.715–723.

Greene, L.M., Meegan, M.J. and Zisterer, D.M. 2015. Minireviews Combretastatins :

More Than Just Vascular Targeting Agents ? *The Journal of pharmacology and experimental therapeutics*. **355**,pp.212–227.

Greene, L.M., O'Boyle, N.M., Nolan, D.P., Meegan, M.J. and Zisterer, D.M. 2012. The vascular targeting agent Combretastatin-A4 directly induces autophagy in adenocarcinoma-derived colon cancer cells. *Biochemical Pharmacology*. **84**,pp.612–624.

Gref, R., Couvreur, P., Barratt, G. and Mysiakine, E. 2003. Surface-engineered nanoparticles for multiple ligand coupling. *Biomaterials*. **24**,pp.4529–4537.

Griggs, J., Hesketh, R., Smith, G.A., Brindle, K.M., Metcalfe, J.C., Thomas, G.A. and Williams, E.D. 2001. Combretastatin-A4 disrupts neovascular development in non-neoplastic tissue. *British journal of cancer*. **84**(6),pp.832–835.

Grosios, K., Holwell, S.E., McGown, A.T., Pettit, G.R. and Bibby, M.C. 1999. In vivo and in vitro evaluation of combretastatin A-4 and its sodium phosphate prodrug. *British journal of cancer*. **81**(8),pp.1318–1327.

Grosios, K., Loadman, P.M., Swaine, D.J., Pettit, G.R. and Bibby, M.C. 2000. Combination Chemotherapy with Combretastatin A-4 Phosphate and 5-Fluorouracil in an Experimental Murine Colon Adenocarcinoma. *Anticancer Research*. **20**,pp.229–234.

Guichard, S., Chatelut, E., Lochon, I., Bugat, R., Mahjoubi, M. and Canal, P. 1998. Comparison of the pharmacokinetics and efficacy of irinotecan after administration by the intravenous versus intraperitoneal route in mice. *Cancer Chemotherapy and Pharmacology*. **42**,pp.165–170.

Guichard, S., Terret, C., Hennebelle, I., Lochon, I., Chevreau, P., Frétigny, E., Selves, J., Chatelut, E., Bugat, R. and Canal, P. 1999. CPT-11 converting carboxylesterase and topoisomerase I activities in tumour and normal colon and liver tissues. *British Journal of Cancer*. **80**(3–4),pp.364–370.

Guinney, J., Dienstmann, R., Wang, X., De Reyniès, A., Schlicker, A., Soneson, C., Marisa, L., Roepman, P., Nyamundanda, G., Angelino, P., Bot, B.M., Morris, J.S., Simon, I.M., Gerster, S., Fessler, E., De Sousa .E Melo, F., Missiaglia, E., Ramay, H., Barras, D., Homicsko, K., Maru, D., Manyam, G.C., Broom, B., Boige, V., Perez-Villamil, B., Laderas, T., Salazar, R., Gray, J.W., Hanahan, D., Tabernero, J., Bernards, R., Friend, S.H., Laurent-Puig, P., Medema, J.P., Sadanandam, A., Wessels, L., Delorenzi, M., Kopetz, S., Vermeulen, L. and Tejpar, S. 2015. The consensus molecular subtypes of colorectal cancer. *Nature Medicine*. **21**,pp.1350–1356.

Gupta, E., Lestingi, T.M., Mick, R., Ramirez, J., Vokes, E.E. and Ratain, M.J. 1994. Metabolic Fate of Irinotecan in Humans: Correlation of Glucuronidation with Diarrhea. *Cancer Research*. **54**(14),pp.3723–3725.

Hak, S., Garaiova, Z., Olsen, L.T., Nilsen, A.M. and De Lange Davies, C. 2015. The effects of oil-in-water nanoemulsion polyethylene glycol surface density on intracellular stability, pharmacokinetics, and biodistribution in tumor bearing mice. *Pharmaceutical Research*. **32**,pp.1475–1485.

Hak, S., Helgesen, E., Hektoen, H.H., Huuse, E.M., Jarzyna, P.A., Mulder, W.J.M., Haraldseth, O. and Davies, C.D.L. 2012. The effect of nanoparticle polyethylene glycol surface density on ligand-directed tumor targeting studied in vivo by dual

modality imaging. *ACS Nano*. **6**(6),pp.5648–5658.

Hanahan, D. and Folkman, J. 1996. Patterns and emerging mechanisms of the angiogenic switch during tumorigenesis. *Cell*. **86**,pp.353–364.

Hanahan, D. and Weinberg, R.A. 2011. Hallmarks of cancer: The next generation. *Cell*. **144**,pp.646–674.

Hanahan, D. and Weinberg, R.A. 2000. The hallmarks of cancer. *Cell*. **100**(1),pp.57–70.

Harris, J.M., Martin, N.E. and Modi, M. 2001. Pegylation: a novel process for modifying pharmacokinetics. *Clinical pharmacokinetics*. **40**(7),pp.539–551.

Hernot, S. and Klibanov, A.L. 2008. Microbubbles in ultrasound-triggered drug and gene delivery. *Advanced Drug Delivery Reviews*. **60**,pp.1153–1166.

Hettiarachchi, K., Talu, E., Longo, M.L., Dayton, P.A. and Lee, A.P. 2007. On-chip generation of microbubbles as a practical technology for manufacturing contrast agents for ultrasonic imaging. *Lab on a Chip*. **7**(4),p.463.

Hill, S.A., Chaplin, D.J., Lewis, G. and Tozer, G.M. 2002. Schedule dependence of combretastatin A4 phosphate in transplanted and spontaneous tumour models. *International Journal of Cancer*. **102**,pp.70–74.

Hodgson, J. 2001. ADMET - Turning chemicals into drugs. Rapidly resolving the pharmacokinetic and toxicological properties of drug candidates remains a key challenge for drug developers. *Nature Biotechnology*. **19**,pp.722–726.

Holwell, S.E., Cooper, P.A., Grosios, K., Lippert, J.W., Pettit, G.R., Shnyder, S.D. and Bibby, M.C. 2002. Combretastatin A-1 phosphate a novel tubulin-binding agent with in vivo anti vascular effects in experimental tumours. *Anticancer Research*. **22**(2 A),pp.707–711.

Houghton, P.J., Cheshire, P.J., Hallman, J.D., Lutz, L., Friedman, H.S., Danks, M.K. and Houghton, J.A. 1995. Efficacy of topoisomerase I inhibitors, topotecan and irinotecan, administered at low dose levels in protracted schedules to mice bearing xenografts of human tumors. *Cancer Chemotherapy and Pharmacology*. **36**,pp.393–403.

Huang, S.L., McPherson, D.D. and MacDonald, R.C. 2008. A Method to Co-Encapsulate Gas and Drugs in Liposomes for Ultrasound-Controlled Drug Delivery. *Ultrasound in Medicine and Biology*. **34**(8),pp.1272–1280.

Hurwitz, H., Fehrenbacker, L., Novotny, W., Cartwright, T., Hainsworth, J., Heim, W., Berlin, J., Baron, A., Griffing, S., Holmgren, E., Ferrara, N., Fyfe, G., Rogers, B., Ross, R. and Kabbinavar, F. 2004. Bevacizumab plus Irinotecan, Fluorouracil, and Leucovorin for Metastatic Colorectal Cancer. *The New England Journal of Medicine*. **350**(23),pp.2545–2559.

Inamura, K. 2018. Colorectal Cancers : An Update on Their Molecular Pathology. *Cancers*. **10**(1).

Ingram, N., Macnab, S.A., Marston, G., Scott, N., Carr, I.M., Markham, A.F., Whitehouse, A. and Coletta, P.L. 2013. The use of high-frequency ultrasound imaging and biofluorescence for in vivo evaluation of gene therapy vectors. *BMC medical imaging*. **13**(1),p.35.

Iversen, T.G., Skotland, T. and Sandvig, K. 2011. Endocytosis and intracellular transport of nanoparticles: Present knowledge and need for future studies. *Nano Today*. **6**,pp.176–185.

Iyer, S., Chaplin, D.J., Rosenthal, D.S., Boulares, A.H., Li, L.-Y. and Smulson, M.E. 1998. Induction of Apoptosis in Proliferating Human Endothelial Cells by the Tumor-specific Antiangiogenesis Agent Combretastatin A4. *Cancer Research*. **58**,pp.4510–4514.

Jäger, W., Moskalev, I., Janssen, C., Hayashi, T., Awrey, S., Gust, K.M., So, A.I., Zhang, K., Fazli, L., Li, E., Thüroff, J.W., Lange, D. and Black, P.C. 2013. Ultrasound-Guided Intramural Inoculation of Orthotopic Bladder Cancer Xenografts: A Novel High-Precision Approach. *PLoS ONE*. **8**(3),pp.1–11.

Jain, A. and Cheng, K. 2017. The principles and applications of avidin-based nanoparticles in drug delivery and diagnosis. *Journal of Controlled Release*. **245**,pp.27–40.

Jain, R.K. 2005. Normalization of Tumor Vasculatur: An Emerging Concept in Antiangiogenic Therapy. *Science*. **307**(5706),pp.58–62.

Jaroch, K., Goryńska, P.Z., Goryński, K., Stefański, T. and Bojko, B. 2018. Untargeted screening of phase I metabolism of combretastatin A4 by multi-tool analysis. *Talanta*. **182**,pp.22–31.

Jaroch, K., Karolak, M., Gorski, P., Jaroch, A., Krajewski, A., Ilnicka, A., Sloderbach, A., Stefanski, T. and Sobiak, S. 2016. Combretastatins: In vitro structure-activity relationship, mode of action and current clinical status. *Pharmacological Reports*. **68**,pp.1266–1275.

Jarzyna, P.A., Skajaa, T., Gianella, A., Cormode, D.P., Samber, D.D., Dickson, S.D., Chen, W., Griffioen, A.W., Fayad, Z.A. and Mulder, W.J.M. 2009. Iron oxide core oil-in-water emulsions as a multifunctional nanoparticle platform for tumor targeting and imaging. *Biomaterials*. **30**,pp.6947–6954.

Jones, S., Chen, W., Parmigiani, G., Diehl, F., Beerenwinkel, N., Antal, T., Traulsen, A., Nowak, M. artin A., Siegel, C., Velculescu, V.E., Kinzler, K.W., Vogelstein, B., Willis, J. and Markowitz, S.D. 2008. Comparative lesion sequencing provides insights into tumor evolution. *Proceedings of the National Academy of Sciences*. **105**(11),pp.4283–4288.

Jordan, M.A. and Wilson, L. 2004. Microtubules as a target for anticancer drugs. *Nature Reviews Cancer*. **4**,pp.253–265.

Kalepu, S. and Nekkanti, V. 2015. Insoluble drug delivery strategies: Review of recent advances and business prospects. *Acta Pharmaceutica Sinica B*. **5**(5),pp.442–453.

Kanthou, C., Greco, O., Stratford, A., Cook, I., Knight, R., Benzakour, O. and Tozer, G. 2004. The tubulin-binding agent combretastatin A-4-phosphate arrests endothelial cells in mitosis and induces mitotic cell death. *American journal of pathology*. **165**(4),pp.1401–1411.

Kanthou, C. and Tozer, G.M. 2002. The tumor vascular targeting agent combretastatin A-4-phosphate induces reorganization of the actin cytoskeleton and early membrane blebbing in human endothelial cells. *Blood*. **99**(6),pp.2060–

2069.

Kaufmann, B.A. 2009. Ultrasound molecular imaging of atherosclerosis. *Cardiovascular Research*. **83**(4),pp.617–625.

Kerbel, R.S. and Kamen, B.A. 2004. The anti-angiogenic basis of metronomic chemotherapy. *Nature Reviews Cancer*. **4**(6),pp.423–436.

Kheirolomoom, A., Dayton, P.A., Lum, A.F.H., Little, E., Paoli, E.E., Zheng, H. and Ferrara, K.W. 2007. Acoustically-active microbubbles conjugated to liposomes: Characterization of a proposed drug delivery vehicle. *Journal of Controlled Release*. **118**,pp.275–284.

Kiessling, F., Fokong, S., Koczera, P., Lederle, W. and Lammers, T. 2012. Ultrasound Microbubbles for Molecular Diagnosis, Therapy, and Theranostics. *Journal of Nuclear Medicine*. **53**(3),pp.345–348.

Kim, S., Peshkin, L. and Mitchison, T.J. 2012. Vascular disrupting agent drug classes differ in effects on the cytoskeleton. *PLoS ONE*. **7**(7),pp.1–8.

Kirwan, I.G., Loadman, P.M., Swaine, D.J., Anthoney, D.A., Pettit, G.R., Lippert, J.W., Shnyder, S.D., Cooper, P.A. and Bibby, M.C. 2004. Comparative Preclinical Pharmacokinetic and Metabolic Studies of the Combretastatin Prodrugs Combretastatin A4 Phosphate and A1 Phosphate. *Clinical Cancer Research*. **10**,pp.1446–1453.

Klibanov, A.L. 2005. Ligand-carrying gas-filled microbubbles: Ultrasound contrast agents for targeted molecular imaging. *Bioconjugate Chemistry*. **16**(1),pp.9–17.

Klibanov, A.L., Shevchenko, T.I., Raju, B.I., Seip, R. and Chin, C.T. 2010. Ultrasound-triggered release of materials entrapped in microbubble-liposome constructs: a tool for targeted drug delivery. *Journal of Controlled Release*. **148**(1),pp.13–17.

Kooiman, K., Foppen-Harteveld, M., Der Steen, A.F.W. Van and De Jong, N. 2011. Sonoporation of endothelial cells by vibrating targeted microbubbles. *Journal of Controlled Release*. **154**,pp.35–41.

Kooiman, K., Vos, H.J., Versluis, M. and De Jong, N. 2014. Acoustic behavior of microbubbles and implications for drug delivery. *Advanced Drug Delivery Reviews*. **72**,pp.28–48.

Kotopoulis, S., Dimcevski, G., Gilja, O.H., Hoem, D. and Postema, M. 2013. Treatment of human pancreatic cancer using combined ultrasound, microbubbles, and gemcitabine: A clinical case study. *The International Journal of Medical Physics Research and Practice*. **40**(7).

Kunimoto, T., Nitta, K., Tanaka, T., Uehara, N., Baba, H., Takeuchi, M., Yokokura, T., Sawada, S., Miyasaka, T. and Mutai, M. 1987. Antitumor activity of 7-ethyl-10-[4-(1-piperidino)-1-piperidino]carbonyloxy-camptothec in, a novel water-soluble derivative of camptothecin, against murine tumors. *Cancer Research*. **47**(22),pp.5944–5947.

Lammertink, B.H.A., Bos, C., Deckers, R., Storm, G., Moonen, C.T.W. and Escoffre, J.M. 2015. Sonochemotherapy: From bench to bedside. *Frontiers in Pharmacology*. **6**,pp.1–17.

Landmann, H., Proia, D.A., He, S., Ogawa, L.S., Kramer, F., Beissbarth, T., Grade, M., Gaedcke, J., Ghadimi, M., Moll, U. and Dobbelstein, M. 2014. UDP glucuronosyltransferase 1A expression levels determine the response of colorectal cancer cells to the heat shock protein 90 inhibitor ganetespib. *Cell Death and Disease*. **5**,p.e1411.

Landuyt, W., Verdoes, O., Darius, D.O., Drijkoningen, M., Nuyts, S., Theys, J., Stockx, L., Wynendaele, W., Fowler, J.F., Maleux, G., Van Den Bogaert, W., Anné, J., Van Oosterom, A. and Lambin, P. 2000. Vascular targeting of solid tumoursa major 'inverse' volume-response relationship following combretastatin A-4 phosphate treatment of rat rhabdomyosarcomas. *European Journal of Cancer*. **36**,pp.1833–1843.

Lankester, K.J., Maxwell, R.J., Pedley, R.B., Dearling, J.L., Qureshi, U.A., El-Emir, E., Hill, S.A. and Tozer, G.M. 2007. Combretastatin A-4-phosphate effectively increases tumor retention of the therapeutic antibody,131I-A5B7, even at doses that are sub-optimal for vascular shut-down. *International Journal of Oncology*. **30**,pp.453–460.

Lentacker, I., De Cock, I., Deckers, R., De Smedt, S.C. and Moonen, C.T.W. 2014. Understanding ultrasound induced sonoporation: Definitions and underlying mechanisms. *Advanced Drug Delivery Reviews*. **72**,pp.49–64.

Lentacker, I., Geers, B., Demeester, J., De Smedt, S.C. and Sanders, N.N. 2010. Design and evaluation of doxorubicin-containing microbubbles for ultrasound-triggered doxorubicin delivery: cytotoxicity and mechanisms involved. *Molecular therapy : the journal of the American Society of Gene Therapy*. **18**(1),pp.101–108.

Lentacker, I., De Geest, B.G., Vandenbroucke, R.E., Peeters, L., Demeester, J., De Smedt, S.C. and Sanders, N.N. 2006. Ultrasound-responsive polymer-coated microbubbles that bind and protect DNA. *Langmuir*. **22**,pp.7273–7278.

Lentacker, I., De Smedt, S.C. and Sanders, N.N. 2009. Drug loaded microbubble design for ultrasound triggered delivery. *Soft Matter*. **5**,pp.2161–2170.

Li, J., Kim, S.G. and Blenis, J. 2009. Rapamycin: one drug, may effects. *Cell Metabolism*. **19**(3),pp.373–379.

Li, J., Wang, X., Zhang, T., Wang, C., Huang, Z., Luo, X. and Deng, Y. 2014. A review on phospholipids and their main applications in drug delivery systems. *Asian Journal of Pharmaceutical Sciences*. **10**(2),pp.81–98.

Li, L., Rojiani, A. and Siemann, D.W. 1998. Targeting the tumor vasculature with combretastatin A-4 disodium phosphate: effects on radiation therapy. *International journal of radiation oncology, biology, physics*. **42**(4),pp.899–903.

Li, X., Wu, M., Pan, L. and Shi, J. 2015. Tumor vascular-targeted co-delivery of anti-angiogenesis and chemotherapeutic agents by mesoporous silica nanoparticle-based drug delivery system for synergetic therapy of tumor. *International Journal of Nanomedicine*. **11**,pp.93–105.

Liang, W., Lai, Y., Zhu, M., Huang, S., Feng, W. and Gu, X. 2016. Combretastatin A4 Regulates Proliferation, Migration, Invasion, and Apoptosis of Thyroid Cancer Cells via PI3K/Akt Signaling Pathway. *Medical Science Monitor*. **22**,pp.4911–4917.

Liang, W., Ni, Y. and Chen, F. 2016. Tumor resistance to vascular disrupting agents: mechanisms, imaging, and solutions. *Oncotarget*. **7**(13),pp.15444–15459.

Lietz, C.B., Gemperline, E. and Li, L. 2013. Qualitative and quantitative mass spectrometry imaging of drugs and metabolites. *Advanced Drug Delivery Reviews*. **65**(8),pp.1074–1085.

Lin, C.M., Ho, H.H., Pettit, G.R. and Hamel, E. 1989. Antimitotic natural products combretastatin A-4 and combretastatin A-2: studies on the mechanism of their inhibition of the binding of colchicine to tubulin. *Biochemistry*. **28**,pp.6984–6991.

Lin, C.M., Singh, S.B., Chu, P.S., Dempcy, R.O., Schmidt, J.M., Pettit, G.R. and Hamel, E. 1988. Interactions of tubulin with potent natural and synthetic analogs of the antimitotic agent combretastatin: a structure-activity study. *Molecular pharmacology*. **34**(2),pp.200–208.

Lin, H.-L., Chiou, S.-H., Wu, C.-W., Lin, W.-B., Chen, L.-H., Yang, Y.-P., Tsai, M.-L., Uen, Y.-H., Liou, J.-P. and Chi, C.-W. 2007. Combretastatin A4-induced differential cytotoxicity and reduced metastatic ability by inhibition of AKT function in human gastric cancer cells. *The Journal of pharmacology and experimental therapeutics*. **323**(1),pp.365–373.

Lindner, J.R., Coggins, M.P., Kaul, S., Klibanov, A.L., Brandenburger, G.H. and Ley, K. 2000a. Microbubble Persistence in the Microcirculation During Ischemia / Reperfusion and Inflammation Is Caused by Activated Leukocytes. *Circulation*. **101**,pp.668–675.

Lindner, J.R., Dayton, P.A., Coggins, M.P., Ley, K., Song, J., Ferrara, K. and Kaul, S. 2000b. Noninvasive imaging of inflammation by ultrasound detection of phagocytosed microbubbles. *Circulation*. **102**,pp.531–538.

Linnekamp, J.F., Hooff, S.R. van, Prasetyanti, P.R., Kandimalla, R., Buikhuisen, J.Y., Fessler, E., Ramesh, P., Lee, K.A.S.T., Bochove, G.G.W., de Jong, J.H., Cameron, K., Leersum, R. van, Rodermond, H.M., Franitza, M., Nürnberg, P., Mangiapane, L.R., Wang, X., Clevers, H., Vermeulen, L., Stassi, G. and Medema, J.P. 2018. Consensus molecular subtypes of colorectal cancer are recapitulated in in vitro and in vivo models. *Cell Death & Differentiation*. **25**(3),pp.616–633.

Liu, L., Mason, R.P. and Gimi, B. 2015. Dynamic bioluminescence and fluorescence imaging of the effects of the antivascular agent Combretastatin-A4P (CA4P) on brain tumor xenografts. *Cancer Letters*. **356**,pp.462–469.

Liu, X., Flinders, C., Mumenthaler, S.M. and Hummon, A.B. 2018. MALDI Mass Spectrometry Imaging for Evaluation of Therapeutics in Colorectal Tumor Organoids. *Amarican Society for Mass Spectrometry*. **29**,pp.516–526.

Liu, X., Weaver, E.M. and Hummon, A.B. 2013. Evaluation of Therapeutics in Three-Dimensional Cell Culture Systems by MALDI Imaging Mass Spectrometry. *Analytical Chemistry*. **85**,pp.6295–6302.

Longley, D.B., Harkin, D.P. and Johnston, P.G. 2003. 5-Fluorouracil: Mechanisms of action and clinical strategies. *Nature Reviews Cancer*. **3**,pp.330–338.

Lu, Y., Chen, J., Xiao, M., Li, W. and Miller, D.D. 2012. An Overview of Tubulin Inhibitors That Interact with the Colchicine Binding site. *Pharmaceutical*

Research. **29**(11),pp.2943–2971.

Lukowski, J.K., Weaver, E.M. and Hummon, A.B. 2017. Analyzing Liposomal Drug Delivery Systems in Three-Dimensional Cell Culture Models Using MALDI Imaging Mass Spectrometry. *Analytical Chemistry*. **89**(16),pp.8453–8458.

Lyshchik, A., Fleischer, A.C., Huamani, J., Hallahan, D., Brissova, M. and Core, J.C. 2007. Molecular Imaging of Vascular Endothelail Growth Factor Receptor 2 Expression Using Targeted Contrast-Enhanced High-Frequency Ultrasonography. *Journal of ultrasound in medicine*. **26**(11),pp.1575–1586.

Maeda, H. 2001. The enhanced permeability and retention (EPR) effect in tumor vasculature: The key role of tumor-selective macromolecular drug targeting. *Advances in Enzyme Regulation*. **41**,pp.189–207.

Maeda, H., Fang, J., Inutsuka, T. and Kitamoto, Y. 2003. Vascular permeability enhancement in solid tumor: Various factors, mechanisms involved and its implications. *International Immunopharmacology*. **3**,pp.319–328.

Malcontenti-Wilson, C., Muralidharan, V., Skinner, S., Christophi, C., Sherris, D. and O'Brien, P.E. 2001. Combretastatin A4 prodrug study of effect on the growth and the microvasculature of colorectal liver metastases in a murine model. *Clinical cancer research*. **7**,pp.1052–1060.

Malvern Instruments 2011. Dynamic Light Scattering COMMON TERMS DEFINED. *Malvern Guides*.,pp.1–6.

Marisa, L., de Reyniès, A., Duval, A., Selves, J., Gaub, M.P., Vescovo, L., Etienne-Grimaldi, M.C., Schiappa, R., Guenot, D., Ayadi, M., Kirzin, S., Chazal, M., Fléjou, J.F., Benchimol, D., Berger, A., Lagarde, A., Pencreach, E., Piard, F., Elias, D., Parc, Y., Olschwang, S., Milano, G., Laurent-Puig, P. and Boige, V. 2013. Gene Expression Classification of Colon Cancer into Molecular Subtypes: Characterization, Validation, and Prognostic Value. *PLoS Medicine*. **10**(5),pp.1–13.

Markowitz, S.D. and Bertagnolli, M.M. 2009. Molecular Basis of Colorectal Cancer. *The New England Journal of Medicine*.,pp.2449–2460.

Martens, T.F., Remaut, K., Demeester, J., De Smedt, S.C. and Braeckmans, K. 2014. Intracellular delivery of nanomaterials: How to catch endosomal escape in the act. *Nano Today*. **9**,pp.344–364.

Martin, H.L., Adams, M., Higgins, J., Bond, J., Morrison, E.E., Bell, S.M., Warriner, S., Nelson, A. and Tomlinson, D.C. 2014. High-content, high-throughput screening for the identification of cytotoxic compounds based on cell morphology and cell proliferation markers. *PLoS ONE*. **9**(2).

Martin, K.H. and Dayton, P.A. 2013. Current Status and Prospects for Microbubbles in Ultrasouns Theranostics. *WIREs Nanomedicine and Nanobiotechnology*. **5**(4),pp.329–345.

Mason, T.G., Wilking, J.N., Meleson, K., Chang, C.B. and Graves, S.M. 2006. Nanoemulsions: Formation, structure, and physical properties. *Journal of Physics Condensed Matter*. **18**,pp.R635–R666.

Mathijssen, R.H.J., Van Alphen, Robbert, J., Verweij, J., Loss, W.J., Nooter, K.,

Stoter, G. and Sparreboom, A. 2001. Clinical pharmacokinetics and metabolism of Irinotecan (CPT-11). *Clinical Cancer Research*. **7**,pp.2182–2194.

Matsumura, Y. and Maeda, H. 1986. A new concept for macromolecular therapeutics in cnacer chemotherapy: mechanism of tumoritropic accumulatio of proteins and the antitumor agents Smancs. *Cancer research*. **46**,pp.6387–6392.

Maxwell, R.J., Pharm, B., F.U., N., Breidahl, T., Stodkilde-Jorgensen, H. and Horsan, M.R. 1998. Effects of Combretastatin on Murine Tumours Moniotred by 31P MRS, 1H MRS and 1H MRI. *International Journal Radiation Oncology Biol. Phys*. **42**(4),pp.891–894.

Maxwell, R.J., Wilson, J., Prise, V.E., Vojnovic, B., Rustin, G.J., Lodge, M.A. and Tozer, G.M. 2002. Evaluation of the anti-vascular effects of combretastatin in rodent tumours by dynamic contrast enhanced MRI. *NMR in Biomedicine*. **15**,pp.89–98.

McLaughlan, J., Ingram, N., Smith, P.R., Harput, S., Coletta, P.L., Evans, S. and Freear, S. 2013. Increasing the sonoporation efficiency of targeted polydisperse microbubble populations using chirp excitation. *IEEE Transactions on Ultrasonics, Ferroelectrics, and Frequency Control*. **60**(12),pp.2511–2520.

McLaughlan, J.R., Harput, S., Abou-Saleh, R.H., Peyman, S.A., Evans, S. and Freear, S. 2017. Characterisation of Liposome-Loaded Microbubble Populations for Subharmonic Imaging. *Ultrasound in Medicine and Biology*. **43**(1),pp.346–356.

Meijering, B.D.M., Juffermans, L.J.M., Van Wamel, A., Henning, R.H., Zuhorn, I.S., Emmer, M., Versteilen, A.M.G., Paulus, W.J., Van Gilst, W.H., Kooiman, K., De Jong, N., Musters, R.J.P., Deelman, L.E. and Kamp, O. 2009. Ultrasound and microbubble-targeted delivery of macromolecules is regulated by induction of endocytosis and pore formation. *Circulation Research*. **104**,pp.679–687.

Mendez, G., Policarpi, C., Cenciarelli, C., Tanzarella, C. and Antoccia, A. 2011. Role of Bim in apoptosis induced in H460 lung tumor cells by the spindle poison Combretastatin-A4. *Apoptosis*. **16**(9),pp.940–949.

Meyer, T., Gaya, A.M., Dancey, G., Stratford, M.R.L., Othman, S., Sharma, S.K., Wellsted, D., Taylor, N.J., Stirling, J.J., Poupard, L., Folkes, L.K., Chan, P.S., Pedley, R.B., Chester, K.A., Owen, K., Violet, J.A., Malaroda, A., Green, A.J., Buscombe, J., Padhani, A.R., Rustin, G.J. and Begent, R.H. 2009. A phase I trial of radioimmunotherapy with 131I-A5B7 anti-CEA antibody in combination with combretastatin-A4-phosphate in advanced gastrointestinal carcinomas. *Clinical Cancer Research*. **15**(13),pp.4484–4492.

Mico, V. 2017. Developing Microbubble-Nanodroplet Composites for Enhanced Hydrophobic Drug Delivery. *Ph.D.thesis, University of Leeds*. (March).

Mico, V., Charalambous, A., Peyman, S.A., Abou-Saleh, R.H., Markham, A.F., Coletta, P.L. and Evans, S.D. 2017. Evaluation of lipid-stabilised tripropionin nanodroplets as a delivery route for combretastatin A4. *International Journal of Pharmaceutics*. **526**(1–2),pp.547–555.

Milton Harris, J. and Chess, R.B. 2003. Effect of pegylation on pharmaceuticals. *Nature Reviews Drug Discovery*. **2**,pp.214–221.

Minchinton, A.I. and Tannock, I.F. 2006. Drug penetration in solid tumours. *Nature Reviews Cancer*. **6**,pp.583–592.

Moiseeva, E. V, Kuznetsova, N.R., Svirshchevskaia, E. V, Bovin, N. V, Sitnikov, N.C., Shavyrin, A.S., Beletskaia, I.P., Combes, S., Fedorov, A.Y. and Vodovozova, E.L. 2012. Liposome formulations of combretastatin A4 and 4-arylcoumarin analog prodrugs: antitumor effect in the mouse model of breast cancer. *Biomeditsinskaia khimiia*. **58**(3),pp.276–283.

Mooney, C.J., Nagaiah, G., Fu, P., Wasman, J.K., Cooney, M.M., Savvides, P.S., Bokar, J.A., Dowlati, A., Wang, D., Agarwala, S.S., Flick, S.M., Hartman, P.H., Ortiz, J.D., Lavertu, P.N. and Remick, S.C. 2009. A phase II trial of fosbretabulin in advanced anaplastic thyroid carcinoma and correlation of baseline serum-soluble intracellular adhesion molecule-1 with outcome. *Thyroid*. **19**(3),pp.233–240.

Morinaga, Y., Suga, Y., Ehara, S., Harada, K., Nihei, Y. and Suzuki, M. 2003. Combination effect of AC-7700, a novel combretastatin A-4 derivative, and cisplatin against murine and human tumors in vivo. *Cancer Science*. **94**(2),pp.200–204.

Morosi, L., Spinelli, P., Zucchetti, M., Pretto, F., Carra, A., Incalci, M.D., Giavazzi, R. and Davoli, E. 2013a. Determination of Paclitaxel Distribution in Solid Tumors by Nano-Particle Assisted Laser Desorption Ionization Mass Spectrometry Imaging. *PLoS ONE*. **8**(8),pp.e72532–e72532.

Morosi, L., Zucchetti, M., Incalci, M.D. and Davoli, E. 2013b. Imaging mass spectrometry : challenges in visualization of drug distribution in solid tumors. *Current Opinion in Pharmacology*. **13**,pp.807–812.

MP Biomedicals 2018. Triacetin. [Accessed 10 January 2018]. Available from: https://www.mpbio.com.

Mukhtar, E., Adhami, V.M. and Mukhtar, H. 2014. Targeting Microtubules by Natural Agents for Cancer Therapy. *Molecular Cancer Therapeutics*. **13**(2),pp.275–284.

Muller, R.H., Jacobs, C. and Kayser, O. 2001. Nanosuspensions as particulate drug formulations in therapy . Rationale for development and what we can expect for the future . *Advanced Drug Delivery Reviews*. **47**(July),pp.3–19.

Murakami, H., Ogata, Y., Akagi, Y., Ishibashi, N. and Shirouzu, K. 2011. Circulating endothelial progenitor cells in metronomic chemotherapy using irinotecan and/or bevacizumab for colon carcinoma: Study of their clinical significance. *Experimental and Therapeutic Medicine*. **2**(4),pp.595–600.

Murata, R., Overgaard, J. and Horsman, M.R. 2001. Comparative effects of combretastatin A-4 disodium phosphate and 5,6-dimethylxanthenone-4-acetic acid on blood perfusion in a murine tumour and normal tissues. *International Journal of Radiation Biology*. **77**(2),pp.195–204.

Murdock, R.C., Braydich-Stolle, L., Schrand, A.M., Schlager, J.J. and Hussain, S.M. 2008. Characterization of nanomaterial dispersion in solution prior to in vitro exposure using dynamic light scattering technique. *Toxicological Sciences*. **101**(2),pp.239–253.

Nabha, S.M., Mohammad, R.M., Dandashi, M.H., Coupaye-Gerard, B., Aboukameel,

A., Pettit, G.R. and Al-Katib, A.M. 2002. Combretastatin-A4 prodrug induces mitotic catastrophe in chronic lymphocytic leukemia cell line independent of caspase activation and poly(ADP-ribose) polymerase cleavage. *Clinical Cancer Research*. **8**,pp.2735–2741.

Nabha, S.M., Mohammad, R.M., Wall, N.R., Dutcher, J.A., Salkini, B.M., Pettit, G.R. and Al-Katib, A.M. 2001. Evaluation of combretastatin A-4 prodrug in a non-Hodgkin's lymphoma xenograft model: preclinical efficacy. *Anti-cancer drugs*. **12**,pp.57–63.

Nabha, S.M., Wall, N.R., Mohammad, R.M., Pettit, G.R. and Al-Katib, A.M. 2000. Effects of combretastatin A-4 prodrug against a panel of malignant human B-lymphoid cell lines. *Anti-cancer drugs*. **11**,pp.385–392.

Nallamothu, R., Wood, G.C., Kiani, M.F., Moore, B.M., Horton, F.P. and Thoma, L.A. 2006a. A targeted liposome delivery system for combretastatin A4: formulation optimization through drug loading and in vitro release studies. *PDA Journal of Pharmaceutical Science and Technology*. **60**(3),pp.144–155.

Nallamothu, R., Wood, G.C., Pattillo, C.B., Scott, R.C., Kiani, M.F., Moore, B.M. and Thoma, L.A. 2006b. A tumor vasculature targeted liposome delivery system for combretastatin A4: Design, characterization, and in vitro evaluation. *AAPS PharmSciTech*. **7**(2),pp.E1–E10.

Nathan, P., Zweifel, M., Padhani, A.R., Koh, D.M., Ng, M., Collins, D.J., Harris, A., Carden, C., Smythe, J., Fisher, N., Taylor, N.J., Stirling, J.J., Lu, S.P., Leach, M.O., Rustin, G.J.S. and Judson, I. 2012. Phase I trial of combretastatin A4 phosphate (CA4P) in combination with bevacizumab in patients with advanced cancer. *Clinical Cancer Research*. **18**(12),pp.3428–3439.

National Center for Biotechnology Information 2005. Glyceryl Tripropanoate. *PubChem Compound Database*. [Online]. [Accessed 24 April 2018]. Available from: https://pubchem.ncbi.nlm.nih.gov.

Ng, Q.S., Mandeville, H., Goh, V., Alonzi, R., Milner, J., Carnell, D., Meer, K., Padhani, A.R., Saunders, M.I. and Hoskin, P.J. 2012. Phase Ib trial of radiotherapy in combination with combretastatin-A4-phosphate in patients with nonsmall-cell lung cancer, prostate adenocarcinoma, and squamous cell carcinoma of the head and neck. *Annals of Oncology*. **23**,pp.231–237.

Nguyen, L., Fifis, T., Malcontenti-Wilson, C., Chan, L.S., Costa, P.N.L., Nikfarjam, M., Muralidharan, V. and Christophi, C. 2012. Spatial morphological and molecular differences within solid tumors may contribute to the failure of vascular disruptive agent treatments. *BMC Cancer*. **12**,pp.1–13.

Olsen, B.N., Bielska, A.A., Lee, T., Daily, M.D., Covey, D.F., Schlesinger, P.H., Baker, N.A. and Ory, D.S. 2013. The structural basis of cholesterol accessibility in membranes. *Biophysical Journal*. **105**(8),pp.1838–1847.

Öztürk-Atar, K., Eroğlu, H. and Çalış, S. 2017. Novel advances in targeted drug delivery. *Journal of Drug Targeting*. **23**,pp.1–10.

Paefgen, V., Doleschel, D. and Kiessling, F. 2015. Evolution of contrast agents for ultrasound imaging and ultrasound-mediated drug delivery. *Frontiers in Pharmacology*. **6**,pp.1–16.

Park, D.J., Won, J.H., Cho, A.R., Yun, H.J., Heo, J.H., Hwhang, T.H., Lee, D.H. and Kim, W.M. 2014. Determination of irinotecan and its metabolite SN-38 in rabbit plasma and tumors using a validated method of tandem mass spectrometry coupled with liquid chromatography. *Journal of Chromatography B*. **962**,pp.147–152.

Park, Y., Pham, T.A., Beigie, C., Cabodi, M., Cleveland, R.O., Nagy, J.O. and Wong, J.Y. 2015. Monodisperse Micro-Oil Droplets Stabilized by Polymerizable Phospholipid Coatings as Potential Drug Carriers. *Langmuir*. **31**,pp.9762–9770.

Parkins, C.S., Holder, a L., Hill, S.A., Chaplin, D.J. and Tozer, G.M. 2000. Determinants of anti-vascular action by combretastatin A-4 phosphate: role of nitric oxide. *British journal of cancer*. **83**(6),pp.811–816.

Patten, S.G., Adamcic, U., Lacombe, K., Minhas, K., Skowronski, K. and Coomber, B.L. 2010. VEGFR2 heterogeneity and response to anti-angiogenic low dose metronomic cyclophosphamide treatment. *BMC cancer*. **10**(683),pp.1–11.

Pattillo, C.B., Sari-Sarraf, F., Nallamothu, R., Moore, B.M., Wood, G.C. and Kiani, M.F. 2005. Targeting of the antivascular drug combretastatin to irradiated tumors results in tumor growth delay. *Pharmaceutical Research*. **22**(7),pp.1117–1120.

Pattillo, C.B., Venegas, B., Donelson, F.J., Del Valle, L., Knight, L.C., Chong, P.L.G. and Kiani, M.F. 2009. Radiation-guided targeting of combretastatin encapsulated immunoliposomes to mammary tumors. *Pharmaceutical Research*. **26**(5),pp.1093–1100.

Pedley, R.B., Hill, S.A., Boxer, G.M., Flynn, A.A., Boden, R., Watson, R., Dearling, J., Chaplin, D.J. and Begent, R.H.J. 2001. Eradication of colorectal xenografts by combined radioimmunotherapy and combretastatin A-4 3-O-phosphate. *Cancer Research*. **61**,pp.4716–4722.

Pettit, G.R., Singh, S.B., Boyd, M.R., Hamel, E., Pettit, R.K., Schmidt, J.M. and Hogan, F. 1995. Antineoplastic agents .291. Isolation and synthesis of combretastatin A-4, A-5 and A-6. *Journal of Medicinal Chemistry*. **38**(10),pp.1666–1672.

Pettit, G.R., Singh, S.B., Hamel, E., Lin, C.M., Alberts, D.S. and Garcia-Kendal, D. 1989. Isolation and structure of the strong cell growth and tubulin inhibitor combretastatin A-4. *Experientia*. **45**,pp.209–211.

Pettit, G.R., Singh, S.B., Schmidt, J.M., Niven, M.L., Hamel, E. and Lin, C.M. 1988. Isolation, structure, synthesis, and antimitotic properties of combretastatins B-3 and B-4 from Combretum caffrum. *Journal of natural products*. **51**(3),pp.517–527.

Peyman, S.A., Abou-Saleh, R.H., McLaughlan, J.R., Ingram, N., Johnson, B.R.G., Critchley, K., Freear, S., Evans, J.A., Markham, A.F., Coletta, P.L. and Evans, S.D. 2012. Expanding 3D geometry for enhanced on-chip microbubble production and single step formation of liposome modified microbubbles. *Lab on a Chip*. **12**,pp.4544–4522.

Pino, M.S. and Chung, D.C. 2010. The Chromosomal Instability Pathway in Colon Cancer. *Gastroenterology*. **138**(6),pp.2059–2072.

Pochon, S., Tardy, I., Bussat, P., Bettinger, T., Brochot, J., von Wronski, M., Passantino, L. and Schneider, M. 2010. BR55: a lipopeptide-based VEGFR2-targeted ultrasound contrast agent for molecular imaging of angiogenesis. *Investigative radiology*. **45**(2),pp.89–95.

Poojari, R., Srivastava, R. and Panda, D. 2015. Nanomechanics of Fosbretabulin A4 polymeric nanoparticles in liver cancer cells. *IEEE-NANO 2015 - 15th International Conference on Nanotechnology*.,pp.1406–1409.

Powell, S.M., Zilz, N., Beazer-Barclay, Y., Bryan, T.M., Hamilton, S.R., Thibodeau, S.N., Vogelstein, B. and Kinzler, K.W. 1992. APC mutations occur early during colorectal tumorigenesis. *Nature*. **359**,pp.235–237.

Presta, L.G., Chen, H., O'Connor, S.J., Chisholm, V., Meng, Y.G., Krummen, L., Winkler, M. and Ferrara, N. 1997. Humanization of an anti-vascular endothelial growth factor monoclonal antibody for the therapy of solid tumors and other disorders. *Cancer Research*. **57**(20),pp.4593–4599.

Prideaux, B. and Stoeckli, M. 2012. Mass spectrometry imaging for drug distribution studies. *Journal of Proteomics*. **75**(16),pp.4999–5013.

Pysz, M.A., Foygel, K., Rosenberg, J., Gambhir, S.S., Schneider, M. and Willmann, J.K. 2010. Antiangiogenic Cancer Therapy : Monitoring With Molecular US and a Clinically Translatable Contrast Agent (BR55). *Radiology*. **256**(2),pp.519–527.

Qian, C. and McClements, D.J. 2011. Formation of nanoemulsions stabilized by model food-grade emulsifiers using high-pressure homogenization: Factors affecting particle size. *Food Hydrocolloids*. **25**,pp.1000–1008.

Quan, H., Xu, Y. and Lou, L. 2008. p38 MAPK, but not ERK1/2, is critically involved in the cytotoxicity of the novel vascular disrupting agent combretastatin A4. *International Journal of Cancer*. **122**,pp.1730–1737.

Rafiei, P. and Haddadi, A. 2017. Docetaxel-loaded PLGA and PLGA-PEG nanoparticles for intravenous application : pharmacokinetics and biodistribution profile. *International Journal of Nanomedicine*. **12**,pp.935–947.

Rafiei, P., Michel, D. and Haddadi, A. 2015. Application of a Rapid ESI-MS/MS Method for Quantitative Analysis of Docetaxel in Polymeric Matrices of PLGA and PLGA-PEG Nanoparticles through Direct Injection to Mass Spectrometer. *American Journal of Analytical Chemistry*. **06**,pp.164–175.

Ramachandran, R. and Kakar, S. 2009. Histological patterns in drug-induced liver disease. *Journal of Clinical Pathology*. **62**,pp.481–492.

Redhead, H.M., Davis, S.S. and Illum, L. 2001. Drug delivery in poly(lactide-co-glycolide) nanoparticles surface modified with poloxamer 407 and poloxamine 908: In vitro characterisation and in vivo evaluation. *Journal of Controlled Release*. **70**,pp.353–363.

Remaut, K., Lucas, B., Braeckmans, K., Demeester, J. and De Smedt, S.C. 2007. Pegylation of liposomes favours the endosomal degradation of the delivered phosphodiester oligonucleotides. *Journal of Controlled Release*. **117**(2),pp.256–266.

Del Rio, M., Mollevi, C., Bibeau, F., Vie, N., Selves, J., Emile, J.F., Roger, P.,

Gongora, C., Robert, J., Tubiana-Mathieu, N., Ychou, M. and Martineau, P. 2017. Molecular subtypes of metastatic colorectal cancer are associated with patient response to irinotecan-based therapies. *European Journal of Cancer*. **76**,pp.68–75.

Rodriguez, P.L., Harada, T., Christian, D.A., Pantano, D.A., Tsai, R.K. and Discher, D.E. 2013. Minimal " Self " Peptides That Inhibit Phagocytic Clearance and Enhance Delivery of Nanoparticles. *Science*. **339**,pp.971–976.

Royal Society of Chemistry 2015. ChemSpider. *Royal Society of Chemistry*. [Online]. [Accessed 5 December 2017]. Available from: http://www.chemspider.com/.

Rozas, I. 2017. Understanding the Binding of cis and trans Isomers of Combretastatin to Tubulin. *Chem*. **2**,pp.11–19.

Rustin, G.J.S., Galbraith, S.M., Anderson, H., Stratford, M., Folkes, L.K., Sena, L., Gumbrell, L. and Price, P.M. 2003. Phase I clinical trial of weekly combretastatin A4 phosphate: Clinical and pharmacokinetic results. *Journal of Clinical Oncology*. **21**(15),pp.2815–2822.

Sahay, G., Alakhova, D.Y. and Kabanov, A. V 2010. Endocytosis of nanomedicines. *Journal of Controlled Release*. **145**,pp.182–195.

Salmon, B.A. and Siemann, D.W. 2007. Characterizing the Tumor Response to Treatment With Combretastatin A4 Phosphate. *International Journal of Radiation Oncology Biology Physics*. **68**(1),pp.211–217.

Samarin, J., Rehm, M., Krueger, B., Waschke, J. and Goppelt-Struebe, M. 2009. Up-Regulation of Connective Tissue Growth Factor in Endothelial Cells by the Microtubule-Destabilizing Agent Combretastatin A-4. *Molecular Cancer Research*. **7**(2),pp.180–188.

Sanhai, W.R., Sakamoto, J.H., Canady, R. and Ferrari, M. 2008. Seven challenges for nanomedicine. *Nature Nanotechnology*. **3**,pp.242–244.

Sano, H., Kawahito, Y., Wilder, R.L., Hashiramoto, A., Mukai, S., Asai, K., Kimura, S., Kato, H., Kondo, M. and Hla, T. 1995. Expression of Cyclooxygene-1 and -2 in Human Colorectal Cancer. *Cancer Research*. **55**,pp.3785–3790.

Segal, N.H. and Saltz, L.B. 2009. Evolving treatment of advanced colon cancer. *Annual review of medicine*. **60**,pp.207–219.

Seiler, G.S., Ziemer, L.S., Schultz, S., Lee, W.M.F. and Sehgal, C.M. 2007. Dose-response relationship of ultrasound contrast agent in an in vivo murine melanoma model. *Cancer imaging*. **7**,pp.216–223.

Selby, L.I., Cortez-Jugo, C.M., Such, G.K. and Johnston, A.P.R. 2017. Nanoescapology: progress toward understanding the endosomal escape of polymeric nanoparticles. *WIREs Nanomedicine and Nanobiotechnology*. **9**,pp.1–23.

Sengupta, S., Eavarone, D., Capila, I., Zhao, G., Watson, N., Kiziltepe, T. and Sasisekharan, R. 2005. Temporal targeting of tumour cells and neovasculature with a nanoscale delivery system. *Nature Letters*. **436**,pp.568–572.

Shaked, Y. 2006. Therapy-Induced Acute Recruitment of Circulating Endothelial Progenitor Cells to Tumors. *Science*. **313**(5794),pp.1785–1787.

Shen, C.H., Shee, J.J., Wu, J.Y., Lin, Y.W., Wu, J. Der and Liu, Y.W. 2010. Combretastatin A-4 inhibits cell growth and metastasis in bladder cancer cells and retards tumour growth in a murine orthotopic bladder tumour model. *British Journal of Pharmacology*. **160**,pp.2008–2027.

Shepherd, J., Fisher, M., Welford, A., Mcdonald, D.M., Kanthou, C. and Tozer, G.M. 2017. The protective role of sphingosine-1-phosphate against the action of the vascular disrupting agent combretastatin A-4 3- O - phosphate. *Oncotarget*. **8**(56),pp.95648–95661.

Sherbet, G. V 2017. Suppression of angiogenesis and tumour progression by combretastatin and derivatives. *Cancer Letters*. **403**,pp.289–295.

Shi, J., Kantoff, P.W., Wooster, R. and Farokhzad, O.C. 2016. Cancer nanomedicine: progress, challenges and opportunities. *Nature Reviews Cancer*. **17**,pp.20–37.

Siebert, A., Gensicka, M., Cholewinski, G. and Dzierzbicka, K. 2016. Synthesis of combretastatin A-4 analogs and their biological activities. *Anti-Cancer Agents in Medicinal Chemistry*. **16**(8),pp.942–960.

Siemann, D.W. 2011. The Unique Characteristics of Tumor Vasculature and Preclinical Evidence for its Selective Disruption by Tumor-Vascular Disrupting Agents. *Cancer Tretment Reviews*. **37**(1),pp.63–74.

Siemann, D.W., Chaplin, D.J. and Horsman, M.R. 2017. Realizing the Potential of Vascular Targeted Therapy: The Rationale for Combining Vascular Disrupting Agents and Anti-Angiogenic Agents to Treat Cancer. *Cancer Investigation*. **35**(8),pp.519–534.

Siemann, D.W., Mercer, E., Lepler, S. and Rojiani, A.M. 2002. Vascular targeting agents enhance chemotherapeutic agent activities in solid tumor therapy. *International Journal of Cancer*. **99**,pp.1–6.

Sing, R. and Lillard Jr, J.W. 2009. Nanoparticle-based targeted drug delivery. *Experimental and Molecular Pathology*. **86**(3),pp.215–223.

Singh, Y., Meher, J.G., Raval, K., Khan, F.A., Chaurasia, M., Jain, N.K. and Chourasia, M.K. 2017. Nanoemulsion: Concepts, development and applications in drug delivery. *Journal of Controlled Release*. **252**,pp.28–49.

Sirsi, S. and Borden, M. 2009. Microbubble Compositions, Properties and Biomedical Applications. *Bubble Science, Engineering & Technology*. **1**(1–2),pp.3–17.

Smith, K.A., Hill, S.A., Begg, A.C. and Denekamp, J. 1988. Validation of the fluorescent dye hoechst 33342 as a vascular space marker in tumours. *British Journal of Cancer*. **57**,pp.247–253.

Snipstad, S., Berg, S., Mørch, Ý., Bjørkøy, A., Sulheim, E., Hansen, R., Grimstad, I., van Wamel, A., Maaland, A.F., Torp, S.H. and Davies, C. de L. 2017. Ultrasound Improves the Delivery and Therapeutic Effect of Nanoparticle-Stabilized Microbubbles in Breast Cancer Xenografts. *Ultrasound in Medicine and Biology*. **43**(11),pp.2651–2669.

Sobhani, H., Tarighi, P., Ostad, S.N., Shafaati, A., Nafissi-Varcheh, N. and Aboofazeli, R. 2015. Formulation development and toxicity assessment of triacetin mediated nanoemulsions as novel delivery systems for rapamycin.

Iranian Journal of Pharmaceutical Research. **14**,pp.3–21.

Stevenson, J.P., Rosen, M., Sun, W., Gallagher, M., Haller, D.G., Vaughn, D., Giantonio, B., Zimmer, R., Petros, W.P., Stratford, M., Chaplin, D., Young, S.L., Schnall, M. and O'Dwyer, P.J. 2003. Phase I trial of the antivascular agent combretastatin A4 phosphate on a 5-day schedule to patients with cancer: Magnetic resonance imaging evidence for altered tumor blood flow. *Journal of Clinical Oncology*. **21**,pp.4428–4438.

Strassburg, C.P., Manns, M.P. and Tukey, R.H. 1998. Expression of the UDP-glucuronosyltransferase 1A locus in human colon. *The Journal of biological chemistry*. **273**(15),pp.8719–8726.

Strassburg, C.P., Nguyen, N., Manns, M.P. and Tukey, R.H. 1999. UDP-glucuronosyltransferase activity in human liver and colon. *Gastroenterology*. **116**(1),pp.149–160.

Stride, E. and Edirisinghe, M. 2008. Novel microbubble preparation technologies. *Soft Matter*. **4**,p.2350.

Su, T., Long, Y., Deng, C., Feng, L., Zhang, X., Chen, Z. and Li, C. 2014. Construction of a two-in-one liposomal system (TWOLips) for tumor-targeted combination therapy. *International Journal of Pharmaceutics*. **476**,pp.241–252.

Talu, E., Lozano, M.M., Powell, R.L., Dayton, P.A. and Longo, M.L. 2006. Long-term stability by lipid coating monodisperse microbubbles formed by a flow-focusing device. *Langmuir*. **22**,pp.9487–9490.

Tartis, M.S., McCallan, J., Lum, A.F.H., LaBell, R., Stieger, S.M., Matsunaga, T.O. and Ferrara, K.W. 2006. Therapeutic effects of paclitaxel-containing ultrasound contrast agents. *Ultrasound in Medicine and Biology*. **32**(11),pp.1771–1780.

Teboul, E. and Chouinard, G. 1990. A guide to benzodiazepine selection. Part I: Pharmacological aspects. *Canadian Journal of Psychiatry*. **35**(8),pp.700–710.

Thomas, C.D., Walczak, C., Kaffy, J., Pontikis, R., Jouanneau, J. and Volk, A. 2006. Early effects of combretastatin A4 phosphate assessed by anatomic and carbogen-based functional magnetic resonance imaging on rat bladder tumors implanted in nude mice. *Neoplasia*. **8**(7),pp.587–595.

Tochinai, R., Nagata, Y., Ando, M., Hata, C., Suzuki, T., Asakawa, N., Yoshizawa, K., Uchida, K., Kado, S., Kobayashi, T., Kaneko, K. and Kuwahara, M. 2016. Combretastatin A4 disodium phosphate-induced myocardial injury. *Journal of Toxicologic Pathology*. **29**,pp.163–171.

Torne, S.J., Ansari, K.A., Vavia, P.R., Trotta, F. and Cavalli, R. 2010. Enhanced oral paclitaxel bioavailability after administration of paclitaxel-loaded nanosponges. *Drug Delivery*. **17**(6),pp.419–425.

Touil, Y.S., Fellous, A., Scherman, D. and Chabot, G.G. 2009. Flavonoid-induced morphological modifications of endothelial cells through microtubule stabilization. *Nutrition and Cancer*. **61**(3),pp.310–321.

Toutain, P.L. and Bousquet-Mélou, A. 2004. Plasma terminal half-life. *Journal of Veterinary Pharmacology and Therapeutics*. **27**,pp.427–439.

Tozer, G.M., Kanthou, C. and Baguley, B.C. 2005. Disrupting tumour blood vessels.

Nature reviews. Cancer. **5**,pp.423–435.

Tozer, G.M., Kanthou, C., Parkins, C.S. and Hill, S.A. 2002. The biology of the combretastatins as tumour vascular targeting agents. *International Journal of Experimental Pathology*. **83**,pp.21–38.

Tozer, G.M., Prise, V.E., Wilson, J., Cemazar, M., Shan, S., Dewhirst, M.W., Barber, P.R., Vojnovic, B. and Chaplin, D.J. 2001. Mechanisms Associated with Tumor Vascular Shut-Down Induced by Combretastatin A-4 Phosphate : Intravital Microscopy and Measurement of Vascular Permeability. *Cancer Research*. **61**,pp.6413–6422.

Tozer, G.M., Prise, V.E., Wilson, J., Locke, R.J., Vojnovic, B., Stratford, M.R.L., Dennis, M.F. and Chaplin, D.J. 1999. Combretastatin A-4 Phosphate as a Tumor Vascular-Targeting Agent : Early Effects in Tumors and Normal Tissues. *Cancer Research*. **59**,pp.1626–1634.

Tran, S., DeGiovanni, P.-J., Piel, B. and Rai, P. 2017. Cancer nanomedicine: a review of recent success in drug delivery. *Clinical and Translational Medicine*. **6**(44),pp.1–21.

Tripodi, F., Pagliarin, R., Fumagalli, G., Bigi, A., Fusi, P., Orsini, F., Frattini, M. and Coccetti, P. 2012. Synthesis and biological evaluation of 1,4-diaryl-2-azetidinones as specific anticancer agents: Activation of adenosine monophosphate activated protein kinase and induction of apoptosis. *Journal of Medicinal Chemistry*. **55**,pp.2112–2124.

Tron, G.C., Pirali, T., Sorba, G., Pagliai, F., Busacca, S. and Genazzani, A.A. 2006. Medicinal chemistry of combretastatin A4: Present and future directions. *Journal of Medicinal Chemistry*. **49**(11),pp.3033–3044.

Tseng, W., Leong, X. and Engleman, E. 2007. Orthotopic Mouse Model of Colorectal Cancer. *Journal of Visualized Experiments*. **484**(10),pp.1–4.

Turner, P. V, Brabb, T., Pekow, C. and Vasbinder, M.A. 2011. Administration of substances to laboratory animals: routes of administration and factors to consider. *Journal of the Amarican Association for Laboratory Animal Science*. **50**(5),pp.600–613.

U.S. Department of Health and Human Services Food and Drug Administration 2013. Guidance for Industry: Bioanalytical Method Validation. *FDA*. [Online]. (May),pp.240–276. Available from: https://www.fda.gov/downloads/drugs/guidances/ucm070107.Pdf.

U.S. Department of Health and Human Services Food and Drug Administration 2017. Guidance for Industry on Drug Products, Including Biological Products, that Contain Nanomaterials. *FDA*. [Online]. (December). [Accessed 1 March 2018]. Available from: https://www.fda.gov/downloads/Drugs/GuidanceComplianceRegulatoryInformation/Guidances/UCM588857.pdf.

U.S. Department of Health and Human Services Food and Drug Administration 2005. Guidance for Industry Starting Dose in Initial Clinical Trials Guidance for Industry Estimating the Maximum Safe. *FDA*. [Online]. (July). Available from: https://www.fda.gov/downloads/Drugs/Guidances/UCM078932.pdf%23search=%27guidekines+for+industry+sfe+starting%27.

Unger, E.C., McCreery, T.P., Sweitzer, R.H., Caldwell, V.E. and Yunqiu, W. 1998. Acoustically Active Lipospheres Containing Paclitaxel : A New Therapeutic Ultrasound Contrast Agent. *Investigative Radiology*. **33**(12),pp.886–892.

Vakifahmetoglu, H., Olsson, M. and Zhivotovsky, B. 2008. Death through a tragedy: Mitotic catastrophe. *Cell Death and Differentiation*. **15**(7),pp.1153–1162.

Valencia, P.M., Hanewich-Hollatz, M.H., Gao, W., Karim, F., Langer, R., Karnik, R. and Farokhzad, O.C. 2011. Effects of ligands with different water solubilities on self-assembly and properties of targeted nanoparticles. *Biomaterials*. **32**,pp.6226–6233.

Valtorta, S., Nicolini, G., Tripodi, F., Meregalli, C., Cavaletti, G., Avezza, F., Crippa, L., Bertoli, G., Sanvito, F., Fusi, P., Pagliarin, R., Orsini, F., Moresco, R.M. and Coccetti, P. 2014. A novel AMPK activator reduces glucose uptake and inhibits tumor progression in a mouse xenograft model of colorectal cancer. *Investigational New Drugs*. **32**(6),pp.1123–1133.

Varenne, F., Makky, A., Gaucher-Delmas, M., Violleau, F. and Vauthier, C. 2016. Multimodal Dispersion of Nanoparticles: A Comprehensive Evaluation of Size Distribution with 9 Size Measurement Methods. *Pharmaceutical Research*. **33**,pp.1220–1234.

Ventola, C.L. 2017. Progress in Nanomedicine: Approved and Investigational Nanodrugs. *Pharmacy and Therapeutics*. **42**(12),pp.742–755.

Vilar, E. and Gruber, S.B. 2010. Microsatellite instability in colorectal cancerthe stable evidence. *Nature Reviews Clinical Oncology*. **7**,pp.153–162.

Villanueva, F.S., Jankowski, R.J., Klibanov, S., Pina, M.L., Alber, S.M., Watkins, S.C., Brandenburger, G.H. and Wagner, W.R. 1998. Microbubbles Targeted to Intercellular Adhesion Molecule-1 Bind to Activated Coronary Artery Endothelial Cells. *Circulation*. **98**,pp.1–5.

Vincent, L., Kermani, P., Young, L.M., Cheng, J., Zhang, F., Shido, K., Lam, G., Bompais-Vincent, H., Zhu, Z., Hicklin, D.J., Bohlen, P., Chaplin, D.J., May, C. and Rafii, S. 2005. Combretastatin A4 phosphate induces rapid regression of tumor neovessels and growth through interference with vascular endothelial-cadherin signaling. *Journal of Clinical Investigation*. **115**(11),pp.2992–3006.

Vitale, I., Antoccia, A., Cenciarelli, C., Crateri, P., Meschini, S., Arancia, G., Pisano, C. and Tanzarella, C. 2007. Combretastatin CA-4 and combretastatin derivative induce mitotic catastrophe dependent on spindle checkpoint and caspase-3 activation in non-small cell lung cancer cells. *Apoptosis*. **12**,pp.155–166.

Vitale, I., Galluzzi, L., Castedo, M. and Kroemer, G. 2011. Mitotic catastrophe: a mechanism for avoiding genomic instability. *Nature reviews. Molecular cell biology*. **12**(6),pp.385–392.

Vogelstein, B., Fearon, E.R., Hamilton, S.R., Kern, S.E., Preisinger, A.C., Leppert, M., Nakamura, Y., White, R., Smits, A.M.M. and Bos, J.L. 1988. Genetic Alterations During Colorectal-Tumour Development. *The New England Journal of Medicine*. **319**(9),pp.525–532.

Vogelstein, B., Papadopoulos, N., Velculescu, V.E., Zhou, S., Diaz Jr, L.A. and Kinzler, K.W. 2013. Cancer Genome Landscapes. *Science*. **339**,pp.1546–1558.

Wakaskar, R.R., Bathena, S.P.R., Tallapaka, S.B., Ambardekar, V. V, Gautam, N., Thakare, R., Simet, S.M., Curran, S.M., Singh, R.K., Dong, Y. and Vetro, J.A. 2015. Peripherally cross-linking the shell of core-shell polymer micelles decreases premature release of physically loaded combretastatin A4 in whole blood and increases its mean residence time and subsequent potency against primary murine breast tumors after I. *Pharmaceutical Research*. **32**,pp.1028–1044.

Walther, A., Johnstone, E., Swanton, C., Midgley, R., Tomlinson, I. and Kerr, D. 2009. Genetic prognostic and predictive markers in colorectal cancer. *Nature Reviews Cancer*. **9**,pp.489–499.

van Wamel, A., Kooiman, K., Harteveld, M., Emmer, M., ten Cate, F.J., Versluis, M. and de Jong, N. 2006. Vibrating microbubbles poking individual cells: Drug transfer into cells via sonoporation. *Journal of Controlled Release*. **112**(2),pp.149–155.

Wang, X., Chen, Z., Che, J., Meng, Q., Shan, C., Hou, Y., Liu, X., Chai, Y. and Cheng, Y. 2009. Development of a rapid and sensitive LC-MS/MS assay for the determination of combretastatin A4 phosphate, combretastatin A4 and combretastatin A4 glucuronide in beagle dog plasma and its application to a pharmacokinetic study. *Journal of Chromatography B*. **877**,pp.3813–3821.

Wang, Y., Chen, H., Liu, Y., Wu, J., Zhou, P., Wang, Y., Li, R., Yang, X. and Zhang, N. 2013. PH-sensitive pullulan-based nanoparticle carrier of methotrexate and combretastatin A4 for the combination therapy against hepatocellular carcinoma. *Biomaterials*. **34**,pp.7181–7190.

Wang, Y. and Kohane, D.S. 2017. External triggering and triggered targeting strategies for drug delivery. *Nature Reviews Materials*. **2**,pp.1–14.

Wang, Y., Yang, T., Wang, X., Wang, J., Zhang, X. and Zhang, Q. 2010. Targeted polymeric micelle system for delivery of combretastatin A4 to tumor vasculature in vitro. *Pharmaceutical Research*. **27**,pp.1861–1868.

Wang, Z. and Ho, P.C. 2010. Self-assembled core-shell vascular-targeted nanocapsules for temporal antivasculature and anticancer activities. *Small*. **6**(22),pp.2576–2583.

Welch, H.G. and Robertson, D.J. 2016. Colorectal Cancer on the Decline - Why Screening Can't Explain It All. *New England Journal of Medicine*. **374**(17),pp.1604–1605.

Wildiers, H., Ahmed, B., Guetens, G., De Boeck, G., de Bruijn, E.A., Landuyt, W. and van Oosterom, A.T. 2004. Combretastatin A-4 phosphate enhances CPT-11 activity independently of the administration sequence. *European Journal of Cancer*. **40**,pp.284–290.

Wildiers, H., Guetens, G., De Boeck, G., Verbeken, E., Landuyt, B., Landuyt, W., De Bruijn, E.A. and Van Oosterom, A.T. 2003. Effect of antivascular endothelial growth factor treatment on the intratumoral uptake of CPT-11. *British Journal of Cancer*. **88**(12),pp.1979–1986.

Wilhelm, S., Tavares, A.J., Dai, Q., Ohta, S., Audet, J., Dvorak, H.F. and Chan, W.C.W. 2016. Analysis of nanoparticle delivery to tumours. *Nature Reviews Materials*. **1**,pp.1–12.

Willett, C.G., Boucher, Y., Di Tomaso, E., Duda, D.G., Munn, L.L., Tong, R.T., Chung, D.C., Sahani, D. V, Kalva, S.P., Kozin, S. V, Mino, M., Cohen, K.S., Scadden, D.T., Hartford, A.C., Fischman, A.J., Clark, J.W., Ryan, D.P., Zhu, A.X., Blaszkowsky, L.S., Chen, H.X., Shellito, P.C., Lauwers, G.Y. and Jain, R.K. 2004. Direct evidence that the VEGF-specific antibody bevacizumab has antivascular effects in human rectal cancer. *Nature Medicine*. **10**(2),pp.145–147.

Williams, L.J., Mukherjee, D., Fisher, M., Reyes-Aldasoro, C.C., Akerman, S., Kanthou, C. and Tozer, G.M. 2014. An in vivo role for Rho kinase activation in the tumour vascular disrupting activity of combretastatin A-4 3-O-phosphate. *British Journal of Pharmacology*. **171**(21),pp.4902–4913.

Willmann, J.K., Bonomo, L., Testa, A.C., Rinaldi, P., Rindi, G., Valluru, K.S., Petrone, G., Martini, M., Lutz, A.M. and Gambhir, S.S. 2017. Ultrasound molecular imaging with BR55 in patients with breast & ovarian lesions: First-in-human results. *Journal of Clinical Oncology*. **35**,pp.2133–2140.

Willmann, J.K., Paulmurugan, R., Chen, K., Gheysens, O., Rodriguez-Porcel, M., Lutz, A.M., Chen, I.Y., Chen, X. and Gambhir, S.S. 2008. US Imaging of Tumor Angiogenesis with Microbubbles Targeted to Vascular Endothelial Growth Factor Receptor Type 2 in Mice. *Radiology*. **246**(2),pp.508–518.

Wolpin, B.M. and Mayer, R.J. 2009. Systemic Treatment of Colorectal Cancer. *Gastroenterology*. **134**(5),pp.1296–1310.

Wooster, T.J., Golding, M. and Sanguansri, P. 2008. Impact of Oil Type on Nanoemulsion Formation and Ostwald Ripening Stability. *Langmuir*. **24**,pp.12758–12765.

Xu, X.P., Wu, X.D., Liang, G.L., Huang, W.S., Wang, L., Jing, H.Y. and Zhong, S.L. 2012. Pharmacokinetics, excretion, and distribution of combretastatin A4 phosphate in rats. *Pharmazie*. **67**,pp.529–533.

Yang, F., Gu, N., Chen, D., Xi, X., Zhang, D., Li, Y. and Wu, J. 2008. Experimental study on cell self-sealing during sonoporation. *Journal of Controlled Release*. **131**,pp.205–210.

Yang, T., Wang, Y., Li, Z., Dai, W., Yin, J., Liang, L., Ying, X., Zhou, S., Wang, J., Zhang, X. and Zhang, Q. 2012. Targeted delivery of a combination therapy consisting of combretastatin A4 and low-dose doxorubicin against tumor neovasculature. *Nanomedicine: Nanotechnology, Biology, and Medicine*. **8**,pp.81–92.

Yao, N., Ren, K., Jiang, C., Gao, M., Huang, D., Lu, X., Lou, B., Peng, F., Yang, A., Wang, X., Ni, Y. and Zhang, J. 2015. Combretastatin A4 phosphate treatment induces vasculogenic mimicry formation of W256 breast carcinoma tumor in vitro and in vivo. *Tumor Biology*. **36**(11),pp.8499–8510.

Yeung, S.C.J., She, M., Yang, H., Pan, J., Sun, L. and Chaplin, D. 2007. Combination chemotherapy including combretastatin A4 phosphate and paclitaxel is effective against anaplastic thyroid cancer in a nude mouse xenograft model. *Journal of Clinical Endocrinology and Metabolism*. **92**(8),pp.2902–2909.

Yokoi, K., Tanei, T., Godin, B., van de Ven, A.L., Hanibuchi, M., Matsunoki, A., Alexander, J. and Ferrari, M. 2014. Serum biomarkers for personalization of

nanotherapeutics-based therapy in different tumor and organ microenvironments. *Cancer Letters*. **345**,pp.48–55.

Yu, B., Tai, H.C., Xue, W., Lee, L.J. and Lee, R.J. 2010. Receptor-targeted nanocarriers for therapeutic delivery to cancer. *Molecular Membrane Biology*. **27**(7),pp.286–298.

Yuan, Y.Y., Mao, C.Q., Du, X.J., Du, J.Z., Wang, F. and Wang, J. 2012. Surface charge switchable nanoparticles based on zwitterionic polymer for enhanced drug delivery to tumor. *Advanced Materials*. **24**,pp.5476–5480.

Zhang, J., Lu, A., Beech, D., Jiang, B. and Lu, Y. 2007. Suppresion of breast cancer metastasis through the inhibition of VEGF-mediated tumour angiogenesis. *Cancer Therapy*. **5**,pp.273–286.

Zhang, M., Guo, R., Wang, Y., Cao, X., Shen, M. and Shi, X. 2011. Multifunctional dendrimer/combretastatin A4 inclusion complexes enable in vitro targeted cancer therapy. *International journal of nanomedicine*. **6**,pp.2337–2349.

Zhang, P., Chen, Y., Liu, J.F., Yang, Y., Lv, Q., Wang, J., Zhang, L. and Xie, M. 2018. Quantitative Evaluation of Combretastatin A4 Phosphate Early Efficacy in a Tumor Model with Dynamic Contrast-Enhanced Ultrasound. *Ultrasound in Medicine and Biology*. **44**(4),pp.840–852.

Zhang, Y., Shang, Z., Gao, C., Du, M., Xu, S., Song, H. and Liu, T. 2014. Nanoemulsion for Solubilization, Stabilization, and In Vitro Release of Pterostilbene for Oral Delivery. *AAPS PharmSciTech*. **15**(4),pp.1000–1008.

Zhang, Y., Wang, J., Bian, D., Zhang, X. and Zhang, Q. 2010. Targeted delivery of RGD-modified liposomes encapsulating both combretastatin A-4 and doxorubicin for tumor therapy : In vitro and in vivo studies. *European Journal of Pharmaceutics and Biopharmaceutics*. **74**,pp.467–473.

Zhao, D., Jiang, L., Hahn, E.W. and Mason, R.P. 2005a. Tumor physiologic response to combretastatin A4 phosphate assessed by MRI. *International Journal of Radiation Oncology Biology Physics*. **62**(3),pp.872–880.

Zhao, Y.Z., Liang, H.D., Mei, X.G. and Halliwell, M. 2005b. Preparation, Characterization and In vivo Observation of Phospholipid-Based Gas-Filled Microbubbles containing Hirudin. *Ultrasound in Medicine and Biology*. **31**(9),pp.1237–1243.

Zhou, Y., Yang, K., Cui, J., Ye, J.Y. and Deng, C.X. 2012. Controlled permeation of cell membrane by single bubble acoustic cavitation. *Journal of Controlled Release*. **157**,pp.103–111.